

Fall 12-18-2015

Electromechanics of an Ocean Current Turbine

Vasileios Tzelepis
University of New Orleans, vtzelepi@uno.edu

Follow this and additional works at: <https://scholarworks.uno.edu/td>



Part of the [Controls and Control Theory Commons](#), [Dynamics and Dynamical Systems Commons](#), [Electrical and Electronics Commons](#), [Electro-Mechanical Systems Commons](#), [Engineering Mechanics Commons](#), [Ocean Engineering Commons](#), [Operations Research](#), [Systems Engineering and Industrial Engineering Commons](#), and the [Power and Energy Commons](#)

Recommended Citation

Tzelepis, Vasileios, "Electromechanics of an Ocean Current Turbine" (2015). *University of New Orleans Theses and Dissertations*. 2112.
<https://scholarworks.uno.edu/td/2112>

This Thesis is protected by copyright and/or related rights. It has been brought to you by ScholarWorks@UNO with permission from the rights-holder(s). You are free to use this Thesis in any way that is permitted by the copyright and related rights legislation that applies to your use. For other uses you need to obtain permission from the rights-holder(s) directly, unless additional rights are indicated by a Creative Commons license in the record and/or on the work itself.

This Thesis has been accepted for inclusion in University of New Orleans Theses and Dissertations by an authorized administrator of ScholarWorks@UNO. For more information, please contact scholarworks@uno.edu.

Electromechanics of an Ocean Current Turbine

A Thesis

Submitted to the Graduate Faculty of the
University of New Orleans
in partial fulfillment of the
requirement for the degree of

Master of Science
in
Engineering

by

Vasileios Tzelepis

B.Sc. Technological Educational Institute of Athens, 2012

December, 2015

Copyright 2015, VASILEIOS TZELEPIS

Cambay's Water

Sailing down the river with the anchors down.
Our navigator had his forehead painted
"and if you are away I'll be waiting for you for 1000 years"
however the ropes stiffened your palm.

Blurry waters and the current for four miles
the coolies eat secretly rice with curry
our captain looks at the moon
which is blurry and red like blood.

The tugboat blew three times and continued
for forty days you were counting the miles
but today you had cobra poison on your lips
when you said "I'm coming out another day" angrily.

At night I told you a story at the forecastle
the same one that all sailors narrate at the port
your eyes were dominated by Sirocco
and you were mumbling all the time "Wrong way".

We're off! We are waited for in Brazil.
Your face must have been wet by cold wind.
The bogaz transmits hot breeze
but neither a skirt in the shore nor a handkerchief.

Nikos Kavvadias

To all the people who love the sea....
and to my parents, who allow me to
dream....

Acknowledgments

I would like to exclusively acknowledge my graduate studies mentor and advisor **Dr. Nikolaos Xiros** for always having the patience, serenity and knowledge to guide me complete this thesis on time and for his unceasing assistance from the first moment I arrived in USA.

I would like also to acknowledge **Dr. James VanZwieten**, research professor at Florida Atlantic University (FAU) and at Southeast National Marine Renewable Energy Center (SNMREC), for helping me with his tremendous knowledge about ocean current technology and also **United States National Science Foundation** (US NSF) for granting this thesis.

On a different note, I should like to particularly mention my wife, **Gloria Nathalie Calderon Garcia**, who supports me and especially state her compromise with my love for that science.

Table of Contents

List of Figures	ix
List of Tables	xx
Abstract	xxi
Chapter 1	1
Introduction.....	1
1.1 Ocean Current Energy.....	1
1.1.1 Current phenomena explanation	1
1.1.2 Resource potential.....	2
1.2 Resource Utilization Technology.....	3
1.2.1 Principle of work.....	4
1.2.2 Anchoring/Mooring Systems and Locations.....	5
1.2.3 Environmental Considerations	6
1.2.4 Economic Considerations	6
1.2.5 Challenges.....	6
1.3 Projects in the World	8
1.3.1 Real Projects and Tidal/Current Turbines.....	8
1.3.2 Projects in Progress.....	13
1.3.3 Southern National Marine Renewable Energy Center (SNMREC)	19
1.4 Generator and Drive-Train Options	21
1.5 Thesis Outline	24
Chapter 2	25
Induction Motors/Generators	25
2.1 Introduction.....	25
2.2 Principles of Design and Operation	25
2.2.1 Basic Construction	25
2.2.2 Stator	26
2.2.3 Rotor (Armature)	27
2.2.4 Number of Poles and Speed	29
2.2.5 Operating Principle of Three (3) Phase.....	31
2.2.5.1 Rotating Magnetic Field.....	31
2.2.5.2 Production of Rotating Magnetic Field.....	32
2.2.5.3 Resultant 3-Phase Field.....	35
2.2.6 Main (Air-Gap) Flux and Leakage Flux	36
2.2.7 Types of AC Induction Motors	36
2.2.7.1 Single-Phase.....	36

2.2.7.2 Three-Phase.....	36
2.2.7.2.1 Squirrel Cage Rotor	41
2.2.7.2.2 Wound Rotor.....	42
2.2.8 Load Characteristics.....	43
2.2.9 Efficiency and Losses	45
2.2.10 Typical Nameplate	46
2.3 Modeling in MATLAB/Simulink®	48
2.3.1 Model Description	48
2.3.2 Model Assumptions	48
2.3.3 Numerical Model	49
2.4 Case Studies.....	53
2.4.1 Case Study I – IG for 20kW OCT.....	53
2.4.1.1 Steady State with Zero Load	53
2.4.1.2 Steady State with Load	54
2.4.1.3 Transient.....	57
2.4.2 Case Study II – IG for 720kW OCT	62
2.4.2.1 Steady State with Zero Load	62
2.4.2.2 Steady State with Load	63
2.4.2.3 Transient.....	68
Chapter 3.....	72
Control of Induction Motors/Generators.....	72
3.1 Classical Steady State Representation of an Induction Machine	72
3.1.1 Steady State Equivalent Circuit	72
3.1.2 Analysis of the Equivalent Circuit	76
3.1.3 Torque and Power by Use of Thevenin’s Theorem	79
3.1.4 Equivalent Circuit under Variable-Frequency Conditions.....	82
3.2 Speed and Torque Control of Induction Motors/Generators.....	82
3.2.1 Scalar Control	83
3.2.1.1 CATEGORY I – Conventional Methods	83
3.2.1.2 CATEGORY II – Methods using Power Electronics.....	86
3.2.2 Vector Control.....	92
3.2.1.1 CATEGORY I – Fully Commercialized.....	93
3.2.1.2 CATEGORY II – Not Fully Commercialized	94
3.2.3 Sensorless Control.....	94
3.2.4 Intelligent Control	94
3.3 Voltage Source Inverter (VSI) with Pulse Width Modulation (PWM) Technique (AC-DC-AC).....	95

3.3.1 Three-Phase Full Wave Rectifier with Diodes.....	96
3.3.2 Intermediate Circuit (DC Link).....	97
3.3.3 Three-Phase Inverter	97
3.3.4 Harmonic Attenuation by a LC Filter	98
3.3.5 Pulse Width Modulation Method	99
3.3.5.1 Sinusoidal Pulse Width Modulation.....	99
3.3.5.2 Operating Principle of VSI with SPWM.....	100
3.3.6 Constant V/f Ratio Control with VSI.....	101
3.4 VSI in MATLAB/Simulink® for the 720 kW OCT	103
3.4.1 Model Description.....	103
3.4.2 Numerical Results	106
3.5 Simplified Version of VSI in MATLAB/Simulink®.....	110
Chapter 4.....	113
Modeling, Control and Simulation of an Overall Ocean Current Energy Conversion System.....	113
4.1 The Ocean Current Energy Conversion System (OCECS).....	113
4.2 Modeling of OCECS in MATLAB/Simulink®	115
4.2.1 Numerical Models and Description	115
4.2.1.1 The OCT Model (Rigidly Mounted).....	116
4.2.1.2 The SCIG Model and the Gearbox.....	117
4.2.1.3 The Shafting System Vibrational Model.....	117
4.2.1.4 The Power Controller (PID Block)	120
4.3 OCECS Simulation Results	122
4.3.1 Scenario I ($V_c = 1$ m/s).....	122
4.3.2 Scenario II ($V_c = 2$ m/s)	129
4.3.3 Estimation of Average Electric Power Generation	136
Chapter 5.....	139
Conclusions and Future Work.....	139
References/Bibliography.....	141
Appendices.....	151
Appendix A: Comparison with Other Renewable Energy Sources and Economic Consideration	151
Appendix B: National Electrical Manufacturers Association (NEMA).....	153
Appendix C: Amplitude-Preservation-Based Park Transformation.....	155
Appendix D: Inputs of Induction Motor/Generator Block in MATLAB/Simulink®.....	156
Appendix E: Tests to Determine Equivalent Circuit Model Parameters	157

Appendix F: Switching Configuration of a SPWP Three Phase Inverter with Space Vector Technique	158
Appendix G:.....	162
Part I – Derivation of Fourier Series Formula for the Square Wave Inverter Voltages	162
Part II – Formula for the SPWM Inverter Voltages	165
Appendix H: Average Electric Power Generation and MATLAB Code	167
Vita.....	169

List of Figures

Figure 1: A summary of the path of the thermohaline circulation. Blue paths represent deep-water currents, while red paths represent surface currents. (Source: NASA Earth Observatory [3]).....	1
Figure 2: Major ocean currents of the world. On this illustration red arrows indicate warm currents, while cold currents are displayed in blue (Source: M. Pidwirny [4]).....	2
Figure 3: Ocean currents in the vicinity of the United States (Source: University of Texas libraries [5])...	3
Figure 4: : A general example of ocean current turbine components based on tidal turbine technology by Verdant Power (left, Source: Ecopedia [11]) and visualization of an underwater cluster of ocean tidal turbines (right, Source: FAU [12]).....	4
Figure 5: Four typical kinetic energy conversion devices (Source: EPRI Ocean Energy Program [13])	4
Figure 6: Schematic of fluid flow through a disk-shaped actuator where A:area, v:velocity. For a constant density fluid, cross sectional area varies inversely with speed (Source: Wikipedia [15])	5
Figure 7: World primary energy consumption (Source: BP [25])	7
Figure 8: SeaFlow turbine. The left picture shows the system in operational mode while the right one shows us the pile and the rotor “roses up for maintenance” (Source: MCT Ltd [27]).....	8
Figure 9: SeaGen S turbine (left), demonstration of SeaGen S operation (right up) and visualization of SeaGen Array farm (right, down) (Source: Sea Generation Ltd [29]).....	9
Figure 10: TidGen power system without dimensions (Source: ORPC [31])	9
Figure 11: Visualization of TidGen power system (Source: ORPC [31])	10
Figure 12: First GEM model of towing tank test (up left and right) and second GEM model for towing tank test (bottom left and right) (Source: ADAG [32])	10
Figure 13: Visualization of GEM turbine (left) and full-scale prototype of GEM (right) (Source: ADAG [33]).....	11
Figure 14: GEM alignment demonstration to the current direction (Source: ADAG [33])	11
Figure 15: Deep Green kite-like turbine components (Source: Minesto [34])	12
Figure 16: Deep Green principle of work (Source: Minesto [35]).....	12
Figure 17: Close-up perspective view of Florida Hydro’s conceptual design for one ocean current turbine that is tethered to the seafloor on adjustable cables to provide repositioning for maintenance service and to maximize capture of high flow velocities (Source: C.W. Finkl and R. Charlier [19]).....	13
Figure 18: Panoramic view of Florida Hydro’s conception of ocean current turbines that could be tethered to the seafloor in groups to form marine current farms of up to eight turbines spread over about 2.6 km ² (Source: C.W. Finkl and R. Charlier [19]).....	13
Figure 19: 3D Rendering of OCGen power system (Source: ORPC [31])	14
Figure 20: The 1-MW turbine of Triton (Source: Triton Submarines LLC [40]).....	14
Figure 21: Crowd Energy full-scale prototype (Source: Crowd Energy [41])	15
Figure 22: Demonstration of ocean current turbine system by IHI and Toshiba (Source: IHI [42]).....	16

Figure 23: NCKU ocean current turbine to be moored in the Pacific Ocean off Jinzun Harbor, Taitung County (left and right) (Source: NCKU-SERC [45])	16
Figure 24: Demonstration of Aquantis C-Plane ocean current turbine (Source: Aquantis [50])	17
Figure 25: Captured test of 1/25 th scale model (Source: H. Swales et al. [49])	17
Figure 26: The fin ring propeller in a 1/5 th scale (2.43 Meter) under testing in a towing tank (Source: W.D. Bolin [51])	18
Figure 27: Four fin-ring propeller system prior to submerged testing in the Gulf of Mexico (left and right) (Source: W.D. Bolin [51])	18
Figure 28: THOR's renewable ocean current turbine (Source: THOR LLC [52])	18
Figure 29: Diagrammatic representation of the Ocean Current Turbine Testbed (OCTT) with a OCDP (left) or a Deployment Vessel (right) (Source: F.R. Driscoll et al. [55])	19
Figure 30: The completed Mooring and Telemetry Buoy (MTB) on stands (left) and without A-frame, hydraulic, and electronic systems (right) (Source: F.R. Driscoll et al. [55])	19
Figure 31: Solid model rendering of the negatively buoyant SNMREC's 20kW 1.6m radius experimental research turbine (left) and neutrally buoyant (right). The rotor blades are not accurately drawn in this Rendering (Source: F.R. Driscoll et al. [55] and J.H. VanZwieten et al. [56])	20
Figure 32: Rendition of the SNMREC's proposed offshore test configuration. "MTB" refers to the buoy (Mooring and Telemetry Buoy) which acts both as a mooring point and persistent environmental measurement platform (Source: M. Borghi et al. [59])	21
Figure 33: SNMREC's research vessel during transportation of the research ocean current turbine offshore Fort Pierce for sea testing (left) and a state of the art rendering SNMREC's experimental turbine, a typical axial-flow configuration with stabilizing buoyancy pods, in operation (right) (Source: FAU SNMREC [53])	21
Figure 34: Principle scheme of ocean current turbine system (Source: M.S. Guney and K. Kaygusuz [67])	22
Figure 35: AC Wound type Induction machine exploded view (left) and AC Permanent magnet machine cutaway view (right) (Source: Leeson Electric Corporation [69])	23
Figure 36: A cutaway basic parts description (left) and breakdown detailed description (right) of a typical three-phase induction motor (Source: Electromotors WEG SA, Brazil [73])	26
Figure 37: Stator windings partially completed (left) and completed (right) (Source: Electrical-Know-How [74])	26
Figure 38: Stator lamination (Source: Electrical-Know-How [74])	26
Figure 39: Form wound coils (left) and random wound coils (right) (Source: Kato Engineering Inc. [75])	27
Figure 40: Different types of stator slots: Semi-closed (left), Open (middle) and Tapered (right) (Source: V-Tech e-Notes [76])	27

Figure 41: Squirrel cage induction rotor (left) and wound type induction rotor (right) (Source: U.S. DOE [77])	28
Figure 42: 3D solid model of squirrel single cage rotor's bars with three iron cores (Sources: Wikipedia [78]).....	28
Figure 43: Squirrel single-cage rotor slots: open type (left) and closed type (right) (Source: W. Tong [75])	29
Figure 44: Cross sectional view of a typical induction motor (Source: EEP [82])	29
Figure 45: Three-phase generator: 24 poles of 18 coils with 80 turns each and 6 coils in each phase connected in series (Source: Instructables [83])	30
Figure 46: Synchronous speed (y-axis) versus number of pole pairs (x-axis) for 50Hz and 60Hz system frequency (Source: W. Tong [75]).....	30
Figure 47: Flux pattern in a 4-pole induction motor at three successive instants of time, each one-quarter of a cycle apart (left) and radial flux density distribution in the air-gap at the three instants shown in the left (right) (Source: A. Hughes and B. Drury [84])	32
Figure 48: Star (wye) and delta (mesh) connection of the three phase-windings of a 3-phase induction motor (Source: A. Hughes and B. Drury [84])	32
Figure 49: Arrangement (up) and developed diagram (down) showing elementary 4-pole, single-layer stator winding consisting of four conductors spaced by 90°. The 'go' side of each coil (shown by the plus symbol) carries current into the paper at the instant shown, while the 'return' side (shown by the dot) carries current out of the paper (Source: A. Hughes and B. Drury [84])	33
Figure 50: Developed diagram showing flux density produced by one phase of a single-layer winding having three slots per pole per phase (Source: A. Hughes and B. Drury [84]).....	33
Figure 51: Developed diagram showing layout of windings in a 3-phase, 4-pole, two layer induction motor winding, together with the flux density wave produced by one phase acting alone. The upper detail shows how the coil-sides form upper and lower layers in the slots (Source: A. Hughes and B. Drury [84]).....	34
Figure 52: Developed diagram showing arrangement of 3-phase, two-layer windings in a 36-slot stator. A 4-pole winding with three slots/pole/phase is shown (up) and a 6-pole winding with two slots/pole/phase is shown (down) (Source: A. Hughes and B. Drury [84]).....	35
Figure 53: Resultant air-gap flux density wave produced by a complete 3-phase, 4-pole winding at three successive instants in time (Source: A. Hughes and B. Drury [84]).....	35
Figure 54: Single-phase AC induction motor with (right) and without (left) a start mechanism (Source: Microchip Technology Inc. [71])	37
Figure 55: Torque-Speed curves of different types of single-phase induction motors for constant voltage and constant frequency operation (Source: Microchip Technology Inc. [71])	38

Figure 56: Torque-Speed characteristic curve (including slip) of a multi-phase induction machine in motoring and generating mode for constant voltage and frequency operation (Source: Electropaedia [85])	39
Figure 57: AC induction machine torque-slip curve showing braking, motor and generator regions (Source: A. E. Fitzgerald et al. [86])	39
Figure 58: Torque/Current versus speed/slip ratio curves with terminology for a typical three-phase induction motor (Source: W. Tong [74])	40
Figure 59: Comparison of torque-speed curves between typical single-cage and double-cage rotors for the same design and operation conditions (Source: W. Tong [74])	41
Figure 60: Cross section of double squirrel cage rotor (Source: ElectricalEasy [87])	42
Figure 61: Wound rotor induction machines using slip rings and brushes to contact rotor winding and external resistances for improving motor start characteristics (Source: W. Tong [74]).....	42
Figure 62: Variations of Torque–Speed characteristics of wound induction motors as a function of rotor resistance. Increasing rotor resistance results in the shift of the breakdown torque toward zero speed, causing the increase of slip and starting torque and the decrease of full-load speed. (Source: W. Tong [74])	43
Figure 63: Constant torque/variable power load curve (Source: Microchip Technology Inc. [71])	44
Figure 64: Variable torque/variable power load curve (Source: Microchip Technology Inc. [71])	44
Figure 65: Variable torque/constant power load curve (Source: Microchip Technology Inc. [71])	44
Figure 66: Constant torque/constant power load curve (Source: Microchip Technology Inc. [71])	45
Figure 67: High starting torque followed by constant torque load curve (Source: Microchip Technology Inc. [71])	45
Figure 68: Typical AC multi-phase motor efficiency versus load at 1800 rpm (Source: US DOE [88]) ..	46
Figure 69: Typical AC induction motor nameplate (Source: Powersystemsloss.blogspot [92])	47
Figure 70: Induction machine block of MATLAB/Simulink® (Source: Mathworks Inc. [108])	48
Figure 71: Block diagram of the 3 phase AC induction motor model (Source: Author)	49
Figure 72: The d-q equivalent circuit model of the three-phase symmetrical squirrel single-cage (constant R_r) or wound (variable R_r) induction motor (Source: P. Krause et al. [109])	49
Figure 73: Angles between electric frames. The letters S and R refer to the stator and rotor respectively while the indices a, b, c refer to the three phase (Source: Author)	50
Figure 74: T_e versus time for 50HP IG under no load.....	54
Figure 75: ω_m ($=\omega_r$) versus time for 50HP IG under no load	54
Figure 76: Slip ratio versus time for 50HP IG under no load	54
Figure 77: i_{ds} (up) and i_{qs} (down) versus time for 50HP IG under load of -100 N·m	55
Figure 78: ϕ_{ds} (up) and ϕ_{qs} (down) versus time for 50HP IG under load of -100 N·m	55
Figure 79: i_{dr} (up) and i_{qr} (down) versus time for 50HP IG under load of -100 N·m	56

Figure 80: ϕ_{dr} (up) and ϕ_{qr} (down) versus time for 50HP IG under load of -100 N·m	56
Figure 81: T_e versus time for 50HP IG under load -100 N·m (value -98 N·m)	57
Figure 82: ω_m ($=\omega_r$) versus time for 50HP IG under load -100 N·m (value 3620 rpm).....	57
Figure 83: Slip ratio versus time for 50HP IG under load -100 N·m (value 0.55%).....	57
Figure 84: T_m versus time for 50HP IG with a reduction step at $t=2$ seconds.....	58
Figure 85: f_s versus time for 50HP IG with a reduction step at $t=5$ seconds.....	58
Figure 86: i_{ds} (up) and i_{qs} (down) versus time for 50HP IG under transient and different steady state conditions.....	59
Figure 87: i_{dr} (up) and i_{qr} (down) versus time for 50HP IG under transient and different steady state conditions	59
Figure 88: ϕ_{ds} (up) and ϕ_{qs} (down) versus time for 50HP IG under transient and different steady state conditions.....	60
Figure 89: ϕ_{dr} (up) and ϕ_{qr} (down) versus time for 50HP IG under transient and different steady state conditions.....	60
Figure 90: T_e versus time for 50HP IG under transient and different steady state conditions.....	61
Figure 91: ω_m ($=\omega_r$) versus time for 50HP IG under transient and different steady state conditions	61
Figure 92: Slip ratio versus time for 50HP IG under transient and different steady state conditions	61
Figure 93: T_e versus time for 720 kW IG under no load	62
Figure 94: ω_m versus time for 720 kW IG under no load	63
Figure 95: ω_r versus time for 720 kW IG under no load	63
Figure 96: Slip ratio versus time for 720 kW IG under no load	63
Figure 97: i_{ds} (up) and i_{qs} (down) versus time for 720 kW IG under load of -2500 N·m.....	64
Figure 98: i_{dr} (up) and i_{qr} (down) versus time for 720 kW IG under load of -2500 N·m	65
Figure 99: ϕ_{ds} (up) and ϕ_{qs} (down) versus time for 720 kW IG under load of -2500 N·m.....	65
Figure 100: ϕ_{dr} (up) and ϕ_{qr} (down) versus time for 720 kW IG under load of -2500 N·m	66
Figure 101: T_e versus time for 720 kW IG under load -2500 N·m (value -2497 N·m)	66
Figure 102: ω_m versus time for 720 kW IG under load -2500 N·m (value 903 rpm)	67
Figure 103: ω_r versus time for 720 kW IG under load -2500 N·m (value 1806 rpm)	67
Figure 104: Slip ratio versus time for 720 kW IG under load -2500 N·m (value 0.33% rpm).....	67
Figure 105: T_m versus time for 720 kW IG with an increment step at $t=4$ seconds.....	68
Figure 106: f_s versus time for 720 kW IG with a reduction step at $t=7$ seconds	68
Figure 107: i_{ds} (up) and i_{qs} (down) versus time for 720 kW IG under transient and different steady state conditions.....	69
Figure 108: i_{dr} (up) and i_{qr} (down) versus time for 720 kW IG under transient and different steady state conditions.....	69
Figure 109: ϕ_{ds} (up) and ϕ_{qs} (down) versus time for 720 kW IG under transient and different steady state conditions.....	70

Figure 110: ϕ_{dr} (up) and i_{qr} (down) versus time for 720 kW IG under transient and different steady state conditions.....	70
Figure 111: T_e versus time for 720 kW IG under transient and different steady state conditions	70
Figure 112: ω_m versus time for 720 kW IG under transient and different steady state conditions.....	71
Figure 113: ω_r versus time for 720 kW IG under transient and different steady state conditions	71
Figure 114: Slip ratio versus time for 720 kW IG under transient and different steady state conditions ..	71
Figure 115: Per-phase stator equivalent circuit of an AC induction motor in steady state conditions (Source: A.E. Fitzgerald et al. [86]).....	73
Figure 116: Per-phase rotor equivalent circuit of an AC induction motor in steady state conditions and at slip frequency (Source: A.E. Fitzgerald et al. [86])	74
Figure 117: Per-phase equivalent circuit of an AC induction motor. The rotor parameters have been referred to the rotor reference frame and for standstill is $s=1$ (Source: Author and [86]).....	74
Figure 118: Per-phase equivalent circuit of an AC induction motor. The rotor parameters have been referred to the stator and for standstill is $s=1$ (Source: A.E. Fitzgerald et al. [86]).....	75
Figure 119: Power flow in AC induction machine in motoring mode (Source: Author).....	76
Figure 120: The complete per-phase equivalent circuit of an AC induction motor with effective rotor resistance (R_2/s) split into R_2 and $R_2(1-s)/s$. The power dissipated in R_2 represents the rotor copper loss per phase, while the power in the shaded resistance $R_2(1-s)/s$ corresponds to the mechanical output power per phase, when the slip is s (Source: Author and [86])	78
Figure 121: IEEE recommended per-phase equivalent circuit of an AC induction motor. The iron loss resistance R_c is neglected corresponding to (left) Figure 118 and (right) Figure 120 (Source: A.E. Fitzgerald et al. [86]).....	79
Figure 122: General linear network and (left) and its equivalent at terminals “ab” by Thevenin's theorem (Source: A.E. Fitzgerald et al. [86])	79
Figure 123: IEEE recommended per-phase equivalent circuit of an AC induction motor simplified by Thevenin's theorem corresponding to Figure 120 (Source: A.E. Fitzgerald et al. [86])	80
Figure 124: Induction-motor torque-slip curves showing effect of changing rotor-circuit resistance (Source: A. E. Fitzgerald et al. [86])	84
Figure 125: Torque-Speed characteristic curve for different values of supply voltage V_1 for a NEMA Class A (left) and NEMA Class D (right) (Source: Author and [112])	85
Figure 126: Pole changing Torque-Speed curves for constant torque (left) and constant power (right) (Source: I. Boldea and S.A. Nasar [112])	85
Figure 127: Per-phase equivalent circuit of an AC induction motor with an external induced EMF source in the rotor. The rotor parameters have been referred to the stator and for standstill is $s=1$ (Source: R. Krishnan [110]).....	87

Figure 128: Typical torque-speed curves (normalized in 2 quadrants) for constant V/f ratio of an induction machine assuming R_1 is zero (Source: R. Krishnan [110])	89
Figure 129: Typical torque-speed curves for constant V/f ratio of a 4-pole induction machine assuming R_1 is not zero (Source: A. E. Fitzgerald et al. [86]).....	90
Figure 130: Typical torque-speed curves for an induction machine with constant flux up to 45Hz (rated speed) and constant voltage at higher frequencies (Source: A. Hughes and B. Drury [84])	90
Figure 131: Typical torque-speed curves for an induction machine under V/f control in Constant Torque, Constant Power and in High-Speed motoring regions (Source: A. Hughes and B. Drury [84]).....	91
Figure 132: Operating regions in all four quadrants of the torque–speed plane of an induction machine under V/f control (Source: A. Hughes and B. Drury [84]).....	92
Figure 133: Circuit diagram for a Pulse Width Modulated (PWM) Voltage Source Inverter (VSI) (Source: A. Hughes and B. Drury [84]).....	96
Figure 134: Circuit diagram of three-phase full-wave bridge rectifier (Q_n : Diode n , $n=1:6$) (Source: Author and [141]).....	97
Figure 135: Switch topology of three-phase inverter (Q_n : IGBT-Diode n , $n=1:6$) (Source: Author and [141]).....	98
Figure 136: 2 nd order three phase passive harmonic filter topology after inverter (Source: N.I. Raju et al. [139])	99
Figure 137: Control signal generators for SPWM (Source: Author and B.K. Bose [150])	101
Figure 138: Typical waveforms of three-phase sinusoidal PWM (from up to down): reference voltages (a,b,c) and triangular wave, V_{ao} , V_{bo} , V_{co} , line-to-line voltage V_{AB} (Source: K. Rajashekara et al. [152])	101
Figure 139: Output of a rectifier (DC voltage) for delay angle $\alpha=45^\circ$ (Source: D.W. Hart [143]).....	102
Figure 140: V/f ratio control of a PWM VSI with controllable (dash line) or uncontrollable (solid line) rectifier (Source: Author and [110]).....	102
Figure 141: Three phase voltage source VSI implemented in MATLAB/Simulink® environment.....	103
Figure 142: The Universal Bridge block for simulation of Rectifier (Source: Mathworks Inc. [108]) ...	104
Figure 143: DC link of LC type (Source: Mathworks Inc. [108])	104
Figure 144: The Universal Bridge block for simulation of Inverter (Source: Mathworks Inc. [108])	104
Figure 145: Three phase 2 nd order LC passive filter (Source: Mathworks Inc. [108]).....	105
Figure 146: Control signal generators for SPWM implemented with relational operators for $m=1$	105
Figure 147: Three phase supply waveform phase voltages, $V_{A(s)}$, $V_{B(s)}$, $V_{C(s)}$ ($321.1 V_{RMS}$).....	106
Figure 148: Three phase supply waveform line to line voltages, $V_{AB(s)}$, $V_{BC(s)}$, $V_{CA(s)}$ ($556.2 V_{RMS}$)	106
Figure 149: DC voltage with ripple	107
Figure 150: DC voltage after DC Link (755 V)	107
Figure 151: Triangular-Control signals (for $m=1.0$) and output pole voltages ($\pm m \cdot V_{DC}/2$) of SPWM circuit	108

Figure 152: Three-phase line-to-line voltages (± 755 V) of the inverter before the harmonic filter.....	108
Figure 153: Three-phase phase voltages (± 503.3 V) of the inverter before the harmonic filter.....	109
Figure 154: Three-phase line-to-line voltage (± 640 V) of the inverter after the harmonic filter.....	109
Figure 155: V_{ab} line-to-line voltage (± 640 V) of the inverter after the harmonic filter.....	110
Figure 156: Three-phase phase voltages (± 369.5 V) of the inverter after the harmonic filter	110
Figure 157: Simplified version of three-phase VSI with different fundamental frequencies and constant voltage in MATLAB/Simulink® environment.....	111
Figure 158: Stator three-phase voltage frequency (fundamental component in case of realistic VSI) versus time. Range from 100% rated frequency (60Hz) up to 50% rated frequency (30 Hz)	111
Figure 159: The line-to-line stator three-phase voltage, V_{ab} , comparison between the realistic VSI and the simplified version with CVS for different frequencies and constant voltage.....	111
Figure 160: The line-to-line stator three-phase voltage, V_{bc} , comparison between the realistic VSI and the simplified version with CVS for different frequencies and constant voltage.....	112
Figure 161: The line-to-line stator three-phase voltage, V_{ca} , comparison between the realistic VSI and the simplified version with CVS for different frequencies and constant voltage.....	112
Figure 162: Major components of an OCECS (Source: Author and [154]).....	113
Figure 163: Grid-connected ocean current farm (Source: Author and [154]).....	113
Figure 164: Block diagram of a variable speed OCECS with full capacity power converters (Source: Author and [154]).....	114
Figure 165: A realistic schematic diagram of a SCIG-based generation OCECS with full capacity power converters (Source: Author and [70]).....	115
Figure 166: Steady-state OCECS model implementation in MATLAB/Simulink® environment.....	116
Figure 167: The OCT simplified model implemented in MATLAB/Simulink® environment.....	116
Figure 168: Representation of the OCECS shaft as a sum of masses and springs. Side view of the discretized shaft model (Source: [157]).....	117
Figure 169: Representation of shafting vibrational model mechanical system for 6 elements, 5 springs and 3 bearings (Source: Author).....	118
Figure 170: Inputs (left) and outputs (right) for the shafting vibrational model block in MATLAB/Simulink® environment.....	120
Figure 171: The shaft vibrational model implemented in MATLAB/Simulink® environment for $n=2$ elements and one bearing	120
Figure 172: Model in MATLAB/Simulink® referred to the implementation of induction generator simplified scalar control (green blocks – supply frequency and voltage) with the closed loop feedback from PI controller (MV)	121
Figure 173: General form of the PI Controller (Source: Author)	121
Figure 174: T_{turbine} versus time for 720 kW OCECS and steady state conditions $V_c = 1$ m/s and $N_{\text{turbine}} = 10$ RPM	123

Figure 175: T_m versus time for 720 kW OCECS and steady state conditions $V_c = 1$ m/s and $N_{\text{turbine}} = 10$ RPM	123
Figure 176: T_c versus time for 720 kW OCECS and steady state conditions $V_c = 1$ m/s and $N_{\text{turbine}} = 10$ RPM	123
Figure 177: PID Correction versus time for 720 kW OCECS and steady state conditions $V_c = 1$ m/s and $N_{\text{turbine}} = 10$ RPM	124
Figure 178: ω_m versus time for 720 kW OCECS and steady state conditions $V_c = 1$ m/s and $N_{\text{turbine}} = 10$ RPM	124
Figure 179: N_{turbine} versus time for 720 kW OCECS and steady state conditions $V_c = 1$ m/s and $N_{\text{turbine}} = 10$ RPM	124
Figure 180: T_{turbine} versus time for 720 kW OCECS and steady state conditions $V_c = 1$ m/s and $N_{\text{turbine}} = 7$ RPM	125
Figure 181: T_m versus time for 720 kW OCECS and steady state conditions $V_c = 1$ m/s and $N_{\text{turbine}} = 7$ RPM	125
Figure 182: T_c versus time for 720 kW OCECS and steady state conditions $V_c = 1$ m/s and $N_{\text{turbine}} = 7$ RPM	125
Figure 183: PID Correction versus time for 720 kW OCECS and steady state conditions $V_c = 1$ m/s and $N_{\text{turbine}} = 7$ RPM	126
Figure 184: ω_m versus time for 720 kW OCECS and steady state conditions $V_c = 1$ m/s and $N_{\text{turbine}} = 7$ RPM	126
Figure 185: N_{turbine} versus time for 720 kW OCECS and steady state conditions $V_c = 1$ m/s and $N_{\text{turbine}} = 7$ RPM	126
Figure 186: T_{turbine} versus time for 720 kW OCECS and steady state conditions $V_c = 1$ m/s and $N_{\text{turbine}} = 4$ RPM	127
Figure 187: T_m versus time for 720 kW OCECS and steady state conditions $V_c = 1$ m/s and $N_{\text{turbine}} = 4$ RPM	127
Figure 188: T_c versus time for 720 kW OCECS and steady state conditions $V_c = 1$ m/s and $N_{\text{turbine}} = 4$ RPM	127
Figure 189: PID Correction versus time for 720 kW OCECS and steady state conditions $V_c = 1$ m/s and $N_{\text{turbine}} = 4$ RPM	128
Figure 190: ω_m versus time for 720 kW OCECS and steady state conditions $V_c = 1$ m/s and $N_{\text{turbine}} = 4$ RPM	128
Figure 191: N_{turbine} versus time for 720 kW OCECS and steady state conditions $V_c = 1$ m/s and $N_{\text{turbine}} = 4$ RPM	128
Figure 192: T_{turbine} versus time for 720 kW OCECS and steady state conditions $V_c = 2$ m/s and $N_{\text{turbine}} = 10$ RPM	130

Figure 193: T_m versus time for 720 kW OCECS and steady state conditions $V_c = 2$ m/s and $N_{\text{turbine}} = 10$ RPM	130
Figure 194: T_e versus time for 720 kW OCECS and steady state conditions $V_c = 2$ m/s and $N_{\text{turbine}} = 10$ RPM	130
Figure 195: PID Correction versus time for 720 kW OCECS and steady state conditions $V_c = 2$ m/s and $N_{\text{turbine}} = 10$ RPM	131
Figure 196: ω_m versus time for 720 kW OCECS and steady state conditions $V_c = 2$ m/s and $N_{\text{turbine}} = 10$ RPM	131
Figure 197: N_{turbine} versus time for 720 kW OCECS and steady state conditions $V_c = 2$ m/s and $N_{\text{turbine}} = 10$ RPM	131
Figure 198: T_{turbine} versus time for 720 kW OCECS and steady state conditions $V_c = 2$ m/s and $N_{\text{turbine}} = 7$ RPM	132
Figure 199: T_m versus time for 720 kW OCECS and steady state conditions $V_c = 2$ m/s and $N_{\text{turbine}} = 7$ RPM	132
Figure 200: T_e versus time for 720 kW OCECS and steady state conditions $V_c = 2$ m/s and $N_{\text{turbine}} = 7$ RPM	132
Figure 201: PID Correction versus time for 720 kW OCECS and steady state conditions $V_c = 2$ m/s and $N_{\text{turbine}} = 7$ RPM	133
Figure 202: ω_m versus time for 720 kW OCECS and steady state conditions $V_c = 2$ m/s and $N_{\text{turbine}} = 7$ RPM	133
Figure 203: N_{turbine} versus time for 720 kW OCECS and steady state conditions $V_c = 2$ m/s and $N_{\text{turbine}} = 7$ RPM	133
Figure 204: T_{turbine} versus time for 720 kW OCECS and steady state conditions $V_c = 2$ m/s and $N_{\text{turbine}} = 4$ RPM	134
Figure 205: T_m versus time for 720 kW OCECS and steady state conditions $V_c = 2$ m/s and $N_{\text{turbine}} = 4$ RPM	134
Figure 206: T_e versus time for 720 kW OCECS and steady state conditions $V_c = 2$ m/s and $N_{\text{turbine}} = 4$ RPM	134
Figure 207: PID Correction versus time for 720 kW OCECS and steady state conditions $V_c = 2$ m/s and $N_{\text{turbine}} = 4$ RPM	135
Figure 208: ω_m versus time for 720 kW OCECS and steady state conditions $V_c = 2$ m/s and $N_{\text{turbine}} = 4$ RPM	135
Figure 209: N_{turbine} versus time for 720 kW OCECS and steady state conditions $V_c = 2$ m/s and $N_{\text{turbine}} = 4$ RPM	135
Figure B.1: Torque–speed characteristics for design A, B, C, and D motors defined by NEMA for constant voltage and frequency operation (Source: W. Tong [75]).....	153

Figure B.2: Rotor typical slots from typical squirrel-cage induction motors, showing the cross section of the rotor bars; (a) NEMA design class A – large bars, near the surface; (b) NEMA design class B – large, deep rotor bars; (c) NEMA design class C – double-cage rotor design; (d) NEMA design class D – small bars near the surface (Source: University of Calgary [B2]).....	154
Figure D.1: Model in MATLAB/Simulink® referred to inputs for the induction motor/generator block	156
Figure F.1: Eight Switching Configuration of a Three-Phase Inverter (Source: K. Zhou and D.Wang [F1]).....	158
Figure F.2: Explanation of pole voltages in three-phase inverter ($m=1$) (Source: [F3])	159
Figure G.1: A typical example of one phase voltage of the three-phase square wave inverter (Source: M. Żelechowski [129]).....	162
Figure G.2: A typical example of line voltage V_{AB} , of the three-phase square wave inverter (Source: M. Żelechowski [129]).....	164
Figure G.3: A typical example of pole voltage V_{ao} , of the three-phase square wave inverter (Source: M. Żelechowski [129]).....	164
Figure G.4: Output voltage of VSI, as a percentage of square wave technique, versus modulation index for different PWM techniques. SVPWM: space vector PWM, ZSS: Zero Sequence Signal, OM: Over-modulation (Source: M.P. Kazmierkowski et al. [G2]).....	166
Figure H.1: Voltage Measurement block of the SimPowerSystems toolbox. The positive input connected with the electrical signal (V_a , V_b or V_c) and the negative with the ground.....	167
Figure H.2: Bus Selector block of Simulink library. The input is the output signal of the Asynchronous Machine block and the output is the signals you choose to demultiplex as shown in Figure H.3.....	167
Figure H.3: Bus Selector output signals in case of Asynchronous Machine as an input. The left list box has shown the three stator currents in abc reference frame.....	168
Figure H.4: MATLAB code for the calculation of average electric power	168

List of Tables

Table 1: IG and PM topology comparison for OCT.....	23
Table 2: Sources of induction motor losses.....	46
Table 3: Nameplate terms and their meaning	47
Table 4: 50 HP induction motor/generator parameters	53
Table 5: 720 kW induction motor/generator parameters	62
Table 6: Rectifier parameters	103
Table 7: DC Link parameters	104
Table 8: Inverter parameters	104
Table 9: LC filter parameters	105
Table 10: Solver parameters for SPWM VSI.....	105
Table 11: Comparison of theory and simulation results in rectifier section.....	107
Table 12: OCECS shaft characteristics	117
Table 13: Controller gains	121
Table 14: Solver parameters for OCECS.....	122
Table 15: Average electric power of OCECS for flow speed 1 m/s and for different operation points...	136
Table 16: Average electric power of OCECS for flow speed 2 m/s and for different operation points...	137
Table 17: Energy production of OCECS for flow speed 1 m/s and for different operation points	137
Table 18: Energy production of OCECS for flow speed 2 m/s and for different operation points	137
Table A.1: Ocean current advantages compared with other energy resources	151
Table B.1: Performance characteristics of NEMA A, B, C and D designs	154
Table D.1: Solver parameters.....	156
Table F.1: Switch States and Voltages for Three-Phase SPWM inverter (for m=1).....	161

Abstract

The development of a numeric simulation for predicting the performance of an Ocean Current Energy Conversion System is presented in this thesis along with a control system development using a PID controller for the achievement of specified rotational velocity set-points. In the beginning, this numeric model is implemented in MATLAB/Simulink® and it is used to predict the performance of a three phase squirrel single-cage type induction motor/generator in two different cases. The first case is a small 3 meter rotor diameter, 20 kW ocean current turbine with fixed pitch blades, and the second case a 20 meter, 720 kW ocean current turbine with variable pitch blades. Furthermore, the second case is also used for the development of a Voltage Source Variable Frequency Drive for the induction motor/generator. Comparison among the Variable Frequency Drive and a simplified model is applied. Finally, the simulation is also used to estimate the average electric power generation from the 720 kW Ocean Current Energy Conversion System which consists of an induction generator and an ocean current turbine connected with a shaft which modeled as a mechanical vibration system.

Keywords: Ocean Current Turbine (OCT), Induction Generator (IG), Variable Frequency Drive (VFD), MATLAB Simulink®, Ocean Current Energy Conversion Systems (OCECS), Shaft Vibrational Model, PID Controller.

CHAPTER 1

INTRODUCTION

1.1 Ocean Current Energy

The movement of ocean currents has often been considered to be capable of providing a source of renewable, clean energy similar to wind farms. One great location that has received much consideration as a site for harnessing power from ocean currents is the Florida Straits Current System, which is a fast, western intensified surface current that runs along the East Coast of the United States [1].

1.1.1 Current Phenomena Explanation

The ocean currents are masses of ocean water that flow from one place to another. The direction toward which water moves is called *set*, and its speed is called *drift*. It transports along the oceans a large quantity of water and energy as temperature of this water. Its thermal energy transport is so important that it has an influence on the temperatures in our planet and on the different climates around the world [1].

The ocean currents phenomenon is mainly due to the radiation of the sun. The energy from the sun heats the air in the atmosphere. The air from the equator zone becomes hotter than the air from the poles, so a wind current is created from the equator to the north and south poles. It is due to the high density of cold air, which tends to go to hotter zones where the density of the air is lower and for this reason, the pressure is also lower [1].

This is the origin of the *Trade Winds*. Other important phenomenon of the wind is the *Coriolis Effect*. Due to the rotation of the planet, the wind does not follow a rectilinear trajectory: it describes clockwise spirals in the northern hemisphere and counter-clockwise spiral in the southern one. These wind currents affect to the surface water of the seas which is the water within 0÷400 meters of depth. At the same time, the gravity and the *Coriolis* forces, the wind and again the heat from the sun, produce a similar effect to the deep oceans water which is the water below 400 meters of depth and represents the 90% of the oceans currents. The depth water of the oceans is not as quiet as it could seem at first sight. The cold of the poles increases the density of the water and its salts solubility (because of the formation of sea ice). This water becomes heavier, and it tends to go down. In the equator, the opposite effect produces light water. For this reason, the cold water from the poles tends to go deeply to the equator, and the warm water from this zone tends to go to the poles by the surface. This density gradient produces global currents called *Thermohaline Circulation* and it is part of the large-scale ocean circulation [1, 2]. It is represented on the Figure 1 below:

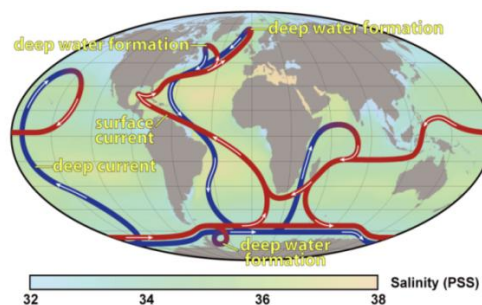


Figure 1: A summary of the path of the thermohaline circulation. Blue paths represent deep-water currents, while red paths represent surface currents.
(Source: NASA Earth Observatory [3])

The wind stress and the density differences explained before, and finally the tidal forces because of the moon attraction, are the responsible of the ocean currents. However, for this moment is not so clear how much each of these phenomenon affect to the currents generation. The surface and subsurface currents produce closed loops, how it can be seen in the Figure 2 [4].

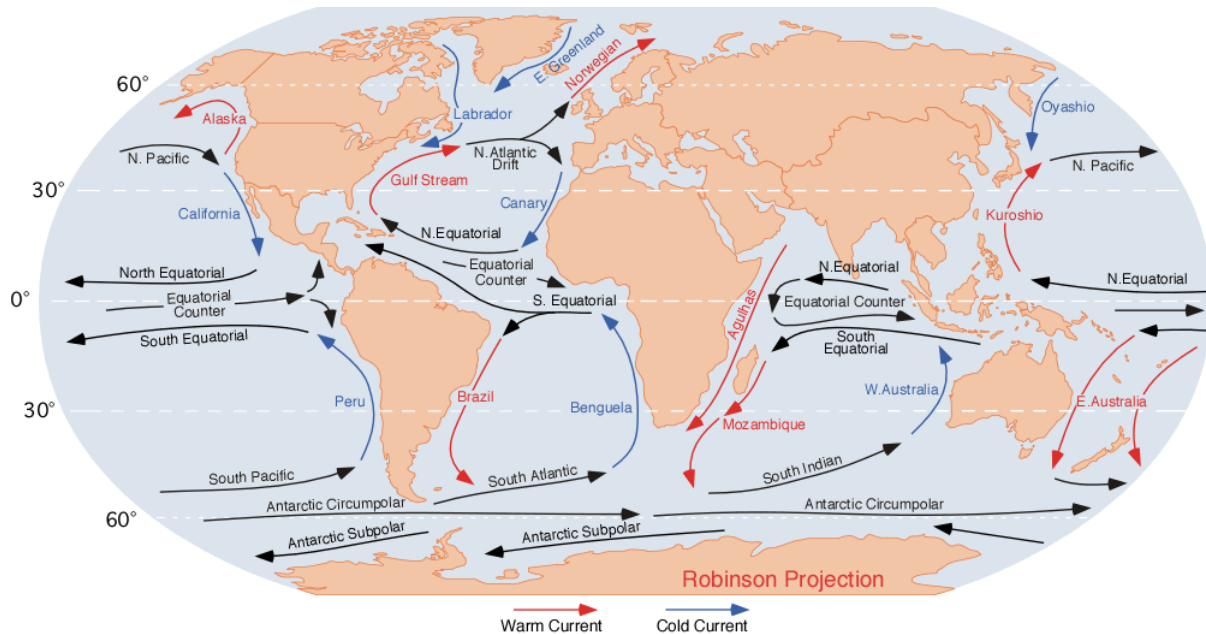


Figure 2: Major ocean currents of the world. On this illustration red arrows indicate warm currents, while cold currents are displayed in blue (Source: M. Pidwirny [4])

1.1.2 Resource Potential

Ocean currents, as already mentioned, are driven by wind and solar heating of the waters near the equator, although some ocean currents result instead from variations in water density and salinity. These types of currents are rarely constant and flow in one direction only, with an exception of the Gulf Stream core and some other few areas, similar to the tidal currents closer to shore where the varying gravitational pulls of the sun and moon result in diurnal high tides. Some examples of ocean currents are the Gulf Stream, Florida Straits Current, and California Current as shown in Figure 3 [5]. The Florida Straits Current starts only 8 km offshore in the southern part of Florida, close to Miami, and sustains relatively large speeds over significant distances in relatively unchanging patterns. In contrast, the California Current has relatively slow speeds and shifts periodically. Ocean currents tend to be concentrated at the surface, although significant current continues at depths below ships' drafts. The Aleutian passages have also been identified as an area for potential development of current energy extraction but they are mainly based on tides.

Ocean current speeds are generally much lower than wind speeds (*typically less than 4 mph*). This is important because the kinetic energy contained in flowing bodies is proportional to the cube of their velocity. However, another more important factor in the power available for extraction from a flowing body is the density of the material. Water is about *835 times denser than air* if assuming same temperature and normal pressure [6], so for the same area of flow being intercepted, the energy contained in a *4-mph* water flow is equivalent to that contained in an air mass moving at about *35 mph* [6]. Thus, ocean currents represent a potentially significant, currently untapped, reservoir of energy.

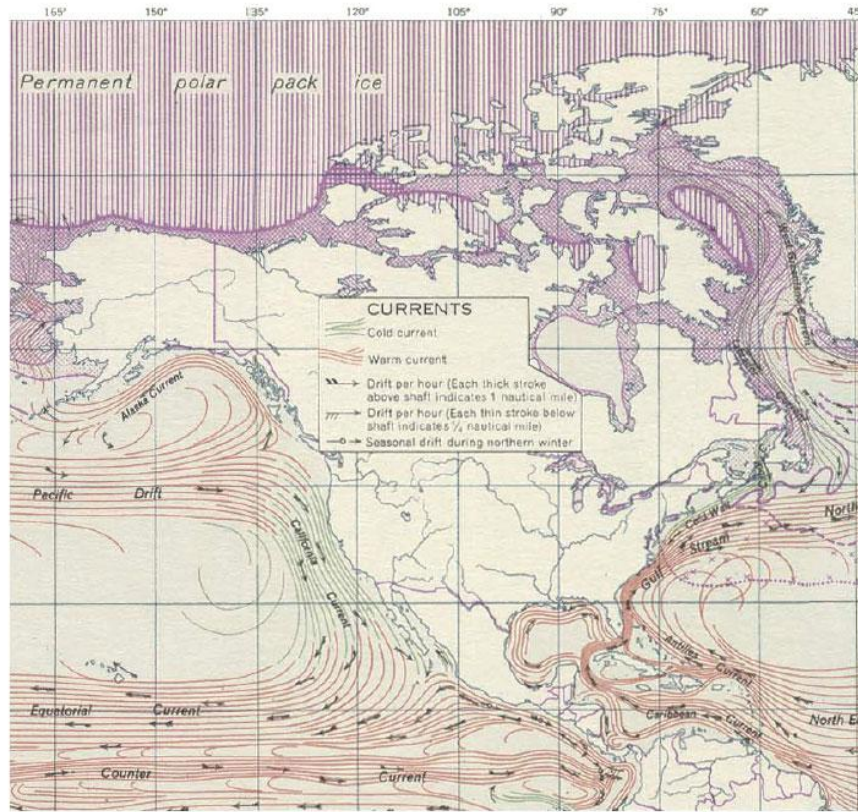


Figure 3: Ocean currents in the vicinity of the United States
(Source: University of Texas libraries [5])

The total worldwide power in ocean and tidal currents has been estimated to be about 5,000GW (while 19 GW are referred to US ocean currents), with power densities of up to 15 kW per m² and 3 kW per m² for tidal and ocean current respectively [7, 8, 9, 10]. The relatively constant extractable energy density near the surface of the Florida Straits Current is about 3 kW/m² of flow area [9, 10]. It has been estimated that capturing just 1/1,000th of the available energy from the Gulf Stream, which has 21,000 times more energy than Niagara Falls in a flow of water that is 50 times the total flow of all the world's freshwater rivers, would supply Florida of USA with 35% of its electrical needs [7] but that estimation is undetermined and it does not correspond to the reality. The situation is almost same in north of California but only for tidal currents. Until now, countries that are interested in and pursuing the application of ocean current energy technologies include the USA (tides and ocean currents), European Union (tides), Australia (tides), Japan (tides and ocean currents), Taiwan (tides and ocean currents), China (tides) and South Africa (ocean currents).

1.2 Resource Utilization Technology

Ocean current energy is at an early stage of development, with small number of prototypes and demonstration units having been tested to date and few real projects around the world as it is mentioned in the section 1.3. One such technology involves submerged turbines. Energy can be extracted from the ocean currents using submerged turbines that are similar in function to wind turbines, capturing energy through the processes of hydrodynamic, rather than aerodynamic, lift or drag.

1.2.1 Principle of Work

The ocean current turbines (*OCT*) have rotor blades, usually three (3), a generator for converting the rotational energy into electricity, means for mooring or anchoring, and means for transporting the electrical current to shore for incorporation into the electrical grid as shown in Figure 4 [11, 12]. Additional components may include concentrators (or shrouds) around the blades to increase the flow and power output from the turbine. They can have either horizontal or vertical axes of rotation as shown in Figure 5 [13].

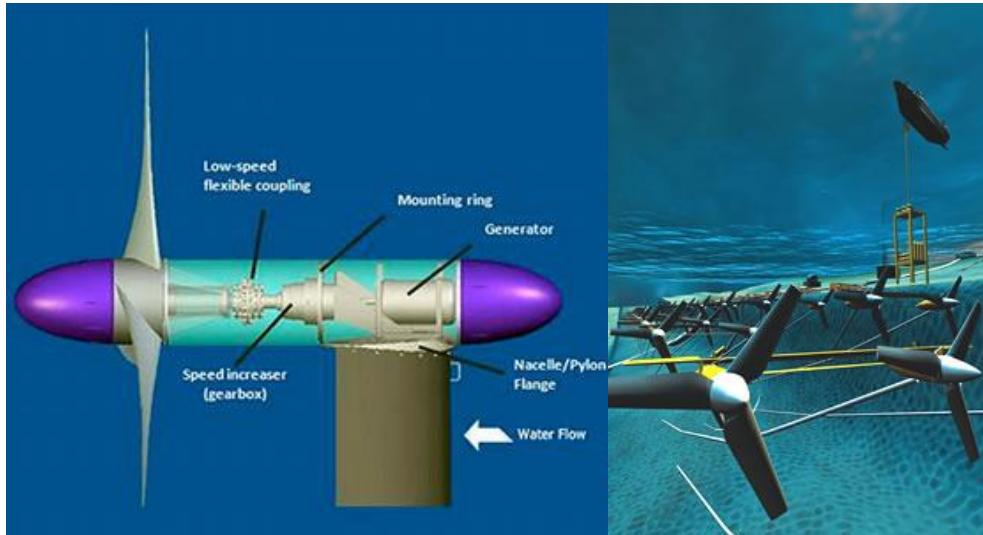


Figure 4: A general example of ocean current turbine components based on tidal turbine technology by Verdant Power (left, Source: Ecopedia [11]) and visualization of an underwater cluster of ocean tidal turbines (right, Source: FAU [12])

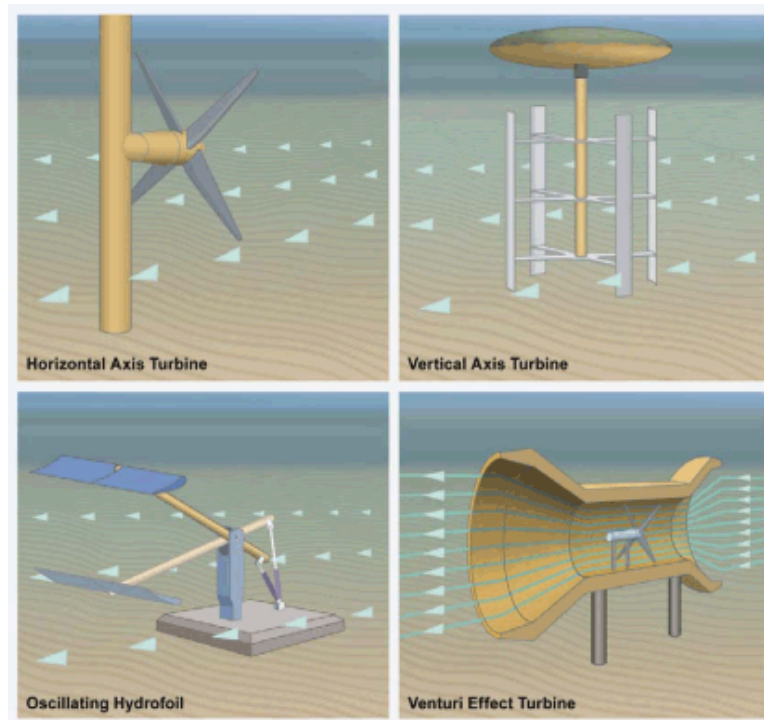


Figure 5: Four typical kinetic energy conversion devices (Source: EPRI Ocean Energy Program [13])

The principle of the oceans current energy is the same as the wind one. As in the wind generation, it can be used the *Betz Principle* [14]. According to Betz principle, it is not possible to extract all the kinetic energy from the flow which is crossing the turbine. There are two parameters that determine the maximum power that can be extracted from the flow which are the velocities of the fluid before and after the turbine. Following the Betz Principle, or the 2nd law of the thermodynamics, the speed of the fluid after the turbine cannot be equal to zero, so it is not possible to get all the kinetic energy of the fluid.

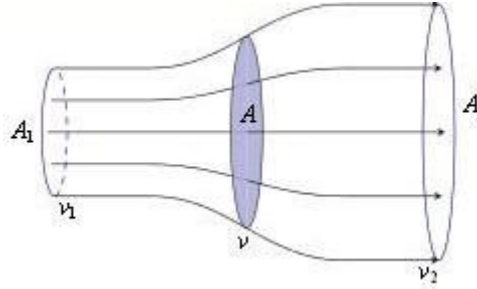


Figure 6: Schematic of fluid flow through a disk-shaped actuator where A:area, v:velocity.

For a constant density fluid, cross sectional area varies inversely with speed.

(Source: Wikipedia [15])

1.2.2 Anchoring/Mooring Systems and Location

Ocean current turbines may be anchored to the sea bed in a variety of ways [16, 17]. They may be tethered with cables, with the relatively constant current interacting with the turbine used to maintain location and stability. Such a configuration would be analogous to underwater kite-flying where the kite would be a turbine designed to keep upright and the kite flyer would be the anchor. Various alternative designs have been proposed, including the use of a barge moored in the current stream with a large cable loop to which water filled parachutes are fastened. The parachutes would be pushed by the current, and then closed on their way back, forming a loop similar to a large horizontal waterwheel. Seabed-mounted turbines are often referred to as *first generation devices* [18]. They can only be used at relatively shallow water depths. For deep sites, floating devices are the most attractive ones, as the water speed is fastest close to the surface.

For this reason, ocean current turbines may be also moored to the sea floor with single-point or multi-point mooring means such as buoys and are often referred to as *second generation devices* [18]. The water depths required for ocean current turbines to extract energy from the ocean make it sometimes impractical to rigidly connect them to the bottom. Therefore, either a single-point or multi-point mooring system will be needed to attach the turbine to the seafloor. To locate an OCT in the strong near-surface current, positive buoyancy and/or lifting surfaces will be required.

In contrast to the tidal energy facilities where the best sites are narrow straits between islands or headlands [7], where the current flows is higher, we can consider a good place for oceans current energy facilities the regions with energy densities above approximately 0.5 kW/m² [9, 10]. It has to be considered also, the closeness between the energy source and the energy demand, because most of the good places to obtain this kind of energy are too much far from the locations which need the result energy. In large areas with powerful currents, it would be possible to install water turbines in *groups or clusters* to create a “marine current facility,” similar in design approach to wind turbine facilities. Turbine spacing would be determined based on wake interactions and maintenance needs [7].

1.2.3 Environmental Considerations

Potential environmental impacts that would need to be considered with the development and utilization of ocean current energy with submerged turbines include impacts on marine ecology and conflicts with other potential uses of the same area of the ocean [19]. Resource requirements associated with the construction and operation of these technologies would also need to be addressed. Regardless of the size and nature of the anticipated environmental impacts, project planning would need to consider the protection of species, particularly fish and marine mammals. The slow blade velocities (*5 rpm to 30 rpm*) should allow water and fish to flow freely and safely through the structure. Protective fences and sonar-activated brakes could prevent larger marine mammals from harm. In the siting of the turbines, consideration of impacts on shipping routes, and present as well as anticipated uses such as commercial and recreational fishing and recreational diving, would be required. Additional considerations include the need to introduce possible mitigating factors, such as the establishment of fishery exclusion zones [7].

Major concerns that have been raised for tidal energy systems about risks from slowing the current flow by extracting energy as well as local effects, such as temperature and salinity changes in estuaries caused by changes in the mixing of salt and fresh waters, and their potential impact on estuary ecosystems are not applied in ocean current energy systems [20]. These concerns could introduce an upper limit on energy extraction, but would likely not become relevant until ocean current energy production reached the multi-GW range.

Finally, the oceans current turbines have a very little impact on the surrounding. They have not any visual impact such as the wind energy, for most of the facility is under the water. They do not produce emissions of any contaminant gas and they do not need any combustible [20].

1.2.4 Economic Considerations

There has been no commercial ocean current turbines are currently in operation and for this reason it is difficult to assess the costs of current-generated energy and its competitiveness with other energy sources [7]. Initial studies suggest that for economic exploitation, velocities of at least 2 m/s (≈ 4 knots) would be required (a 3.5 knots current has the kinetic energy equivalent of wind at more than 30 knots), although it is possible to generate energy from velocities as low as 1 m/s [7]. Major costs of these systems would be the cables to transport the electricity to the onshore grid (See Appendix A).

1.2.5 Challenges

For ocean current energy to be used successfully at a commercial scale, a number of engineering and technical challenges need to be addressed [18, 21, 22], including:

- Avoidance of drag from cavitation (air bubble formation that creates turbulence and substantially decreases the efficiency of current-energy harvest)
- Prevention of marine growth buildup
- High maintenance costs
- Corrosion control

- Generation of electromagnetic fields (EMFs)
- Toxicity of paints, lubricants, and antifouling coatings
- Interference with animal movements and migrations, including entanglement and strike by rotor blades or other moving parts

To calculate the potential energy, as the number of joules, available for extraction by ocean current turbines in all the oceans of the entire world, let's speculate that the ocean ubiquitously is moving at a speed in a certain direction, equal to that of the Gulf Stream; about **1 meters per second** [9, 10]. Therefore, each cubic meter of water has a kinetic energy of **500 Joules** (using the kinetic energy equation: $0.5 \cdot m \cdot v^2$, where m and v are the mass and velocity of the object respectively). This may be an extreme overestimate since most of the ocean moves much more slowly than the Gulf Stream, but assuming the larger number, we then multiply it by the number of cubic meters of all the oceans of the entire world:

- The radius of the earth is approximately $R = 6371 \text{ km}$ [23], the average depth of the ocean is $d = 4.27 \text{ km}$ [24], and assuming that 70% of the world's surface is ocean, the total volume of water in the world's oceans, Ω , is:

$$\begin{aligned}\Omega &= 0.7 \cdot 4\pi \cdot R^2 \cdot d \\ &= 1.528 \cdot 10^{18} \text{ m}^3\end{aligned}$$

Therefore, the total amount of energy available for extraction in the world's ocean is:

$$500 \text{ (Joules/m}^3\text{)} \cdot 1.528 \cdot 10^{18} \text{ (m}^3\text{)} = 7.65 \cdot 10^{20} \text{ Joules.}$$

When you compare this total to the annual energy demand per year for the entire world [25], as shown in Figure 7, you see that it's only 1.5 years' worth.

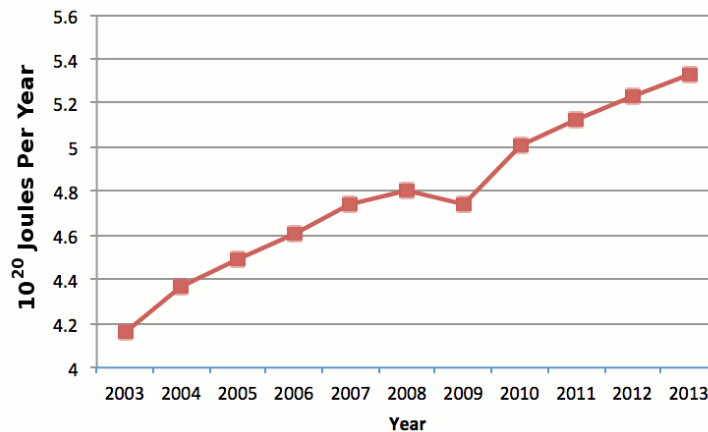


Figure 7: World primary energy consumption
(Source: BP [25])

1.3 Projects in the World

Since current power is an immature technology and no full-scale ocean current turbine installations are routinely providing power yet, the commercial status is judged purely on the most promising technologies to date. More specifically, the marine current industry is at an early stage of development. The business is characterized by prototype building and new ideas being brought forward. Many different designs have been considered in recent years and some have been patented and tested at a prototype scale [18, 26]. Main study and work on the development of ocean current energy and ocean current turbines, or tidal/river systems that may be transferable to the ocean current energy sector, has been carried out in United Kingdom, Canada, USA, Norway, Australia, France, Taiwan and Japan as shown in the below pages.

1.3.1 Real Projects and Tidal/Current Turbines

In contrast with the tidal turbines projects, where some of them are already connected to the distribution grid, some others are in the test process with *full-scale or scale prototypes* and many projects in the *design stage* [18, 26], there are no commercial ocean current turbines currently connected to an electric-power transmission or distribution grid.

In addition, *there are a few tidal turbines where, according to the design company, can be used also to harvest the ocean current energy as current turbines but they do not consider original OCTs.* The first example is the **SeaFlow** project, a marine turbine prototype, developed by Marine Current Turbines Limited (MCT Ltd) [27, 28]. It is considered as the world's first tidal current turbine, but it was not connected to the grid. Concerning the firm, it was the first stage in a commercial way to exploit marine currents. It has been implanted in 2003 in Lynmouth, a city of Bristol's Bay in the United Kingdom, above 1.1 km offshore and the first run occurs the 30th May of 2003. The turbine is composed of a single axial flow rotor, which supporting 2 blades, installed on a steel pile fixed into a socket on the sea floor, about 20 meter undersea. The diameter of the pile is 2.1 meter, the rotor diameter is 11 meter and the turbine's rated power is estimated at 300 kW. The power train (which includes the rotor, the gearbox and the generator) can slide up and down the pile in order to facilitate the maintenance¹⁸. The Figure 8 below shows us the SeaFlow technology. The cost of the project was estimated at 3.4 million £ and had been financed by the UK DTI, the German government, the European Community and some other partners. This full-scale prototype has been test in 2003 and 2004, mostly during the autumn and spring tides (about 30 days). The experiment has shown that the concept of marine turbine worked well. It has delivered electricity that fluctuated up to 30-50 kW; with some electrical peak power just less than 300 kW. The engineers working on the project conclude that this fluctuation are similar are those found in wind turbines due to turbulence of the fluid. Those turbulences depend on the site and another site could be more or less turbulent.



Figure 8: SeaFlow turbine. The left picture shows the system in operational mode while the right one shows us the pile and the rotor “roses up for maintenance”.

(Source: MCT Ltd [27])

According to these results, Marine Current Turbines Ltd has decided to develop a second project with the name *SeaGen S* [29, 30]. The system is composed of two (2) sixteen (16) meters diameter rotors installed on a pile, as shown in the Figure 9, and will be able to produce 1.2 MW. This system uses the same technology as SeaFlow for maintenance where the rotors can be raised above the sea level. The blades are pitch-controlled and the mechanical energy is transferred through a gearbox to the asynchronous generator. The turbine, contrary to the first project, is connected to the grid since 2009. However, the visual impact will be the same as the SeaFlow project. The company is also developing a turbine with the same powertrain for use at deeper locations with the name SeaGen U [27].

Finally, Marine Current Turbines has planed the third phase of its development which it consists on a farm of 5 MW named *SeaGen Array* project [29]. It will be a farm of several turbines similar to the SeaGen project, and will be located in the same place. The final aim is to install a capacity of 500 MW in the United Kingdoms.



Figure 9: SeaGen S turbine (left), demonstration of SeaGen S operation (right up) and visualization of SeaGen Array farm (right, down)
(Source: Sea Generation Ltd [29])

The second example is the modular turbine system with horizontal axis Darrieus turbines from Ocean Renewable Power Company (ORPC) with the name “*TidGen*” as shown in Figures 10 and 11 [31]. Based on ORPC website, small versions can be installed in rivers, bigger versions in shallow tidal streams, and the biggest version is to be installed in deep water tidal or ocean current sites. The company based in Portland, Maine of USA.

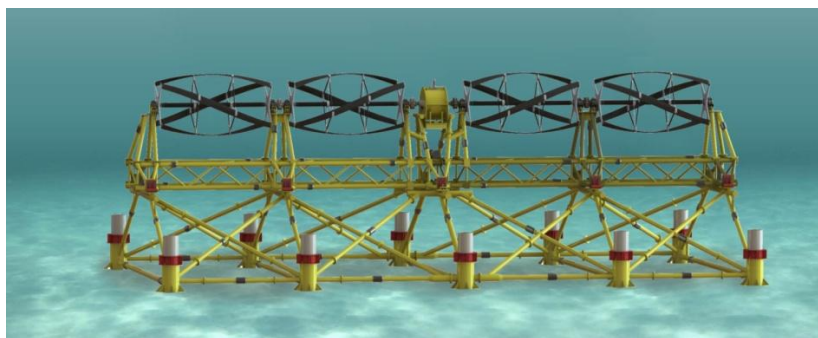


Figure 10: TidGen power system without dimensions
(Source: ORPC [31])



Figure 11: Visualization of TidGen power system
(Source: ORPC [31])

The third example, as shown in Figures 12 and 13, is the horizontal axis marine turbine **GEM** “*the Ocean’s Kite*” which is a hydrokinetic turbine designed to be driven by slow-moving flows of water, namely river, tidal or water currents in general from Aircraft Design and Aeroflight Dynamic Group (ADAG) [32], a part of the Department of Industrial Engineering - Aerospace Engineering Division at University of Naples in Italy. Detailed numerical analysis and two different scaled models, as shown in Figure 12, have been tested in the towing tank of the "Federico II" University of Naples. As a next step, the first full-scale GEM prototype has been built by a consortium of Venetian companies and partially sponsored by Veneto Regional and has been deployed in the Venetian Lagoon. For this prototype as shown in Figure 13, the expected power is approximately 20 kW with lagoon maximum current speed of 1.5 m/s.



Figure 12: First GEM model of towing tank test (up left and right) and second GEM model for towing tank test (bottom left and right)
(Source: ADAG [32])



Figure 13: Visualization of GEM turbine (left) and full-scale prototype of GEM (right)
(Source: ADAG [33])

Based on the company statements [33], the main characteristic of the GEM is its passive capacity of aligning itself along the current direction, as shown in the Figure 14, and this reminds the typical behavior of a kite from which the name "Ocean's Kite". In case of need, however, it is possible to control this alignment through the aid of a controlled designed system which uses the turbines as propellers

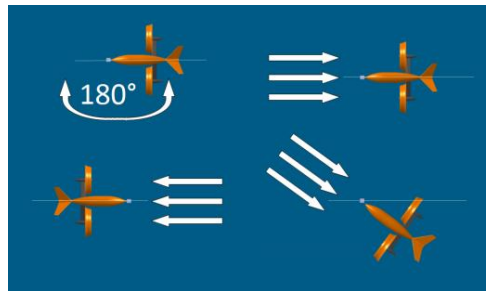


Figure 14: GEM alignment demonstration to the current direction (Source: ADAG [33])

An ocean tidal and current energy device which is significantly different from the rest is Minesto's **Deep Green** concept [34]. It is a turbine attached to a wing, as shown in Figure 15, which moves in loops through the water, while attached to the seabed with a moving wire, like a kite. The device moves through the water with a speed significantly higher than the water speed, reducing torque per power and hence weight and cost, compared to other device types. According to the company, a 1 meter diameter turbine can generate 500 kW, while a fixed turbine with the same capacity would be 30 meters in diameter. The company states that "the device is sufficiently different from competing designs to potentially offer either a significantly lower cost of energy, or the ability to exploit an entirely new resource". Deep Green is the only known power plant that cost-effectively produces electricity at sites with velocities between 1.2÷2.5 m/s and depths between 60÷120 meters while small boats and equipment are used for installation, service and maintenance. Thus, the offshore operations are minimized since only attachment and detachment has to be done offshore.

Deep Green produces electricity by a unique principle illustrated in the Figure 16 [35]. The water current creates a hydrodynamic lift force on the wing which pushes the kite forward (1). The kite is steered in an 8-shaped trajectory by a rudder and reaches a speed ten times the water current speed (2). As the kite moves, water flows through the turbine and electricity is produced in the

gearless generator (3). The electricity is transmitted through a cable in the tether attached to the wing (4). The electricity continues in sub-sea cables on the seabed to the shore (5).

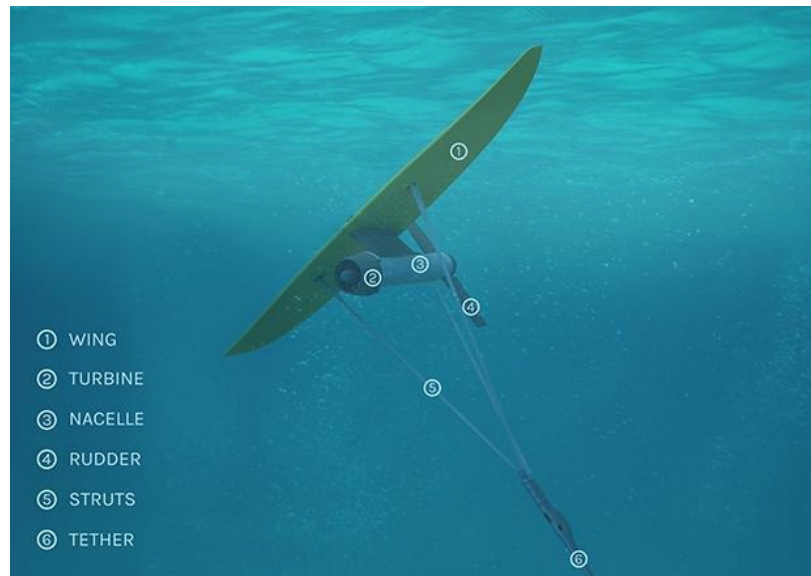


Figure 15: Deep Green kite-like turbine components
(Source: Minesto [34])

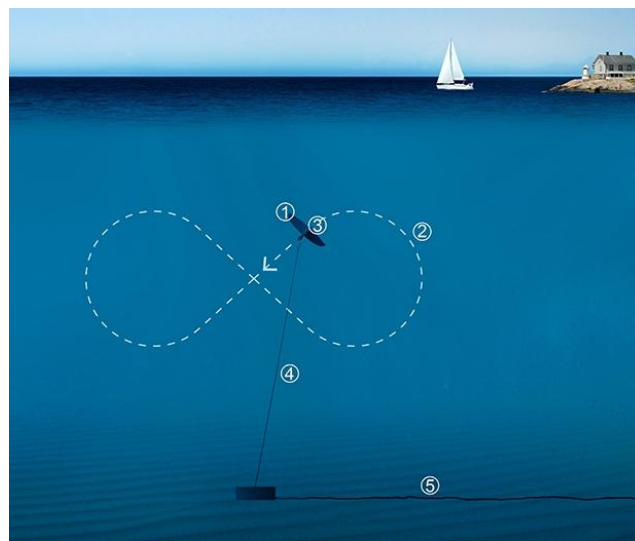


Figure 16: Deep Green principle of work
(Source: Minesto [35])

The only original ocean current turbine system tested in situ before 2005, which was designed to operate in deep-water offshore currents, is the vertical axial flow hydro-turbine developed by Blue Energy (Halifax, NS, Canada), previously Nova Energy Limited, and the National Research Council of Canada (Ottawa, ON, Canada) with the name **VEGA** (*Venturi Energy Generating Apparatus*) [36]. This system was tested in the Gulf Stream from an anchored vessel during a one day mission in April 1985 and generated up to 4 kW electricity from Florida Stream [37].

1.3.2 Projects in Progress

There are some projects in progress with the majority of them in design and analysis stage. One of the first companies who study the design and operation of an ocean current turbine to convert the energy of the Gulf of Mexico Stream in electricity was the Florida Hydro Power and Light Company based in Palatka, FL, USA [38]. One **Florida Hydro** ocean current turbine (approximately 45 m in length) is designed to produce approximately 2-3MW of electricity, as shown in Figures 17 and 18. Each of it is capable of powering about 1500 homes. The units will be installed in groups or clusters to form a marine current farm as shown in Figure 18, with a predicted capacity of up to eight turbines 2.6 km². This grouping is intended to avoid wake-interaction effects between the turbines and to allow access by maintenance vessels. An 80% capacity factor is targeted, averaging approximately 17,520 MWh per unit per year. It is expected that the overall capacity associated with the project in Palm Beach County, Florida, will be determined by research, which identifies the best number of units and transmission lines to provide power while avoiding significant use conflicts and avoiding impacts on significant environmental resources. The U.S. Navy's Surface Warfare Center's Carderock Division examined the system in 2003 and subsequently agreed to pursue a Cooperative Research and Development Agreement (CRADA) with Florida Hydro to commercialize the technology [19].

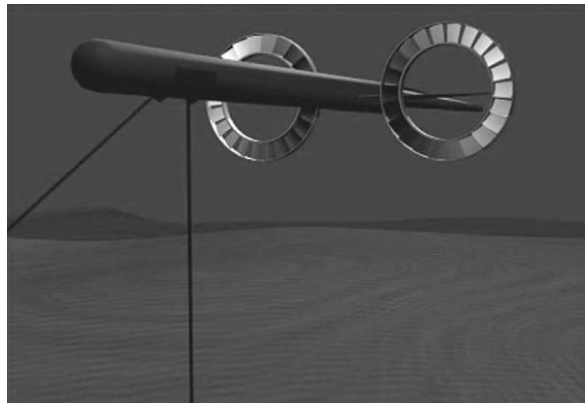


Figure 17: Close-up perspective view of Florida Hydro's conceptual design for one ocean current turbine that is tethered to the seafloor on adjustable cables to provide repositioning for maintenance service and to maximize capture of high flow velocities
(Source: C.W. Finkl and R. Charlier [19])

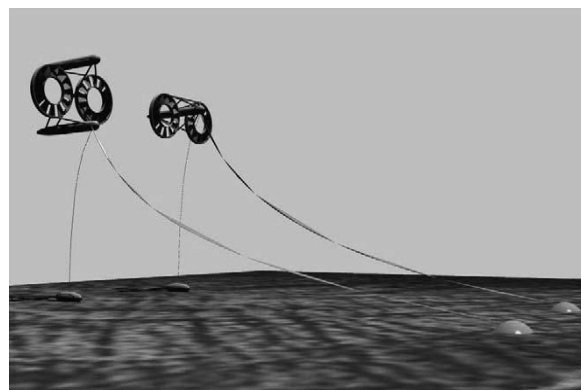


Figure 18: Panoramic view of Florida Hydro's conception of ocean current turbines that could be tethered to the seafloor in groups to form marine current farms of up to eight turbines spread over about 2.6 km²
(Source: C.W. Finkl and R. Charlier [19])

The Ocean Renewable Power Company (ORPC) is studying and designing the **OCGen Power System** with the goal to generate a nearly constant supply of electricity from deep water offshore ocean currents such as the Florida Current that flows 15 miles off the east coast of Florida [31]. Since these deep water currents are unidirectional and flow continuously, the power generated could provide a continuous supply of electricity that varies within a reasonable range. The OCGen Power System incorporates the same proven technology platform as TidGen Power Systems, and a buoyant tensioned mooring system modified for water depths in the hundreds of feet as shown in Figure 19. ORPC plans to test a prototype of the OCGen Power System at Florida Atlantic University's Southeast National Marine Renewable Energy Center by 2020 [31].

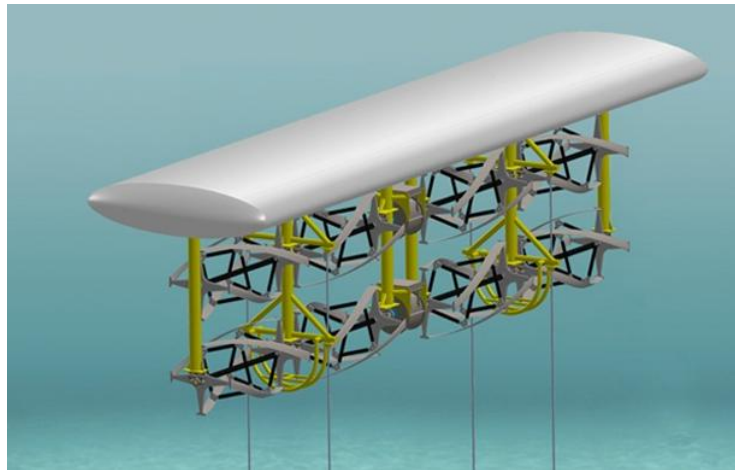


Figure 19: 3D Rendering of OCGen power system
(Source: ORPC [31])

A new type of ocean power generator could harvest the steady, reliable energy of deep ocean currents, and a group of companies are working together to place the first 1 MW system on the seafloor. The companies are currently raising money for the demonstration project and say they're investigating R&D funding from the U.S. Navy and the Department of Energy. The grid connections and system software are being designed by Eaton Corporation [39], a power management company with experience in linking renewable energy sources like wind and solar farms to the grid. The 1-MW turbine, as shown in Figure 20, will come from **Triton** [40], a Florida of USA based company that primarily builds deep-ocean subs. Eaton representatives say the 1-MW demonstration project could easily be built up to a utility-scale current farm by adding more turbines.

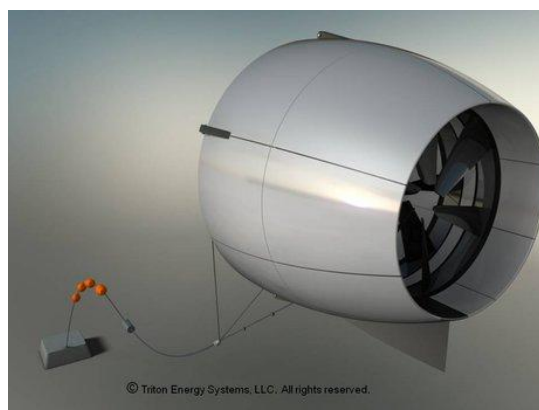


Figure 20: The 1-MW turbine of Triton
(Source: Triton Submarines LLC [40])

Crowd Energy with a new type of design and a full-scale first generation prototype, as shown in Figure 21, is trying to find funding for the next step which is to build the second generation turbine prototype and test tank and do the required data collection and design optimization [41]. The next step will be to move the turbine prototype and test tank to Florida Atlantic University to have their data and design verified. Once verified, they will build a larger sea trial prototype and install it in the Florida Atlantic University open ocean testing site, off the coast of South Florida, USA. At the FAU test site they can collect data and generate electricity on a small scale. Using the data collected from the FAU test site they can build the first production scale turbine. Crowd Energy is trying to have four production scale turbines installed and feeding the power grid by 2016.



Figure 21: Crowd Energy full-scale prototype
(Source: Crowd Energy [41])

IHI Corporation and Toshiba Corporation have been selected by Japan's New Energy and Industrial Technology Development Organization (NEDO) as co-researchers in the "Research and Development ("R&D") of Ocean Energy Technology - Demonstration Research of Ocean Energy Power Generation". After concluding the formal contract with NEDO, they will conduct demonstration research of a turbine system driven by the ocean current [42, 43, 44]. IHI and Toshiba, together with the University of Tokyo and Mitsui Global Strategic Studies Institute, have conducted R&D financed by NEDO's "R&D of Ocean Energy Technology - R&D of Next-Generation Ocean Energy Power Generation (Underwater Floating Type Ocean Current Turbine System)" since 2011. The demonstration research is based on their achievements to date. Within this framework, the unique "underwater floating type ocean current turbine system" developed by IHI and Toshiba will demonstrate power generation in a real ocean environment, in a project expected to continue until 2017. The research work is expected to prove the viability of ocean energy power generation and to create the framework for an industry, and also to contribute to improved energy security for Japan. The underwater floating type ocean current turbine system, as shown in Figure 22, is a power generation device with two counter-rotating turbines. It is anchored to the sea floor and floats like a kite carried and driven by the ocean current [42]. IHI is the lead company in the co-research project and will manufacture the turbine and floating body. Toshiba will supply electric devices, such as the generator and transformer. The Kuroshio Current is a natural energy resource with little fluctuation in flow regardless of time or season. In Japan, an island nation, success in converting the massive power of the ocean current will create a large-scale, stable power source.

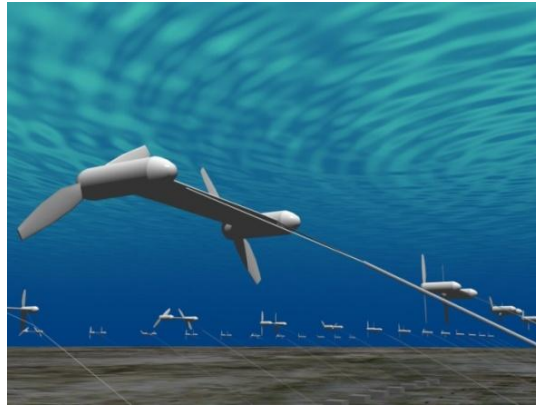


Figure 22: Demonstration of ocean current turbine system by IHI and Toshiba (Source: IHI [42])

National Cheng Kung University's Tainan Hydraulics Laboratory is preparing to install a submerged turbine off the coast of Taitung County in a full-scale experiment to generate electricity from the energy of the Kuroshio Current in Taiwan as shown in Figure 23 [45]. If the test is successful in harnessing the energy of the current, which flows north in the Pacific Ocean to the east of Taiwan at a rate of 1 to 1.5 meters per second, it could generate 10 to 15 kilowatts of electricity per second, enough to supply 9,000 households for an hour. Before mooring the turbine offshore, the research team will meet with fishermen and county government representatives to make sure the turbine does not interfere with fishing. Taiwan's frequent typhoons, earthquakes and northeast monsoons pose other difficulties for the experiment, which is scheduled to test the electricity-generating potential of the current over a two-year period [45].



Figure 23: NCKU ocean current turbine to be moored in the Pacific Ocean off Jinzun Harbor, Taitung County (left and right) (Source: NCKU-SERC [45])

The **Aquantis Current Plane** (“C-Plane”) technology developed by Dehlsen Associates, LLC (DA) and Aquantis, Inc. is an ocean current turbine designed to extract kinetic energy from ocean currents [46, 47]. Figure 24 shows the C-Plane design concept. Aquantis Inc. designed, built, and tested a 1/25th scale model of their ‘C-Plane’ dual-rotor moored ocean current turbine as shown in Figure 25 [48, 49]. This effort was conducted in cooperation with the US Naval Surface Warfare Center at the David Taylor Model Basin and was funded in part under a grant awarded to Dehlsen Associates by the U.S. Department of Energy. The Aquantis Inc. C-Plane is a dual-rotor marine turbine designed to generate up to 2.4MW per unit in the Gulf Stream and other ocean currents.. The

C-Plane is designed to operate in water depths from 100m to 400m, but is capable of being adapted to other applications such as shallow water tidal flows and extreme deep water. In order to operate in deep ocean currents, the C-Plane utilizes a 3-point mooring system which includes two forward mooring lines to react the thrust of the rotors, and one vertical mooring line to keep the platform submerged at its minimum operating depth. As the C-Plane is a fully submerged moored device, the steady-state stability and the dynamic stability of the system are very important.

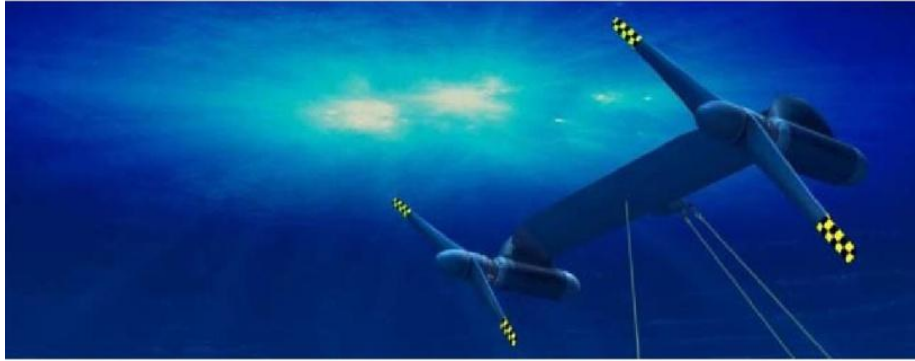


Figure 24: Demonstration of Aquantis C-Plane ocean current turbine
(Source: Aquantis [50])

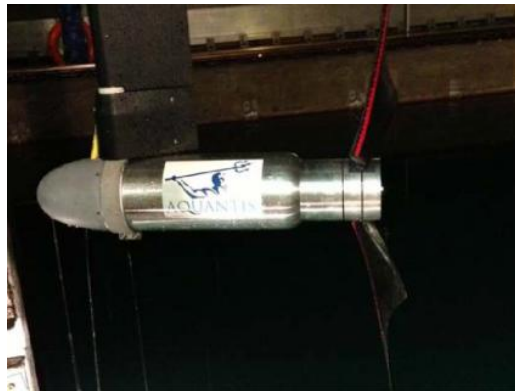


Figure 25: Captured test of 1/25th scale model
(Source: H. Swales et al. [49])

Anadarko Petroleum Corporation in Texas of USA presents the ***Ocean Stream Power Generation (OSPG)*** concept which is a fin-ring propeller to that targets operating rotational speed of a set frequency power from a flowing ocean current [51]. This patented propeller has outer rings that direct the water flow and provides a protective ring that would keep fish from being struck by the outer fins of the propeller as shown in Figure 26. The fin-ring design reduces the effects of cavitation by directing the flow with the rings inside the propeller. There is no tip of a fin to experience cavitation. These rings act like the curved tips of the newer air-plane wings that improve efficiency of lift and drag. The University of Michigan Hydrodynamics Lab provided their facilities for testing the fin-ring propeller which was in a 1/10th scale (32 cm diameter). Following the initial test, they built a 1/5th scale system with four fin-ring propellers and 2.44 meter diameter each one. Moreover, each propeller consists of 7 rings which results to 80 fins. This was tested as a fully functional support submerged generation structure in the Gulf of Mexico by pulling it with a boat to simulate various ocean stream velocities as shown in Figure 27. The structure held stable during test operations. Power was generated at 60 Hz and fed back to the boat at levels exceeding the expected generation power for the speeds. The structure was controlled with a local PLC and communicated back to the boat prior to testing in the Gulf of Mexico.

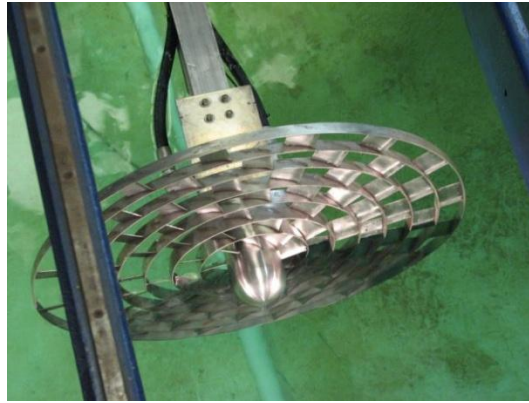


Figure 26: The fin ring propeller in a 1/5th scale (2.43 Meter) under testing in a towing tank (Source: W.D. Bolin [51])



Figure 27: Four fin-ring propeller system prior to submerged testing in the Gulf of Mexico (left and right) (Source: W.D. Bolin [51])

Turner Hunt Ocean Renewable LLC (THOR LLC), which is located in Cincinnati, Ohio, USA, is developing a family of fully submersible horizontal axis tethered ocean current turbines, as shown in Figure 28, for use off the southeastern United States in the Gulf Stream [52]. THOR LLC is working on a lease that would allow for the deployment of the company's scaled prototype off the east coast of Fort Lauderdale, Florida, USA, with future deployments as far north as Hatteras, N.C. THOR's ocean current turbine is completing testing and evaluation as a scale model in a unique ocean current simulator built by THOR [52]. THOR's ocean current turbine provides near base load capacity factors (about 80%) using a proprietary power control protocol method of operation. The current status of the development is not known, but the target commercial scale turbines rotor diameters are from 40 to 60 meters and the capability of producing up to 2 megawatts of electrical power output.

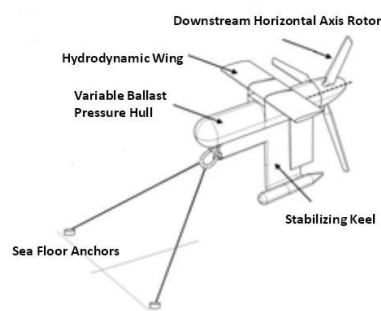


Figure 28: THOR's renewable ocean current turbine (Source: THOR LLC [52])

1.3.3 Southeast National Marine Renewable Energy Center (SNMREC)

The *Southeast National Marine Renewable Energy Center (SNMREC)*, formerly the Center for Ocean Energy Technology (COET), at Florida Atlantic University (FAU), Boca Raton, Florida, USA, has been established to pursue research and technologies that will aid industry in harnessing the vast ocean energy resources off the coast of Florida [53, 54].

One of the goals of the SNMREC is developing an instrumented testing range including deploying a single-point mooring system, as shown in Figures 29, 30 and 31, in the Gulf Stream that will be used to test its experimental OCT and OCTs developed by other entities from the surface [54]. The SNMREC's experimental OCT, as well as OCTs developed by other entities will be deployed to determine (1) system performance and enhancements for future development, (2) environmental concerns and potential effects, and (3) methodologies for further scaled testing. This *Ocean Current Turbine Testbed (OCTT)* consists of a permanently anchored *Mooring and Telemetry Buoy (MTB)* with a gravity anchor, a tested ocean current turbine, and a twin-hull *Observation, Control, Deployment, Platform (OCDP)* or a support vessel as shown in Figures 29 and 30 [55].

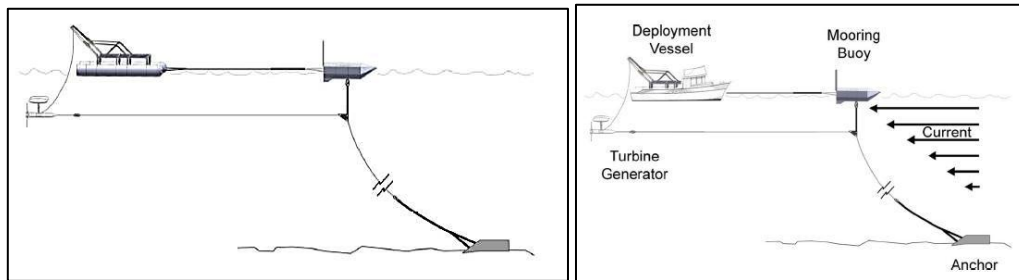


Figure 29: Diagrammatic representation of the Ocean Current Turbine Testbed (OCTT) with a OCDP (left) or a Deployment Vessel (right) (Source: F.R. Driscoll et al. [55])



Figure 30: The completed Mooring and Telemetry Buoy (MTB) on stands (left) and without A-frame, hydraulic, and electronic systems (right) (Source: F.R. Driscoll et al. [55])

The SNMREC has designed and has currently constructed an experimental 20 kW *horizontal axis OCT* to quantify and overcome some of the many hurdles involved with placing such a system in the Gulf Stream [55]. The underwater turbine is a 20 kW open blade axial-flow horizontal turbine design, driven by a 3 m diameter 3-blade rotor. The rotor on this OCT uses airfoil shapes that range from approximately a NACA 4412 shape at the hub to a NACA 4421 shape at the tip.

A 30 HP motor-generator is housed within a water-tight pressure vessel, and it is connected to the rotor through a 25:1 step-up planetary gear box with a 3 inch outside diameter (OD) drive shaft. The motor-generator is Sumitomo Cyclo 6000 AC Induction Motor (Frame 180 MG, Type TK-F) with rated nameplate values of 230 V_{AC}, 3-Phase, 4-Pole, 60 Hz., 1740 RPM and 74.7 Amps. As a *NEMA Design Class A*, which is a standard AC induction motor design, the motor features normal starting torque, normal starting current and low slip [55, 56]. The whole system is 2.5 m in total length, has a total mass of 1680 kg and is designed to be either negatively buoyant or nearly neutrally buoyant. The two positively buoyant elliptically shaped floats where are rigidly attached to the turbine's main body are to counteract the hydrodynamic torque of the rotor as shown in Figure 31.

All structural components, including: the main generator housing, the drive shaft, and the mooring connection assembly are made from 316L stainless steel. 316L was chosen for its strength, excellent forming and welding characteristics, high creep resistance, and corrosion and pitting resistance. Nickel Copper Alloy 400 was the chosen material for all bolting hardware because of its anti-galling properties, and its proximity to 316L with regard to galvanic corrosion [56].

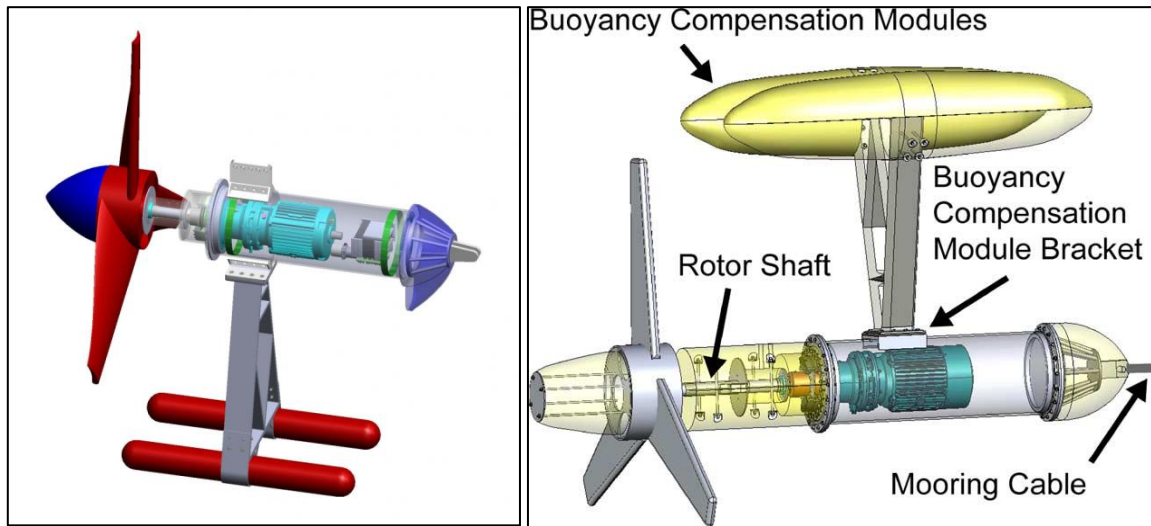


Figure 31: Solid model rendering of the negatively buoyant SNMREC's 20kW 1.5m radius experimental research turbine (left) and neutrally buoyant (right). The rotor blades are not accurately drawn in this rendering (Source: F.R. Driscoll et al. [55] and J.H. VanZwieten et al. [56])

The performance of the experimental 20 kW ocean current turbine with or without the generator has been numerically quantified in many studies [57, 58, 59, 60, 61, 62] while studies has been conducted for mooring analysis [63], anchor selection, [16, 17], and necessary instrumentation as well as intelligent monitoring system [53]. In December 2013, the SNMREC researchers conducted an experimental offshore tow test, in the Gulf Stream, of the 20 kW ocean current turbine as shown in Figure 33 [64]. Although this test did not include a generator to convert the rotor's motion into electrical energy, very valuable hydrodynamic motion data was collected by them. Electrical systems are separately being prepared in a laboratory setting for future integration and towed turbine experiments. Finally, the next phase of the project is the numerical performance analysis and linearization of the models for advance control system development in a scale experimental ocean current turbine of 720 kW. Some studies have already been conducted according to the references [65, 66].

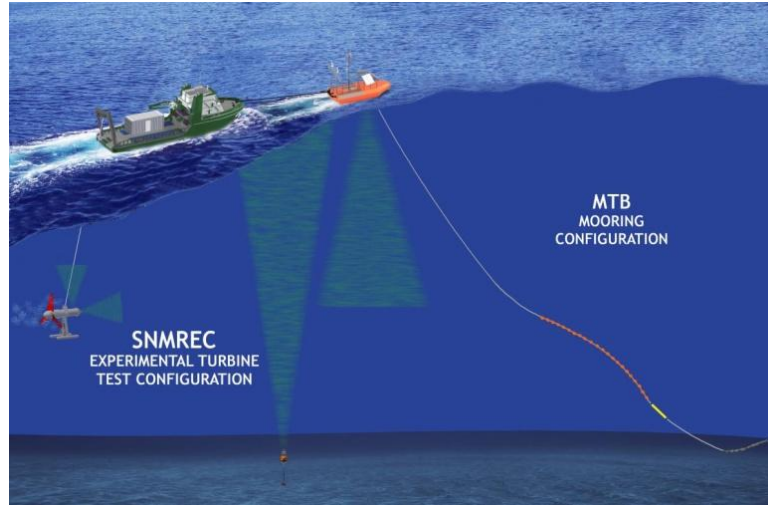


Figure 32: Rendition of the SNMREC's proposed offshore test configuration. “MTB” refers to the buoy (Mooring and Telemetry Buoy) which acts both as a mooring point and persistent environmental measurement platform. (Source: M. Borghi et al. [59])



Figure 33: SNMREC's research vessel during transportation of the research ocean current turbine offshore Fort Pierce for sea testing (left) and a state of the art rendering SNMREC's experimental turbine, a typical axial-flow configuration with stabilizing buoyancy pods, in operation (right) (Source: FAU SNMREC [53])

1.4 Generator and Drive-Train Options

The ocean current industry and, especially, the drive-train are at an early stage of development. While many different designs are possible for OCTs, most designs will use *a rotor blade to rotate the shaft of a motor/generator* as shown in Figure 34 [67]. To minimize the cost of creating initial experimental and prototype turbines, these systems will likely use *off-the-shelf motors* (non custom) for generators [56]. However the business is characterized by prototype building and new ideas being brought forward. There is a significant risk if the generator is also a prototype. The environment also requires the generator to be enclosed in an air tight capsule and protect the capsule from flooding and corrosion.

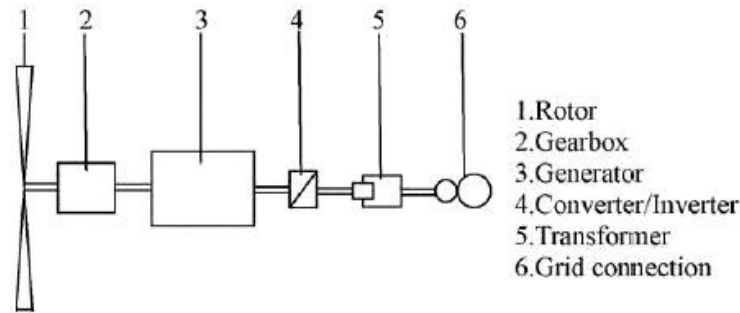


Figure 34: Principle scheme of ocean current turbine system
(Source: M.S. Guney. and K. Kaygusuz [67])

As new technology is being tested on prototype devices, many developers choose geared solutions with off-the shelf generators, reducing the number of prototype elements to a minimum. Both induction machines and synchronous machines are being used. OCTs that have no choice should use prototype generators such as *Permanent Magnet (PM) synchronous machines*. Some developers choose to use gearless solutions, and these tend to utilize PM generators. **Removing gears increases the size of the generator significantly.** For seabed-mounted turbines there is no clear pattern when it comes to drive trains. Most of them are geared, but some are direct driven. Those which are direct driven seem to utilize PM generators. Both synchronous and asynchronous generators are in use, but it may seem like some asynchronous generators are being replaced by synchronous generators in later designs [18]. Compared to seabed-mounted devices, floating turbines have the added constraint of keeping weight as low as possible. This may be the reason why almost all manufacturers have chosen gearbox in their powertrain [18]. It is interesting to see some ocean current turbine developers choose geared solutions since maintenance and repair is even more costly in underwater equipment. The cause could be that the expected lifetime of mechanical gears has increased lately.

Because ocean current turbines are always placed under water, and often far from docks and workshops, it is of utmost importance to design a system that requires as little maintenance as possible, and that has the lowest possible risk of failure. This is a problem for all components in the ocean turbine, and the manufacturers try to keep the number of risky components to a minimum. This includes all moving parts, like seals, gears, breaks etc. Machines with brushes are not desirable in such underwater structures, because brushes are a common source of failure, although brush quality has improved greatly in the last decades [18].

The general trend is that several drive train options are being tested and all of them are variable speed driven and alternative current (AC) generators. Direct Current (DC) cannot be transmitted across the long distances and their usage is restricted in very nearly environment from utilization place. On the other hand, AC can be transferred easily over long distances. Additionally high voltage AC has good transmitting efficiency and it is excellently suitable for providing electricity in remote areas [67]. For manufacturers seeking to minimize risk for prototype turbines, prototype generators are avoided, and *induction generators (IG) which are robust and reliable seem to be the preferred choice.* Most powertrains include a gearbox, reducing the size and weight of the generator. Especially for floating turbines, this seems to be the trend.

The selection of generator is also dependent on the question, how big or small is the power of the system relatively to the other generators of the land grid. Most cases are confronted that the power of hydrokinetic system is very small as compared to other generator connected to the grid. Then the following control mechanisms for induction generator are possible, with the most suitable the variable speed drive train, such as [68]:

- Induction generator connected directly to the grid. This is the cheapest system, in which the current turbine must run at nearly constant speed. A stationary water regime is a must for this system.
- Induction generator with multi-winding of motor to balance of speed fluctuation of the current turbine.
- Variable speed generator can be chosen. The output of this type of generator is rectified to DC. Then the defined AC is produced by a suitable for the grid DC–AC inverter.
- Double-fed induction generator also can be used. Active change of the current and phase in the generator's rotor constitutes the increasing of the effective slip on induction generator.

Finally, an exploded view and a cutaway view is shown in Figure 35 for an IG and PM respectively [69] while a comparison between them as an ocean current turbine generator is given in Table 1 [70].



Figure 35: AC Wound type Induction Machine exploded view (left) and AC Permanent magnet machine cutaway view (right)
(Source: Leeson Electric Corporation [69])

Table 1: IG and PM topology comparison for OCT

Type	Pros	Cons
IG	<ul style="list-style-type: none"> ✓ Full speed range ✓ No brushes on the generator ✓ Complete control of active and reactive power ✓ Proven technology ✓ Limited speed range -30% to +30% around synchronous speed (for wound type) 	<ul style="list-style-type: none"> ✓ Full scale power converter ✓ Need for gear ✓ Need slip rings (for wound type)
PM	<ul style="list-style-type: none"> ✓ Full speed range ✓ Possible to avoid gear ✓ Inexpensive small capacity PWM inverter ✓ Complete control of active and reactive power 	<ul style="list-style-type: none"> ✓ Full scale power converter ✓ Multipole generator (big and heavy) ✓ Permanent magnets needed

1.5 Thesis Outline

The development of a numeric simulation for predicting the performance of an Ocean Current Energy Conversion System is presented in this thesis along with a control system development using a PID controller for the achievement of specified rotational velocity set-points. In the beginning, this numeric model is implemented in MATLAB/Simulink® and it is used to predict the performance of a three phase squirrel single-cage type induction motor/generator in two different cases. The first case is a small 3 meter rotor diameter, 20 kW ocean current turbine with fixed pitch blades, and the second case a 20 meter, 720 kW ocean current turbine with variable pitch blades. Furthermore, the second case is also used for the development of a Voltage Source Variable Frequency Drive for the induction motor/generator. Comparison among the Variable Frequency Drive and a simplified model is applied. Finally, the simulation is also used to estimate the average electric power generation from the 720 kW Ocean Current Energy Conversion System which consists of an induction generator and an ocean current turbine connected with a shaft which modeled as a mechanical vibration system.

CHAPTER 2

INDUCTION MOTORS/GENERATORS

2.1 Introduction

Alternative current (AC) induction motors are the most common electric motors used in industrial motion control systems, onboard vessels, ocean engineering applications as well as in main powered home appliances. They have *simple and rugged design, natural protection against short circuits, low build cost, low maintenance cost* and *direct connection* to an AC power source are some of the main advantages of AC induction motors [71].

Various types of AC induction motors are available in the market. Different motors are suitable for different applications. Although AC induction motors are easier to design than DC motors, the speed and the torque control in various types of AC induction motors require a greater understanding of the design and the characteristics of these motors [71].

In the next sections, is discussed the principles of design and operation of an AC induction motor/generator; the different types, their characteristics, the selection criteria for different applications etc. as well as the modeling and performance analysis via MATLAB/Simulink® for OCTs application.

2.2 Principles of Design and Operation

In this section, the principles of design and operation of an AC induction motor/generator (IM/IG) are presented with details. More specifically, the three-phase AC squirrel single cage induction motor/generator is presented comprehensively with many figures and diagrams.

2.2.1 Basic Construction

Like most motors, an AC induction motor has a fixed outer portion, called the *stator* and a *rotor* that spins inside with a carefully engineered *air gap* between the two [71]. A cutaway and a breakdown description of a typical three-phase induction motor are shown in Figure 36.

Two sets of electromagnets are formed inside any motor. In an AC induction motor, one set of electromagnets is formed in the stator because of the AC supply connected to the stator windings. The alternating nature of the supply voltage induces an *Electro-Motive Force (EMF)* in the rotor as per *Lenz's law* [72], thus generating another set of electromagnets; hence the name – induction motor. Interaction between the magnetic field of these electromagnets generates twisting force, or torque. *As a result, the motor rotates in the direction of the resultant torque.* The rotation of the magnetic field in an induction motor has the advantage that *no electrical connections need to be made to the rotor* [71].

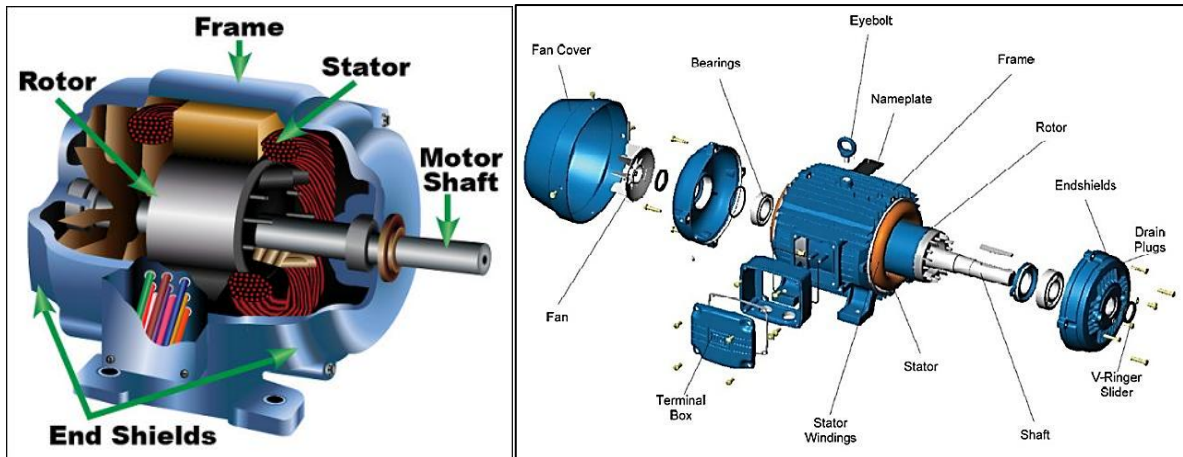


Figure 36: A cutaway basic parts description (left) and breakdown detailed description (right) of a typical three-phase induction motor (Source: Electromotors WEG SA, Brazil [73])

2.2.2 Stator

The stator is the *stationary part* of the induction motor. The stator consists of the *frame (yoke)* and the *stationary core*. The frame is only as a support of the stator core and can be smooth (Figure 36 – left) or ribbed (Figure 36 – right) while the core is made up of several thin laminations of aluminum or cast iron. They are punched and clamped together to form a hollow cylinder (*stator core*) with slots so that *carry the magnetic flux* as shown in Figures 37 and 38. **The stator core is laminated to reduce eddy currents, reducing losses and heating** [74].

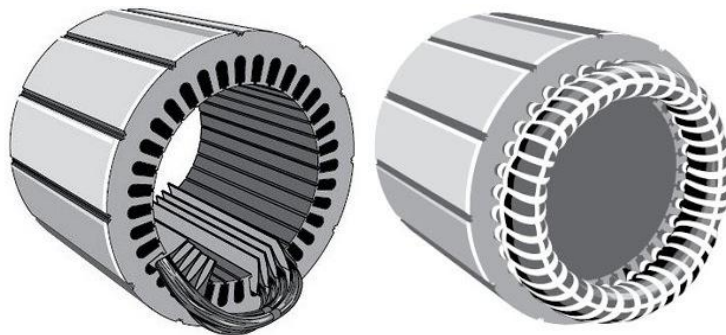


Figure 37: Stator windings partially completed (left) and completed (right) (Source: Electrical-Know-How [74])

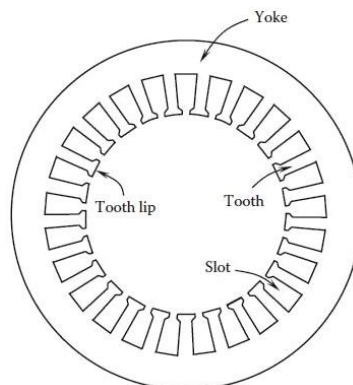


Figure 38: Stator lamination (Source: W. Tong [74])

Coils of *insulated wires* are inserted into these slots so that carry the electric current. These coils can either be *form wound*, where the wire is square or rectangular and the turns are systematically arranged, or *random wound*, where the wire is round and the arrangement between the turns is not definite as shown in Figure 39. Random windings are used on lower kW machines where it is impractical to use form coils. Random windings are made from a lower cost magnet wire that is film coated and round while the form windings use square or rectangular magnet wire. With random windings, the mechanization of manufacturing is also increased to add to a lower cost. Moreover, the cross-sectional area of these windings must be large enough for the power rating of the motor and for a three-phase motor, three (3) sets of winding are required, one for each phase connected in either star or delta [76].



Figure 39: Form wound coils (left) and random wound coils (right)
(Source: Kato Engineering Inc. [76])

Each grouping of coils, together with the core it surrounds, forms an electromagnet (a pair of poles) on the application of AC supply. ***The number of poles of an AC induction motor depends on the internal connection of the stator windings.*** The stator windings are connected directly to the power source. *Internally they are connected in such a way, that on applying AC supply, a rotating magnetic field is created* [71].

Finally, the slots employed in the stator are in general three types [77]. The entirely open type, the *semi-closed type* and the *tapered type* as displayed in Figure 40. Operating performance of the induction motors depends upo the shape and the number of the stator slots.

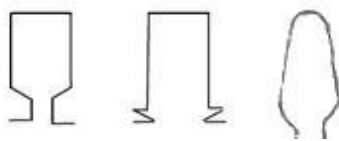


Figure 40: Different types of stator slots:
Semi-closed (left), Open (middle) and Tapered (right)
(Source: V-Tech e-Notes [77])

2.2.3 Rotor (Armature)

The rotor is the *rotating part* of the induction motor. The rotor is made up of several thin steel laminations with evenly spaced bars, which are made up of aluminum or copper, along the periphery. In the most popular type of rotor, which is the squirrel cage rotor, these bars are *connected at ends mechanically and electrically by the use of rings*. Almost **90%** of induction motors have *squirrel cage rotors*, either single cage or double cage while the rest **10%** have *wound type rotors*. This is because the squirrel cage rotor has a simple and rugged construction. The rotor consists of a cylindrical laminated core with axially placed parallel slots for carrying the conductors. Each slot carries a

copper, aluminum, or alloy bar. *These rotor bars are permanently short-circuited at both ends by means of the end rings*, as shown in Figure 41. This total assembly resembles the look of a squirrel cage, as shown in Figure 42, which gives the rotor its name [71].

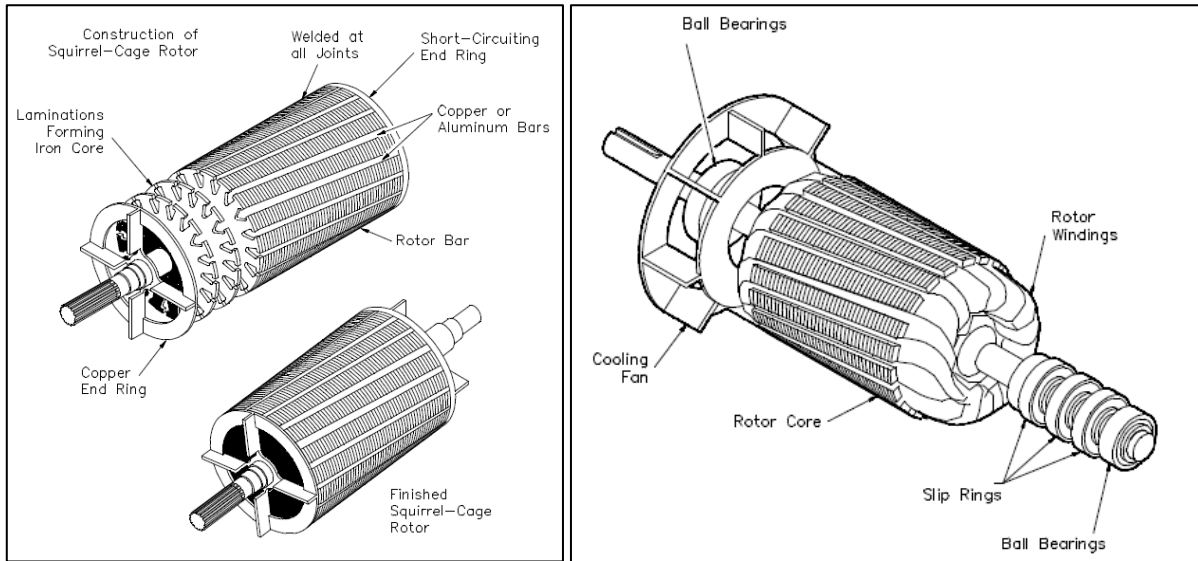


Figure 41: Squirrel cage induction rotor (left) and wound type induction rotor (right)
(Source: U.S. DOE [78])

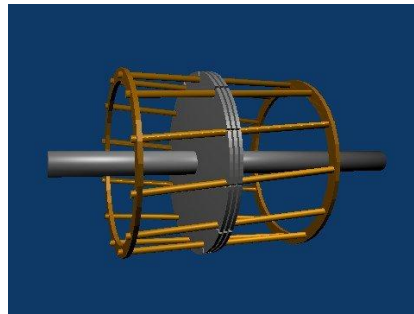


Figure 42: 3D solid model of squirrel single cage rotor's bars with three iron cores
(Sources: Wikipedia [79])

The rotor slots are not exactly parallel to the shaft. Instead, they are given a *skew* for two main reasons. The first reason is to make the motor run quietly by reducing magnetic hum and to decrease slot harmonics. The second reason is to help reduce the *locking tendency* of the rotor (avoid “cogging”). The rotor teeth tend to remain locked under the stator teeth due to direct magnetic attraction between the two. ***This happens when the number of stator teeth is equal to the number of rotor teeth.*** Another reason is that the rotor resistance is increased due to comparatively lengthier rotor conductor bar [71].

The number of rotor slots is selected in relation to number of stator slots otherwise undesirable effects will be found at the starting of the motor [80, 81]. Operating performance of the induction motors depends upon the shape and the number of the rotor slots. The slots are employed in the squirrel single-cage rotors are generally two types; the *open type* and the *close type* as shown in Figure 43 [75]. The selection of open or closed rotor slot design involves the trade-off because each design has its own advantages and disadvantages, depending on different applications. Various double-cage rotor slots for improving motor start-up and normal operation can be found in Reference [82].

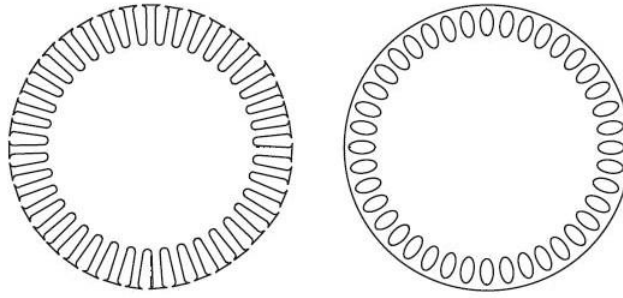


Figure 43: Squirrel single-cage rotor slots:
open type (left) and closed type (right)
(Source: W. Tong [75])

The armature winding are not connected to the other parts of the motor. The rotor is mounted on the shaft using bearings on each end; one end of the shaft is normally kept longer than the other for driving the load. Some motors may have an accessory shaft on the non-driving end for mounting speed or position sensing devices. Between the stator and the rotor, there exists an air gap, through which due to induction, *the energy is transferred from the stator to the rotor*. The generated torque forces the rotor and then the load to rotate. Regardless of the type of rotor used, the principle employed for rotation remains the same [71]. A cross sectional view of a typical induction motor is shown in Figure 44.

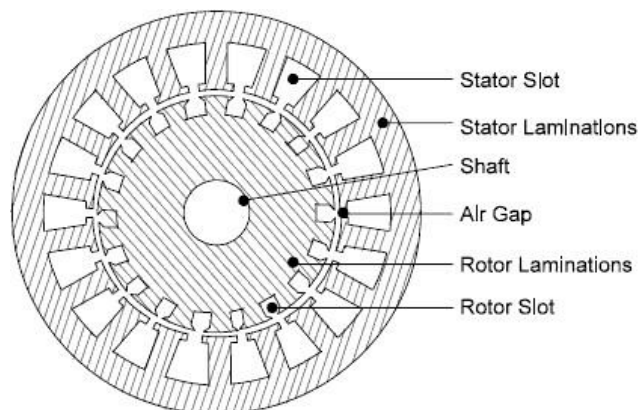


Figure 44: Cross sectional view of a typical
induction motor (Source: EEP [82])

2.2.4 Number of Poles and Speed

Every AC induction motor has poles, just like a magnet. However, unlike a simple magnet, these poles are formed by *bundles of magnet wire (**windings**) wound together in the slots of the stator core*. In most cases, you can look inside the motor and count the number of poles in the winding since they are distinct bundles of wire evenly spaced around the stator core as shown in Figure 45. *It is possible to determine the number of poles by looking at the stator but it usually a very tedious process because it is necessary to determine which slot each coil is in and how each coil is connected to every other coil.*

The number of poles, which is always an even number since the magnetic poles always occurs in pairs, combined with the AC line frequency (Hz) is all that determine the *no-load revolutions per minute (rpm)* of the induction motor or the speed of the rotating magnetic field created by the stator

which called *synchronous speed*. So, all four-pole motors will run at the same speed under no-load conditions, all six-pole motors will run at the same speed, and so on as shown in Figure 46 [75].



Figure 45: Three-phase generator: 24 poles of 18 coils with 80 turns each and 6 coils in each phase connected in series (Source: Instructables [83])

If the rotor were turning at the synchronous speed, there would be no relative velocity between the rotor conductors and the stator *Electro-Motive Force (EMF)*. This would result in **zero EMF along the rotor conductors and also no current and no force on them**. Thus, the *induction motor never reaches synchronous speed and operates at some speed less than synchronous speed*. The difference between the rotating rotor speed and the synchronous speed is defined as the *sleep speed*. The sleep speed normalized to the synchronous speed is defined as *slip s*. So, if the induction rotor speed is equal the synchronous speed then $s=0$ and if the motor is stationary then $s=1$ [84].

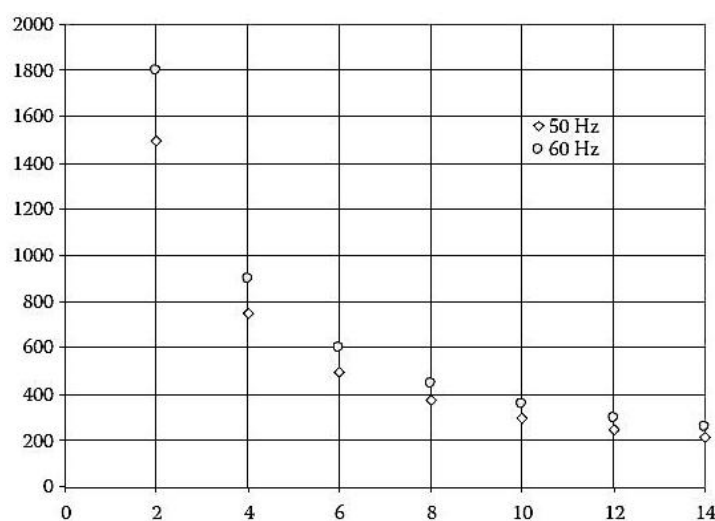


Figure 46: Synchronous speed (y-axis) versus number of pole pairs (x-axis) for 50Hz and 60Hz system frequency (Source: W. Tong [75])

2.2.5 Operating Principle for Three (3) Phase

Virtually all electrical motors use magnetic field rotation to spin their rotors. A three-phase AC induction motor is the *only type where the rotating magnetic field is created naturally* in the stator because of the nature of the supply. DC motors depend either on mechanical or electronic commutation to create rotating magnetic fields. A single-phase AC induction motor depends on extra electrical components to produce this rotating magnetic field [84].

According to *Faraday's law* "***an EMF induced in any circuit is due to the rate of change of magnetic flux linkage through the circuit***". As the rotor winding in an induction motor are either closed through an external resistance or directly shorted by end ring, and cut the stator rotating magnetic field, an EMF is induced in the rotor copper bar and due to this EMF a current flows through the rotor conductor. Here the relative velocity between the rotating flux and static rotor conductor is the cause of current generation; hence as per *Lenz's law* the rotor will rotate in the same direction to reduce the cause i.e. the relative velocity [84].

2.2.5.1 Rotating Magnetic Field

More specifically, to understand how an induction motor operates, we must first unravel the mysteries of the rotating magnetic field. Because both the rotor and stator iron surfaces are smooth (apart from the regular slotting), and are separated by a small air-gap, *the flux produced by the stator windings crosses the air-gap radially*. The behavior of the motor is dictated by this radial flux, so it is easier to concentrate first on establishing a mental picture of what is meant by the 'flux wave' in an induction motor [84].

The pattern of flux in an ideal four (4) pole motor supplied from a balanced three (3) phase source is shown in Figure 47 (left). The top sketch corresponds to time $t = 0$ seconds; the middle one shows the flux pattern one-quarter of a cycle of the supply later (i.e. 5 ms if the frequency is 50 Hz); and the lower one corresponds to a further quarter cycle later. It should be noted that the pattern of flux lines is repeated in each case, except that the middle and lower ones are rotated by 45° and 90° , respectively, with respect to the top sketch [84].

The term '4-pole' reflects the fact that flux leaves the stator from two N poles, and returns at two S poles. Note, however, that there are no physical features of the stator iron that mark it out as being 4-pole, rather than say 2-pole or 6-pole. *As already mentioned, it is the layout and interconnection of the stator coils which set the pole-number.* If the variation of the radial air-gap flux density with respect to distance round the stator can be plotted, at each of the three instants of time, the patterns shown in Figure 47 (right) are appeared. The first feature to note is that the radial flux density varies sinusoidal in space. There are two N peaks and two S peaks, but the transition from N to S occurs in a smooth sinusoidal way, giving rise to the term 'flux wave'. The distance from the center of one N pole to the center of the adjacent S pole is called the pole-pitch, for obvious reasons. The pole-number must be an even integer, since for every N pole there must be an S pole [84].

Staying with Figure 47 (right), it can be mentioned that after one-quarter of a cycle of the mains frequency, the flux wave retains its original shape, but has moved round the stator by half a pole-pitch, while after half a cycle it has moved round by a full pole-pitch. If we had plotted the patterns at intermediate times, we would have discovered that the wave maintained a constant shape, and progressed smoothly, advancing at a uniform rate of two pole-pitches per cycle of the supply. The term 'traveling flux wave' is thus an appropriate one to describe the air-gap field [84].

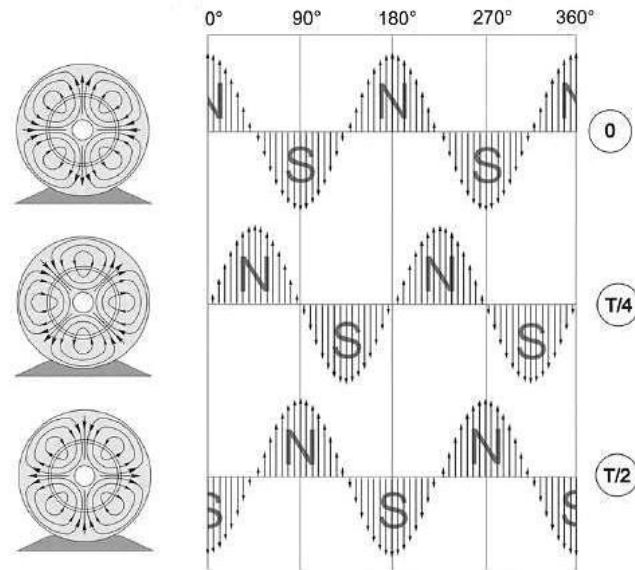


Figure 47: Flux pattern in a 4-pole induction motor at three successive instants of time, each one-quarter of a cycle apart (left) and radial flux density distribution in the air-gap at the three instants shown in the left (right)
(Source: A. Hughes and B. Drury [84])

2.2.5.2 Production of Rotating Magnetic Field

As already mentioned, the stator winding of an induction motor consists of a uniform array of identical coils, located in slots. The coils are in fact connected to form three identical groups or phase-windings, distributed around the stator, and symmetrically displaced with respect to one another. The three phase-windings are connected either in *star (wye)* or *delta (mesh)*, as shown in Figure 48 [84].

The three phase-windings are connected to a balanced 3-phase AC supply, and so the currents (which produce the EMF that sets up the flux) are of equal amplitude but differ in time-phase by one-third of a cycle (120°), forming a balanced 3-phase set [84].

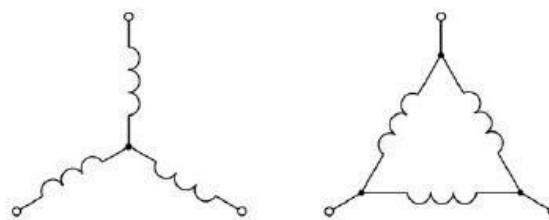


Figure 48: Star (wye) and delta (mesh) connection of the three phase-windings of a 3-phase induction motor
(Source: A. Hughes and B. Drury [84])

The aim of the winding designer is to arrange the layout of the coils so that each phase-winding, acting alone, produces an *EMF wave* (and hence an air-gap flux wave) of the desired pole-number, and with a *sinusoidal variation of amplitude with angle*. Getting the desired pole-number is not difficult: you simply have to choose the right number and pitch of coils, as shown by the diagrams of an elementary 4-pole winding in Figure 49 [84].

In Figure 49 (up) it can be seen that by positioning two coils (each of which spans one pole-pitch) 180° apart the correct number of poles can be obtained (i.e. 4). However, the air gap field – shown by only two flux lines per pole for the sake of clarity – is uniform between each go and return coil-side, not sinusoidal. A clearer picture of the air-gap flux wave is presented in the developed view in Figure 49 (down), where more equally spaced flux lines have been added to emphasize the uniformity of the flux density between the ‘go’ and ‘return’ sides of the coils. Finally, the plot of the air-gap flux density underlines the fact that this very basic arrangement of coils produces a rectangular flux density wave, whereas what we are seeking is a sinusoidal wave [84].

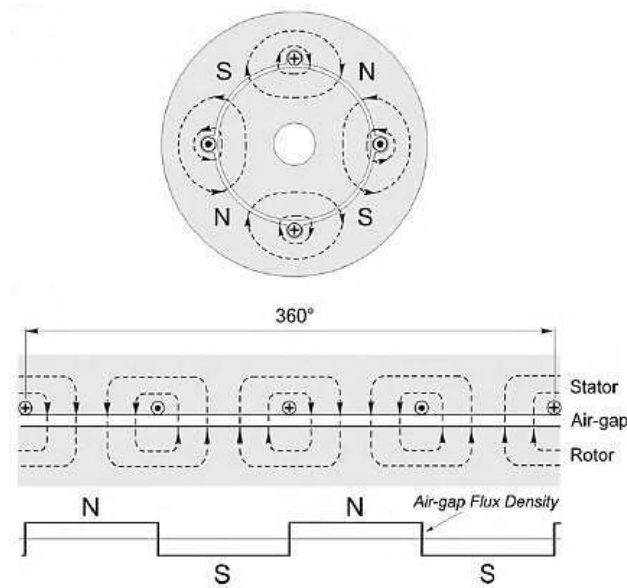


Figure 49: Arrangement (up) and developed diagram (down) showing elementary 4-pole, single-layer stator winding consisting of four conductors spaced by 90° . The ‘go’ side of each coil (shown by the plus symbol) carries current into the paper at the instant shown, while the ‘return’ side (shown by the dot) carries current out of the paper (Source: A. Hughes and B. Drury [84])

We can improve matters by adding more coils in the adjacent slots, as shown in Figure 50. All the coils have the same number of turns, and carry the same current. The addition of the extra slightly displaced coils gives rise to the stepped waveform of MMF and air-gap flux density shown in Figure 50. It is still not sinusoidal, but is much better than the original rectangular shape [84].

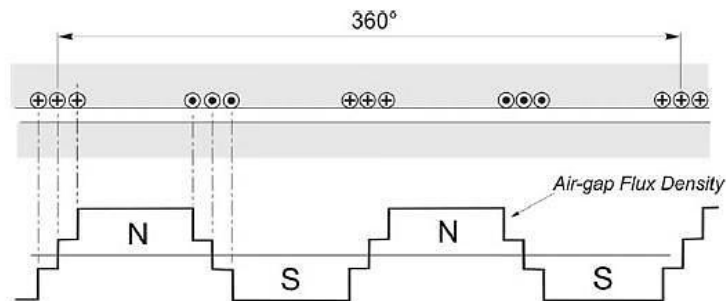


Figure 50: Developed diagram showing flux density produced by one phase of a single-layer winding having three slots per pole per phase (Source: A. Hughes and B. Drury [84])

It turns out that if we were to insist on having a perfect sinusoidal flux density waveform, we would have to distribute the coils of one phase in a smoothly varying sinusoidal pattern over the whole periphery of the stator. This is not a practicable proposition, first because we would also have to vary the number of turns per coil from point to point, and secondly because we want the coils to be in slots, so it is impossible to avoid some measure of discretization in the layout. For economy of manufacture we are also obliged to settle for all the coils being identical, and we must make sure that the three identical phase-windings fit together in such a way that all the slots are fully utilized [84].

Despite these constraints we can get remarkably close to the ideal sinusoidal pattern, especially when we use a ‘two-layer’ winding (in which case the stator slots may contain turns from more than one phase winding). A typical arrangement of one phase is shown in Figure 51. The upper expanded sketch shows how each coil sits with its ‘go’ side in the top of a slot while the ‘return’ side occupies the bottom of a slot rather less than one pole-pitch away. Coils which span less than a full pole-pitch are known as short-pitch or short-chorded: in this particular case the coil pitch is six slots and the pole-pitch is nine slots, so the coils are short pitched by three slots. This type of winding is almost universal in all but small induction motors, the coils in each phase being grouped together to form ‘phase-bands’ or ‘phase-belts’. Since we are concentrating on the field produced by only one of the phase-windings (or ‘phases’), only one-third of the coils in Figure 51 are shown carrying current. The remaining two-thirds of the coils form the other two phase-windings, as discussed below. Returning to the flux density plot in Figure 5.5 we see that the effect of short pitching is to increase the number of steps in the waveform, and that as a result the field produced by one phase is a fair approximation to a sinusoid [84].

The current in each phase pulsates at the supply frequency, so the field produced by say phase A, pulsates in sympathy with the current in phase A, the axis of each ‘pole’ remaining fixed in space, but its polarity changing from N to S and back once per cycle. There is no hint of any rotation in the field of one phase, but when the fields produced by each of the three phases are combined, matters change dramatically [84].

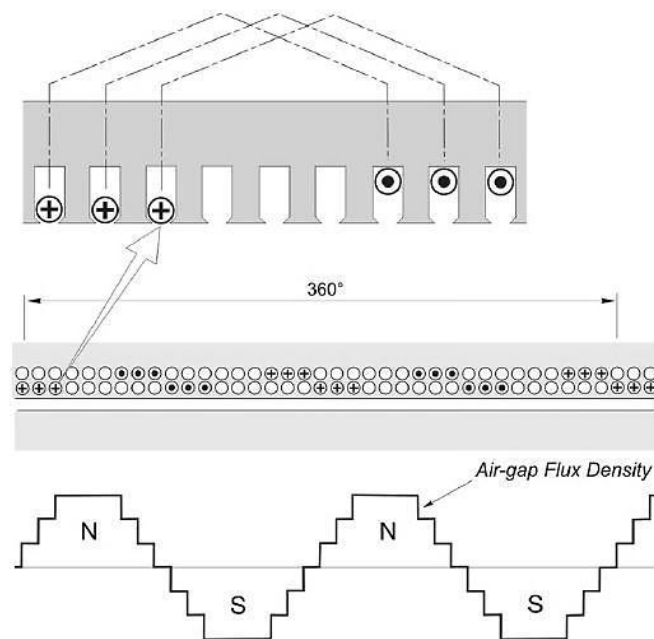


Figure 51: Developed diagram showing layout of windings in a 3-phase, 4-pole, two layer induction motor winding, together with the flux density wave produced by one phase acting alone. The upper detail shows how the coil-sides form upper and lower layers in the slots (Source: A. Hughes and B. Drury [84])

2.2.5.3 Resultant 3-phase Field

The layout of coils for the complete 4-pole winding is shown in Figure 52 (up). The ‘go’ sides of each coil are represented by the capital letters (A, B, C) and the ‘return’ sides are identified by bars over the letters (A; B; C). For the sake of comparison, a 6-pole winding layout that uses the same stator slotting is shown in Figure 5.6 (down): here the pole-pitch is six slots and the coils are short-pitched by one slot [84].

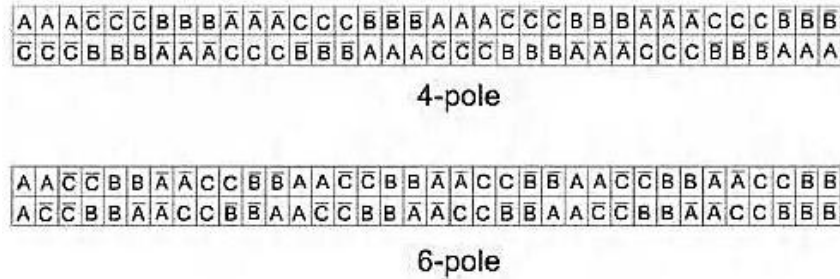


Figure 52: Developed diagram showing arrangement of 3-phase, two-layer windings in a 36-slot stator. A 4-pole winding with three slots/pole/phase is shown (up) and a 6-pole winding with two slots/pole/phase is shown (down)
(Source: A. Hughes and B. Drury [84])

Returning to the 4-pole winding, it can be seen that the windings of phases B and C are identical with that of phase A apart from the fact that they are displaced in space by plus and minus two-thirds of a pole-pitch, respectively. Phases B and C therefore also produce pulsating fields, along their own fixed axes in space. But the currents in phases B and C also differ in time-phase from the current in phase A, lagging by one-third and two-thirds of a cycle, respectively. *Therefore, to find the resultant field the fields of the three phases must be superimposed, taking account not only of the spatial differences between windings, but also the time differences between the currents.* This is a tedious process, so the intermediate steps have been omitted and instead we move straight to the plot of the resultant field for the complete 4-pole machine, for three discrete times during one complete cycle, as shown in Figure 53 [84].

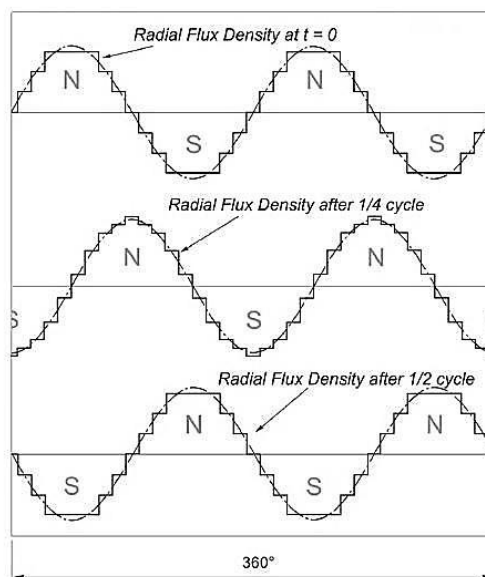


Figure 53: Resultant air-gap flux density wave produced by a complete 3-phase, 4-pole winding at three successive instants in time
(Source: A. Hughes and B. Drury [84])

It is obvious that the three pulsating fields combine beautifully and lead to a resultant 4-pole field which rotates at a uniform rate, advancing by two pole-pitches for every cycle of the supply. The resultant field is not exactly sinusoidal in shape (though it is actually more sinusoidal than the field produced by the individual phase-windings), and its shape varies a little from instant to instant; but these are minor worries. The resultant field is amazingly close to the ideal traveling wave and yet the winding layout is simple and easy to manufacture. This is an elegant engineering achievement, however one looks at it [84].

The direction of rotation depends on the order in which the currents reach their maxima, i.e. on the phase-sequence of the supply. Reversal of direction is therefore simply a matter of interchanging any two of the lines connecting the windings to the supply [84].

2.2.6 Main (Air-Gap) Flux and Leakage Flux

Broadly speaking the motor designer shapes the stator and rotor teeth to encourage as much as possible of the flux produced by the stator windings to pass right down the rotor teeth, so that before completing its path back to the stator it is fully linked with the rotor conductors which are located in the rotor slots. This tight magnetic coupling between stator and rotor windings is necessary for good running performance, and the field which provides the coupling is of course the main or air-gap field. In practice the vast majority of the flux produced by the stator is indeed main or ‘mutual’ flux. But there is some flux which *bypasses the rotor conductors*, linking only with the stator winding, and known as **stator leakage flux**. Similarly not all the flux produced by the rotor currents links the stator, but some (the **rotor leakage flux**) links only the rotor conductors [84].

The use of the pejorative-sounding term ‘leakage’ suggests that these leakage fluxes are unwelcome imperfections, which we should go out of our way to minimize. However, while the majority of aspects of performance are certainly enhanced if the leakage is as small as possible, others (notably the large and unwelcome current drawn from the mains when the motor is started from rest directly on the utility supply) are made much worse if the coupling is too good. So it comes up the somewhat paradoxical situation in which the designer finds it comparatively easy to lay out the windings to produce a good main flux, but is then obliged to juggle the detailed design of the slots in order to obtain just the right amount of leakage flux to give acceptable all-round performance [84].

2.2.7 Types of AC Induction Motors

Generally, induction motors are categorized based on the number of stator windings. They are:

- *Single-phase induction motor*
- *Three-phase induction motor*

2.2.7.1 Single-Phase

There are probably more single-phase AC induction motors in use today than the total of all the other types put together. It is logical that the least expensive, lowest maintenance type motor should be used most often. The single-phase AC induction motor best fits this description [71].

As the name suggests, this type of motor has only *one stator winding (main winding)* and operates with a single-phase power supply. ***In all single-phase induction motors, the rotor is the squirrel cage type*** [71].

The single-phase induction motor is *not self-starting*. When the motor is connected to a single-phase power supply, the main winding carries an alternating current. This current produces a pulsating magnetic field. Due to induction, the rotor is energized. As the main magnetic field is pulsating, the torque necessary for the motor rotation is not generated. This will cause the rotor to vibrate, but not to rotate. Hence, the single phase induction motor is required to have a starting mechanism that can provide the starting kick for the motor to rotate [71].

The starting mechanism of the single-phase induction motor is mainly an *additional stator winding (start/auxiliary winding)* as shown in Figure 54. The start winding can have a series capacitor and/or a centrifugal switch. When the supply voltage is applied, current in the main winding lags the supply voltage due to the main winding impedance. At the same time, current in the start winding leads/lags the supply voltage depending on the starting mechanism impedance. Interaction between magnetic fields generated by the main winding and the starting mechanism generates a resultant magnetic field rotating in one direction. The motor starts rotating in the direction of the resultant magnetic field. Once the motor reaches about 75% of its rated speed, a centrifugal switch disconnects the start winding. From this point on, the single-phase motor can maintain sufficient torque to operate on its own [71].

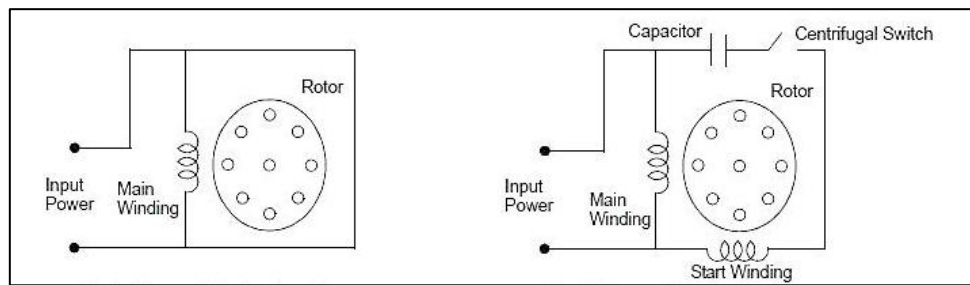


Figure 54: Single-phase AC induction motor with (right) and without (left) a start mechanism (Source: Microchip Technology Inc. [71])

Except for special capacitor start/capacitor run types, all single-phase motors are generally used for applications up to 3/4 HP only. Depending on the various start techniques, single phase AC induction motors are further classified as shown below [71]:

- ✦ *Split-Phase AC Induction Motor*
- ✦ *Capacitor Start AC Induction Motor*
- ✦ *Permanent Split Capacitor AC Induction Motor (PSC)*
- ✦ *Capacitor Start/Capacitor Run AC Induction Motor*
- ✦ *Shaded-Pole AC Induction Motor*

Torque-Speed characteristic curves of different types of single-phase induction motors are shown in Figure 55 [71]. Bear in mind that the curves shown in Figure 55 are *general shapes* and *each single-phase induction motor design would have its own distinct values different from the percentages reflected in these curves*. However, ***the shape of the curves remains the same***.

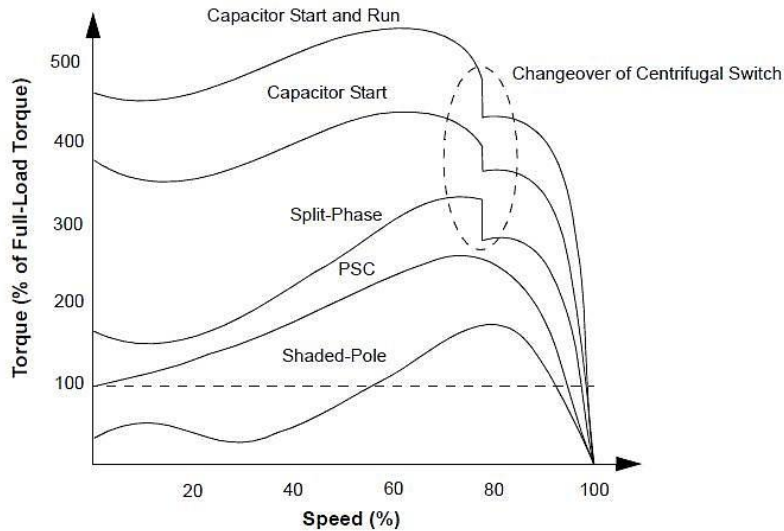


Figure 55: Torque-Speed curves of different types of single-phase induction motors for constant voltage and constant frequency operation
(Source: Microchip Technology Inc. [71])

2.2.7.2 Three-Phase

Three-phase AC induction motors are widely used in industrial and commercial applications. They are classified, as already mention, either as *squirrel cage* or *wound-rotor motors*. These motors are self-starting and use no capacitor, start winding, centrifugal switch or other starting device. They produce medium to high degrees of starting torque. The power capabilities and efficiency in these motors range from medium to high compared to their single-phase counterparts. Popular applications include grinders, lathes, drill presses, pumps, compressors, conveyors, also printing equipment, farm equipment, electronic cooling, other mechanical duty applications etc. [71].

The following diagram illustrates the characteristics of a multi-phase induction motor when configured as either motor or as a generator. A detailed description about the motoring mode has already mentioned in previous pages. In **generator mode** however, the stator is still connected to the power grid providing the necessary rotating field, but the *rotor shaft is driven by external means at a speed faster than the synchronous speed so that the electromagnetic reactions are reversed since the rotor will rotate faster than the rotating magnetic field of the stator so that the polarity of the slip is reversed and the polarity of the voltage and current induced in the rotor will likewise be reversed*. At the same time, by transformer action, the *current in the rotor will induce a current in the stator coils which now supply the generator's output energy to the load*. As the rotor speed is increased above the synchronous speed, the induced voltage and the current in the rotor bars and the stator coils will increase as the relative speed between the rotor and the stator's rotating field and hence the slip increases. This in turn will require a higher torque to maintain the rotation [85].

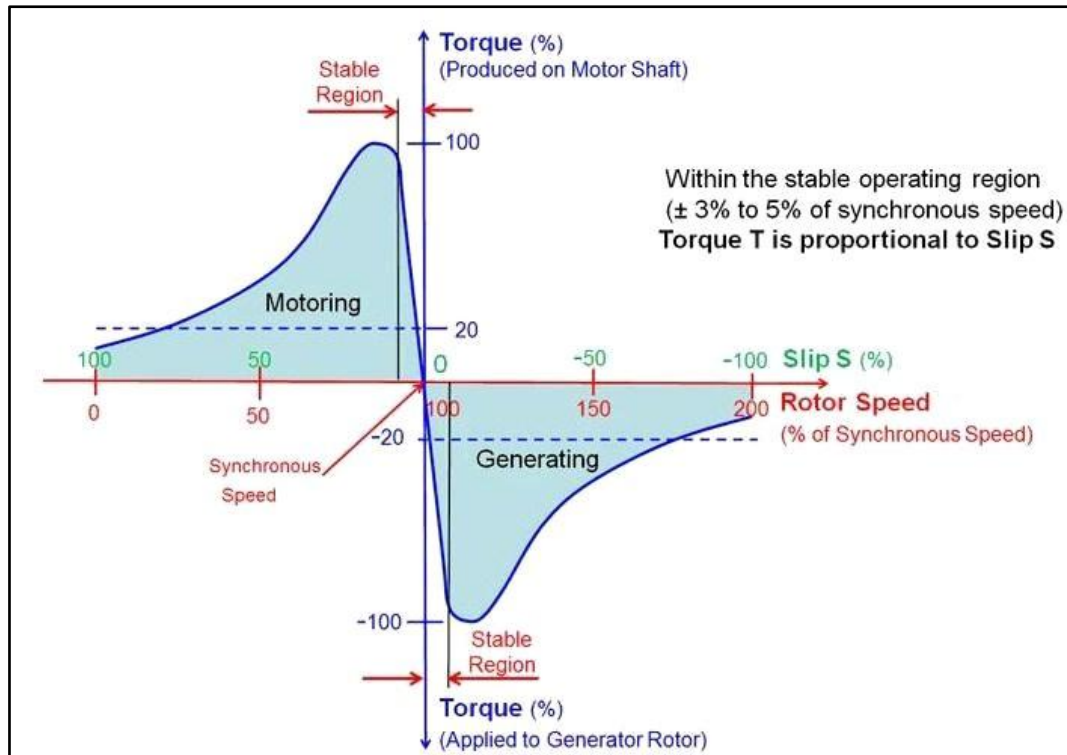


Figure 56: Torque-Speed characteristic curve (including slip) of a multi-phase induction machine in motoring and generating mode for constant voltage and frequency operation (Source: Electropaedia [85])

As it can be seen from Figure 56, the *torque is directly proportional (linear) to the slip s within the stable operating region around the synchronous speed of the machine and the frequency of the rotor current is the same as the slip frequency*. Moreover, the torque-speed characteristic curve of a multi-phase induction machine working as a brake, motor or generator is shown in Figure 57 [86].

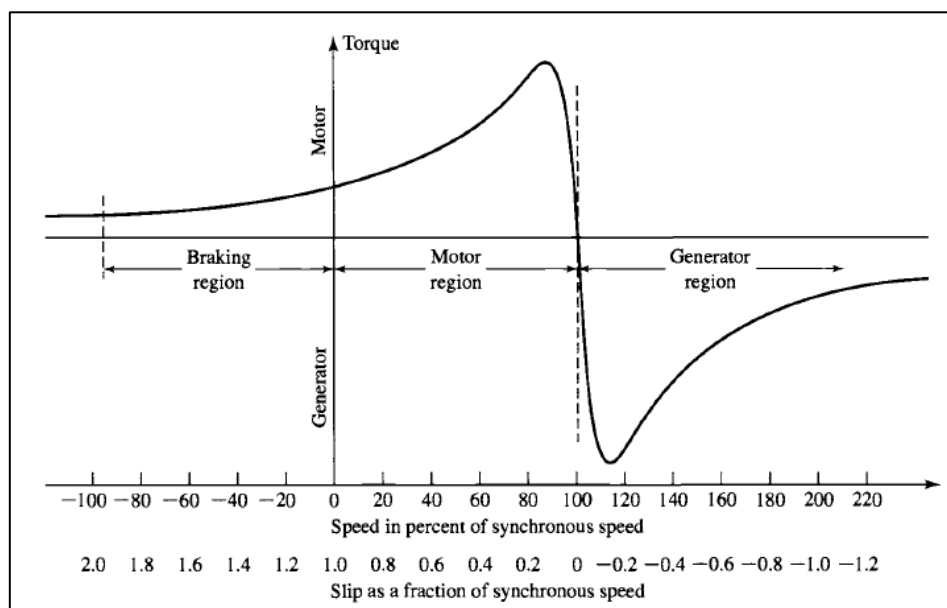


Figure 57: AC induction machine torque-slip curve showing braking, motor and generator regions for constant voltage and frequency operation (Source: A. E. Fitzgerald et al. [86])

Based on Figure 57, the slip values for different operations are as shown below:

- If $0 < s < 1$: *Motor region* (absorb electric power and convert to mechanical power)
- If $-1 < s < 0$: *Generator region* (mechanical power is converted to electric power)
- If $s \geq 1$: *Braking region* (absorb mechanical power)
- If $s = 0$: *No torque* (no conversion of one type of power to another)

The torque developed by a typical multi-phase induction motor depends on its speed but the relation between the two cannot be represented by a simple equation. However, it is easier to show the relationship in the form of a curve as shown in previous pages for single phase and three-phase induction machines.

The Torque–Speed characteristic curve terminology of a typical multi-phase induction motor along with the current curve is displayed in Figure 58 [74]. When the motor is initially started from standstill at the *Starting Current* I_s or *Locked Rotor Current (LRC)*, the *Starting Torque* T_s , also called *Locked Rotor Torque (LRT)*, is produced by the motor to overcome the inertia of the motor drive system. The starting torque depends on the terminal voltage and the stator and rotor design. As the motor accelerates, the torque generated by the motor may drop slightly to the local minimum point known as the *Pull-up Torque* T_{pull} . In the case that the Pull-up torque of the motor is less than that required by its application load, the motor will overheat and eventually stall. Then, a further increase in motor speed will lead to the increase in torque until it reaches the *Breakdown Torque* T_b , which is the highest torque the motor can attain without stalling and also called *Pull-out Torque*. Starting from this point, the continuous increase in speed causes the sharp decrease in torque, as well as in motor current. When the rotor of the motor reaches its *full operation speed*, ω_r , it is loaded to its *full-load torque* T_r and the corresponding *rated current* I_r and *slip* s_r . At the synchronous speed, no torque can be developed as zero slip ($s = 0$) implies no induced rotor current ($I = 0$) and thus no torque ($T = 0$) as already mentioned above. This situation only occurs for motors that run while not connected to a load. Therefore, in the strict sense, an induction machine can never reach the *synchronous speed* ω_s [74].

In order to clearly present the relationship between rotor torque and speed, an absolute value of torque (usually in N·m) is used in Figure 58. More frequently, *torque is expressed in terms of a percentage of full-load torque*, together with *speed in terms of a percentage of synchronous speed* [74].

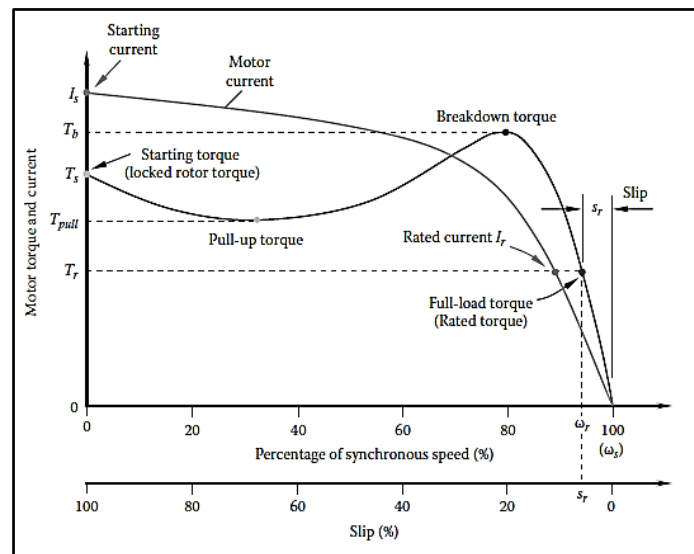


Figure 58: Torque/Current versus speed/slip ratio curves with terminology for a typical three-phase induction motor (Source: W. Tong [74])

2.2.7.2.1 Squirrel Cage Rotor

Almost 90% of the three-phase AC induction motors are of this type. Here, the rotor is of the squirrel cage type, *single or double*, and it works as explained in previous pages. The power ratings range from *one-third* ($1/3$) to *several hundred* HP. Motors of this type rated one horsepower or larger, cost less and can start heavier loads than their single-phase counterparts [71]. The detailed description about single cage motor construction is shown in previous pages.

The invention of *double-cage rotor* was motivated to develop a type of motor that is characterized by a variable rotor resistance during motor operation. This type of motor offers preferably high rotor resistance at the motor start-up, high locked torque, low starting current, and high pull-up torque, while maintaining higher efficiencies when compared to the same power ratings with single-cage designs. For the specific rotor designs and operating conditions, the comparison of torque–speed curves of double-cage and single-cage rotors is presented in Figure 59 [74].

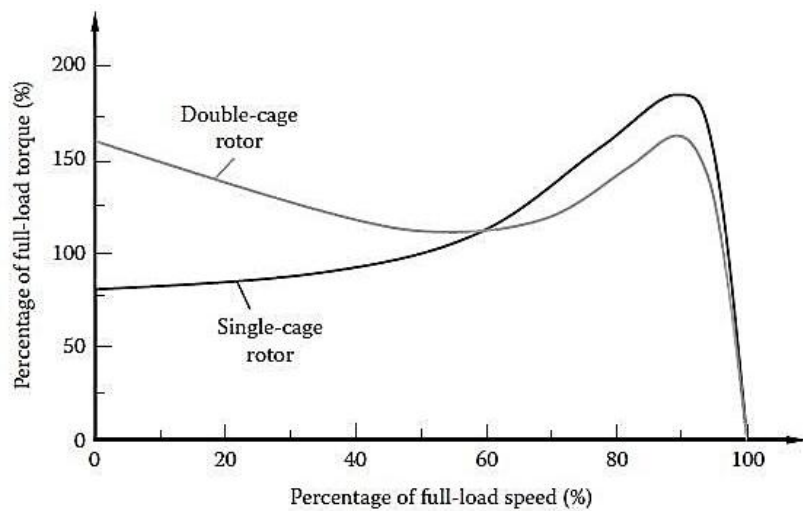


Figure 59: Comparison of torque-speed curves between typical single-cage and double-cage rotors for the same design and operation conditions (Source: W. Tong [74])

A double-cage consists of a large cage buried deeply in the rotor and a small cage located near the rotor surface. The conducting bars in the large cage are loosely linked with the stator and have low resistance and high leakage inductance. In contrary, the conductors in the small cage are closely linked with the stator and have high resistance and low leakage inductance. At the motor start-up stage, only the conductor bars in the small cages that have high resistance are effective, providing high starting torque. In the motor normal operation stage, the conducting bars in both large and small cages become effective. Some motor manufacturers use a high resistance material such as brass for the outer cage and a low-resistance material such as copper for the inner cage [74]. A cross section view of a squirrel double-cage induction motor with an emphasis on the “cages” is shown in Figure 60 [87].

Some large-size motors with double-cage rotors may employ separated end rings to connect the inner and outer cage, respectively. One of the reasons for this is to reduce thermal stresses induced in the end rings due to the different coefficients of thermal expansion of the inner and outer cages [74].

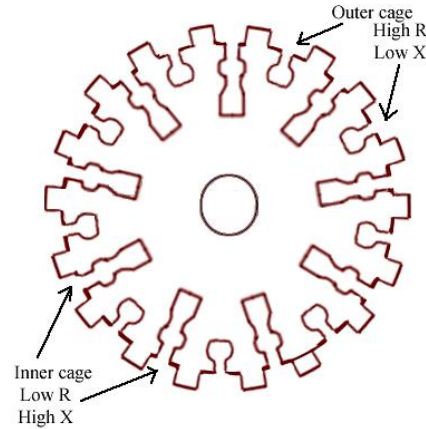


Figure 60: Cross section of double squirrel cage rotor (Source: ElectricalEasy [87])

2.2.7.2.2 Wound Rotor

The slip-ring motor or wound-rotor motor is a variation of the squirrel cage induction motor. While the stator is the same as that of the squirrel cage motor, it has a set of windings on the rotor which are not short-circuited, but are terminated to a set of slip rings [71]. These are helpful in adding external resistors and contactors as shown in Figure 61 [74].

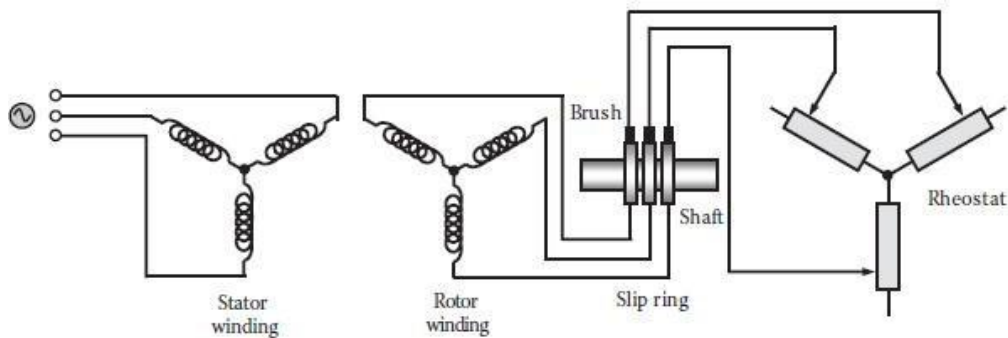


Figure 61: Wound rotor induction machines using slip rings and brushes to contact rotor winding and external resistances for improving motor start characteristics (Source: W. Tong [74])

The slip which is necessary to generate the maximum torque (pull-out torque) is directly proportional to the rotor resistance. In the slip-ring motor, the effective rotor resistance is increased by adding external resistance through the slip rings. Thus, it is possible to get higher slip and hence, the pull-out torque at a lower speed. A particularly high resistance can result in the pull-out torque occurring at almost zero speed, providing a very high pull-out torque at a low starting current. As the motor accelerates, the value of the resistance can be reduced, altering the motor characteristic to suit the load requirement. Once the motor reaches the base speed, *external resistors are removed from the rotor*. This means that now the motor is working as the standard induction motor [71].

This motor type is ideal for very high inertia loads, where it is required to generate the pull-out torque at almost zero speed and accelerate to full speed in the minimum time with minimum current draw. The downside of the slip ring motor is that slip rings and brush assemblies need regular maintenance, which is a cost not applicable to the standard squirrel cage motor. If the rotor windings are shorted and a start is attempted (i.e., the motor is converted to a standard induction motor), it will

exhibit an extremely high locked rotor current – typically as high as 1400% and a very low locked rotor torque, perhaps as low as 60%. In most applications, this is not an option [71].

Modifying the speed torque curve by altering the rotor resistors, the speed at which the motor will drive a particular load can be altered as shown in Figure 62 [74]. At full load, you can reduce the speed effectively to about 50% of the motor synchronous speed, particularly when driving variable torque/variable speed loads, such as printing presses or compressors. Reducing the speed below 50%, results in very low efficiency due to the higher power dissipation in the rotor resistances. This type of motor is used in applications for driving variable torque/variable speed loads, such as in printing presses, compressors, conveyer belts, hoists and elevators [71].

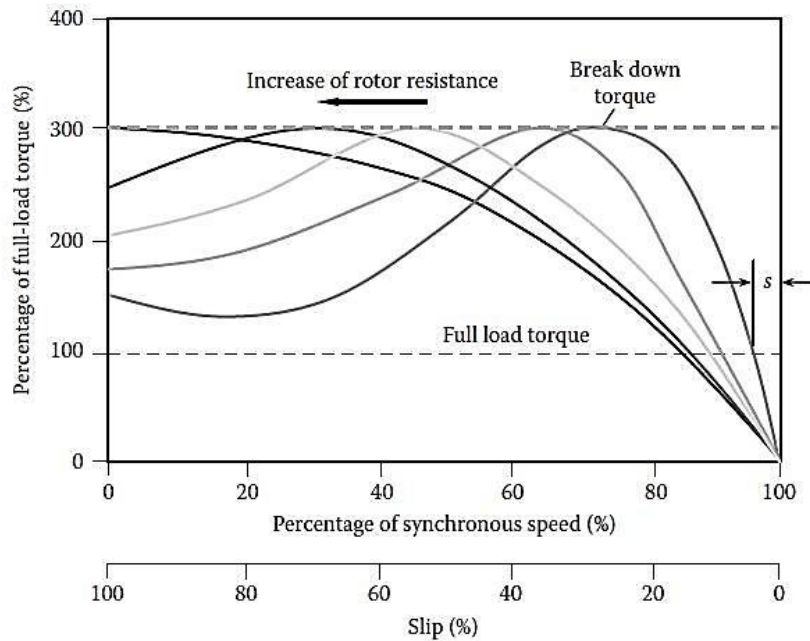


Figure 62: Variations of Torque–Speed characteristics of wound induction motors as a function of rotor resistance. Increasing rotor resistance results in the shift of the breakdown torque toward zero speed, causing the increase of slip and starting torque and the decrease of full-load speed. (Source: W. Tong [74])

2.2.8 Load Characteristics

In real applications, various kinds of loads exist with different torque-speed curves. For example, *Constant Torque-Variable Speed Load* (screw compressors, conveyors, feeders), *Variable Torque-Variable Speed Load* (fan, pump), *Constant Power Load* (traction drives), *Constant Power-Constant Torque Load* (coiler drive) and *High Starting/Breakaway Torque* followed by *Constant Torque Load* (extruders, screw pumps). The motor load system is said to be stable when the developed motor torque is equal to the load torque requirement. The motor will operate in a steady state at a fixed speed. The response of the motor to any disturbance gives the idea about the stability of the motor load system. This concept helps to quickly evaluate the selection of a motor for driving a particular load.

The typical existing loads with their torque-speed curves are described below.

Constant Torque - Variable Speed Loads

The torque required by this type of load is constant regardless of the speed. In contrast, the power is linearly proportional to the speed. Equipments, such as screw compressors, conveyors and feeders, have this type of characteristic [71].

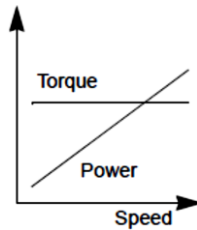


Figure 63: Constant torque/variable power load curve
(Source: Microchip Technology Inc. [71])

Variable Torque - Variable Speed Loads

This is most commonly found in the industry and sometimes is known as a quadratic torque load. The torque is the square of the speed, while the power is the cube of the speed. This is the typical torque-speed characteristic of a fan or a pump [71].

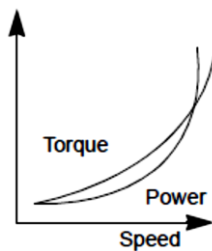


Figure 64: Variable torque/variable power load curve
(Source: Microchip Technology Inc. [71])

Constant Power Loads

This type of load is rare but is sometimes found in the industry. The power remains constant while the torque varies. The torque is inversely proportional to the speed, which theoretically means infinite torque at zero speed and zero torque at infinite speed. In practice, there is always a finite value to the breakaway torque required. This type of load is characteristic of the traction drives, which require high torque at low speeds for the initial acceleration and then a much reduced torque when at running speed [71].

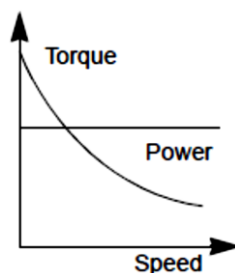


Figure 65: Variable torque/constant power load curve
(Source: Microchip Technology Inc. [71])

Constant Power - Constant Torque Loads

This is common in the paper industry. In this type of load, as speed increases, the torque is constant with the power linearly increasing. When the torque starts to decrease, the power then remains constant [71].

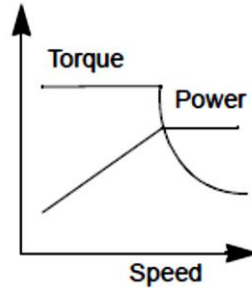


Figure 66: Constant torque/constant power load curve
(Source: Microchip Technology Inc. [71])

High Starting/Breakaway Torque followed by Constant Torque

This type of load is characterized by very high torque at relatively low frequencies. Typical applications include extruders and screw pumps [71].

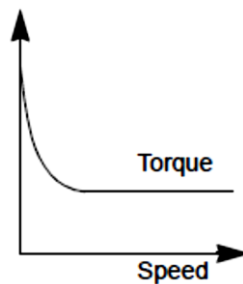


Figure 67: High starting torque followed by constant torque load curve
(Source: Microchip Technology Inc. [71])

2.2.9 Efficiency and Losses

The efficiency of general purpose motors has significantly improved in the last 25 years, largely as a result of the efforts of motor manufacturers, with assistance from DOE [88]. The Energy Policy Act (EPAct) of 1992 required that manufacturers meet a set of energy efficiency motor standard levels for many general purpose motors from 1 HP to 200 HP by 1997 [89]. EPAct has had several effects on the design and performance of motors. To achieve the required efficiency levels, motor manufacturers have had to change the designs of many of their NEMA Design A and B models (*see Appendix B*).

These changes have at times included reducing the resistance of the rotor and stator circuits; using electrical grade steel with improved magnetic characteristics for the stator and rotor laminations to reduce core losses; and redesigning the cooling fan to decrease fan windage losses. Other changes have included designing motors with a smaller slip (higher speed) and using lower-loss core iron [88]. Losses vary among motors of different sizes and designs; Table 2 shows some typical ranges [88].

Table 2: Sources of induction motor losses

Friction and Windage	5%–15%
Core (Iron) Losses	15%–25%
Stator	25%–40%
Rotor	15%–25%
Stray Load	10%–20%

The motor redesign process resulted in slight changes in some motor operating characteristics. Although the initial costs of motors increased 10% to 20% in high-run hour applications, improvements in motor efficiency can result in very favorable payback periods [88].

Motor *AC induction motor efficiencies* vary according to several factors, but generally range from **85% to 97% at full load**. The primary factors affecting efficiency are speed, where high-speed motors tend to be more efficient, and the size of the motor, where larger motors tend to be more efficient [88].

Additional factors include type of enclosure, where open enclosures tend to be more efficient, and design classification, where lower-slip motors tend to be more efficient. Figure 68 shows how efficiency varies with respect to motor horsepower rating and load [88].

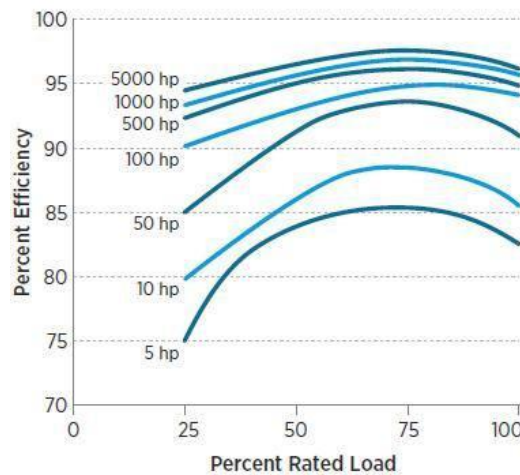


Figure 68: Typical AC multi-phase motor Efficiency versus load at 1800 rpm
(Source: US DOE [88])

2.2.10 Typical Nameplate

Motor standards are established on a country by country basis. Although fortunately, the standards can be grouped into two major categories: NEMA and IEC (and its derivatives). In North America, the **National Electric Manufacturers Association (NEMA)** sets motor standards, including what should go on the nameplate (*NEMA Standard MG 1-10.40 "Nameplate Marking for Medium Single-Phase and Polyphase Induction Motors"* [90]).

In most of the rest of the world, the **International Electrotechnical Commission (IEC)** sets the standards (IEC 60034- Part 1) [91]. Or at least many countries base their standards very closely on the IEC standards (for example, Germany and Great Britain standard closely parallel the IEC standard). The NEMA and IEC standards are quite similar, although they sometimes use different terminology. Thus, if one understands the IEC nameplate, it is fairly easy to understand a NEMA nameplate, and vice versa.

Most manufacturers display information differently, and name plates often get dirty, damaged, and occasionally are removed. This can make reading a motor name plate a difficult or frustrating task. It is useful to have access to the information from the motor name plate throughout the life of the motor. If a *Variable Frequency Drive (VFD)* needs to be sized, a motor needs to be replaced or repaired, correct power factor, purchase parts, or do just about anything with a motor it is necessary to have the information on the motor name plate.

A typical name plate on an AC induction motor is shown in Figure 69 [92] and the terminology in Table 3. Finally, some nameplates may even include data such as model and serial number and specifies the motor safety standard with symbols and logos such as SA, CE etc.




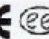

AC Induction Motor					
HIGH EFFICIENT					
ORD. NO.	1LA0264SE41		E NO.		
TYPE	RGZESD		FRAME	286T	
H.P.	30.0		SERVICE FACTOR	1.15	3 PH
AMPS.	35.0		VOLTS	460	
R.P.M	1765		HERTZ	60	
DUTY	CONT 40 °C AMB		DATE CODE		
CLASS INSUL	F	NEMA DESIGN B	KVA CODE G	NEMA NOM. EFF	93.0
SH END BRG	50RU03K30		OPP END BRG	50BC03JPP3	
Made in Mexico			    		

Figure 69: Typical AC induction motor nameplate
(Source: Powersystemsloss.blogspot [92])

Table 3: Nameplate terms and their meaning

Term	Description
Volts	Rated terminal supply voltage
H.P.	Rated motor power output
AMPS.	Rated full-load supply current
R.P.M.	Rated full-load speed of the motor
Hertz	Rated supply frequency
Frame	External physical dimension of the motor and shaft dimensions based on the NEMA standards.
Duty	Motor load condition
Date	Date of manufacturing
Code	AC motors that are started at full voltage will draw a greater current (amps) than during normal operations. This is commonly referred to as inrush current or starting current. These codes represent a range of inrush current.
Class Insulation	Insulation class used for the motor construction. This specifies max. limit of the motor winding temperature
NEMA Design	This specifies to which NEMA design class the motor belongs to
Service Factor	Factor by which the motor can be overloaded beyond the full load
NEMA Nominal Efficiency	Motor operating efficiency at full load
PH	Specifies number of stator phases of the motor
Pole	Specifies number of poles of the motor
(Y) or (Δ)	Specifies whether the motor windings are star (Y) connected or delta (Δ) connected
CT/VT	CT stands for Constant Torque and VT stands for Variable Torque
Enclosure Type	Displays information about how well the motor is protected from the environment. The most common enclosure types are Open Drip-Proof (ODP) and Totally Enclosed Fan Cooled (TEFC).
Bearings	The drive shaft bearing and the opposite drive shaft bearing specifications. The different between these two are location in the motor. Every manufacturer has their own way of displaying bearing information and this can vary widely between manufacturers.

2.3 Modeling in MATLAB/Simulink®

In this section, a numerical approach used to model *symmetrical poly-phase induction motors/generators under transient states* is presented. There are three ways of how you can build that numerical model. The first way, and the easier one, is using the SimPowerSystems toolbox of MATLAB/Simulink® as shown in the below sub-sections [93, 94]. The second way is to “build” the differential equations which described the symmetrical induction motor in MATLAB/Simulink® (.mdl file) without using the SimPowerSystems toolbox [95, 96, 97, 98, 99, 100, 101, 102, 103]. The third and the most difficult way is the creation of a Script file in MATLAB (.m file) where the numerical approach is coded without using MATLAB/Simulink® [104]. The model description, the assumptions have been made and the numerical model is presented below.

2.3.1 Model Description

MATLAB/Simulink® provides SimPowerSystems toolbox which is a library containing dynamic models of three-phase asynchronous/induction machines [105, 106, 107]. The toolbox provides a set of predetermined electrical and mechanical parameters for various asynchronous machine ratings of power, phase-to-phase voltage, electrical frequency and rpm. One important characteristic of this library is that all machines are able to operate either as motors or as generators. The mode of operation is decided by the sign of the load torque T_m . If the load torque is positive, the machine operates as a motor, otherwise it operates as a generator [108].

The induction (asynchronous) machine block implements a three-phase squirrel single-cage induction machine. The toolbox is based on the standard Direct-Quadrature (DQ or dq) analysis shown in Appendix C. The mathematical modeling based on a fourth-order state-space model that represents the electrical part of the machine and a second-order system represents the mechanical part [108].

In order for the motor to operate, a *mechanical load*, T_m , needs to be defined as an input of the block as well as the *three phase stator voltage terminal ports* (Equations 2.15) which are identified by A, B and C letters as shown in Figure 70 [108]. The three phase ports connected in Wye (Y) configuration. The output of the machine block is a vector, with the symbol m , containing *measurement signals* such as rotor or stator currents, fluxes and voltages, rotor electrical angular velocity and electromagnetic torque.

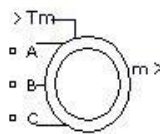


Figure 70: Induction machine block of MATLAB/Simulink® (Source: Mathworks Inc. [108])

2.3.2 Model Assumptions

The numerical analysis based on the below assumptions [109, Author]:

1. Both stator and rotor have a symmetric three-phase identical winding system with an angle of $2\pi/3$ while in steady state the voltages and currents are taken to be sinusoidal.
2. All the stator/rotor inductances and resistances are constants and independent of the temperature and current.
3. All iron losses, the slots, magnetic saturation and eddy currents are neglected.
4. The machine air gap is constant, smooth, and symmetric and the flux density is radial.
5. The magnetic circuits are linear (the stator/rotor permeabilities are assumed to be infinite) and the operating conditions are balanced.

2.3.3 Numerical Model

The below section provides the numerical approach, which is a *transient non-linear approach using flux linkages as variables*, used to model the symmetrical induction motor. Even when the voltages and currents are discontinuous the flux linkages are continuous. This gives the advantage of differentiating these variables with numerical stability. In addition, the flux-linkages representation is used in motor drives to highlight the process of the decoupling of the flux and torque channels in the induction machines. This numerical model was developed in the MATLAB/Simulink® environment using induction motor toolbox (SimPowerSystem library) as already mentioned. The induction motor model (Equations 1÷11) consists of two main modules: the *flux and current model (FCM)* and the *electromagnetic torque model (EMTM)*, as shown in Figure 71.

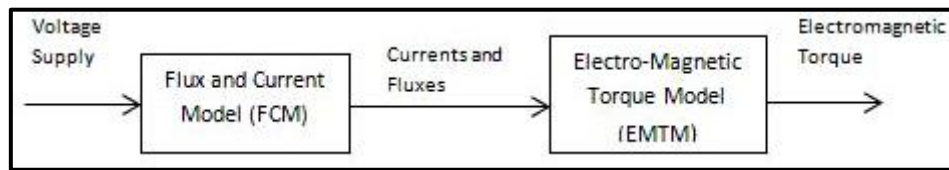


Figure 71: Block diagram of the 3 phase AC induction motor model (Source: Author)

The FCM solves the induction motor voltage equations, taking into account a stator reference frame. The *Direct-Quadrature or d-q equivalent circuit on stator (synchronous) reference frame* is used (see Appendix C). The electrical circuit diagram of the utilized FCM model is given in Figure 72 [109].

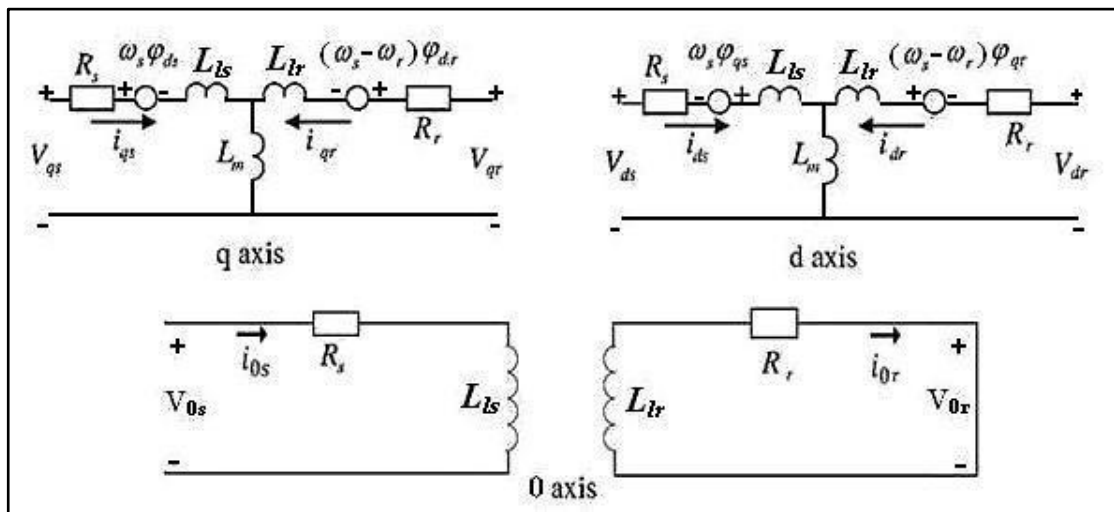


Figure 72: The d-q equivalent circuit model of the three-phase symmetrical squirrel single-cage (constant R_r) or wound (variable R_r) induction motor (Source: P. Krause et al. [109])

Using *Kirchhoff's Voltage Law* [86], the equations describing the voltages of the FCM for stator and rotor are the following [109]:

$$V_{qs} = R_s \cdot i_{qs} + \frac{d\phi_{qs}}{dt} + \omega_s \cdot \phi_{ds} \quad (2.1.1)$$

$$V_{ds} = R_s \cdot i_{ds} + \frac{d\phi_{ds}}{dt} - \omega_s \cdot \phi_{qs} \quad (2.1.2)$$

$$V_{qr} = R_r \cdot i_{qr} + \frac{d\phi_{qr}}{dt} + (\omega_s - \omega_r) \cdot \phi_{dr} \quad (2.1.3)$$

$$V_{dr} = R_r \cdot i_{dr} + \frac{d\varphi_{dr}}{dt} - (\omega_s - \omega_r) \cdot \varphi_{qr} \quad (2.1.4)$$

$$V_{0s} = R_s \cdot i_{0s} + \frac{d\varphi_{0s}}{dt} \quad (2.1.5)$$

$$V_{0r} = R_r \cdot i_{0r} + \frac{d\varphi_{0r}}{dt} \quad (2.1.6)$$

In these equations the corresponding fluxes can be calculated according to [109]:

$$\varphi_{qs} = L_s \cdot i_{qs} + L_m \cdot i_{qr} \quad (2.2.1)$$

$$\varphi_{ds} = L_s \cdot i_{ds} + L_m \cdot i_{dr} \quad (2.2.2)$$

$$\varphi_{qr} = L_r \cdot i_{qr} + L_m \cdot i_{qs} \quad (2.2.3)$$

$$\varphi_{dr} = L_r \cdot i_{dr} + L_m \cdot i_{ds} \quad (2.2.4)$$

$$\varphi_{0s} = L_{ls} \cdot i_{0s} \quad (2.2.5)$$

$$\varphi_{0r} = L_{lr} \cdot i_{0r} \quad (2.2.6)$$

The inductance values in the above equations are calculated by [109]:

$$L_s = L_{ls} + L_m \quad (2.3.1)$$

$$L_r = L_{lr} + L_m \quad (2.3.2)$$

In these equations R , L , ω , V , i , and φ denote resistance, inductance, electrical frequency, voltage, current, and flux respectively, referred to rotor (subscript r) and stator (subscript s) on d-q axes (subscript d and q respectively). Moreover the subscript m and l referred to magnetizing inductance and leakage inductance respectively.

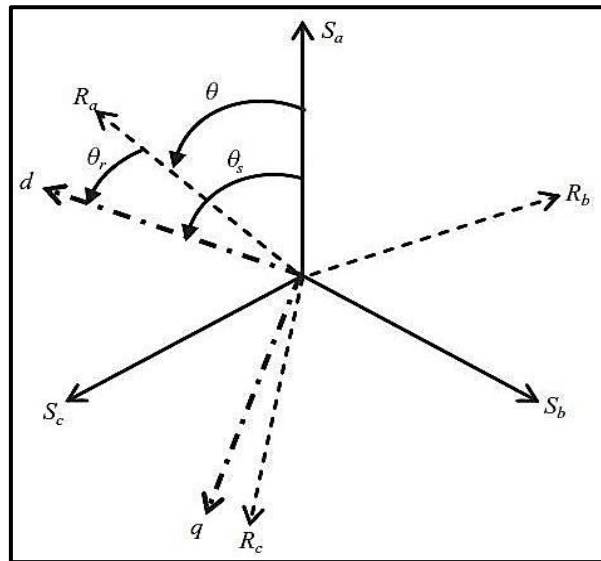


Figure 73: Angles between electric frames. The letters S and R refer to the stator and rotor respectively while the indices a, b, c refer to the three phase (Source: Author)

The rotor electrical angular velocity ω_r and reference frame or synchronous angular velocity ω_s are defined, according to Figure 73 [109], as:

$$\omega_r = \frac{d\theta_r}{dt}, \quad \omega_s = \frac{d\theta_s}{dt} \quad (2.4)$$

where θ_s and θ_r are the stator (reference frame) angular position and rotor electrical angular position respectively.

Solving stator and rotor current from equations 2.2.1÷2.2.4 yields to:

$$i_{qr} = \frac{\varphi_{qs} - L_s \cdot i_{qs}}{L_m} \quad (2.5.1)$$

$$i_{dr} = \frac{\varphi_{ds} - L_s \cdot i_{ds}}{L_m} \quad (2.5.2)$$

$$i_{qs} = \frac{\varphi_{qr} - L_r \cdot i_{qr}}{L_m} \quad (2.5.3)$$

$$i_{ds} = \frac{\varphi_{dr} - L_r \cdot i_{dr}}{L_m} \quad (2.5.4)$$

Replacing equations 2.5.1 and 2.5.2 into 2.5.3 and 2.5.4 respectively yields to:

$$i_{qs} = \frac{L_m \cdot \varphi_{qr} - L_r \cdot \varphi_{qs}}{L_m^2 - L_r \cdot L_s} \quad (2.6.1)$$

$$i_{ds} = \frac{L_m \cdot \varphi_{dr} - L_r \cdot \varphi_{ds}}{L_m^2 - L_r \cdot L_s} \quad (2.6.2)$$

and similarly equations 2.6.1 and 2.6.2 into 2.5.1 and 2.5.2 respectively yields to:

$$i_{qr} = \frac{L_m \cdot \varphi_{qs} - L_s \cdot \varphi_{qr}}{L_m^2 - L_r \cdot L_s} \quad (2.7.1)$$

$$i_{dr} = \frac{L_m \cdot \varphi_{ds} - L_s \cdot \varphi_{dr}}{L_m^2 - L_r \cdot L_s} \quad (2.7.2)$$

As the induction machine is assumed to have balanced three-phase voltages, the zero sequence components of the stator and rotor voltages, V_{0s} and V_{0r} , are equal to zero. Moreover, as the induction machine has a squirrel cage rotor, the q and d-axis rotor voltages, V_{qr} and V_{dr} , are equal to zero [109]. So, replacing rotor and stator currents from equations 2.6.1, 2.6.2 and 2.7.1, 2.7.2 back to equations 2.1.1÷2.1.4 yields to:

$$\frac{d\varphi_{qs}}{dt} = V_{qs} - R_s \cdot \left(\frac{L_m \cdot \varphi_{qr} - L_r \cdot \varphi_{qs}}{L_m^2 - L_r \cdot L_s} \right) - \omega_s \cdot \varphi_{ds} \quad (2.8.1)$$

$$\frac{d\varphi_{ds}}{dt} = V_{ds} - R_s \cdot \left(\frac{L_m \cdot \varphi_{dr} - L_r \cdot \varphi_{ds}}{L_m^2 - L_r \cdot L_s} \right) + \omega_s \cdot \varphi_{qs} \quad (2.8.2)$$

$$\frac{d\varphi_{qr}}{dt} = -R_r \cdot \left(\frac{L_m \cdot \varphi_{qs} - L_s \cdot \varphi_{qr}}{L_m^2 - L_r \cdot L_s} \right) - (\omega_s - \omega_r) \cdot \varphi_{dr} \quad (2.8.3)$$

$$\frac{d\varphi_{dr}}{dt} = -R_r \cdot \left(\frac{L_m \cdot \varphi_{ds} - L_s \cdot \varphi_{dr}}{L_m^2 - L_r \cdot L_s} \right) + (\omega_s - \omega_r) \cdot \varphi_{qr} \quad (2.8.4)$$

The EMTM calculates the electromagnetic torque, T_e , from the current and flux values of the stator by [109]:

$$T_e = \frac{3}{2} \cdot p \cdot (\varphi_{ds} \cdot i_{qs} - \varphi_{qs} \cdot i_{ds}) \quad (2.2.9)$$

where p is the number of pole pairs. If replacing the stator currents (equations 2.6.1 and 2.6.2) in Equation 2.2.9 making the electromagnetic torque depending only of the fluxes which is useful because fluxes can be found from the four (4) *first order coupled differential equations* 2.8.1÷2.8.4.

$$T_e = \frac{3}{2} \cdot p \cdot \left(\varphi_{ds} \cdot \frac{L_m \cdot \varphi_{qr} - L_r \cdot \varphi_{qs}}{L_m^2 - L_r \cdot L_s} - \varphi_{qs} \cdot \frac{L_m \cdot \varphi_{dr} - L_r \cdot \varphi_{ds}}{L_m^2 - L_r \cdot L_s} \right) \quad (2.10)$$

The above mentioned mathematical model is a system of 4 first order coupled differential equations (2.8.1 to 2.8.4), and along with the electromagnetic torque (Equation 2.10) form a system of **5 unknowns and 5 equations, depending only on the d-q voltages**.

This electromechanical shaft torque, along with the shaft mechanical load torque, T_m , can then be used by the mechanical induction model to calculate rotational states of the rotor. These are calculated according to [108, 109]:

$$\dot{\omega}_m = \frac{(T_e - F \cdot \omega_m - T_m - T_d)}{J} \quad (2.11.1)$$

$$\omega_m = \frac{d\theta}{dt} = \int_0^t \dot{\omega}_m dt \quad (2.11.2)$$

where ω_m is the rotor mechanical angular velocity of the electric motor, J is the combined rotor and load moment of inertia, F is the viscous friction coefficient of the induction motor and T_d is the dry torque which is neglected for simplicity.

The synchronous angular velocity, ω_s , is given also by the following equation, where f_s is the AC system frequency in Hz [75]:

$$\omega_s(\text{rad/s}) = \frac{4 \cdot \pi \cdot f_s}{P} \quad (2.12.1)$$

$$\omega_s(\text{rpm}) = \frac{120 \cdot f_s}{P} \quad (2.12.2)$$

which describes, in rpm, the *number of times per second a rotor pole passes in front of a certain stator pole*.

The rotor electrical angular velocity, ω_r , is given also by the following equation [75]:

$$\omega_r = (P/2) \omega_m \quad (2.13)$$

and the slip ratio, s , according to the below formula [75]:

$$s (\%) = \frac{\omega_s - \omega_r}{\omega_s} \cdot 100 \quad (2.14)$$

It is important to be noticed that the variable P in Equations 2.12 and 2.13 is the *number of poles*. Finally, the induction machine block requires the stator three-phase voltages as an input except for the mechanical load, T_m , as already mentioned and is shown in *Appendix D* as well as the solver parameters. For a stator reference frame the following set of equal-amplitude sinusoidal quantities that are displaced by 120° can be used [109]:

$$V_{as} = V_{LN} \cdot \cos(2\pi f) \quad (2.15.1)$$

$$V_{bs} = V_{LN} \cdot \cos(2\pi f + \frac{2\pi}{3}) \quad (2.15.2)$$

$$V_{cs} = V_{LN} \cdot \cos(2\pi f + \frac{4\pi}{3}) \quad (2.15.3)$$

where V_{LN} is the line to neutral supply voltage and is equal to $\frac{\sqrt{2}}{\sqrt{3}} V_{LL(\text{rms})}$ with the $V_{LL(\text{rms})}$ to be the RMS value of the line to line supply voltage.

2.4 Case Studies

In this section, two different case studies are examined. The first case is the induction generator (IG) for the small 3 meter rotor diameter SNMREC's 20 kW ocean current turbine (OCT) with fixed pitch blades, and the second case is the induction generator (IG) for the 20 meter rotor diameter SNMREC's 720 kW ocean current turbine (OCT) with variable pitch blades.

The first induction generator was sized in 50HP (≈ 37.3 kW) because the 3 meter rotor diameter OCT can produce about 20 kW of shaft power for a flow speed of around 2.2 m/s. The ocean currents off South-East Florida seldom usually exceed 2.2 m/s and if we put this OCT in a flow speed of 3.0 m/s, there are some current energy sites that have this flow speed and SNMREC measured it in the ocean, it will produce around 50 kW of shaft power and therefore sizing the generator at 50HP is something necessary for current locations where the flow is strong.

On the other hand, the second induction generator was sized in 720 kW so that match with the 20 meter rotor diameter SNMREC's ocean current turbine. Based on SNMREC's ocean current measurements, in the South-East Florida seldom and at a depth of 25 m, the mean measured kinetic energy flux is approximately 2.32 kW/m^2 , which yielding a mean power flux over the swept area of a 20 m diameter rotor of 720 kW.

Steady state analysis with zero and non-zero load, and the behavior of the above mentioned IGs during transient periods are presented in the below sections.

2.4.1 Case Study I – IG for 20kW OCT

The 3-phase induction motor/generator numerically characteristics used by the model presented in 2.3.3 are shown in Table 4 and refer to a motor for marine applications. Simulation in steady state conditions with zero or non-zero load and in transient conditions are shown in Figures 74÷92.

Table 4: 50 HP induction motor/generator parameters

AC Induction Motor/Generator Parameters <i>37.3 kW, 460 V_{LL (rms)}, 60 Hz, 3600 rpm, Squirrel Single-Cage Rotor</i>	
Stator Resistance (R_s)	0.09961 Ω
Rotor Resistance (R_r)	0.05837 Ω
Magnetizing Inductance (L_m)	0.03039 H
Total (Rotor & Stator) Inductance ($L_{ls} + L_{lr}$)	0.001734 H
Total Moment of Inertia (J)	0.40 $\text{kg}\cdot\text{m}^2$
Friction Factor (F)	0.002187 $\text{N}\cdot\text{m}\cdot\text{s}$
Number of Pole Pairs (p)	1

2.4.1.1 Steady State with Zero Load

This numerical simulation run was conducted to evaluate the steady state behavior of the 50HP generator under zero mechanical load ($T_m = 0 \text{ Nm}$). The system frequency, f_s , is **60Hz** and the voltage line-to-line is kept constant with an RMS value of **460V**. Moreover, the synchronous speed of the generator which also based on the pole numbers (=2) is **3600 rpm**. The initial conditions, at $t=0$ second, are all set to zero except for the initial slip ratio which set to start from 100%.

As it expected, the electromagnetic torque, T_e , is equal to zero, the mechanical and electrical speed of the rotor are the same at 3600 rpm because the number of poles, and the slip ratio is zero as shown in Figures 74÷76.

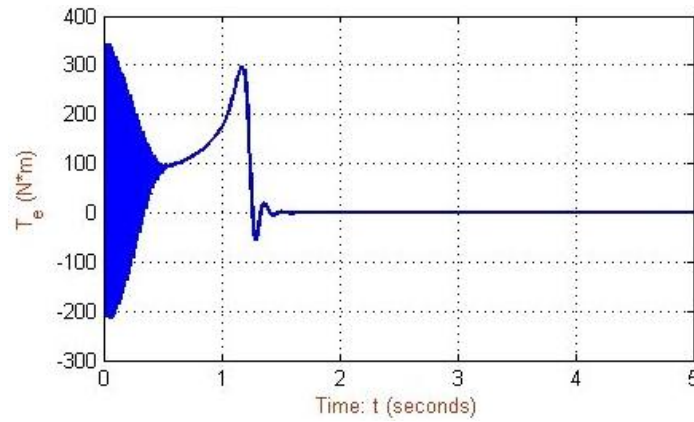


Figure 74: T_e versus time for 50HP IG under no load

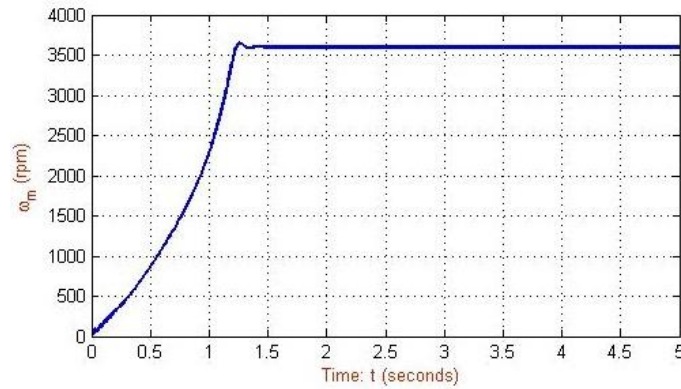


Figure 75: $\omega_m (= \omega_r)$ versus time for 50HP IG under no load

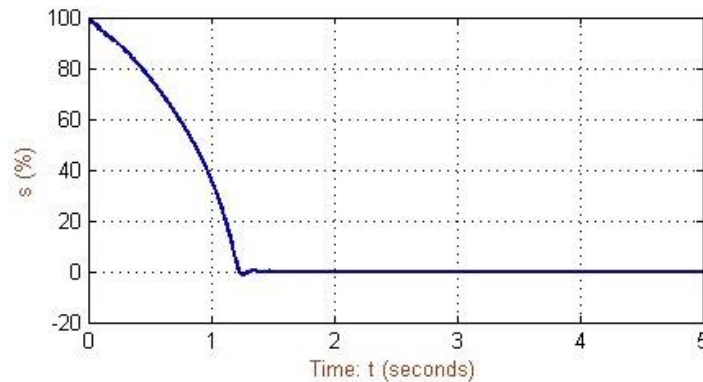


Figure 76: Slip ratio versus time for 50HP IG under no load

2.4.1.2 Steady State with Load

This numerical simulation run was conducted to evaluate the steady state behavior of the 50HP generator under mechanical load ($T_m = -100 \text{ N}\cdot\text{m}$). The system frequency, f_s , is 60Hz and the voltage line-to-line is kept constant with an RMS value of 460V as previous. Moreover, the synchronous speed of the generator which also based on the pole numbers (=2) is 3600 rpm. The initial conditions, at $t=0$ second, are all set to zero except for the initial slip ratio which set to start from 100%.

The currents and fluxes in stator and rotor are presented with Figures 77÷80 and based on d-q axis. The electromagnetic torque, T_e , is almost equal to the mechanical load, T_m , and the small difference is based on the friction factor F while the rotor's mechanical and electrical speed is the same at 3620 rpm with a *slip ratio* of 0.55%.

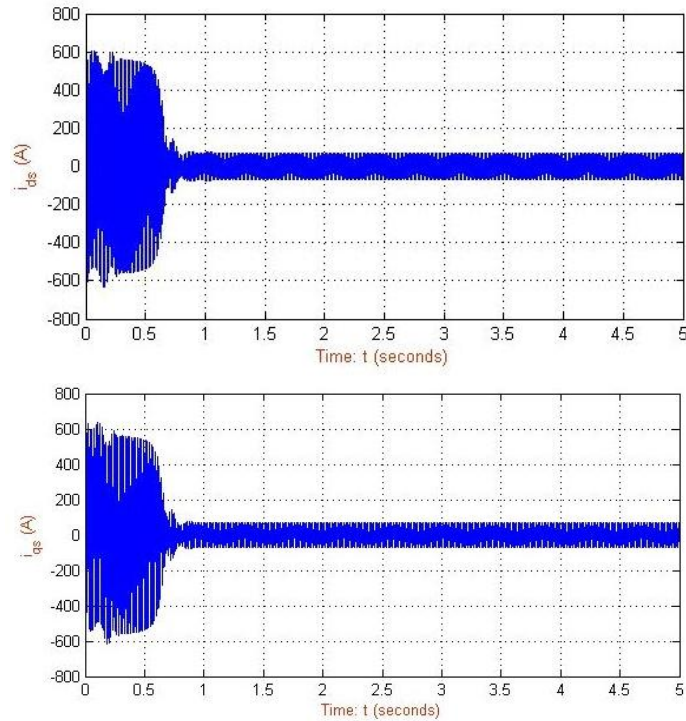


Figure 77: i_{ds} (up) and i_{qs} (down) versus time for 50HP IG under load of -100 N·m

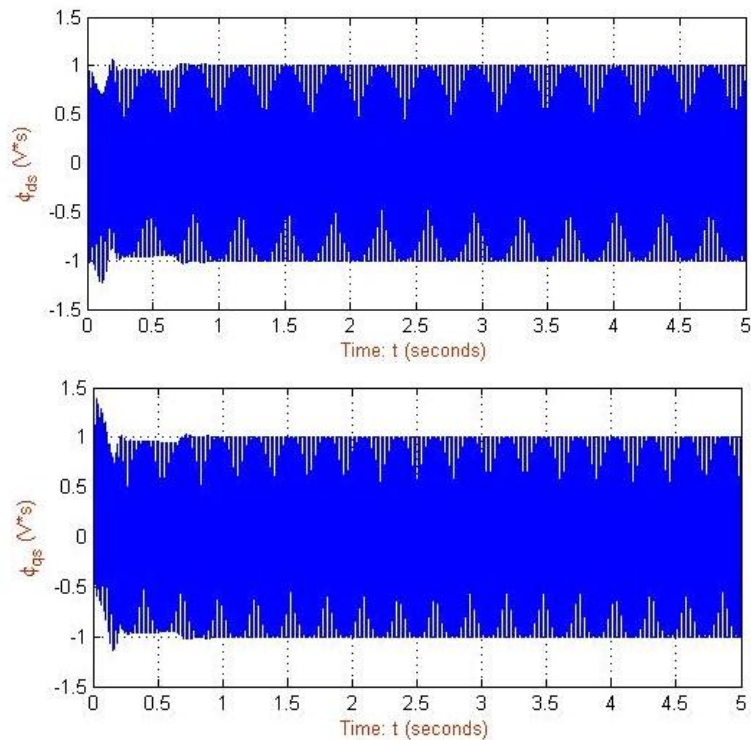


Figure 78: ϕ_{ds} (up) and ϕ_{qs} (down) versus time for 50HP IG under load of -100 N·m

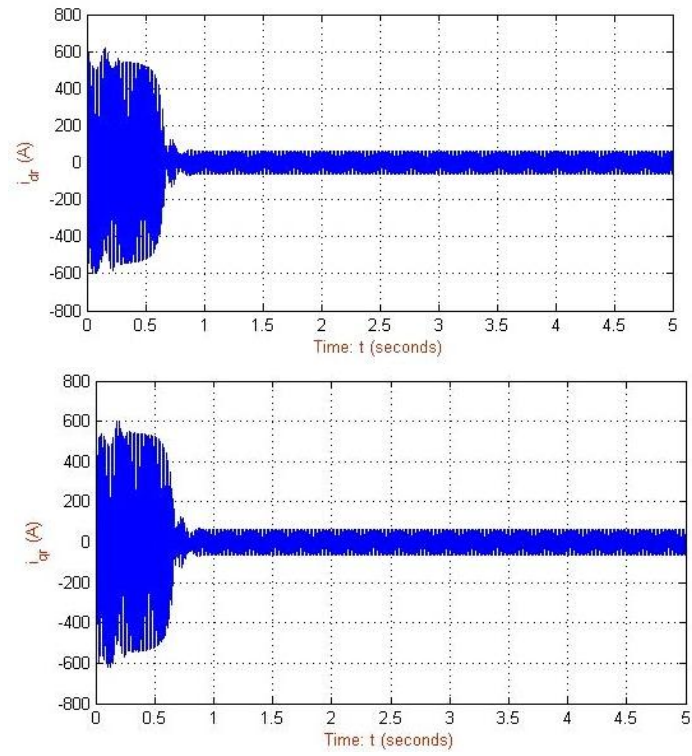


Figure 79: i_{dr} (up) and i_{qr} (down) versus time for 50HP IG under load of -100 N·m

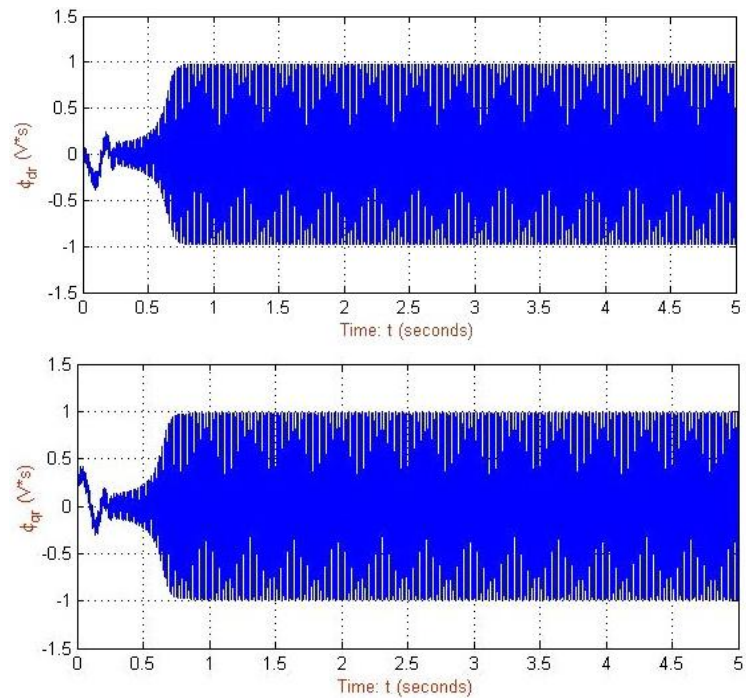


Figure 80: ϕ_{dr} (up) and ϕ_{qr} (down) versus time for 50HP IG under load of -100 N·m

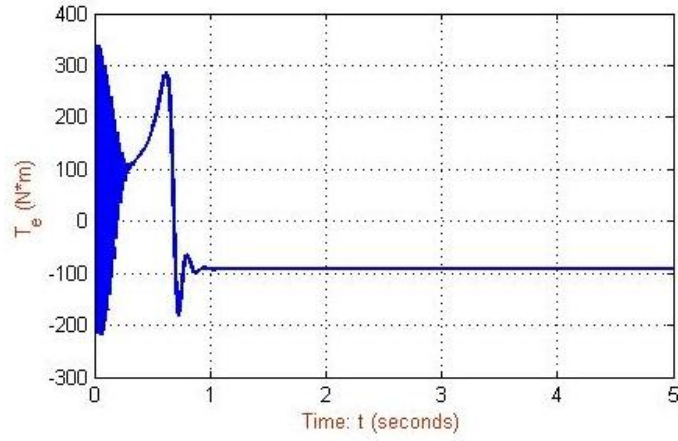


Figure 81: T_e versus time for 50HP IG under load -100 N·m (value -98 N·m)

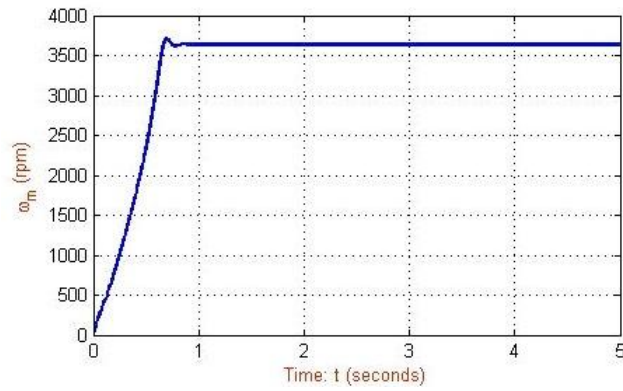


Figure 82: $\omega_m (= \omega_r)$ versus time for 50HP IG under load -100 N·m (value 3620 rpm)

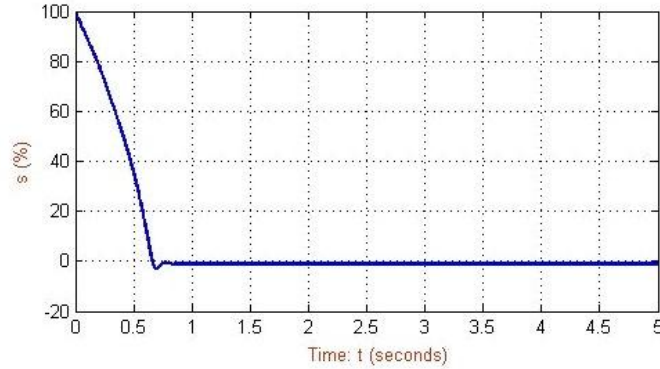


Figure 83: Slip ratio versus time for 50HP IG under load -100 N·m (value 0.55%)

2.4.1.3 Transient

This numerical simulation run was conducted to evaluate the transient behavior and different steady state conditions of the 50HP generator with initial mechanical load $T_m = -100 \text{ N}\cdot\text{m}$ and a reduction step with $T_m = -60 \text{ N}\cdot\text{m}$ at $t=2 \text{ seconds}$. The system frequency, f_s , is **60Hz** (100% of rated frequency) and at $t=5 \text{ seconds}$ is decreased 25% at $f_s = 45\text{Hz}$ (75% of the rated frequency). The voltage line-to-line is kept constant with an RMS value of 460V as previous. Moreover, the

synchronous speed of the generator which also based on the pole numbers ($=2$) is 3600 rpm at 100% rated frequency and 2700 rpm at 75% rated frequency. The initial conditions, at $t=0$ second, are all set to zero except for the initial slip ratio which set to start from 100%.

The mechanical load and frequency of the system with the step changes are presented in Figures 84 and 85 respectively. The currents and fluxes in stator and rotor during the transient period and in different steady state conditions are presented in Figures 86÷89 and based on d-q axis. The electromagnetic torque, T_e , follows the changes of mechanical load and its value is decreased from -98 $N\cdot m$ to -59 $N\cdot m$ while the specific change in system frequency has no influence on its final value as shown in Figure 90. On the other hand, the reduction step of mechanical load at $t=2$ seconds affect slightly the rotor's mechanical and electrical speed (from 3620 rpm to 3610 rpm) as well as the slip ratio (from 0.55% to 0.27%) while the reduction in system frequency at $t=5$ seconds, of course, decrease the rotor's speed but has minor effect in slip ratio (from 0.27% to 0.5%) as shown in Figures 91 and 92.

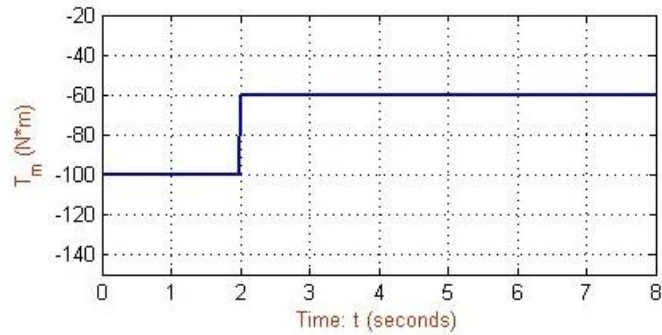


Figure 84: T_m versus time for 50HP IG with a reduction step at $t=2$ seconds

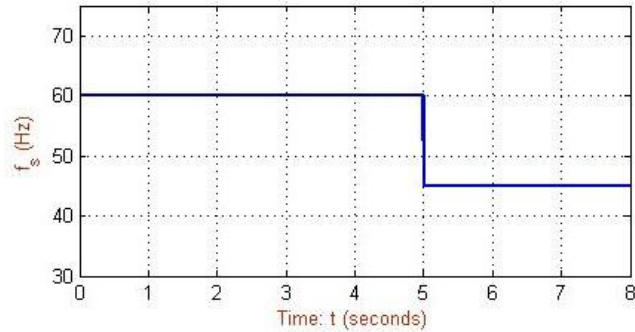


Figure 85: f_s versus time for 50HP IG with a reduction step at $t=5$ seconds

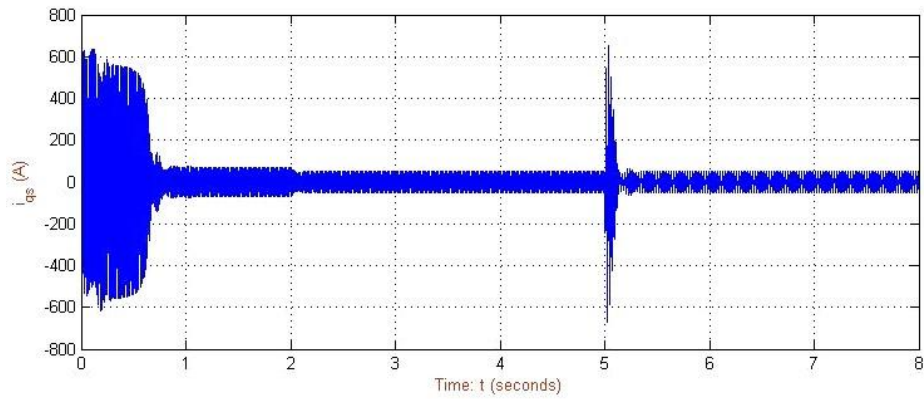
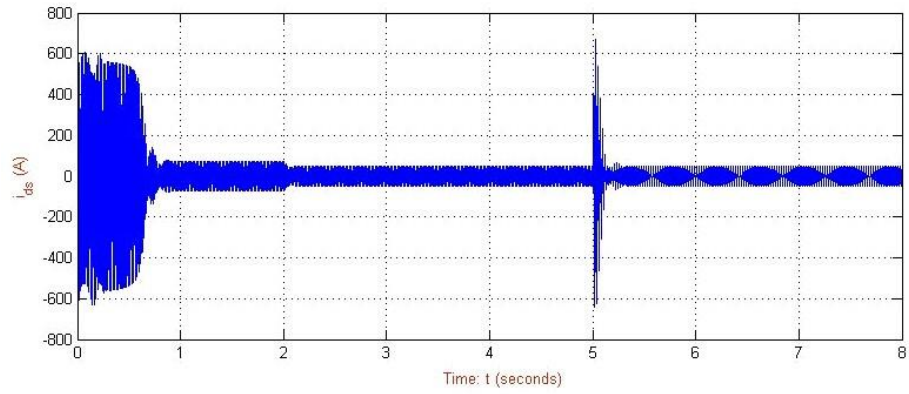


Figure 86: i_{ds} (up) and i_{qs} (down) versus time for 50HP IG under transient and different steady state conditions

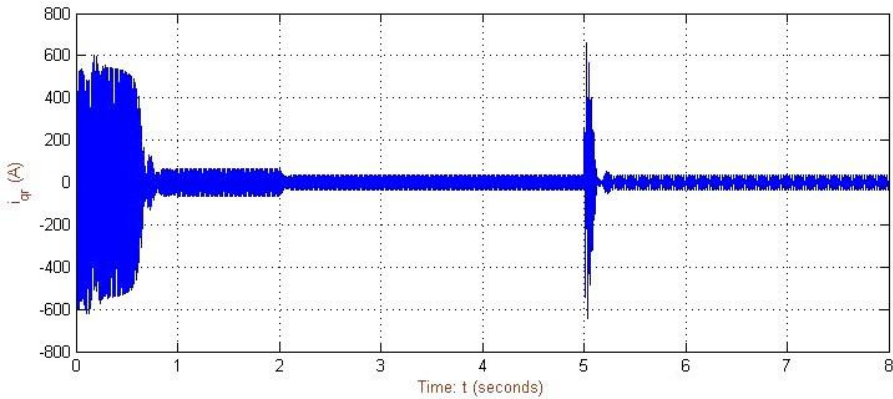
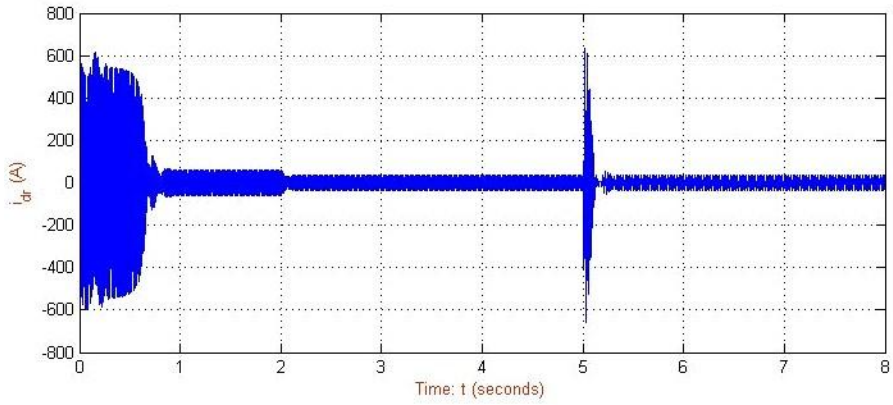


Figure 87: i_{dr} (up) and i_{qr} (down) versus time for 50HP IG under transient and different steady state conditions

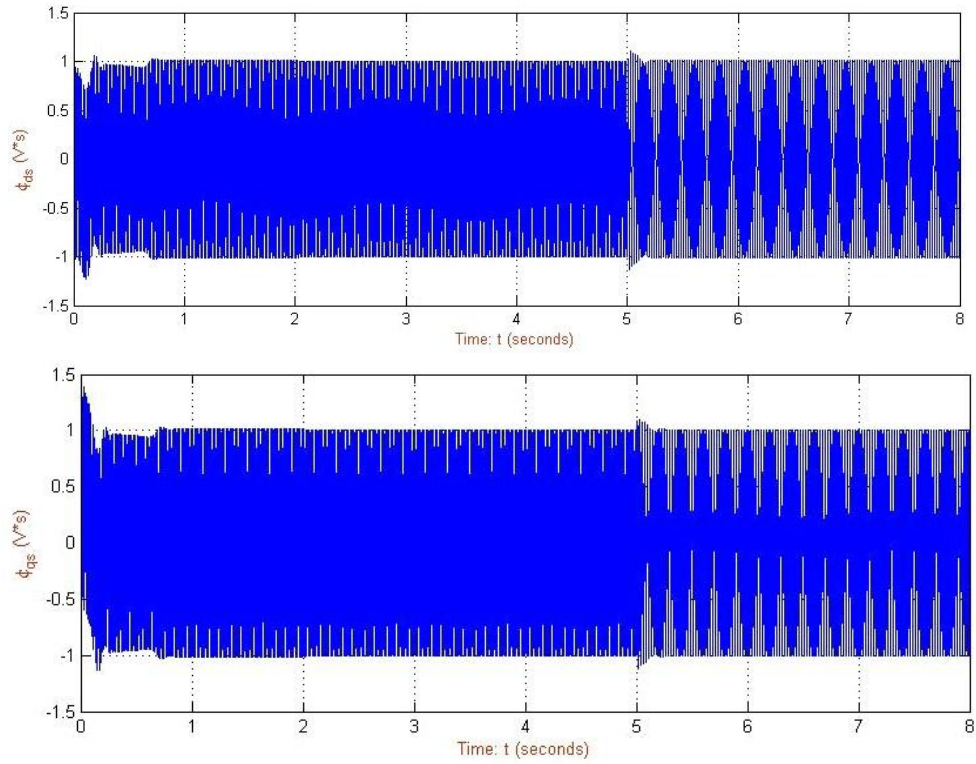


Figure 88: ϕ_{ds} (up) and ϕ_{qs} (down) versus time for 50HP IG under transient and different steady state conditions

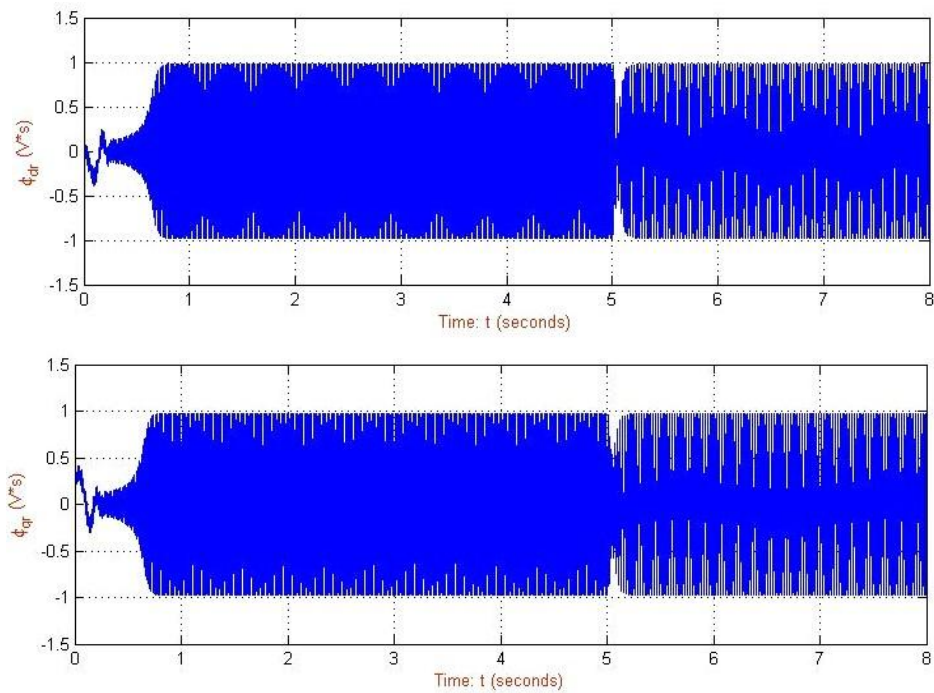


Figure 89: ϕ_{dr} (up) and ϕ_{qr} (down) versus time for 50HP IG under transient and different steady state conditions

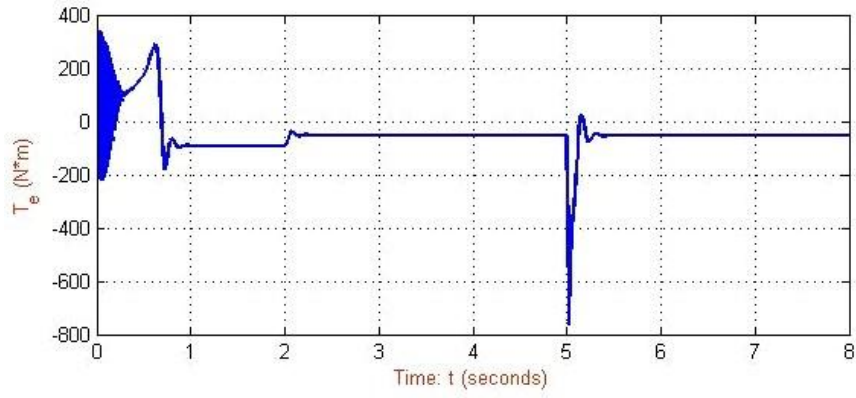


Figure 90: T_e versus time for 50HP IG under transient and different steady state conditions

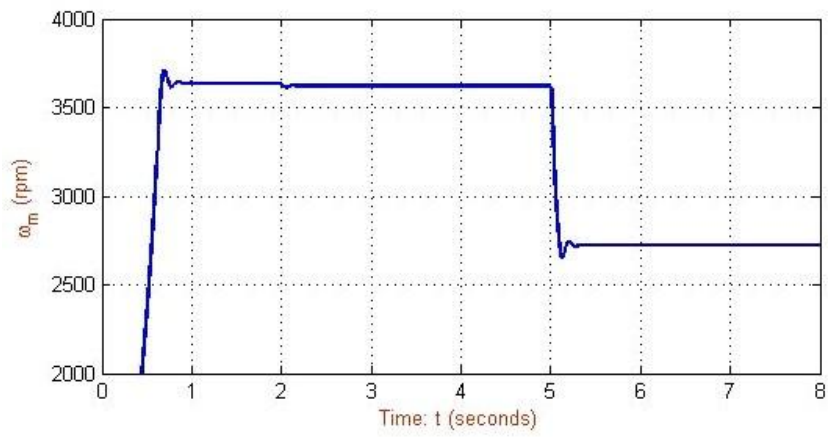


Figure 91: $\omega_m (= \omega_r)$ versus time for 50HP IG under transient and different steady state conditions

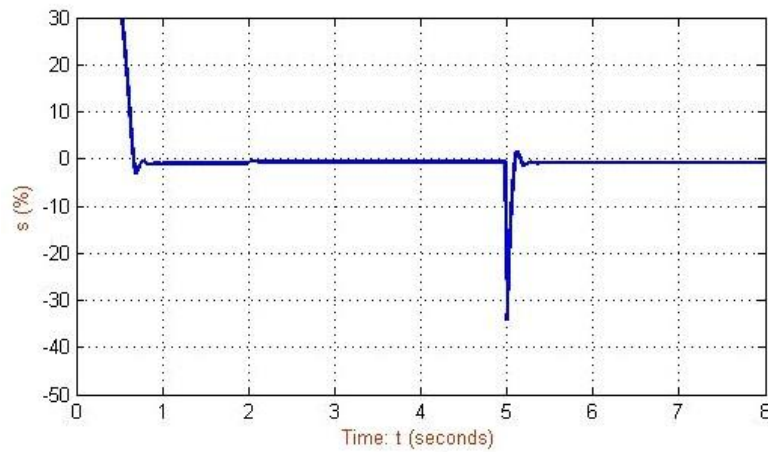


Figure 92: Slip ratio versus time for 50HP IG under transient and different steady state conditions

2.4.2 Case Study II – IG for 720kW OCT

The 3-phase induction motor/generator numerically characteristics used by the model presented in 2.3.3 are shown in Table 5. Simulation in steady state conditions with zero or non-zero load and in transient conditions are shown in Figures 93÷114.

Table 5: 720 kW induction motor/generator parameters

AC Induction Motor/Generators Parameters 720 kW , 460 V_{LL(rms)} , 60 Hz , 1800 rpm , Squirrel Single-Cage Rotor	
Stator Resistance (R_s)	0.001379 Ω
Rotor Resistance (R_r)	0.0007728 Ω
Magnetizing Inductance (L_m)	0.000769 H
Total (Rotor & Stator) Inductance ($L_{ls} + L_{lr}$)	0.0000304 H
Total Moment of Inertia (J)	80 kg·m ²
Friction Factor (F)	0.099 N·m·s
Number of Pole Pairs (p)	2

2.4.2.1 Steady State with Zero Load

This numerical simulation run was conducted to evaluate the steady state behavior of the 720 kW generator under zero mechanical load ($T_m = 0 \text{ N}\cdot\text{m}$). The system frequency, f_s , is **60Hz** and the voltage line-to-line is kept constant with an RMS value of **460V**. Moreover, the synchronous speed of the generator which also based on the pole numbers (=4) is **1800 rpm**. The initial conditions, at $t=0$ second, are all set to zero except for the initial slip ratio which set to start from 100%.

As it expected, the electromagnetic torque, T_e , is equal to zero, the electrical speed of the rotor are the same with synchronous speed at 1800 rpm and the mechanical speed of the rotor is 900 rpm because the number of poles while the slip ratio is zero as shown in Figures 93÷95.

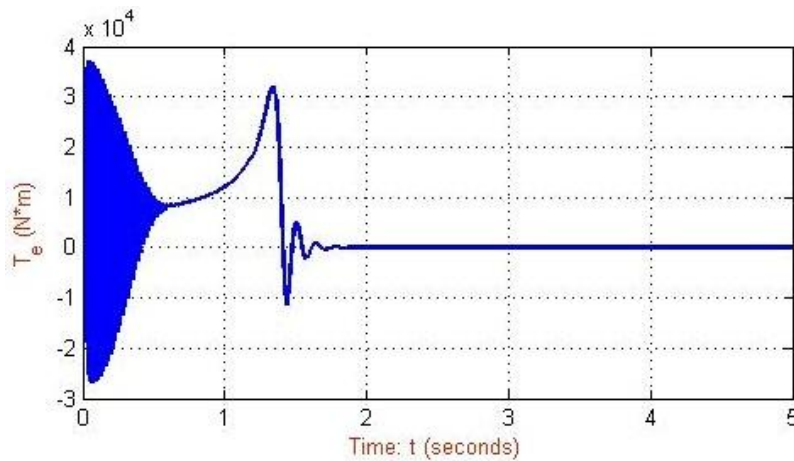


Figure 93: T_e versus time for 720 kW IG under no load

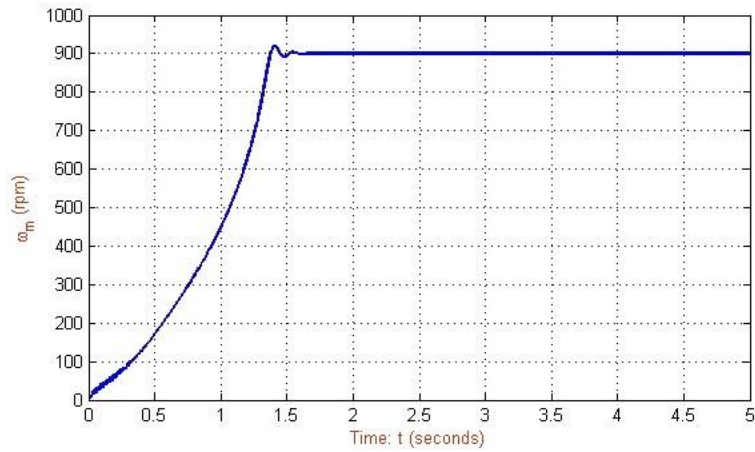


Figure 94: ω_m versus time for 720 kW IG under no load

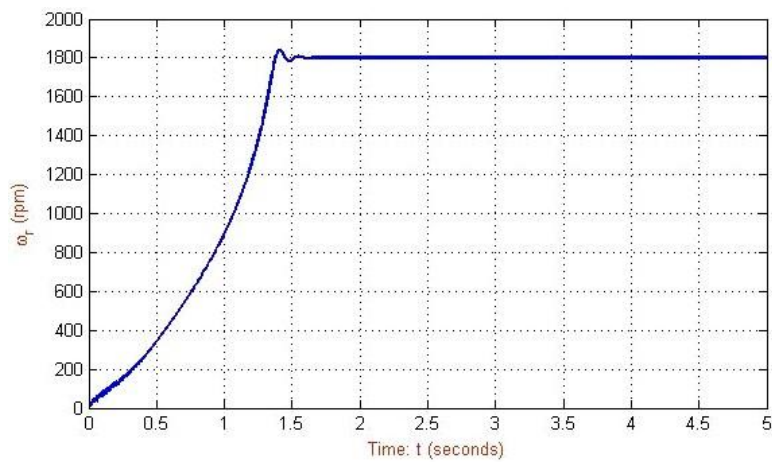


Figure 95: ω_r versus time for 720 kW IG under no load

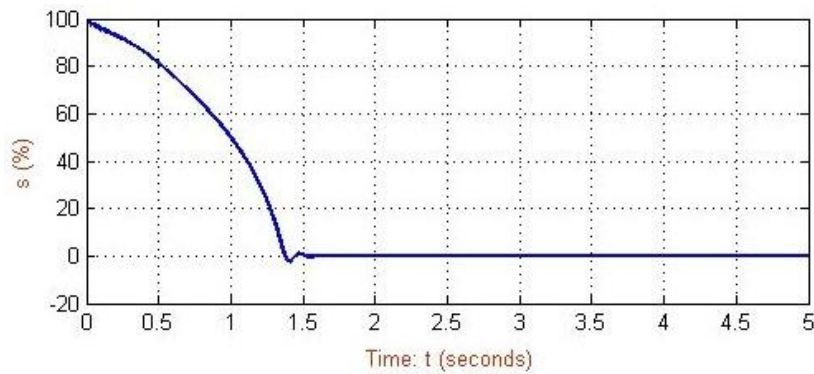


Figure 96: Slip ratio versus time for 720 kW IG under no load

2.4.2.2 Steady State with Load

This numerical simulation run was conducted to evaluate the steady state behavior of the 720 kW generator with mechanical load ($T_m = -2500 \text{ N}\cdot\text{m}$). The system frequency, f_s , is **60Hz** and the voltage line-to-line is kept constant with an RMS value of **460V** as previous. Moreover, the synchronous speed of the generator which also based on the pole numbers (4) is **1800 rpm**. The initial

conditions, at $t=0$ second, are all set to zero except for the initial slip ratio which set to start from 100%.

The currents and fluxes in stator and rotor are presented with Figures 97÷100 and based on d-q axis. The electromagnetic torque, T_e , is almost equal to the mechanical load, T_m , and the small difference is based on the friction factor F while the rotor's electrical speed is at 1806 rpm with a slip ratio of 0.33% as shown in Figures 101, 103 and 104 respectively. The mechanical speed of the rotor is at 903 rpm as shown in Figure 102.

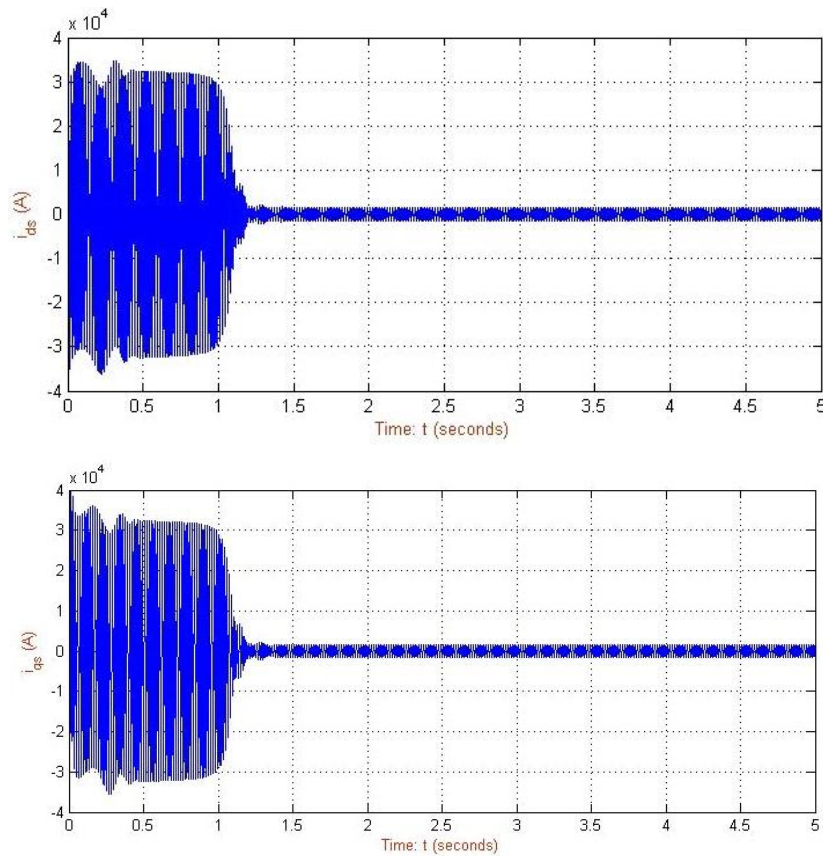


Figure 97: i_{ds} (up) and i_{qs} (down) versus time for 720 kW IG under load of -2500 N·m

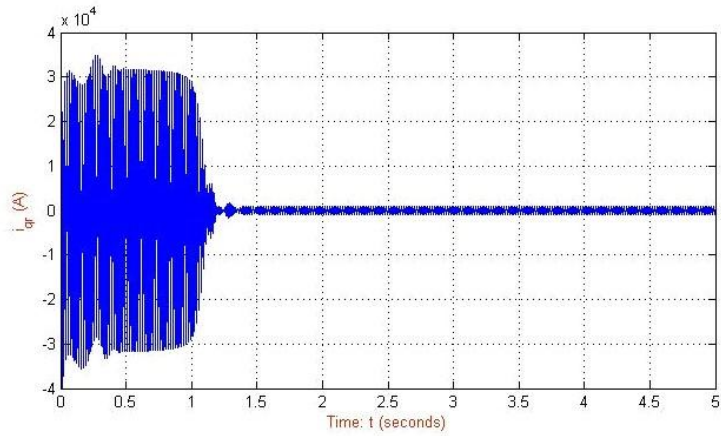
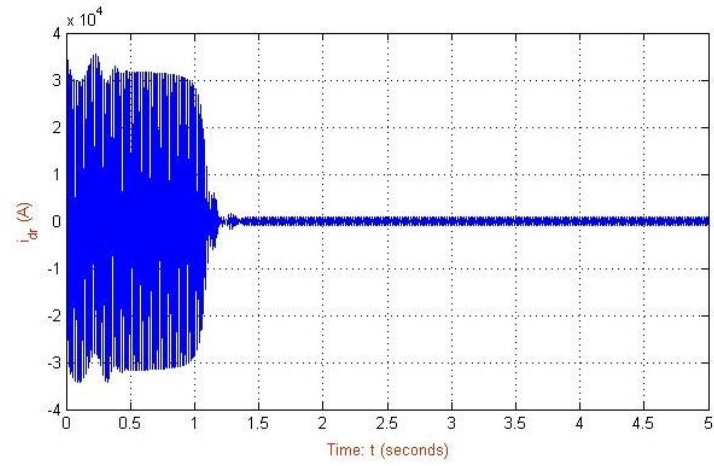


Figure 98: i_{dr} (up) and i_{qr} (down) versus time for 720 kW IG under load of -2500 N·m

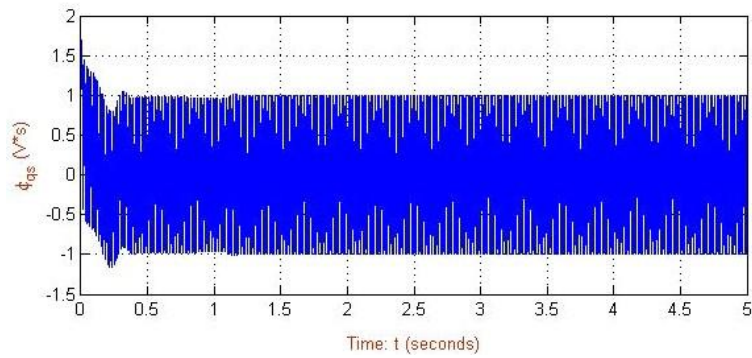
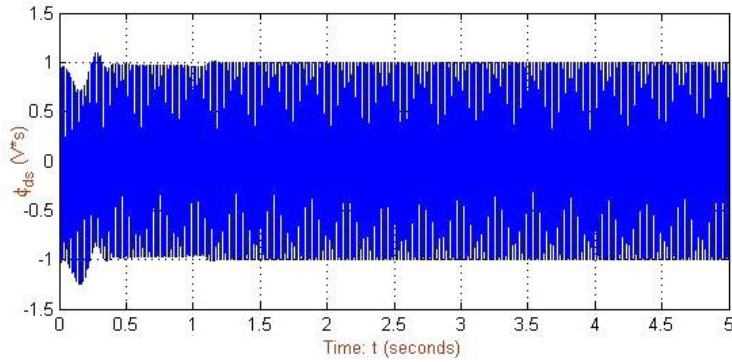


Figure 99: ϕ_{ds} (up) and ϕ_{qs} (down) versus time for 720 kW IG under load of -2500 N·m

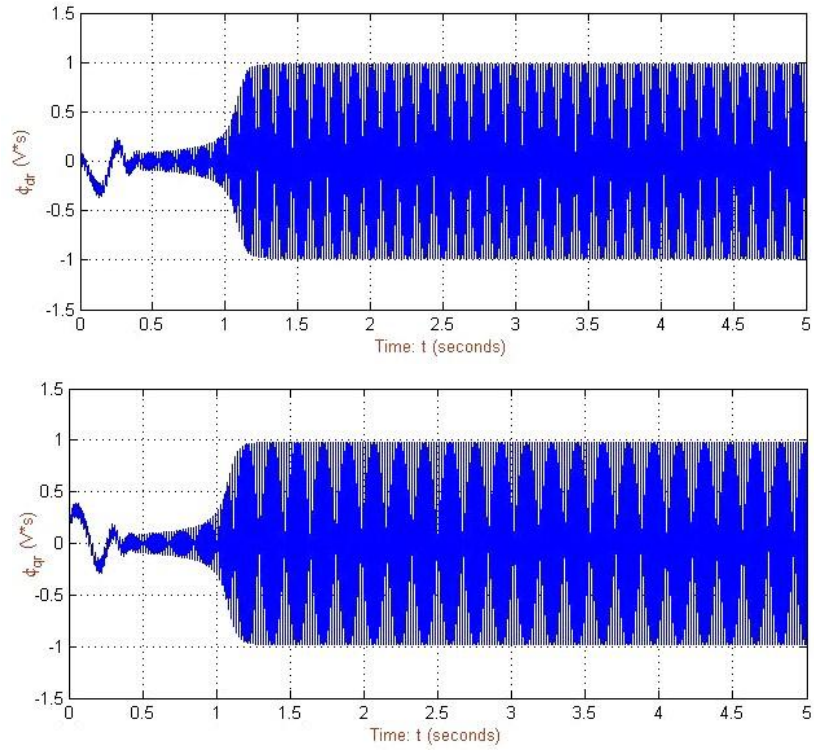


Figure 100: ϕ_{dr} (up) and ϕ_{qr} (down) versus time for 720 kW IG under load of -2500 N·m

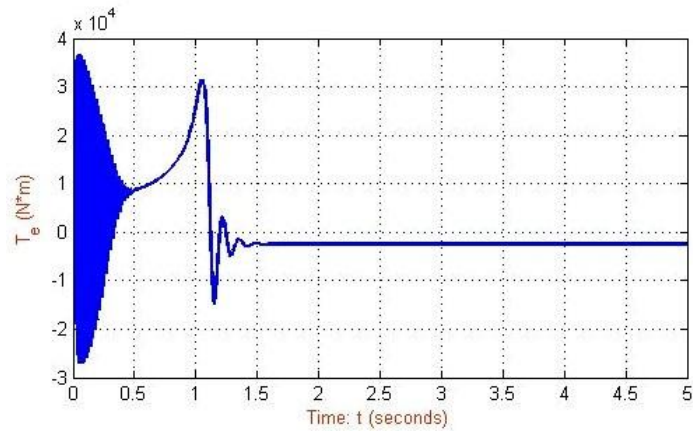


Figure 101: T_e versus time for 720 kW IG under load -2500 N·m (value -2497 N·m)

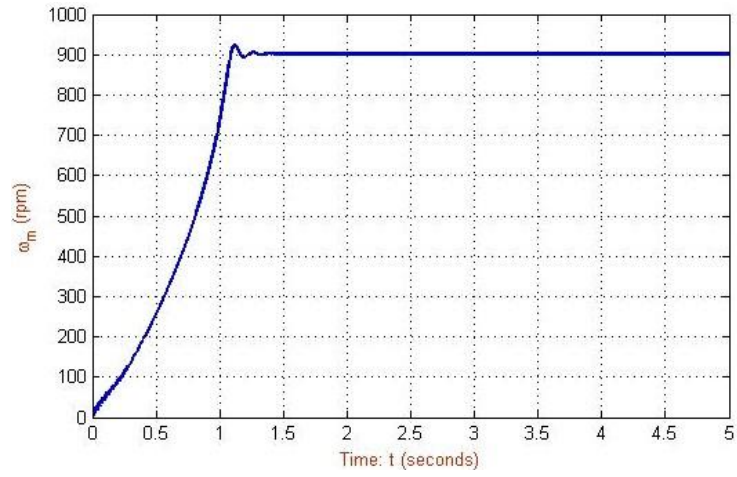


Figure 102: ω_m versus time for 720 kW IG under load -2500 N·m (value 903 rpm)

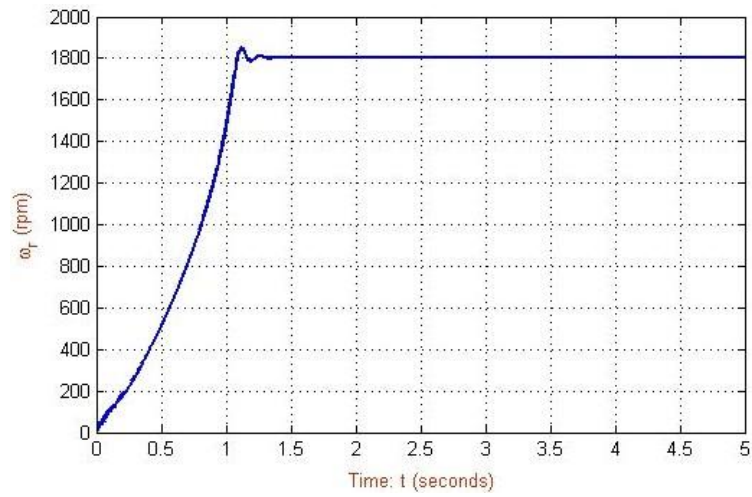


Figure 103: ω_r versus time for 720 kW IG under load -2500 N·m (value 1806 rpm)

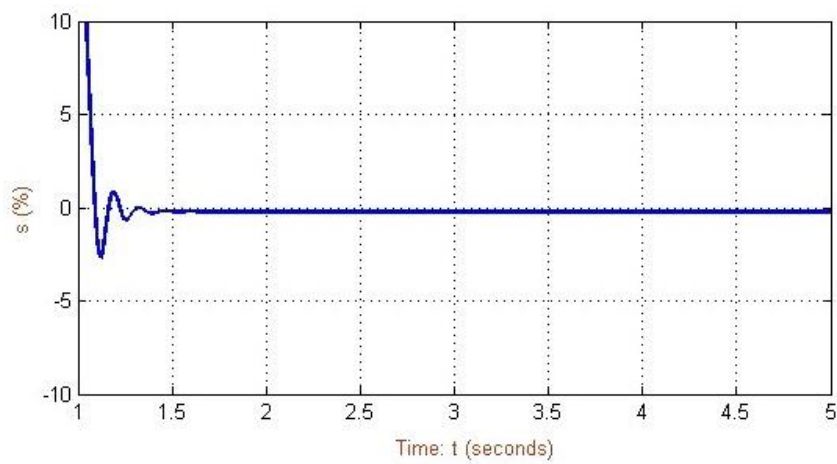


Figure 104: Slip ratio versus time for 720 kW IG under load -2500 N·m (value 0.33% rpm)

2.4.2.3 Transient

This numerical simulation run was conducted to evaluate the transient behavior of the 720 kW generator with initial mechanical load $T_m = -2500 \text{ N}\cdot\text{m}$ and an increment step with $T_m = -3000 \text{ N}\cdot\text{m}$ at $t=4$ seconds. The system frequency, f_s , is **60Hz** (100% of rated frequency) and at $t=7$ seconds is decreased 25% at $f_s = 45\text{Hz}$ (75% of the rated frequency). The voltage line-to-line is kept constant with an RMS value of **460V** as previous. Moreover, the synchronous speed of the generator which also based on the pole numbers ($=4$) is 1800 rpm at 100% rated frequency and 1350 rpm at 75% rated frequency. The initial conditions, at $t=0$ second, are all set to zero except for the initial slip ratio which set to start from 100%.

The mechanical load and frequency of the system with the step changes are presented in Figures 105 and 106 respectively. The currents and fluxes in stator and rotor during the transient period and in different steady state conditions are presented in Figures 107÷110 and based on d-q axis. The electromagnetic torque, T_e , follows the changes of mechanical load and its value is increased from $-2497 \text{ N}\cdot\text{m}$ to $-2996 \text{ N}\cdot\text{m}$ while the specific change in system frequency has no influence on its final value as shown in Figure 111. On the other hand, the increment step of mechanical load at $t=4$ seconds affect slightly the rotor's mechanical and electrical speed (from 1806 rpm to 1803 rpm) as well as the slip ratio (from 0.33% to 0.17%) while the reduction in system frequency at $t=7$ seconds, of course, decrease the rotor's speed but has minor effect in slip ratio (from 0.17% to 0.3%) as shown in Figures 113 and 114.

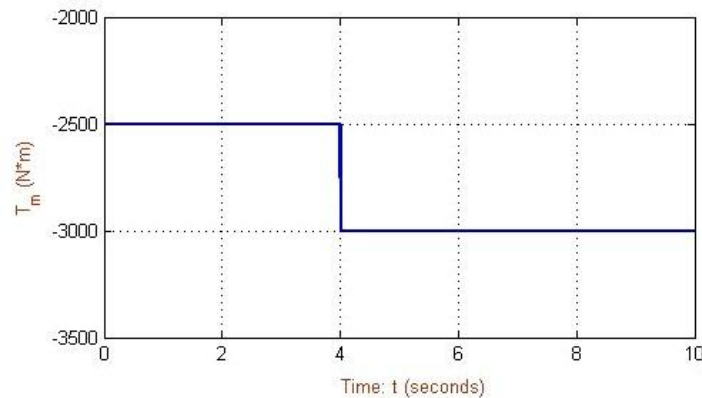


Figure 105: T_m versus time for 720 kW IG with an increment step at $t=4$ seconds

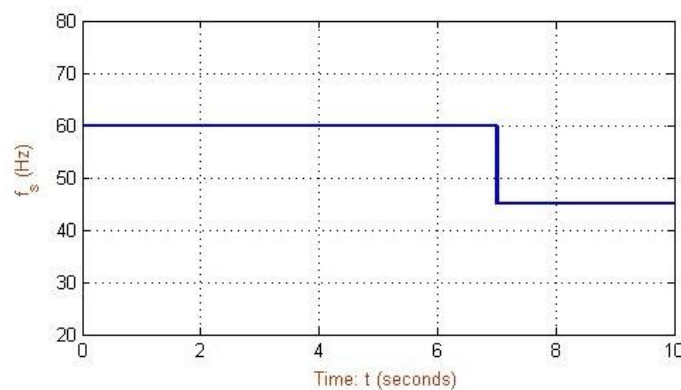


Figure 106: f_s versus time for 720 kW IG with a reduction step at $t=7$ seconds

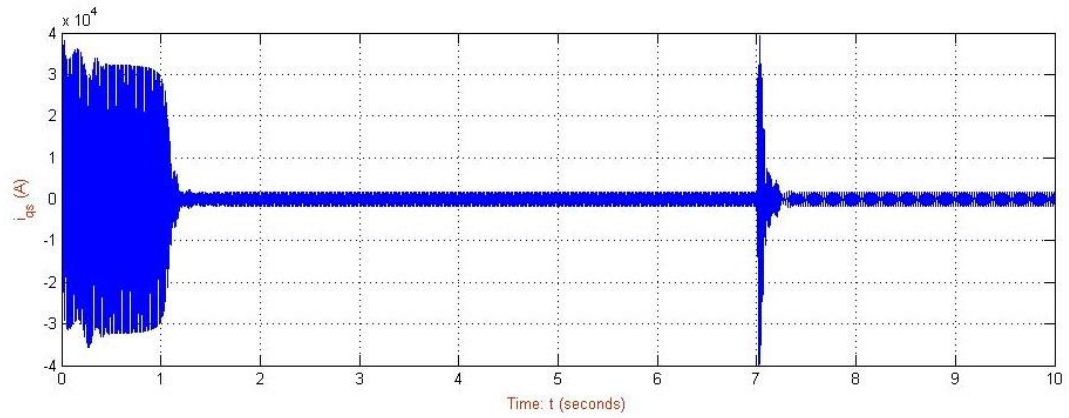
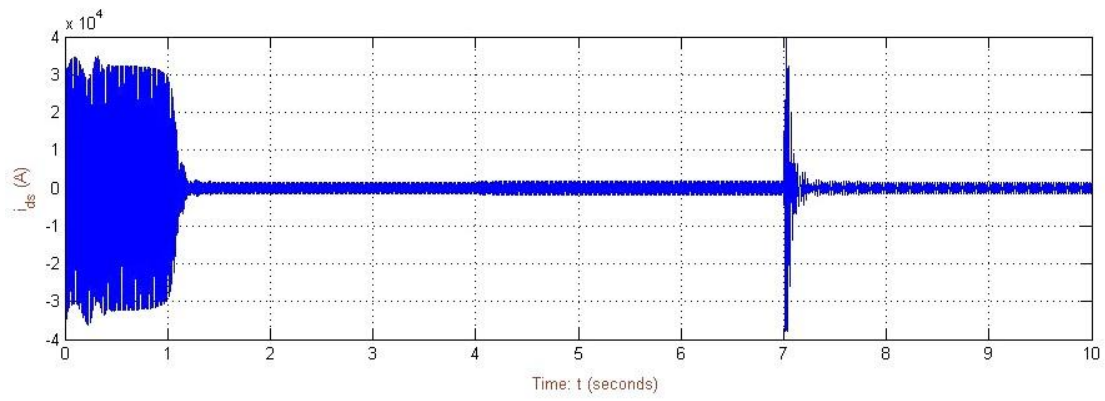


Figure 107: i_{ds} (up) and i_{qs} (down) versus time for 720 kW IG under transient and different steady state conditions

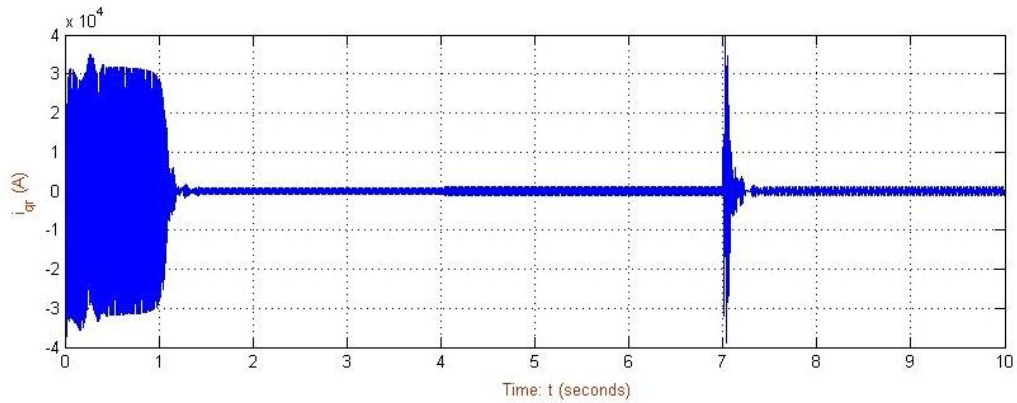
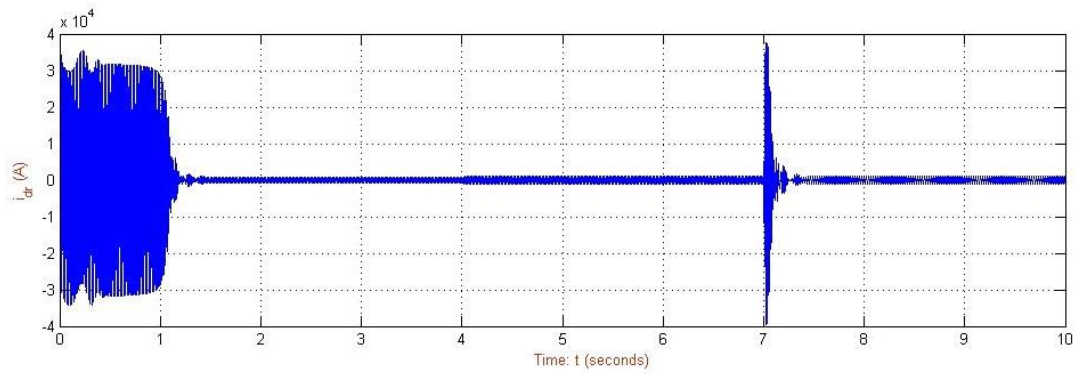


Figure 108: i_{dr} (up) and i_{qr} (down) versus time for 720 kW IG under transient and different steady state conditions

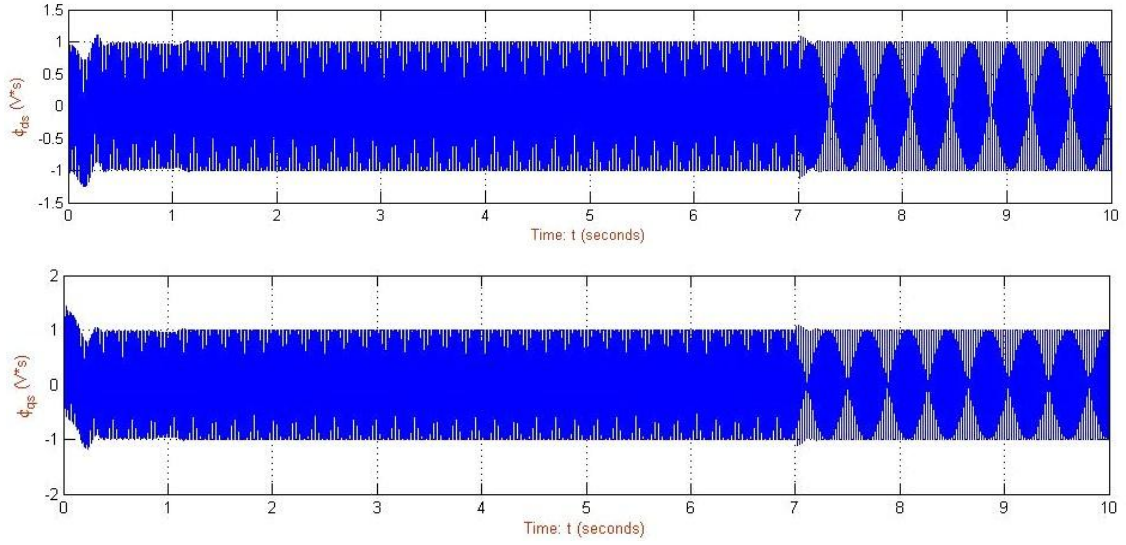


Figure 109: ϕ_{ds} (up) and ϕ_{qs} (down) versus time for 720 kW IG under transient and different steady state conditions

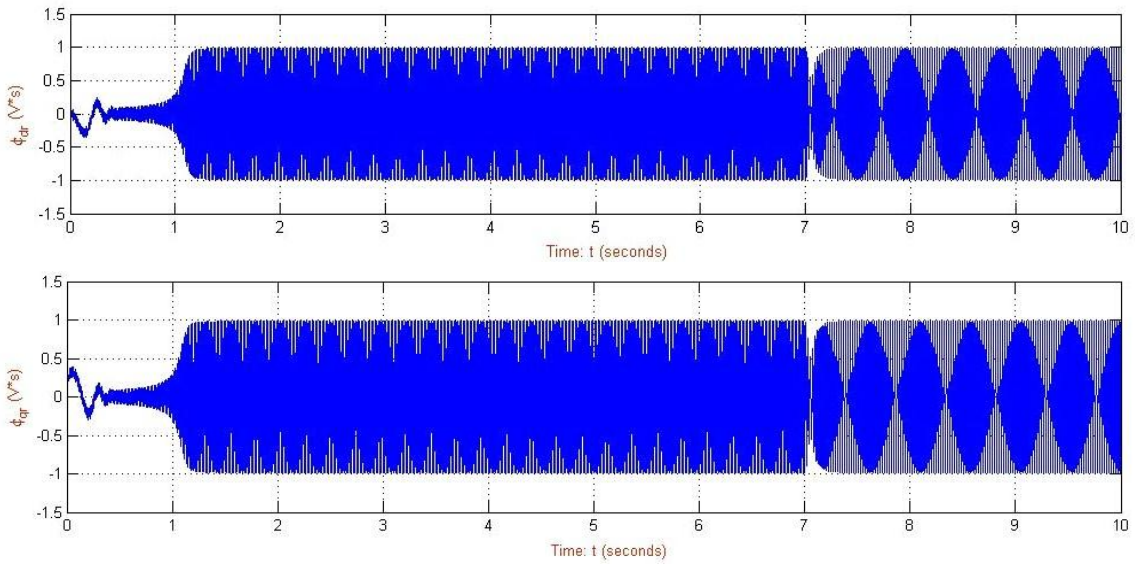


Figure 110: ϕ_{dr} (up) and i_{qr} (down) versus time for 720 kW IG under transient and different steady state conditions

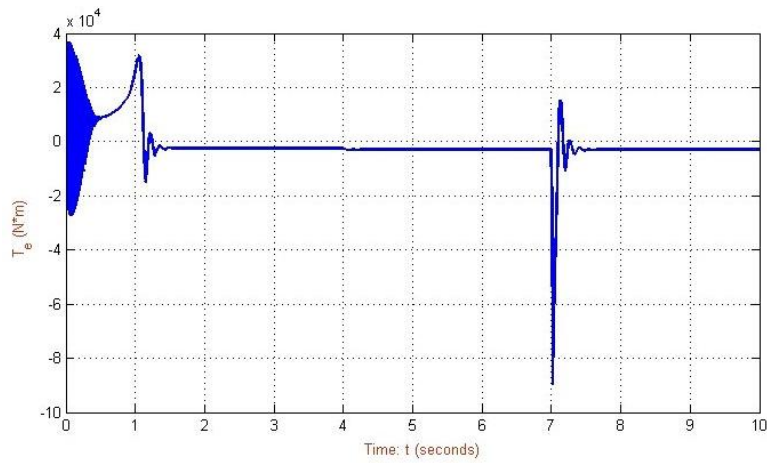


Figure 111: T_e versus time for 720 kW IG under transient and different steady state conditions

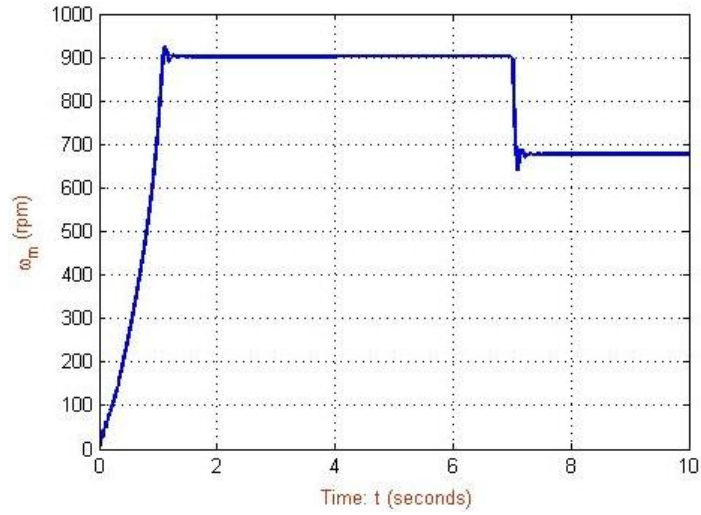


Figure 112: ω_m versus time for 720 kW IG under transient and different steady state conditions

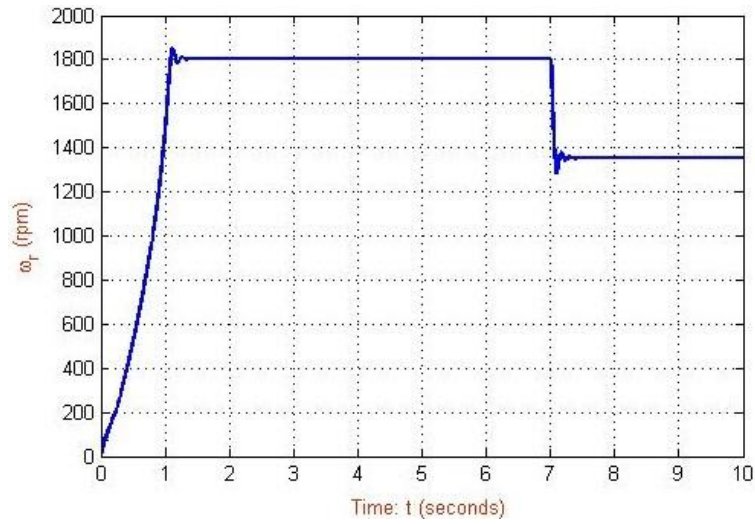


Figure 113: ω_r versus time for 720 kW IG under transient and different steady state conditions

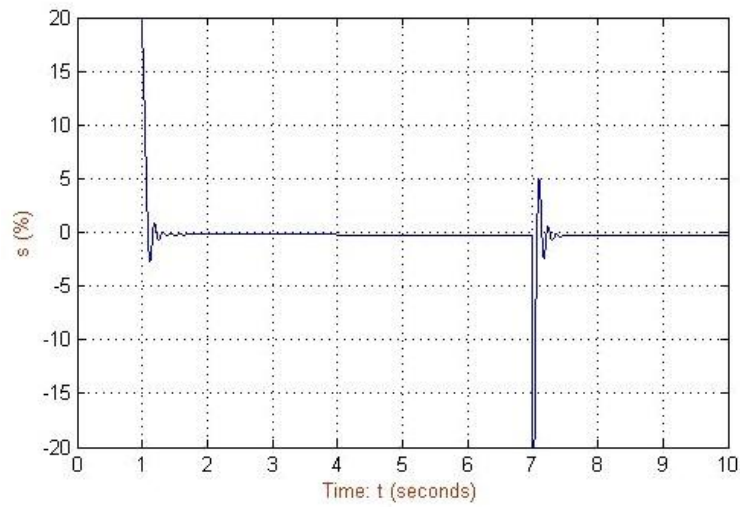


Figure 114: Slip ratio versus time for 720 kW IG under transient and different steady state conditions

CHAPTER 3

CONTROL OF INDUCTION MOTORS/GENERATORS

3.1 Classical Steady State Representation of an Induction Machine

The steady state model and equivalent circuit developed below are useful for studying the performance of the machine in steady state. This implies that *all electrical transients are neglected during load changes and stator frequency variations*. On the other hand, the dynamic model considers the instantaneous effects of varying voltages/currents, stator frequency and torque disturbance [110].

3.1.1 Steady State Equivalent Circuit

The foregoing considerations of flux and MMF waves can readily be translated to a steady-state equivalent circuit for a polyphase induction machine. *In this derivation, only machines with symmetric polyphase windings excited by balanced polyphase voltages are considered*. As in many other discussions of polyphase devices, it is helpful to think of three-phase machines as being Y-connected, so that *currents are always line values and voltages always line-to-neutral values*. In this case, we can derive the equivalent circuit for one phase, with the understanding that the voltages and currents in the remaining phases can be found simply by an appropriate phase shift of those of the phase under study ($\pm 120^\circ$ in the case of a three-phase machine) [86].

First, consider conditions in the stator. The synchronously-rotating air-gap flux wave generates balanced polyphase counter EMFs in the phases of the stator. The stator terminal voltage differs from the counter EMF by the voltage drop in the stator leakage impedance $Z_l = R_l + jX_l$ [86]. Thus:

$$V_l = E_2 + I_l(R_l + jX_l) \quad (3.1)$$

where (all values are per phase):

V_l = Stator line-to-neutral (phase) terminal voltage (V)

E_2 = Counter EMF (line-to-neutral) generated by the resultant air-gap flux (V)

I_l = Stator current (A)

R_l = Stator effective resistance (represent the stator resistive losses) (Ω)

X_l = Stator inductance (represent stator leakage reactance) = $j \cdot 2\pi \cdot f_s \cdot L_{ls}$ (Ω)

Z_l = Stator leakage impedance (Ω)

X_m = magnetizing inductance (represent leakage reactance produces the magnetic field flux) = $j \cdot 2\pi \cdot f_s \cdot L_m$ (Ω)

The polarity of the voltages and currents are shown in the equivalent circuit of Figure 114. *The resultant air-gap flux is created by the combined MMF's of the stator and rotor currents*. Just as in the case of a transformer, the stator current can be resolved into two components: *a load component, which is transfer to the rotor to provide shaft torque, and an exciting (magnetizing) component which provides the rotating magnetic field*. The load component I_2 produces an MMF that corresponds to the MMF of the rotor current. The exciting component I_ϕ is the additional stator current required to create the resultant air-gap flux and is a function of the EMF E_2 . The exciting current can be resolved into a core-loss component I_c in phase with E_2 and a magnetizing component I_m lagging E_2 by 90° . In the equivalent circuit, the exciting current can be accounted for by means of a shunt branch, formed by a core-loss resistance R_c (*represent the core losses, bearing friction windage losses etc.*) and a magnetizing inductance X_m (*represent the leakage reactance which produces the magnetic field flux*)

in parallel, connected across E_2 , as in Figure 115. Both R_c and X_m are usually determined at rated stator frequency and for a value of E_2 close to the expected operating value; they are then assumed to remain constant for the small departures of E_2 associated with normal operation of the motor [86].

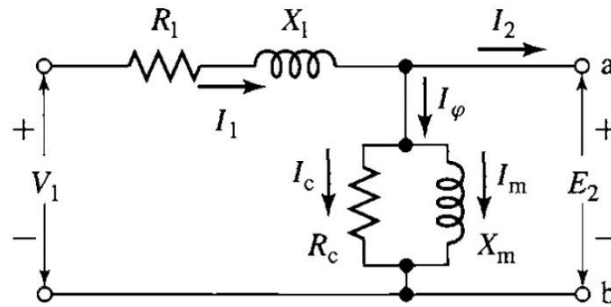


Figure 115: Per-phase stator equivalent circuit of an AC induction motor in steady state conditions (Source: A.E. Fitzgerald et al. [86])

The equivalent circuit representing stator phenomena is exactly like that used to represent the primary of a transformer. To complete the above mentioned model, the effects of the rotor must be incorporated. From the point of view of the stator equivalent circuit of Figure 115, *the rotor can be represented by an equivalent impedance Z_2 corresponding to the leakage impedance of an equivalent stationary secondary* [86].

$$Z_2 = E_2/I_2 \quad (3.2)$$

To complete the equivalent circuit, we must determine Z_2 by representing *the stator and rotor voltages and currents in terms of rotor quantities as referred to the stator*. From the point of view of the primary, the secondary winding of a transformer can be replaced by an equivalent secondary winding having the same number of turns as the primary winding. In a transformer where the turns ratio and the secondary parameters are known, this can be done by referring the secondary impedance to the primary by multiplying it by the square of the primary-to-secondary turns ratio. The resultant equivalent circuit is perfectly general from the point of view of primary quantities [86].

Similarly, in the case of a poly-phase induction motor, if the rotor were to be replaced by an equivalent rotor with a *poly-phase winding with the same number of phases and turns as the stator but producing the same MMF and air gap flux as the actual rotor, the performance as seen from the stator terminals would be unchanged* [86].

This concept, which we will adopt here, is especially *useful in modeling squirrel-cage rotors for which the identity of the rotor "phase windings" is in no way obvious*. The rotor of an induction machine is short-circuited, and hence the impedance seen by induced voltage is simply the rotor short circuit impedance. Consequently the relation between the slip-frequency leakage impedance Z_{2s} of the equivalent rotor and the slip-frequency leakage impedance Z_{rotor} of the actual rotor must be [86]:

$$Z_{2s} = E_{2s}/I_{2s} = N_{eff}^2 (E_{rotor}/I_{rotor}) = N_{eff}^2 Z_{rotor} \quad (3.3)$$

where N_{eff} is the effective turns ratio between the stator winding and that of the actual rotor winding. Here the subscript $2s$ refers to quantities associated with the referred rotor. Thus E_{2s} is the voltage induced in the equivalent rotor by the resultant air-gap flux, and I_{2s} is the corresponding induced current [86].

When one is concerned with the actual rotor currents and voltages, the turns ratio N_{eff} must be known in order to convert back from equivalent-rotor quantities to those of the actual rotor. However,

for the purposes of studying induction-motor performance as seen from the stator terminals, there is no need for this conversion and *a representation in terms of equivalent-rotor quantities is fully adequate. Thus an equivalent circuit based upon equivalent-rotor quantities can be used to represent both coil-wound and squirrel-cage rotors* [86].

Having taken care of the effects of the stator-to-rotor turns ratio, we next must take into account the relative motion between the stator and the rotor with the objective of replacing the actual rotor and its slip-frequency voltages and currents with an equivalent stationary rotor with stator-frequency voltages and currents. Consider first the *slip-frequency leakage impedance of the referred rotor* [86]:

$$Z_{2s} = E_{2s}/I_{2s} = R_2 + j \cdot s \cdot X_2 \quad (3.4)$$

where:

R_2 = referred rotor resistance (represent the rotor resistive losses) (Ω)

$X_r = s \cdot X_2$ = referred rotor inductance at slip frequency (represent the rotor leakage reactance) = $s \cdot j \cdot 2\pi \cdot f_s \cdot L_{lr}$ (Ω)

X_2 = referred rotor leakage reactance at stator frequency f_s (Ω)

Note that here X_2 has been defined as the referred rotor leakage reactance at stator frequency f_s . Since the actual rotor frequency $f_r = s f_s$, it has been converted to *the slip-frequency reactance simply by multiplying by the slip s* . The slip-frequency equivalent circuit of one phase of the referred rotor is shown in Figure 116. This is the *equivalent circuit of the rotor as seen in the slip-frequency rotor reference frame* [86].

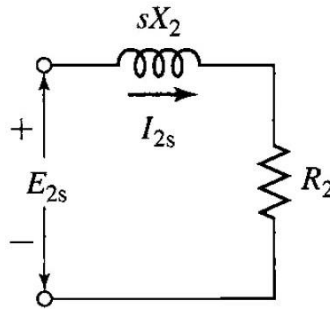


Figure 116: Per-phase rotor equivalent circuit of an AC induction motor in steady state conditions and at slip frequency
(Source: A.E. Fitzgerald et al. [86])

The final result, which is the per-phase equivalent circuit of an AC induction motor where the rotor parameters have been referred to the rotor reference frame, are shown in Figure 117.

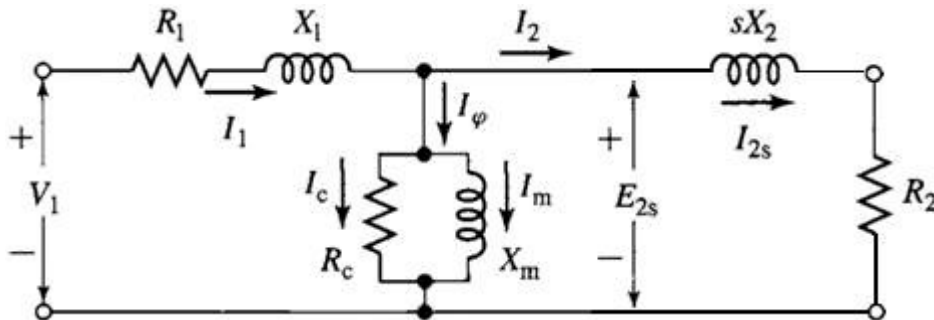


Figure 117: Per-phase equivalent circuit of an AC induction motor. The rotor parameters have been referred to the rotor reference frame and for standstill is $s=1$ (Source: Author and [86])

We next observe that the *resultant air-gap MMF wave is produced by the combined effects of the stator current I_1 and the equivalent load current I_2* . Similarly, it can be expressed in terms of the stator current and the equivalent rotor current I_{2s} . These two currents *are equal in magnitude* since I_{2s} is defined as the current in an equivalent rotor with the same number of turns per phase as the stator. Because the resultant air-gap MMF wave is determined by the phasor sum of the stator current and the rotor current of either the actual or equivalent rotor, I_2 and I_{2s} must also be equal in phase (at their respective electrical frequencies) and hence we can write [86]:

$$I_{2s} = I_2 \quad (3.5)$$

Finally, consider that the resultant flux wave induces both the slip-frequency EMF induced in the referred rotor E_{2s} and the stator counter EMF E_2 . If it were not for the effect of speed, these voltages would be equal in magnitude since the referred rotor winding has the same number of turns per phase as the stator winding. However, because the relative speed of the flux wave with respect to the rotor is s times its speed with respect to the stator, the relation between these EMFs is [86]:

$$E_{2s} = s \cdot E_2 \quad (3.6)$$

We can furthermore argue that since the *phase angle between each of these voltages and the resultant flux wave is 90°* , then these two voltages must also be equal in a phasor sense at their respective electrical frequencies [86].

Division of Equation 3.6 by Equation 3.5 and use of Equation 3.4 then gives:

$$E_{2s}/I_{2s} = s \cdot E_2/I_2 = Z_{2s} = R_2 + j \cdot s \cdot X_2 \quad (3.7)$$

Division by the slip s then gives:

$$Z_2 = E_2/I_2 = R_2/s + j \cdot X_2 \quad (3.8)$$

We have achieved our objective. Z_2 is the impedance of the equivalent stationary rotor which appears across the load terminals of the stator equivalent circuit of Figure 115. The final result is shown in the single-phase equivalent circuit of Figure 118. *The combined effect of shaft load and rotor resistance appears as a reflected resistance R_2/s , a function of slip and therefore of the mechanical load*. The current in the reflected rotor impedance equals the load component I_2 of stator current; the voltage across this impedance equals the stator voltage E_2 . Note that when rotor currents and voltages are reflected into the stator, their frequency is also changed to stator frequency. *All rotor electrical phenomena, when viewed from the stator, become stator-frequency phenomena, because the stator winding simply sees MMF and flux waves traveling at synchronous speed* [86].

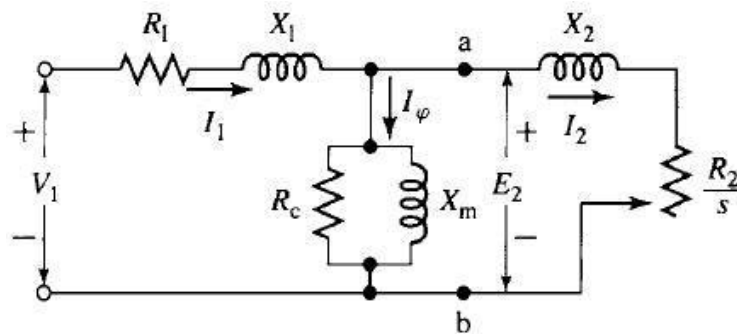


Figure 118: Per-phase equivalent circuit of an AC induction motor. The rotor parameters have been referred to the stator and for standstill is $s=1$ (Source: A.E. Fitzgerald et al. [86])

3.1.2 Analysis of the Equivalent Circuit

The equivalent circuit of induction machine which is presented in Figure 118, also known as *the per-phase equivalent model*, can be used to determine a wide variety of *steady-state performance characteristics* of polyphase induction machines. These include variations of current, speed, and losses as the load-torque requirements change, as well as the starting torque, and the maximum torque [86].

The power balance in an induction machine or any machine can be expressed as follows [111]:

$$P_{out} = P_{in} - P_{losses} \quad (3.9)$$

while the *power flow in an AC induction machine* is shown in Figure 119.

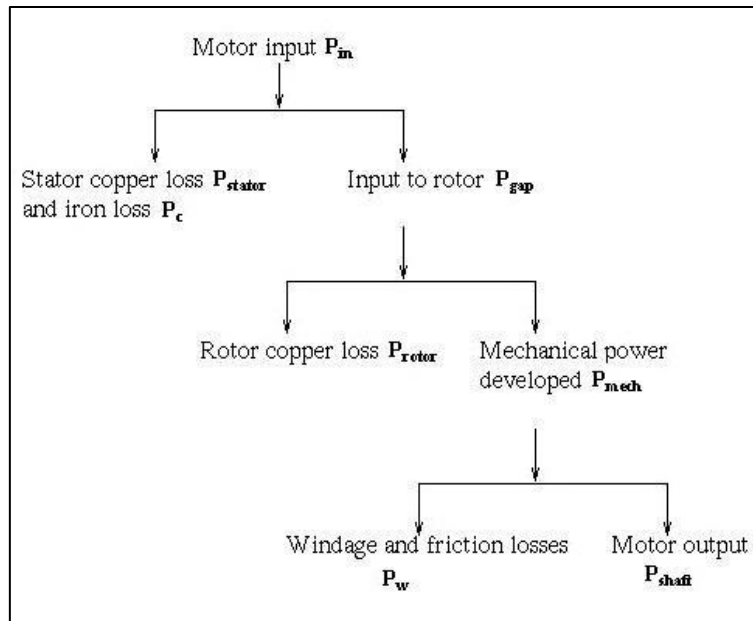


Figure 119: Power flow in AC induction machine in motoring mode
(Source: Author)

The input power, P_{in} , can be given in the form of three balanced voltages and three balanced currents (considering motoring mode), each one shifted by 120° and expressed in phase values as follows [86]:

$$P_{in} = n_{ph} \cdot V_1 I_1 \cos \phi \quad (3.10)$$

where n_{ph} is the number of stator phases and $\cos \phi$ is the power factor.

Like any other electric machine, an induction generator has inherent losses that can be combined in the following expression [111]:

$$P_{losses} = P_{stator} + P_c + P_{rotor} + P_w + \text{stray} \quad (3.11)$$

The total rotor copper losses, P_{rotor} , can be calculated from the $I^2 R$ loss in the equivalent rotor circuit as [86]:

$$P_{rotor} = n_{ph} \cdot I_{2s}^2 \cdot R_2 \quad (3.12)$$

Since $I_{2s} = I_2$, we can write Equation. 3.12 as [86]:

$$P_{rotor} = n_{ph} \cdot I_2^2 R_2 \quad (3.13)$$

Similar someone can calculate the total stator copper losses, P_{stator} , as shown below [111]:

$$P_{stator} = n_{ph} \cdot I_1^2 R_1 \quad (3.14)$$

The *iron losses* are due to the *hysteresis current* (magnetizing) and *Foucault current* (current induced in the iron). It should be said at this point that the stator and rotor iron losses usually appear mixed, although in the latter they are much smaller and more difficult to distinguish. So the iron loss resistance, R_m , in the equivalent circuit of the induction generator *practically represents these losses with the other mechanical losses*. So they may be given as follows [111]:

$$P_c = n_{ph} \cdot \frac{E_1^2}{R_c} \quad (3.15)$$

The equivalent circuit shows that the total power transferred across the air gap, P_{gap} , from the stator is [86]:

$$P_{gap} = n_{ph} \cdot I_2^2 \cdot \left(\frac{R_2}{s} \right) \quad (3.16)$$

The electromagnetic power, P_{mech} , developed by the motor can now be determined by subtracting the rotor power dissipation of Equation 3.13 from the air-gap power of Equation 3.16 [86].

$$P_{mech} = P_{gap} - P_{rotor} = n_{ph} \cdot I_2^2 \cdot \left(\frac{R_2}{s} \right) - n_{ph} \cdot I_2^2 \cdot R_2 \quad (3.17)$$

or equivalently

$$P_{mech} = n_{ph} \cdot I_2^2 R_2 \cdot \left(\frac{1-s}{s} \right) \quad (3.18)$$

Comparing Equation 3.16 with Equation 3.18 gives:

$$P_{mech} = (1 - s) \cdot P_{gap} \quad (3.19)$$

and

$$P_{rotor} = s \cdot P_{gap} \quad (3.20)$$

with the rotor efficiency (considering motoring mode) given as follow [112]:

$$\eta_{rotor} = \frac{P_{mech}}{P_{gap}} = 1 - s \quad (3.21)$$

We see then that, of the total power delivered across the air gap to the rotor, the fraction $1 - s$ is converted to *mechanical power* and the fraction s is dissipated as *$I^2 R$ loss in the rotor conductors*. From this it is evident that an induction motor operating at high slip is an inefficient device. When power aspects are to be emphasized, the equivalent circuit can be redrawn in the manner of Figure 120 [86]. The electromechanical power per stator phase is equal to the power delivered to the resistance $R_2(1 - s)/s$.

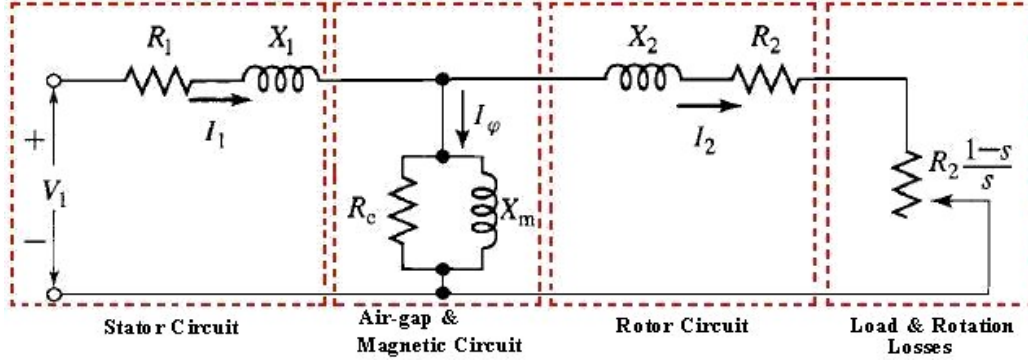


Figure 120: The complete per-phase equivalent circuit of an AC induction motor with effective rotor resistance (R_2/s) split into R_2 and $R_2(1-s)/s$. The power dissipated in R_2 represents the rotor copper loss per phase, while the power in the shaded resistance $R_2(1-s)/s$ corresponds to the mechanical output power per phase, when the slip is s (Source: Author and [86])

The electromechanical torque T_e corresponding to the power P_{mech} can be obtained by recalling that mechanical power equals torque times angular velocity [86]. Thus:

$$P_{mech} = T_e \cdot \omega_m = T_e \cdot (2/P) \cdot \omega_r = T_e \cdot (2/P) \cdot (1-s) \omega_s \quad (3.22)$$

For P_{mech} in *Watts* and ω_s in *rad/sec*, T_e will be in *Nm*. Use of Equations 3.18 and 3.19 leads to:

$$T_e = \frac{P_{mech}}{\omega_m} = \left(\frac{P}{2}\right) \cdot \frac{n_{ph} \cdot I_2^2 \cdot \left(\frac{R_2}{s}\right)}{\omega_s} \quad (3.23)$$

with the synchronous mechanical angular velocity ω_s being given by:

$$\omega_s (\text{rad/s}) = \frac{4\pi f_s}{P} \quad (\text{Equation 2.12.1})$$

The mechanical torque, T_e , and power, P_{mech} , are not the output values available at the shaft because *friction, windage, and stray-load losses remain to be accounted for*. It is obviously correct to subtract friction, windage, and other rotational losses from T_e or P_{mech} and it is generally assumed that stray load effects can be subtracted in the same manner. The remainder is available as output power from the shaft for useful work [86]. Thus:

$$P_{shaft} = P_{mech} - P_{w+stray} \quad (3.23)$$

and

$$T_{shaft} = P_{shaft} / \omega_m = T_e - T_{w+stray} \quad (3.24)$$

where $P_{w+stray}$ and $T_{w+stray}$ are the *power and torque associated with the friction, windages, and remaining rotational losses* respectively [86].

Analysis of the transformer equivalent circuit is often simplified by *either neglecting the magnetizing branch entirely or adopting the approximation of moving it out directly to the primary terminals*. Such approximations are not used in the case of induction machines under normal running conditions because the presence of the air gap results in relatively lower magnetizing impedance and correspondingly a relatively higher exciting current 30 to 50 percent of full-load current and because

the leakage reactances are also higher. Some simplification of the induction-machine equivalent circuit results if the core-loss resistance R_c is omitted and the associated core-loss effect is deducted from T_e or P_{mech} at the same time that rotational losses and stray load effects are subtracted. The equivalent circuit then becomes that of Figure 121 (left or right), and the error introduced is often relatively insignificant. Such a procedure also has an advantage during motor testing, for then the no-load core loss need not be separated from friction and windage [86].

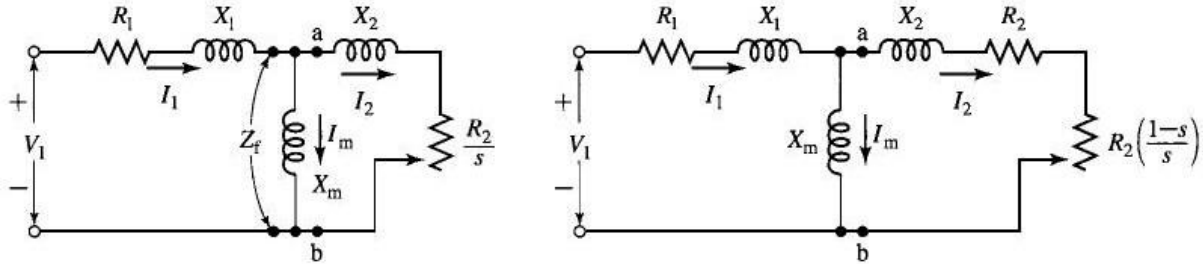


Figure 121: IEEE recommended per-phase equivalent circuit of an AC induction motor. The iron loss resistance R_c is neglected corresponding to (left) Figure 118 and (right) Figure 120 (Source: A.E. Fitzgerald et al. [86])

Finally, to estimate the motor total efficiency, we use [111]:

$$\eta_{rotor} = \frac{P_{shaft}}{P_{in}} \quad (3.25)$$

3.1.3 Torque and Power by Use of Thevenin's Theorem

When torque and power relations are to be emphasized, considerable simplification are resulted from application of *Thevenin's network theorem* to the induction-motor equivalent circuit. In its general form, Thevenin's theorem permits the replacement of any network of linear circuit elements and complex voltage sources, such as viewed from two terminals "a" and "b" (Figure 122-left), by a single complex voltage source V_{th} in series with a single impedance Z_{th} (Fig. 122-right). The Thevenin-equivalent voltage V_{th} is that appearing across terminals "a" and "b" of the original network when these terminals are open-circuited; the Thevenin-equivalent impedance Z_{th} is that viewed from the same terminals when all voltage sources within the network are set equal to zero [86].

For application to the induction-motor equivalent circuit, points "a" and "b" are taken as those so designated in Figure 122 left and right. The equivalent circuit then assumes the forms given in Figure 123 where Thevenin's theorem has been used to transform the network to the left of points a and b into an equivalent voltage source V_{1th} in series with an equivalent impedance $Z_{1th} = R_{1th} + jX_{1th}$ [86].

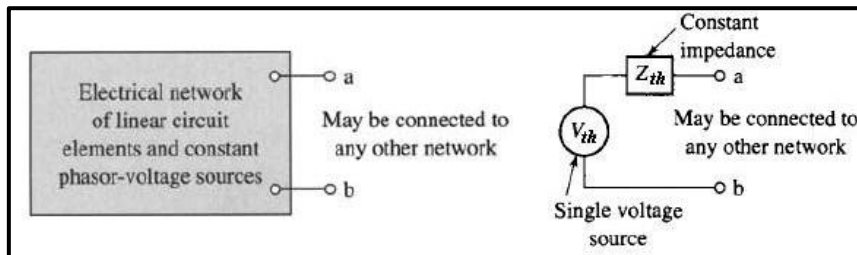


Figure 122: General linear network and (left) and its equivalent at terminals "ab" by Thevenin's theorem. (Source: A.E. Fitzgerald et al. [86])

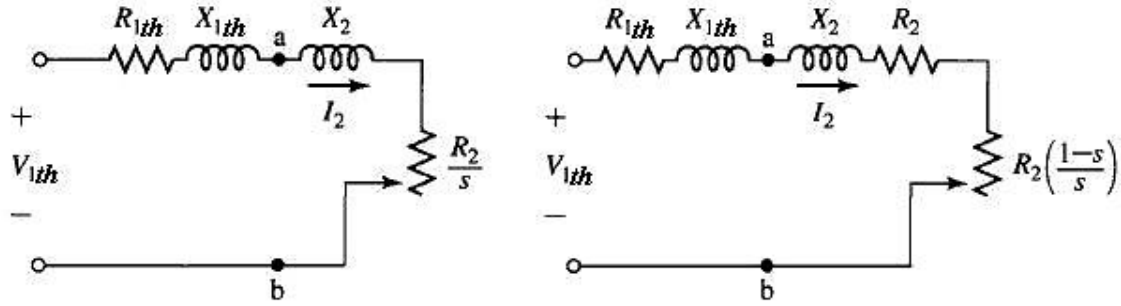


Figure 123: IEEE recommended per-phase equivalent circuit of an AC induction motor simplified by Thevenin's theorem corresponding to Figure 120 (Source: A.E. Fitzgerald et al. [86])

According to Thevenin's theorem, the equivalent source voltage V_{1th} is the voltage that would appear across terminals “a” and “b” of Figure 120 with the rotor circuits removed. The result is a simple voltage divider and thus [86]:

$$V_{1th} = V_1 \cdot \left(\frac{jX_m}{R_1 + j(X_1 + X_m)} \right) \quad (3.26)$$

with a magnitude of (*ratio of magnitudes*):

$$V_{1th} = V_1 \cdot \left(\frac{X_m}{\sqrt{R_1^2 + (X_1 + X_m)^2}} \right) \quad (3.27)$$

For most induction motors, *negligible error results from neglecting the stator resistance* in Equation 3.26. The Thevenin equivalent stator impedance Z_{1th} is the impedance between terminals “a” and “b” of Figure 121 viewed toward the source with the source voltage set equal to zero (or equivalently replaced by a short circuit) and therefore is [86]:

$$Z_{1th} = R_{1th} + jX_{1th} = \{(R_1 + jX_1) \text{ in parallel with } jX_m\} \quad (3.28)$$

or

$$Z_{1th} = \frac{jX_m \cdot (R_1 + jX_1)}{R_1 + j(X_1 + X_m)} \quad (3.29)$$

thus:

$$R_{1th} = \frac{X_m^2 R_1}{R_1^2 + (X_1 + X_m)^2} \quad (3.30)$$

$$X_{1th} = \frac{X_m^2 X_1 + X_m R_1^2 + X_1^2 X_m}{R_1^2 + (X_1 + X_m)^2} \quad (3.31)$$

Note that the **iron-loss resistance R_c has been neglected in the derivation** of Equations 3.26 through 3.29. Although this is a very commonly used approximation, its effect can be readily incorporated in the derivations presented here by replacing the magnetizing reactance $j \cdot X_m$ by the magnetizing impedance Z_m , equal to the parallel combination of the iron-loss resistance R_c and the magnetizing reactance $j \cdot X_m$ [86]. From the Thevenin-equivalent circuit, as shown in Figure 123, [86]:

$$I_2 = \frac{V_{1th}}{Z_{1th} + Z_2} = \frac{V_{1th}}{Z_{1th} + jX_2 + \frac{R_2}{s}} = \frac{V_{1th}}{\left(R_{1th} + \frac{R_2}{s}\right) + j(X_2 + X_{1th})} \quad (3.32)$$

with a magnitude of (*ratio of magnitudes*):

$$I_2 = \frac{V_{1th}}{\sqrt{\left(R_{1th} + \frac{R_2}{s}\right)^2 + (X_2 + X_{1th})^2}} \quad (3.33)$$

and thus from the torque expression (Equation 3.23):

$$T_e = \left(\frac{P}{2}\right) \cdot \frac{n_{ph} \cdot I_2^2 \cdot \left(\frac{R_2}{s}\right)}{\omega_s} \Leftrightarrow \quad (3.34)$$

$$T_e = n_{ph} \cdot \left(\frac{P}{2}\right) \cdot \left(\frac{R_2}{s}\right) \frac{1}{\omega_s} \frac{V_{1th}^2}{\left(R_{1th} + \frac{R_2}{s}\right)^2 + (X_2 + X_{1th})^2}$$

where ω_s is the synchronous angular velocity as given by Equation 2.12.1. The general shape of the torque-speed or torque-slip curve with the motor connected to a constant-voltage, constant-frequency source has already shown in Figures 56 and 57 (motoring mode).

An expression for the maximum electromechanical torque, or breakdown torque, $T_{e(max)}$, indicated in Figure 58, can be obtained readily from circuit considerations. As can be seen from Equation 3.23, the electromechanical torque is a maximum when the power delivered to R_2/s in Figure 123 (left) is a maximum [86]. However, a mathematical approach is always a standard way of proof.

For maximum torque, $T_{e(max)}$ [112]:

$$dT_e / ds = 0 \quad (3.35)$$

from which the slip at maximum torque will be [112]:

$$s_{T_{e(max)}} = \frac{R_2}{\sqrt{R_{1th}^2 + (X_2 + X_{th})^2}} \quad (3.36)$$

and the corresponding torque is, from Equation 3.34:

$$T_{e(max)} = n_{ph} \cdot \left(\frac{P}{2}\right) \cdot \frac{0.5}{\omega_s} \left(\frac{V_{1th}^2}{R_{1th} + \sqrt{R_{1th}^2 + (X_2 + X_{th})^2}} \right) \quad (3.37)$$

Moreover, at the starting torque or locked rotor torque, $T_{e(st)}$, the *slip is equal of 1*:

$$s=1 \quad (3.38)$$

and the corresponding torque is, from Equation 3.34:

$$T_{st} = n_{ph} \cdot \left(\frac{P}{2}\right) \cdot \frac{R_2}{\omega_s} \left(\frac{V_{1th}^2}{(R_{1th} + R_2)^2 + (X_2 + X_{1th})^2} \right) \quad (3.39)$$

If the stator resistance is small, so R_{1th} may be neglected and thus [112]:

$$s_{T_{e(max)}} \simeq \frac{R_2}{(X_2 + X_{th})} \quad (3.40)$$

and

$$T_{e(max)} \simeq n_{ph} \left(\frac{P}{2} \right) \cdot \frac{0.5}{\omega_s} \frac{V_{1th}^2}{(X_2 + X_{th})} \quad (3.41)$$

and

$$T_e = n_{ph} \cdot \left(\frac{P}{2} \right) \cdot \left(\frac{R_2}{s} \right) \frac{1}{\omega_s} \frac{V_{1th}^2}{\left(\frac{R_2}{s} \right)^2 + (X_2 + X_{th})^2} \quad (3.42)$$

Therefore, the ratio between the maximum torque and the torque developed at any speed is given by [112]:

$$\frac{T_{e(max)}}{T_e} = \frac{s_{T_{e(max)}}^2 + s^2}{2 \cdot s_{T_{e(max)}} \cdot s} \quad (3.43)$$

3.1.4 Equivalent Circuit under Variable-Frequency Conditions

More and more induction motors now operate from variable-frequency inverters, the frequency (and voltage) being varied not only to *control steady-state speed*, but also to profile torque during acceleration and deceleration. Two questions that we might therefore ask are (a) *does the equivalent circuit remains valid for other than the “rated” Hz operation*; and (b) if so, do *the approximations that have been developed remain useful*? [84].

The answer to question (a) is that the form of the equivalent circuit is independent of the supply frequency. This is to be expected because we are simply representing in circuit form the linking of the electric and magnetic circuits that together constitute the motor, and these physical properties do not depend on the excitation frequency [84].

The answer to the question of the validity of approximations is less straightforward, but broadly speaking all that has so far been said is applicable except at low frequencies, say below about 10 Hz for 50 or 60 Hz motors (as the frequency approaches zero, the volt-drop due to stator resistance becomes important) [84].

3.2 Speed and Torque Control of Induction Motors/Generators

In this section various methods for the control of induction machines are presented. We will present scalar control techniques with conventional methods or using variable frequency drives as well as vector control techniques using variable frequency drives also.

The *scalar control methods are limited to steady-state operation*. The steady-state picture is quite adequate for a wide variety of induction machine applications. However, it should be mentioned that system dynamics can play a critical role in some applications, with concerns ranging from speed of response to overall system stability. For this reason, *vector control techniques were developed for dynamic control of the system in transient state operation as well*.

Finally, intelligent methods represent recent research trends of induction motor control and the sensorless method are mentioned nominally.

3.2.1 Scalar Control

Scalar control of induction motors and generators means *control of only the magnitude and/or frequency of their voltage or current to achieve suitable torque and speed with an impressed slip*. Scalar control can be easily understood based on the fundamental principles of induction-machine steady-state modeling. Scalar control *disregards the coupling effect on the motor/generator; that is, the voltage will be set to control the flux and the frequency in order to control the torque*. However, flux and torque are functions of frequency and voltage, respectively. *Scalar control is different from vector control in which both magnitude and phase alignment of the vector variables are directly controlled*. Scalar control drives give an inferior performance, but they are not difficult to implement and are very popular in machine drives for pumping, several industrial applications, and large megawatt systems [111].

The main constraint on the use of a scalar control method for induction motors and generators is related to the transient response. If shaft torque and speed are bandwidth-limited and torque varies slowly (within hundreds of milliseconds up to the order of almost a second), scalar control may be a good control approach. *Ocean current power and wind power applications have slower mechanical dynamics for the scalar control method. Therefore, it seems that scalar control is a good control approach for renewable energy applications* [111].

3.2.1.1 CATEGORY I - Conventional Methods

Conventional methods are methods where the *variable frequency drives are not used*. The speed control is achieved either by *changing the operating slip* or by *changing the synchronous speed* of the machine [86, 113].

Modified Operating Slip

Changing the operating slip is a major category that involves changing the torque-speed characteristic curve by *modifying the rotor resistance or the supply voltage while the system frequency remains constant*. Thus, by altering the Torque-Speed characteristic curve in combination with the Load curve results to an operation point with a different slip [86, 113]. Using Equations 2.12.2 and 2.14, it can be written:

$$\omega_r = 120 \cdot (f_s/P) \cdot (1-s) \quad (3.44)$$

a) *Change of Rotor Resistance while frequency is constant (Wound-rotor type only)*

The speed of a wound rotor induction machine can be controlled by *connecting external resistance in the rotor circuit through the slip rings by adding a three-phase resistance bank*. The main drawback of this method is that efficiency is reduced at lower speeds due to additional losses in resistors connected in the rotor circuit. In practice, this method is used for applications with short periods of lower-speed operation (such as cranes) where they need a large starting torque and large pull-out torque at small values of slip [86, 113].

The internal torque developed by an induction machine is dependent to the rotor resistance R_2 as shown by the Equation 3.34 in which for a specific design all the variables are constant except for the slip s and the resistance R_2 . So from Equation 3.34:

$$T_e = f\left(\frac{R_2}{s}\right) \quad (3.45)$$

Notice from Equations 3.36 and 3.37 that the *slip at maximum torque is directly proportional to the rotor resistance R_2 but the value of the maximum torque is independent of R_2* . Thus, when R_2 is increased by inserting external resistance in the rotor of a wound rotor motor, the maximum electromechanical torque is unaffected but the speed/slip at which it occurs can be directly controlled. This result can also be seen by observing that the electromechanical torque expression of Equation 6.33 is a function of the ratio R_2/s . Thus, the torque is unchanged as long as the ratio R_2/s remains constant. The torque-speed characteristic curves for three external resistances are shown in Figure 124. Note that at $s=0$, $T_e = 0$ so that all Torque-Speed characteristic curves end at the synchronous speed.

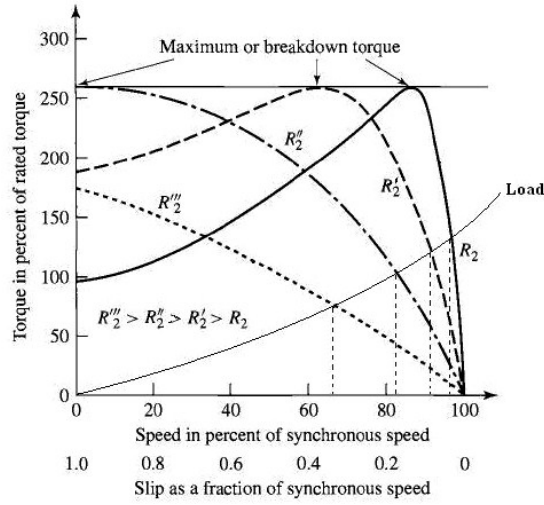


Figure 124: Induction-motor torque-slip curves showing effect of changing rotor-circuit resistance (Source: A. E. Fitzgerald et al. [86])

b) Change of Supply Voltage while frequency is constant

The supply voltage V_1 can be varying by using a **three-phase auto-transformer**. Moreover, the internal torque developed by an induction machine is proportional to the square of the voltage applied to its primary terminals, as shown by the Equation 3.34 in which for a specific design all the variables are constant except for the slip s and the voltage V_{1th} [86]. So, from Equation 3.34:

$$T_e = f(s) \cdot V_{1th}^2 \quad (3.46)$$

Therefore, the electromagnetic torque, T_e , is very *sensitive to changes in value of the supply voltage*. As the supply voltage is decreased, the value of maximum torque also decreases (Equation 3.37) as well as the starting torque (Equation 3.39). For example a drop of 10% in supply voltage will decrease the starting torque by about 20%. However, the maximum torque still occurs at the same slip as in the beginning (Equation 3.36) as shown in Figure 125 [112].

This method makes the induction machine highly underutilized because **large change in supply voltage will result in large change in flux density and thus altering the magnetic condition of the machine**. For this reason, it has very limited applications and it is generally used for small squirrel-cage motors where cost is an important criterion and efficiency is not (for example a fan). Moreover, this method has rather limited range of speed control because a large change in supply voltage is

required for relatively small change in speed [86]. Note that the *NEMA class D motor* will allow speed variation over a wider speed range as clearly shown in Figure 125 [112].

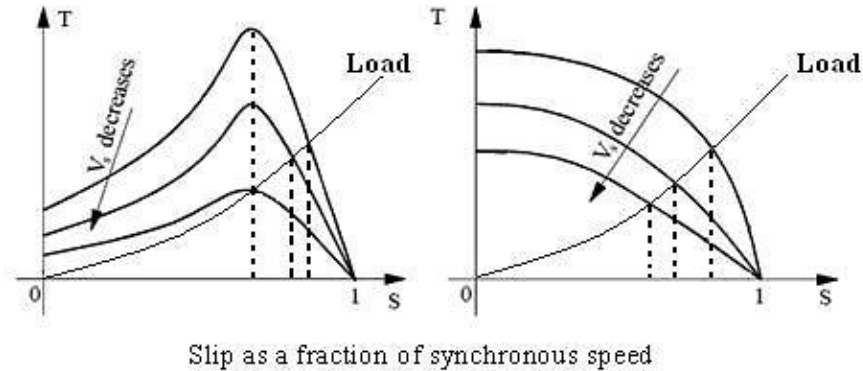


Figure 125: Torque-Speed characteristic curve for different values of supply voltage V_1 for a NEMA Class A (left) and NEMA Class D (right) (Source: Author and [112])

Modified Synchronous Speed

The speed of the rotating magnetic field created by the stator is called synchronous speed as already mentioned in Chapter 2. The synchronous speed has already been given by Equation 2.12.2 as shown again below:

$$\omega_s \text{ rpm} = \frac{120 \cdot f_s}{P} \quad (\text{Equation 2.12.2})$$

So by changing the *supply/system frequency*, f_s , or the *number of poles*, P , the synchronous speed is changing also [86, 113].

a) Change of Stator Poles number (Squirrel cage type only)

The number of stator poles can be changed by i) *multiple stator windings*, ii) *method of consequent poles* and iii) *pole-amplitude modulation or PAM* [113]. The above methods are ***suitable for squirrel cage machines only because the squirrel cage rotor automatically develops number of poles equal to the poles of stator winding*** [86]. All of the above methods are rarely used anymore with the only exception when it is absolutely necessary and in specific applications. In Figure 126, there are two different cases, one for the same torque and one for the same power, while the number of stator poles is changed by the method of multiple stator windings [112].

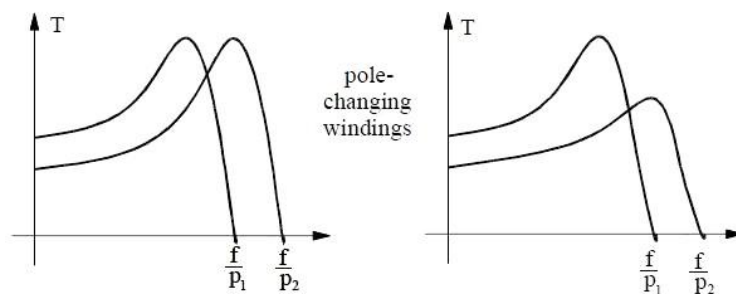


Figure 126: Pole changing Torque-Speed curves for constant torque (left) and constant power (right) (Source: I. Boldea and S.A. Nasar [112])

b) *Change of Supply Frequency while voltage is constant*

This method is not widely used. It is used where, *the induction motor is supplied by a generator so that the supply frequency can be easily change by changing the speed of the prime mover or using cycloconverters without phase control* [114].

The disadvantage of this method, when you use it in occasions such as with cycloconverters, is ***directly connected with the magnetic capacity of the machine's magnetic (iron) circuit which is designed to the ratio Voltage/Frequency***. Thus, if the frequency drops, the V/f ratio increases. This means that the motor needs a larger magnetic circuit otherwise it can be overloaded. This is called *saturation and it leads to a rapid increase in current draw and a corresponding large increase in temperature*. On the other hand, if the frequency increases, the V/f drops with no issued since the magnetic circuit will remain large enough but the machine may have a worse power factor [115].

3.2.1.2 **CATEGORY II - Methods using Power Electronics**

Methods using power electronics and usually variable frequency drives, ***which are types of adjustable-speed drive used in electro-mechanical drives systems to control AC motor speed and torque by varying the motor input frequency and voltage***, are very common nowadays . However, the importance of scalar control through VFDs has diminished recently because of the superior performance of the vector-controlled drives and the introduction of high-performance inverters [111].

The speed control is achieved by changing the *operating slip or by changing the synchronous speed of the machine or a combination of them*.

a) *Change of Rotor Resistance while frequency is constant (Wound-rotor type only)*

It is the same method as above (***Scalar Control/Conventional Methods/Modifying Operation Slip/a)***) but using a *three-phase diode bridge and a single variable resistor*. Thus the effective value of the external resistance can be changed by varying the on-time (also called the duty ratio) [116].

b) *Change of Supply Voltage while Frequency is constant*

It is the same method as above (***Scalar Control/Conventional Methods/Modifying Operation Slip/b)***) but using a *solid-state voltage controller such as transistors or thyristors*. The solid-state controller application is commonly used with small squirrel-cage motors driving fan loads. In large power applications an input filter is required; otherwise, large harmonic currents will flow in the supply line [116].

c) *Slip-energy Recovery System while frequency is constant (Wound-rotor type only)*

Instead of wasting rotor circuit power in an external resistance, it can be converted and returned to the mains supply though a VFD. Frequency conversion is necessary because the rotor circuit operates at slip frequency, so it cannot be connected directly to the mains [84].

This slip power can be recovered by *introducing a variable EMF source in the rotor of the induction motor and absorbing the slip power into it. By linking the EMF source to ac supply lines through a suitable power converter, the slip energy is sent back to the ac supply*. This is illustrated in Figure 127 [110]. By varying the magnitude of the EMF source in the rotor, the rotor current, torque, and slip are controlled. The rotor current is controlled and hence the rotor copper losses, and a

significant portion of the power that would have been dissipated in the rotor is absorbed by the EMF source, thereby improving the efficiency of the motor drive [109].

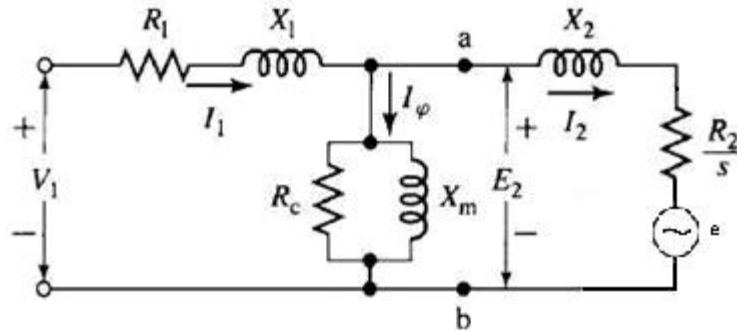


Figure 127: Per-phase equivalent circuit of an AC induction motor with an external induced EMF source in the rotor. The rotor parameters have been referred to the stator and for standstill is $s=1$ (Source: R. Krishnan [110])

More specifically, in a slip energy recovery system, the *slip frequency from the rotor is first rectified in a 3-phase diode bridge and smoothed before being returned to the mains supply via a 3-phase thyristor bridge converter operating in the inverting mode*. A transformer is usually required to match the output from the controlled bridge to the mains voltage [84].

Since the cost of both converters depends on the slip power they have to handle, this system (**which is known as the static Kramer drive**) is most often used where only a modest range of speeds (say from 80% of synchronous and above) is required, such as in large pump and compressor drives. Speed control is obtained by varying the firing angle of the controlled converter, the torque–speed curves for each firing angle being fairly steep (i.e. approximating to constant speed), thereby making closed-loop speed control relatively simple [84].

d) Constant V/f ratio

There are basically **two different ways** how to change the V/f ratio. The **direct** way is through **cycloconverters (AC-to-AC conversion)** with phase control and the **indirect** way through a **voltage source or current source inverter (AC-to-DC-to-AC conversion)** [110].

The cycloconverters are thyristors (Silicon Control Rectifier-SCR type) with phase control switching and provide an adjustable-voltage, adjustable-frequency power supply. They are capable for small range of frequency variation and for this reason are suitable for low-speed, large-power applications such as ball mills and cement kilns. For a majority of applications a wide range of frequency variation is desirable. In that case indirect frequency conversion methods are appropriate.

*The indirect frequency changer consists of a rectification (AC to DC) and an inversion (DC to AC) power conversion stage. They are broadly classified depending on the source feeding them: **voltage or current sources**. In both these sources the magnitude should be adjustable. **The output frequency becomes independent of the input supply frequency, by means of the DC link** [110].*

For a given induction motor, *the torque developed depends on the magnitude of the rotating flux density wave, and on the slip speed of the rotor (the relative velocity of the rotor with respect to the flux wave). Secondly, the strength or amplitude of the flux wave depends directly on the supply voltage to the stator windings, and inversely on the supply frequency. Thirdly, the absolute speed of the flux wave depends directly on the supply frequency. The slip for a given torque depends on the amplitude of the rotating flux wave: the higher the flux, the smaller the slip needed for a given torque. It follows that having set the desired speed of rotation of the flux wave by controlling the output*

frequency of the inverter or cycloconverter, we must also ensure that the magnitude of the flux is adjusted so that it is at its full (rated) value regardless of the speed of rotation. This is achieved, in principle, by making the output voltage from the inverter vary in the appropriate way in relation to the frequency. Given that the amplitude of the flux wave is proportional to the supply voltage and inversely proportional to the frequency, it follows that if we arrange that *the voltage supplied by the inverter/cycloconverter varies in direct proportion to the frequency, the flux wave will have a constant amplitude* and thus the air-gap flux maintain approximately constant so that avoid saturation. This simple mode of operation – where the V/f ratio is constant – was for many years the basis of the control strategy applied to most inverter-fed induction motors, and it can still be found in some commercial products [84].

To get a first-order picture of how an induction machine works at adjustable speed, consider the equivalent circuit shown in Figure 118. If the stator resistance is small, so *R_1 may be neglected* and thus:

$$V_{1th} = V_1 \cdot \left(\frac{X_m}{(X_1 + X_m)} \right) \quad (3.47)$$

$$Z_{1th} = R_{1th} + jX_{1th} = jX_{1th} \quad (3.48)$$

$$X_{1th} = \frac{X_m X_1}{X_1 + X_m} \quad (3.49)$$

and the corresponding torque is, from Equation 3.34:

$$T_{e(R_1=0)} = n_{ph} \cdot \left(\frac{P}{2} \right) \cdot \left(\frac{R_2}{s} \right) \frac{1}{\omega_s} \frac{V_{1th}^2}{\left(\frac{R_2}{s} \right)^2 + (X_2 + X_{1th})^2} \quad (3.50)$$

Assume that the *applied voltage is proportional to the frequency* and the subscript (b) represents rated-frequency values of each of the induction machine parameters [86]. So:

$$V_1 = \frac{\omega_s}{\omega_{s(b)}} \cdot V_{1(b)} \quad (3.51)$$

and thus:

$$V_{1th} = \frac{\omega_s}{\omega_{s(b)}} \cdot V_{1th(b)} \quad (3.52)$$

and

$$(X_{1th} + X_2) = \frac{\omega_s}{\omega_{s(b)}} \cdot (X_{1th} + X_2)_{(b)} \quad (3.53)$$

$$s = \frac{\Delta\omega}{\omega_s} \quad (3.54)$$

where $\Delta\omega = \omega_s - \omega_r$.

Substitution of Equations 3.51÷3.54 into Equation 3.50 gives:

$$T_e = n_{ph} \cdot \left(\frac{P}{2} \right) \cdot \frac{\left(\frac{R_2}{\Delta\omega} \right) V_{1th(b)}^2}{\left(\omega_{s(b)} \cdot \frac{R_2}{\Delta\omega} \right)^2 + (X_{1th} + X_2)_{(b)}^2} \quad (3.55)$$

Equation 3.55 shows the general trend in which the frequency dependence of the torque-speed characteristic of an induction motor appears only in the term $R_2/\Delta\omega$. Thus, under the assumption that R_1 is negligible, as the electrical supply frequency to an induction machine is changed, ***the shape of the speed-torque curve as a function of $\Delta\omega = \omega_s - \omega_r$ will remain unchanged. As a result, the torque-speed characteristic will simply shift along the speed axis as ω_r is varied*** [86]. A set of such curves is shown in Figure 128 [110]. It is obvious that by varying the voltage and frequency by the same ratio, flux and hence, the pull-out torque can be kept constant throughout the speed range. Note that as the electrical frequency (and hence the synchronous speed) is decreased, a given value of $\Delta\omega$ corresponds to a larger slip. Thus, for example, if the peak torque of a 4-pole motor driven at 60 Hz occurs at 1638 rpm, corresponding to a slip of 9%, when driven at 30 Hz, the peak torque will occur at 738 rpm, corresponding to a slip of 18% [86].

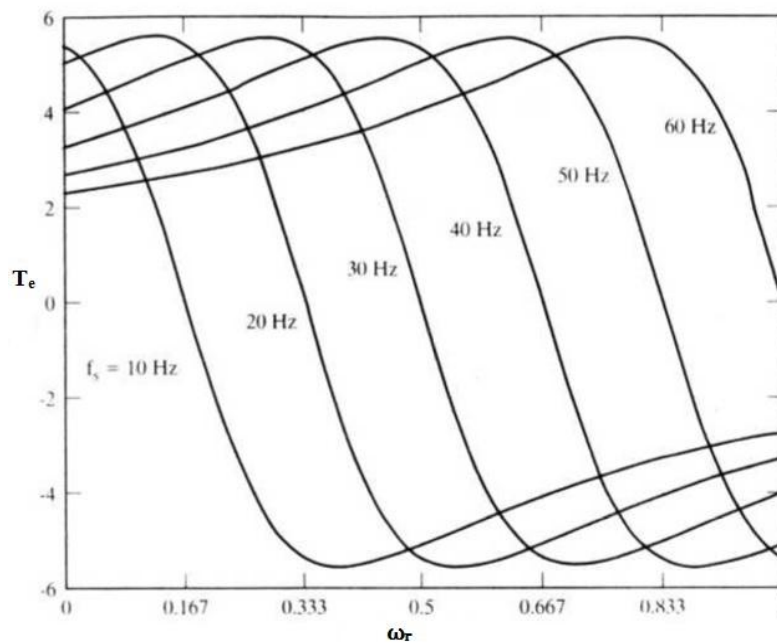


Figure 128: Typical torque-speed curves (normalized in 2 quadrants) for constant V/f ratio of an induction machine assuming R_1 is zero (Source: R. Krishnan [110])

In practice, the effects of R_1 may not be fully negligible, especially for large values of slip. If this is the case, the shape of the speed-torque curves will vary somewhat with the applied electrical frequency [86]. Figure 129 shows a typical family of curves for this case [86].

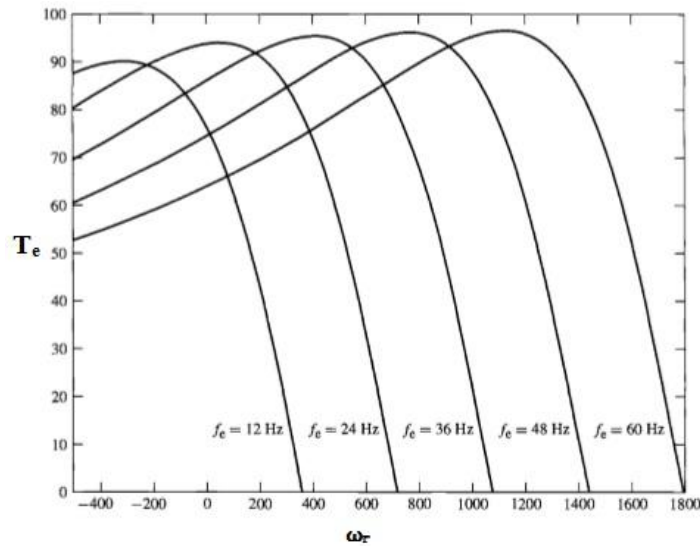


Figure 129: Typical torque-speed curves for constant V/f ratio of a 4-pole induction machine assuming R_1 is not zero (Source: A. E. Fitzgerald et al. [86])

From Figure 129, it can be noted that *the pull-out torque and the torque stiffness (i.e. the slope of the torque–speed curve in the normal operating region) is more or less the same at all points below base speed, except at low frequencies where the voltage drop over the stator resistance R_1 , becomes very significant as the applied voltage is reduced. A simple V/f control system would therefore suffer from significantly reduced flux and hence less torque at low speed* [84].

The low-frequency performance can be improved *by increasing the V/f ratio at low frequencies in order to restore full flux, a technique which is referred to as ‘voltage boost’*. In modern drive control schemes with vector control the voltage is automatically boosted from the linear V/f characteristic that the approximate theory leads us to expect. A typical set of torque–speed curves for a drive with the improved low-speed torque characteristics obtained with voltage boost is shown in Figure 130 [84].

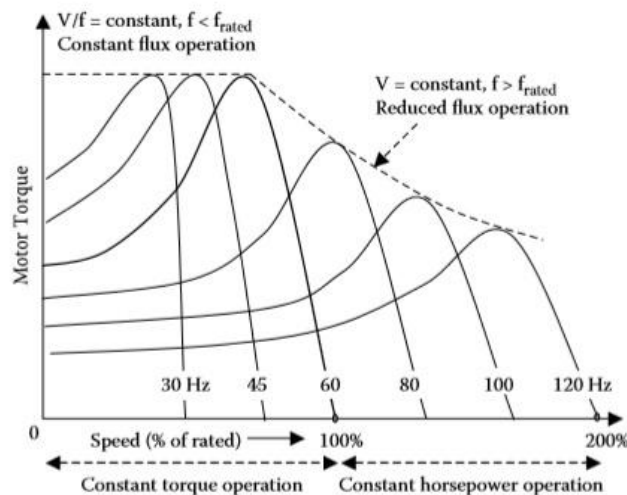


Figure 130: Typical torque-speed curves for an induction machine with constant flux up to 45Hz (rated speed) and constant voltage at higher frequencies (Source: A. Hughes and B. Drury [84])

The characteristics in Figure 130 have an obvious appeal because they indicate that the motor is capable of producing practically the same maximum torque at all speeds from zero up to the rated (45 Hz) speed. *This region of the characteristics is known as the ‘constant torque’ region, which means that for frequencies up to rated speed, the maximum possible torque which the motor can deliver is independent of the set speed.* Beyond the base frequency, the flux (“V/f ratio”) reduces because V remains constant. The amplitude of the flux wave therefore reduces inversely with the frequency. Under constant flux operation, the maximum torque always occurs at the same absolute value of slip, but in the constant-voltage region the peak torque reduces inversely with the square of the frequency and the torque–speed curve becomes less steep, as shown in Figure 130 [84].

A primary concern in this method is to limit the currents to a safe value as far as the main switching devices and the machine are concerned. The current limit will be typically set to the rated current of the motor, and the inverter control circuits will be arranged so that no matter what the user does the output current cannot exceed this safe (thermal) value, other than for clearly defined overload (e.g. 120% for 60 seconds) for which the motor and inverter will have been specified and rated. (For some applications involving a large number of starts and stops, the motor and drive may be specially designed for the specific duty.) [84]

In modern control schemes (such as vector control) it is possible to have independent control of the flux- and torque-producing components of the current, and in this way the current limit imposes an upper limit on the permissible torque. In the region below rated speed, this will normally correspond to the rated torque of the motor, which is typically about half the pull-out torque, as indicated by the shaded region in Figure 131. *Note that this is usually a thermal limit imposed by the motor design.* Above rated speed, it is not possible to increase the voltage and so the flux reduces inversely with the frequency. Since the stator (and therefore rotor) currents are again thermally limited (as we saw in the constant torque region), the maximum permissible torque also reduces inversely with the speed, as shown in Figure 130. ***This region is consequently known as the ‘constant power’ region.*** The voltage drop over the stator leakage inductance increases with frequency. At typically twice base speed the extent of this voltage drop reduces the available voltage to such an extent that it is no longer possible for the motor to provide constant power operation, as indicated by the cross-hatched area in Figure 131 [84].

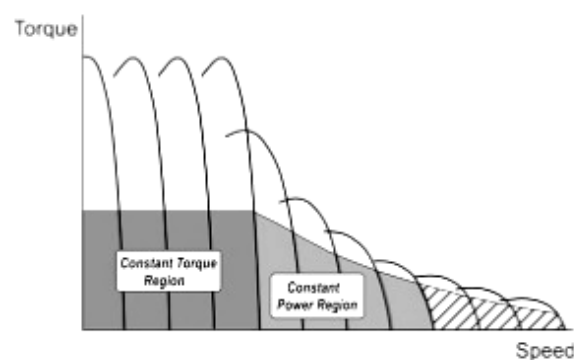


Figure 131: Typical torque-speed curves for an induction machine under V/f control in Constant Torque, Constant Power and in High-Speed motoring regions (Source: A. Hughes and B. Drury [84])

Finally, a four quadrant capability of an induction machine under V/f control in different regions is shown in Figure 132 [84].

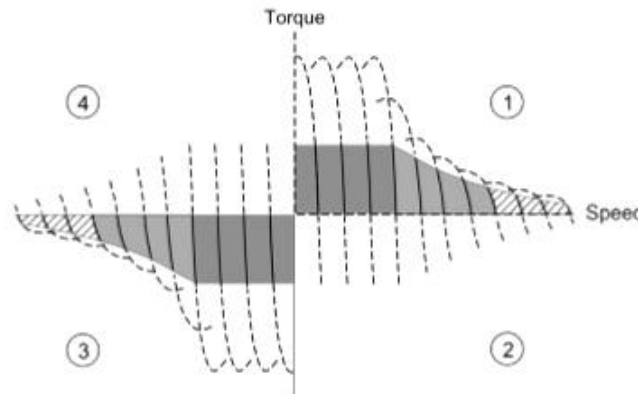


Figure 132: Operating regions in all four quadrants of the torque-speed plane of an induction machine under V/f control
(Source: A. Hughes and B. Drury [84])

e) Alternative ways of V/f ratio control

There are some different control strategies about how can you implement the control of V/f ratio [110]. *The basics of each strategy depend on how you express the steady state equation for electromagnetic torque.* More specifically, in order to explore the possibilities for each strategy it is necessary to express the electromagnetic torque in terms of different variables (for example in terms of stator currents or in terms of fluxes).

In these strategies, the V/f ratio is constant not via the directly control of voltage or frequency but through other *control variables such as stator current and air-gap flux* [110]. However, the topology of the variable frequency drives is the same as above through the AC-DC-AC conversion. The name of the two alternative strategies is shown below [110]:

- Constant Slip-Speed control (also known as *Constant Slip and Current control*)
- Constant Air-Gap Flux control

It is important to note that *in constant slip-speed control strategy, an independent torque control is realized by the current amplitude control.* Moreover, keeping a constant slip level, a torque control is occurred by voltage or current amplitude, [117] as it is obvious from Equation 3.34.

Based on the market evidence up to present, the above control strategies of V/f ratio are not in such a general use as the direct control of V/f ratio [118].

3.2.2 Vector Control

The various scalar control methods for the control of induction machine have provided good steady state results but poor dynamic response. From the traces of the dynamic responses, the cause of such poor dynamic response is found to be *that the air gap flux linkages deviate from their set values.* The deviation is not only in magnitude but also in phase. The ***variations in the flux linkages have to be controlled by the magnitude and the frequency of the stator and rotor phase currents and their instantaneous phases.*** The scalar control methods have utilized the stator phase current

magnitude and frequency and not their phases. This resulted in the deviation of the phase and magnitudes of the air-gap flux linkages from their set values [110].

The oscillations in the air gap flux linkages result in oscillation in electromagnetic torque and reflect as speed oscillations. This is undesirable in many high-performance applications such as robotic actuators etc. Further, air gap flux variations result in large excursions of stator currents requiring large peak VFDs ratings to meet the dynamics and thus increase of the VFDs cost [110].

Vector control provides the solution to the poor dynamic response of various scalar control methods. ***It is the foundation of modern high-performance drives and also known as decoupling, orthogonal, or transvector control.*** In vector control both magnitude and phase (angle) alignment of the vector variables is directly controlled [111].

3.2.2.1 CATEGORY I – Fully Commercialized

All the vector control methods are using power electronics and especially variable frequency drives. In a general view, there are two categories of it which is the *indirect torque control or field/flux oriented control (ITC or FOC)* and *direct torque control (DTC)* [118]. As the names imply, the major difference is in the way you control the electromagnetic torque (direct or indirect) and it is not related with the speed control.

a) Indirect Torque Control or Field/Flux Oriented Control (FOC)

The principles of indirect torque control originated in West Germany in the work of Hasse and Blaschke at the technical universities of Darmstadt and Braunschweig and in the laboratories of Siemens AG respectively [111].

In the indirect torque control method, the phase (angle), frequency and magnitude control of the ***stator currents*** and hence of the flux phasor is occurred by inverter control. The control is achieved in field coordinates (*hence the name of this control strategy – field/flux oriented control*) and related to the phasor control of the flux linkages [110]. There are a number of permutations of this control—***stator flux oriented, rotor flux oriented, and air-gap (magnetizing) flux oriented***, and of these types there are ***direct*** (by Blaschke [119]) and ***indirect*** (by Hasse [120]) methods of implementation [109, 110, 111, 112, 118, 121, 122].

The direct or indirect method based on how the instantaneous position of the machine flux (feedback signal –rotor, stator or magnetizing flux angle) can be finding. *On the other hand, the type of the flux oriented control is associated with which one the instantaneous magnitude and position flux vector is calculated* (stator, rotor or magnetizing) by imposing alignment of the machine stator current vector to obtain decoupled control [111].

b) Direct Torque Control (DTC)

There are some alternatives for the classical vector control - field/flux oriented control (FOC). These new strategies for the torque control of induction motor was presented by I. Takahashi and T. Noguchi as *Direct Torque Control (DTC)*, [123], and by M. Depenbrock as *Direct Self Control (DSC)*, [124, 125, 126]. *The only difference between DTC and DSC is the shape of the path along which the flux vector is controlled, the former path being quasi-circular whereas the latter is hexagonal* such that the switching frequency of DTC is higher than DSC. DTC is accordingly aimed at low-to-mid power drives whereas DSC is usually used for higher power drives [127].

The direct torque control (**DTC/DSC**), which ABB developed the first commercial product, is set to replace traditional PWM inverters of the open- and closed-loop type in the near future. Direct torque control describes the way in which the control of torque and speed are directly based on the electromagnetic state of the motor, similar to a DC motor, but contrary to the way in which traditional PWM drives use input frequency and voltage. DTC is the first technology to control the “real” motor control variables of torque and flux [128].

More specifically, it is based on the theory developed by German doctor Blaschke and his colleague Depenbrock *where two different loops, corresponding to the magnitudes of the stator flux and torque, directly control the switching of the converter. **The main advantage is because torque and flux are motor parameters that are being directly controlled***; there is no need for a modulator, as used in PWM converters, to control the frequency and voltage. This, in effect, cuts out the middle man and dramatically speeds up the response of the drive to changes in required torque. DTC also provides precise torque control without the need for a feedback device [128]. Although DTC boasts a lot of successful applications in drives, its use for induction generators is not yet fully prove. Another strategy of DTC is the *Space Vector Modulation (DTC-SVM)* schemes which are proposed in order to improve the classical DTC. The DTC-SVM strategies operate at a constant switching frequency. In the control structures, *space vector modulation (SVM) algorithm* is used. The type of DTC-SVM strategy depends on the applied flux and torque control algorithm. Basically, the controllers calculate the required stator voltage vector and then it is realized by space vector modulation technique [129].

3.2.2.2 CATEGORY II – Not Fully Commercialized

Some types of vector control methods have not found their way to practical adjustable speed drives. However, they represent research trends of induction machine control for almost two decades [130].

The first method, known as *Feedback Linearization Control (FLC)*, introduces a new nonlinear transformation of the IM state variables, so that in the new coordinates, the speed and rotor flux amplitude are decoupled by feedback [131, 132].

The second method which based on the variation theory and energy shaping, is called *Passivity Based Control (PBC)*. In this case the induction motor is described in terms of the Euler-Lagrange equations expressed in generalized coordinates [133].

3.2.3 Sensorless Control

There is intensive research worldwide devoted to sensorless methods (using mainly vector control techniques). *Motor drives without a speed or position sensor have received much research attention in recent years, especially for induction machines [118]. **Such techniques typically measure stator quantities, usually current, directly via existing transducers normally present in the inverter and voltage, although not often with a direct measurement.*** Despite much effort and progress, operation at very low speed is still problematic. This is mainly because a standard set of tests or benchmarks has not been agreed [118].

3.2.4 Intelligent Control

Despite the great efforts devoted to induction motor control, many of the theoretical results cannot be directly applied to practical systems. The difficulties that arise in induction motor control

are complex computations, model nonlinearity, and uncertainties in machine parameters. Recently, intelligent techniques are introduced in order to overcome these difficulties. *Intelligent control methodology uses human motivated techniques and procedures (for example, forms of knowledge representation or decision making) for system control.* Intelligence is defined as the ability to comprehend, reason, and learn. The definition of intelligent control from Astrom and McAvoy has been used widely [118, 134]:

“An intelligent control system has the ability to comprehend, reason, and learn about processes, disturbances and operating conditions in order to optimize the performance of the process under consideration”.

Intelligent control techniques are generally classified as [118]:

- 1) Expert System
- 2) Fuzzy-Logic
- 3) Neural-Network
- 4) Genetic Algorithm

Intelligent induction motor control thus refers to the control of an induction motor drive using the above artificial intelligence techniques. The applications of expert system, fuzzy-logic, neural-network, and genetic algorithm in induction motor drive system have been proposed in the literature [118]. All the above mentioned intelligent-based algorithm, represent recent research trends of induction motor control, required further investigation and development and they have found in very few practical applications (only with fuzzy-logic technique) [118].

3.3 Voltage Source Inverter (VSI) with Pulse Width Modulation (PWM) Technique (AC-DC-AC)

Understanding the basic principles behind VSI operation requires understanding the three basic sections of the VFD: the rectifier, DC bus, and inverter, [135], as you can see in Figure 133 [84].

Rectifier: One of the three primary sections of VSI's main power circuit and first in terms of power flow. Its function is to change 3-phase AC into DC. The 3-phase AC voltage from an electric energy source goes into the rectifier section which is consist of a group of diodes, silicon controlled rectifiers (SCR) or insulated gate bipolar transistors (IGBTs) connected in a full wave bridge configuration. For example if $240\text{ V}_{\text{ph(RMS)}}$ is coming in, 324 V_{DC} is generated.

Intermediate Circuit (DC Link/DC Bus): The second primary sections of VSI's main power circuit. Using a large bank of capacitors and DC reactors the rippling DC voltage becomes more stable.

Inverter: The third and final primary sections of VSI's main power circuit. The Inverter consist of IGBTs which take the voltage from the DC Bus and using Pulse Width Modulation (PWM) technique, send a signal which appears to the induction machine as an AC signal.

Sinusoidal Pulse Width Modulation (SPWM): A VSI control scheme in which a constant DC voltage is used to reconstruct a pseudo AC voltage waveform using a set of six power switches, usually IGBTs (for three-phase), varying the width of the fixed-amplitude pulses controls effective voltage. This pulse width modulation scheme works because the induction machine is a large inductor that does not allow current to pulse like the voltage. Sinusoidal pulse width modulation (SPWM) is widely used in power electronics to digitize the power so that a sequence of voltage pulses can be generated by the on and off of the power switches. The PWM inverter has been the main choice in power electronic for decades, because of its circuit simplicity and rugged control scheme [136]. Sinusoidal Pulse Width Modulation switching technique is commonly used in industrial applications or solar electric vehicle applications [137].

Harmonic Attenuation by a filter: The last and very important section of VSI. The AC output voltage waveform of the inverter composed of discrete values and thus the filter after the inverter should be inductive at the harmonic frequencies in order to produce a smooth current waveform [138]. *Harmonic attenuation can be achieved by passive filters.* There are different types of filtering circuits such as RC & LC filters which are the most used passive filters (R: resistor, C: capacitor and L: inductor). They are divided into 1st order, 2nd order & 3rd order according to the combination of the passive components. L or C is the first order filter, LC is the second order filter and LCL is the third order filter [139, 140].

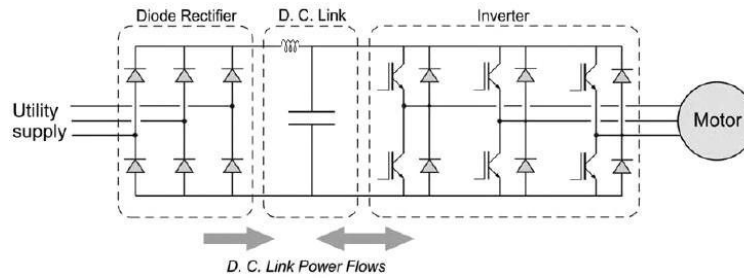


Figure 133: Circuit diagram for a Pulse Width Modulated (PWM) Voltage Source Inverter (VSI)
(Source: A. Hughes and B. Drury [84])

3.3.1 Three-Phase Full Wave Rectifier with Diodes

The *line commutated three phase, six-pulse, full-wave rectifier with diodes* is shown in Figure 134 (Author and [141]). The supply three voltage (A, B and C) system specified by the below voltages:

$$V_{A(s)} = V_{ph(s)} \sin(2\pi f t + 0) \quad (3.56.1)$$

$$V_{B(s)} = V_{ph(s)} \sin(2\pi f t - 2\pi/3) \quad (3.56.1)$$

$$V_{C(s)} = V_{ph(s)} \sin(2\pi f t - 4\pi/3) \quad (3.56.3)$$

where $V_{ph(s)}$ is the amplitude of supply phase voltage, f is the supply frequency and t is time. The amplitude of supply phase voltage is given below [142]:

$$V_{ph(s)} = \sqrt{2} \cdot V_{ph(s)-(rms)} = (\sqrt{2}/\sqrt{3}) V_{L(s)-(rms)} = V_{L(s)} / \sqrt{3} \quad (3.57)$$

where $V_{L(s)}$ is the amplitude of line-to-line supply voltage, $V_{ph(s)-(rms)}$ is the RMS value of supply phase voltage and $V_{L(s)-(rms)}$ is the RMS value of line-to-line supply voltage.

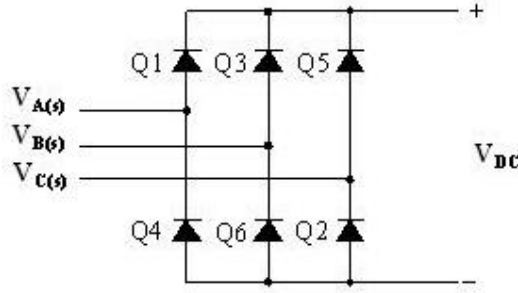


Figure 134: Circuit diagram of three-phase full-wave bridge rectifier (Q_n : Diode n , $n=1:6$) (Source: Author and [141])

The average output voltage of rectifier with diodes, the DC voltage, is [143]:

$$V_{DC} = (3\sqrt{2}/\pi) \cdot V_{L(s)-(rms)} = (3/\pi) \cdot V_{L(s)} = 0.9549 \cdot V_{L(s)} \quad (3.58)$$

The DC voltage, V_{DC} , has an AC ripple which is given by the following equation [143]:

$$V_{ripple} = 0.0408 \cdot V_{L(s)} \quad (3.59)$$

and the *Voltage Ripple Factor (VRF)* is given from the following ratio [143]:

$$VRF = V_{ripple} / V_{DC} \quad (3.60)$$

3.3.2 Intermediate Circuit (DC Link)

The output of a full-wave rectifier circuit is not pure DC but it contains fluctuations (or) ripple, which are undesired. To minimize the ripple content in the output, filter circuits are used. These circuits are connected between the rectifier and the inverter. Ideally, the output of the filter should be pure DC practically; the filter circuit will try to minimize the ripple at the output, as far as possible [144].

Basically, the ripple is AC, i.e., varying with time, while DC is a constant with respect to time. *Hence in order to separate DC from ripple, the filter circuit should use components such as inductance and capacitance.* Ideally, the **inductance acts as a short circuit for DC**, but it has large impedance for AC. Similarly, the **capacitor acts as open for DC** if the value of capacitance is sufficiently large enough. Hence, in a filter circuit, the inductance is always connected in series with the load, and the capacitance is connected in parallel to the load [144].

3.3.3 Three-Phase Inverter

The three phase inverter has a DC input voltage (V_{DC}) which is the voltage after the DC Link. *The inverter job is to take this DC input and to give AC output, where the magnitude and frequency can be controlled,* while this performed in the switched mode [143].

This mode consists in power semiconductor switches are controlled in an on-off fashion and only one switch can be turned on at a time, to avoid a short circuit in the dc-link. The three-phase inverter is usually modeled with six (6) pair of IGBT-Diodes as shown in Figure 135

(Author and [141]). The actual power flow in each motor phase is controlled by the duty cycle of the respective switches (the percentage of one period in which a signal is active). To obtain a suitable duty cycle for each switches technique pulse width modulation is used [129].

There are several techniques of *Pulse Width Modulation (PWM)*. The *Sinusoidal Pulse Width Modulation (SPWM)* technique has been used for controlling the inverter as it can be directly controlled the inverter output voltage and output frequency according to the sine control functions (see 3.3.5.2).

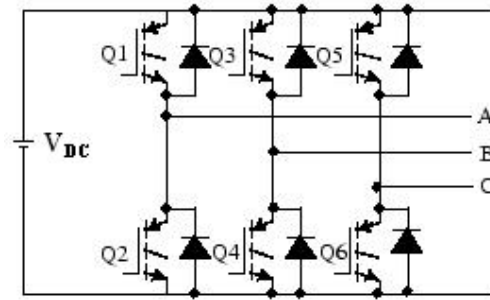


Figure 135: Switch topology of three-phase inverter
(Q_n : IGBT-Diode n , $n=1:6$) (Source: Author and [141])

In the linear region ($m \leq 1.0$), the *fundamental-frequency component in the output voltage varies linearly with the amplitude modulation ratio m* (Equation 3.63 and Appendix G) [143]. The line-to-line RMS voltage at the fundamental frequency, due to 120° phase displacement between phase voltages, can be written as [145, 146]:

$$V_{LL(rms)}^{inverter} = \frac{m \sqrt{3}}{2 \sqrt{2}} V_{DC} \quad (3.61)$$

and is called the ***amplitude of the first harmonic or fundamental amplitude***. The term *fundamental frequency* is used to describe the frequency of the sinusoidal control voltages (Equations 3.62.1÷3.62.3). For most practical loads only the fundamental component of the inverter output voltage is of interest. However the inverter output also contains significant amount of higher order harmonic voltages, which are voltages that operate at a frequency that is an integer multiple of the fundamental frequency and their amplitude are very low, that cause undesirable distortion of the output waveform [145, 147, 148].

3.3.4 Harmonic Attenuation by an LC Filter

Harmonics are the by-products of modern electronics. ***All variable frequency drives cause harmonics because of the nature of the front-end rectifier design***. Three-phase harmonics occur when incoming AC voltage is rectified by the three-phase full wave diode bridge, which charges the capacitor banks in the DC bus. The conversion from AC to DC is used to charge the capacitors to a rated potential [149].

As the motor draws the voltage from the DC bus supply, the potential on the capacitors is less than the incoming line supply voltage. Before reaching a lower regulated limit, the DC bus capacitors recharge again in the next half cycle of the voltage sine wave to the peak. This process is repeated twice in each peak of the sine wave from the process of continuously charging and discharging of the

DC bus capacitors. The capacitors draw a pulse of current only during the first and second half peak of the voltage sine wave [149].

The harmonic attenuation of the inverter AC output voltage waveform can be achieved by passive filters [145]. The passive filter is modeled as a LC circuit and the topology is shown in Figure 136 [139].

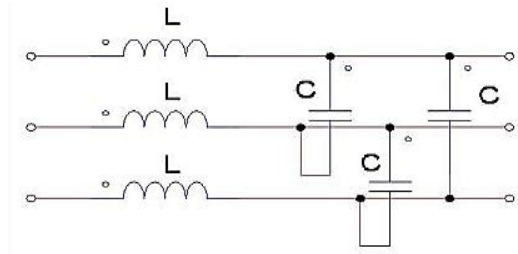


Figure 136: 2nd order three phase passive harmonic filter
Topology after inverter (Source: N.I. Raju et al. [139])

3.3.5 Pulse Width Modulation Method

Pulse width modulation is the process of modifying the width of the pulses in a pulse train in direct proportion to a small control signal; the greater the control voltage the wider the resulting pulses becomes. Many different modulation methods were proposed and development of it is still in progress [129]. The modulation method is an important part of the control structure. It should provide features like:

- wide range of linear operation,
- low content of higher harmonics in voltage and current,
- low frequency harmonics,
- operation in overmodulation,
- reduction of common mode voltage,
- minimal number of switching to decrease switching losses in the power components.

All PWM methods have specific features. However, there is not just one PWM method which satisfies all requirements in the whole operating region. Therefore, in the literature are proposed modulators, which contain from several modulation methods. The content of the higher harmonics voltage (current) and electromagnetic interference generated in the inverter fed drive depends on the modulation technique [129].

3.3.5.1 Sinusoidal Pulse Width Modulation

The most widely used method of pulse width modulation is *Sinusoidal Pulse Width Modulation*. This method is also known as the *carrier based PWM, triangulation, subharmonic, or suboscillation method* [150, 151].

3.3.5.2 Operating Principle of VSI with SPWM

The inverter is fed by a DC voltage, V_{DC} , and has three phase-legs each consisting of two transistors (IGBT) and two diodes. **With SPWM control, the switches of the inverter are controlled based on a comparison of a sinusoidal control signal and a triangular switching signal** as shown in Figure 137 [150]. In most instances the magnitude of the triangle wave is held fixed and its value is always in the range -1 to 1. The sinusoidal waves are called reference signals and they have 120° phase difference with each other. **The frequency of these sinusoidal waves is chosen based on the required inverter output frequency (for instance 50/60 Hz) and it is called the fundamental frequency.** The carrier triangular wave is usually a high frequency (in several KHz) wave in order to eliminate a large number of lower harmonics and it is called the PWM or Switching frequency, f_{sw} . The switching/logical signals, S_A , S_B , S_C , are generated by comparing the sinusoidal waves with the triangular wave. The comparator gives out a pulse when sine voltage is greater than the triangular voltage and this pulse is used to trigger the respective inverter switches [129, 145, 150, 151, 152] (see Appendix F).

The amplitude of the inverter output voltages is therefore controlled by adjusting the amplitude of the sinusoidal control voltages. The diodes provide paths for current when a transistor is gated on but cannot conduct the polarity of the load current. For example, if the load current is negative at the instant the upper transistor is gated on, the diode in parallel with the upper transistor will conduct until the load current becomes positive at which time the upper transistor will begin to conduct. By controlling the switches in this manner, the line-to-line inverter voltages at the output of the inverter are AC, with a fundamental frequency corresponding to the frequency of the sinusoidal control voltage [145, 150].

More analytically, in three-phase SPWM a triangular voltage waveform, V_T , with values from -1 up to 1 and with a frequency f_{sw} , is compared with three sinusoidal control voltages, V_a , V_b , and V_c , also called reference signals (as already stated above) or *modulating signals* and the relative levels of the waveforms are used to control the switching of the devices in each phase leg of the inverter [129, 145, 150, 151].

$$V_a = V_m \cdot \sin(2\pi \cdot f_1 \cdot t) \quad (3.62.1)$$

$$V_b = V_m \cdot \sin(2\pi \cdot f_1 \cdot t + 120) \quad (3.62.2)$$

$$V_c = V_m \cdot \sin(2\pi \cdot f_1 \cdot t + 240) \quad (3.62.3)$$

where V_m is the amplitude of the reference signal which is equal with the amplitude modulation ratio m (Equation 3.63) and f_1 is the fundamental frequency which is also called frequency of the inverter. The amplitude modulation ratio or modulation index, m , is the ratio of the peak magnitudes of the reference signal and the triangular carrier signal as shown below [129, 145, 150, 151]:

$$m = V_m / V_T \quad (3.63)$$

The modulation index m can be varied between 0 and 1 to give a linear relation between the reference and output wave (see Appendix G).

Furthermore, the inverter is composed of six switches, Q_1 through Q_6 , with each phase output connected to the middle of each inverter leg as shown in Figure 135. The output of the comparators in Figure 137 forms the control signals, S_A , S_B , S_C , for the three legs of the inverter. Two switches in each phase make up one leg and open and close in a complementary fashion. That is, when one switch is open, the other is closed and vice-versa. The output pole voltages V_{ao} , V_{bo} , and V_{co} of the inverter

switch between $-0,5m \cdot V_{DC}$ and $+0,5m \cdot V_{DC}$ voltage levels where V_{DC} is the total DC voltage [129, 150] (see Appendix F).

The peak of the sine modulating waveform is always less or equal than the peak of the triangle carrier voltage waveform (for $m \leq 1$). When the sinusoidal waveform is greater than the triangular waveform, the upper switch is turned on and the lower switch is turned off. Similarly, when the sinusoidal waveform is less than the triangular waveform, the upper switch is off and the lower switch is on. Depending on the switching states, either the positive or negative half DC bus voltage is applied to each phase [129, 150, 152]. Typical waveforms of SPWM technique is shown in Figure 138 [152].

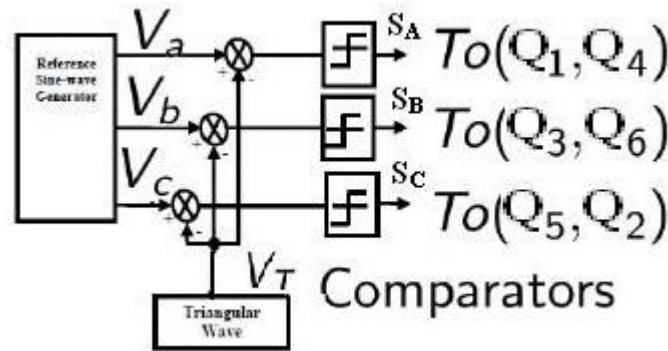


Figure 137: Control signal generators for SPWM
(Source: Author and B.K. Bose [150])

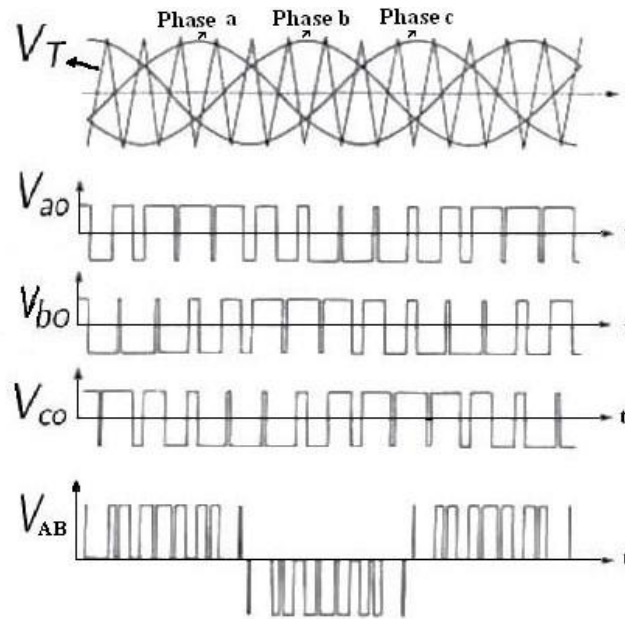


Figure 138: Typical waveforms of three-phase sinusoidal PWM (from up to down): reference voltages (a,b,c) and triangular wave, V_{a0} , V_{b0} , V_{c0} , line-to-line voltage V_{AB}
(Source: K. Rajashekara et al. [152])

3.3.6 Constant V/f Ratio Control with VSI

Maintaining the *V/f ratio constant at all speeds requires controlling the rectifier firing delay angle in proportion to the desired speed* [153]. The exact VFD design with a constant V/f ratio requires controlling the induction machine terminal voltage through the *control the rectifier firing delay angle “ α ” in proportion to the desired speed* as discussed next.

The output of the three-phase rectifier can be controlled by *substituting SCRs for diodes*. Figure 133 shows a controlled six-pulse three-phase rectifier. With SCRs, conduction does not begin until a gate signal is applied while the SCR is forward-biased. Thus, the transition of the output voltage to the maximum instantaneous line-to-line source voltage can be delayed. The delay angle is referenced from where the SCR would begin to conduct if it were a diode. The delay angle is the interval between when the SCR becomes forward-biased and when the gate signal is applied. Figure 139 shows the output of the controlled rectifier for a delay angle of 45° [143].

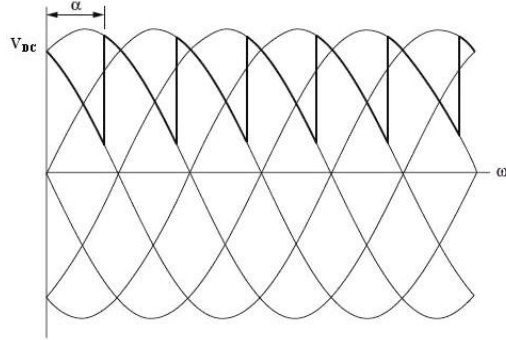


Figure 139: Output of a rectifier (DC voltage) for delay angle $\alpha=45^\circ$ (Source: D.W. Hart [143])

The average output voltage of the line commutated three phase, six-pulse, full-wave rectifier with SCRs, the DC voltage, is [143]:

$$V_{DC} = (3\sqrt{2}/\pi) \cdot V_{L(s)-(rms)} \cdot \cos\alpha = (3/\pi) \cdot V_{L(s)} \cdot \cos\alpha = 0.9549 \cdot V_{L(s)} \cdot \cos\alpha \quad (3.64)$$

Equation 3.64 shows that the **average output voltage is reduced as the delay angle α increases**.

The Torque-Speed curves of Figures 128÷130 are for different frequencies and constant V/f ratio. **The three-phase SPWM voltage source inverter can be used for this application if the DC input is adjustable**. Based on the configuration of Figure 133, **an adjustable DC voltage can be produced from a controlled rectifier (rectifier with SCRs - controlling the delay angle α and thus the V_{DC} amplitude), and an inverter produces an AC voltage at the desired fundamental frequency (controlling the frequency of the sinusoidal control signals – Equations 3.62.1÷3.62.3).**

The PWM technique is useful in a constant V/f ratio control application because the amplitude of the inverter output voltage can be also adjusted by changing the amplitude modulation ratio m . The DC input to the inverter can come from an uncontrolled source (rectifier with diodes) in this case [143] as shown in Figure 140 (Author and [110]).

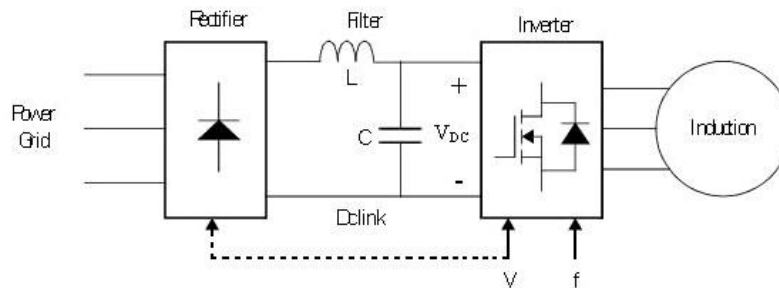


Figure 140: V/f ratio control of a PWM VSI with controllable (dash line) or uncontrollable (solid line) rectifier (Source: Author and [110])

3.4 VSI in MATLAB/Simulink® for the 720 kW OCT

In this section, the MATLAB/Simulink® model for the three-phase SPWM VSI and numerical results are presented based on the 720 kW IG for the 20 meters diameter OCT. The model description and the numerical model are presented below.

3.4.1 Model Description

MATLAB/Simulink® provides SimPowerSystems toolbox, as already explained in section 2.3.1, which is a library containing dynamic models of power electronics systems and electrical/electronic elements such as rectifiers, inverters, RLC circuits, LC filters etc. In Figure 141 the three-phase VSI complete model is presented while in Figures 142÷145 each part of the entire model is shown separately. The design parameters for the rectifier, the DC link, the inverter and the harmonic filter are presented in Tables 6÷9 respectively. The rectifier parameters were chosen based on the utility supply voltage and frequency (input) as well as the required DC voltage (output). The DC link parameters were selected so that the DC voltage has minimum fluctuations and the response of the DC link is adequate for simulation purposes. In addition, the inverter parameters were chosen so that the inverter internal design is as simple as possible and the results are the required. Finally, the LC harmonic filter parameters were selected based on the trial and error method. The trial and error method also used for the final adjustment of the entire system response including minor changes in each one of the above mentioned VSI's part.

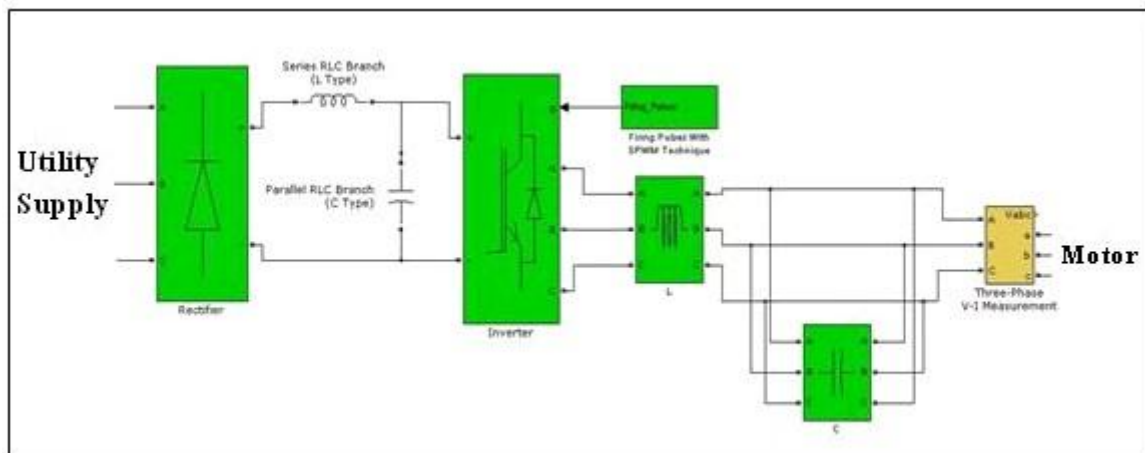


Figure 141: Three phase voltage source VSI implemented in MATLAB/Simulink® environment

Table 6: Rectifier parameters

Number Of Bridge Arms	3
Snubber Resistance (R_s)	$10^7 \Omega$
Snubber Capacitance (C_s)	Inf (Resistive)
Device Used	Diodes
Internal Resistance of Diodes (R_{on})	0.001Ω
Internal Inductance of Diodes (L_{on})	0.000 H
Forward Voltage (V_f)	0.8 V

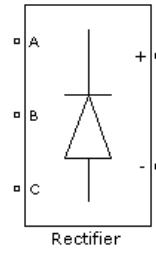


Figure 142: The Universal Bridge block for simulation of Rectifier (Source: Mathworks Inc. [108])

Table 7: DC link parameters

Inductance (L)	$200 \cdot 10^{-5} \text{ H}$
Capacitance (C)	$5000 \cdot 10^{-4} \text{ F}$

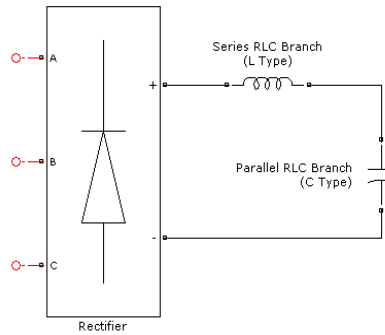


Figure 143: DC link of LC type (Source: Mathworks Inc. [108])

Table 8: Inverter parameters

Bridges	3
Snubber Resistance (R_s)	$10^5 \Omega$
Snubber Capacitance (C_s)	Inf
Device Used	IGBT/Diodes
Internal Resistance of Diodes (R_{on})	0.002Ω
Device Forward Voltage (V_f)	0.0 V
Diode Forward Voltage (V_{fd})	0.0 V
Fall Time (T_f)	10^{-6} s
Tail Time (T_t)	$2 \cdot 10^{-6} \text{ s}$

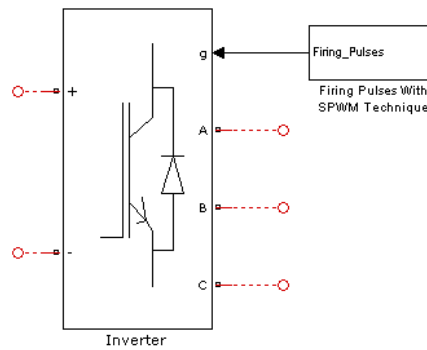
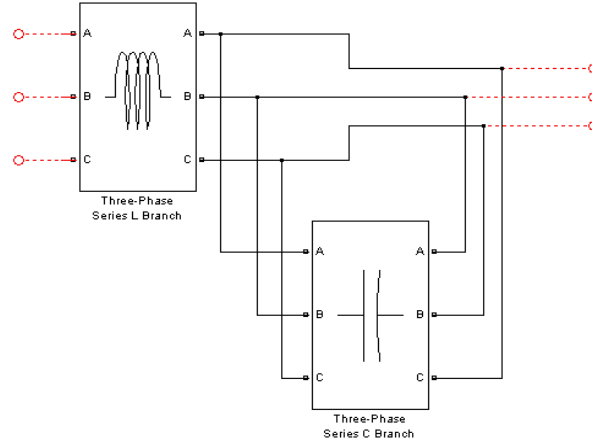


Figure 144: The Universal Bridge block for simulation of Inverter (Source: Mathworks Inc. [108])

Table 9: LC filter parameters

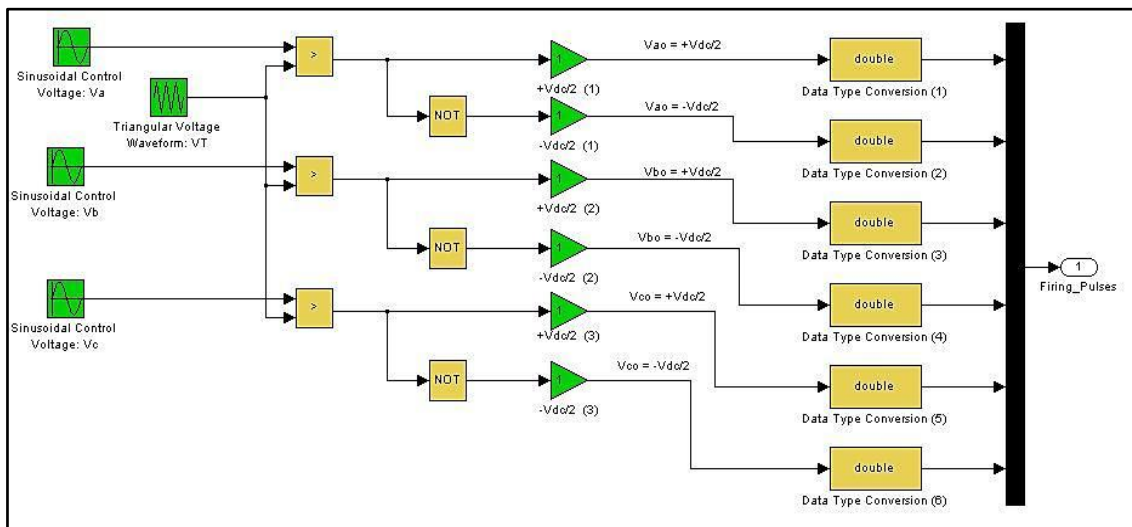
Inductance (L)	$1 \cdot 10^{-4}$ H
Capacitance (C)	$6 \cdot 10^{-5}$ F

**Figure 145:** Three phase 2nd order LC passive filter
(Source: Mathworks Inc. [108])

The implementation of Sinusoidal Pulse Width Modulation technique in MATLAB/Simulink® environment is shown in Figure 146. Using *relational operator* (“>” and “NOT”) and for amplitude modulation ratio equal to 1 ($m=1$) the output pole voltages value range from $-V_{DC}/2$ to $V_{DC}/2$ and as a result the firing pulses are generated which are a required input of the inverter block as shown in Figure 144. The solver parameters were used, for the simulation of the SPWM VSI, are given in Table 10.

Table 10: Solver parameters for SPWM VSI

Type	Variable-Step
Solver	ode23tb
Relative Tolerance	0.0001
Max Step Size	0.001
Min Step Size	0.00000000001
Solver Reset Method	Fast

**Figure 146:** Control signal generators for SPWM implemented with relational operators for $m=1$

3.4.2 Numerical Results

The 720 kW IG for the 20 meters diameter OCT has a rated line-to-line voltage of **460 V RMS**, as shown in Table 5 (Chapter 2). Thus, based on Equation 3.61 and considering $m=1$, the DC voltage should be approximately **750V**. According to Equation 3.58, the DC voltage after the rectifier depends on the supply voltage amplitude. So, for a DC voltage of **750V** the supply phase voltage amplitude should be **454 V** and it is assuming a frequency of **60Hz**. Numerical results of the VSI and comparison with the theory are shown below.

The three-phase supply waveform phase voltages $V_{A(s)}$, $V_{B(s)}$, $V_{C(s)}$ and line voltages $V_{AB(s)}$, $V_{BC(s)}$, $V_{CA(s)}$, are shown in Figure 147 and 148 respectively. The line-to-line supply voltages are **556.2 V RMS**. The voltage after the rectifier which is a DC voltage with an AC ripple is shown in Figure 149. A comparison between the theory and the simulation results from MATLAB environment is shown in Table 11. According to Equation 3.58, the V_{DC} theoretical value is **751.2 V** with an AC ripple almost 32 V where the simulation gives sufficient result of a $V_{DC} = 745 V$ with a V_{RIPPLE} of 35 V. Finally the ripple factor, VRF , is **less than 5%** which is very tolerable.

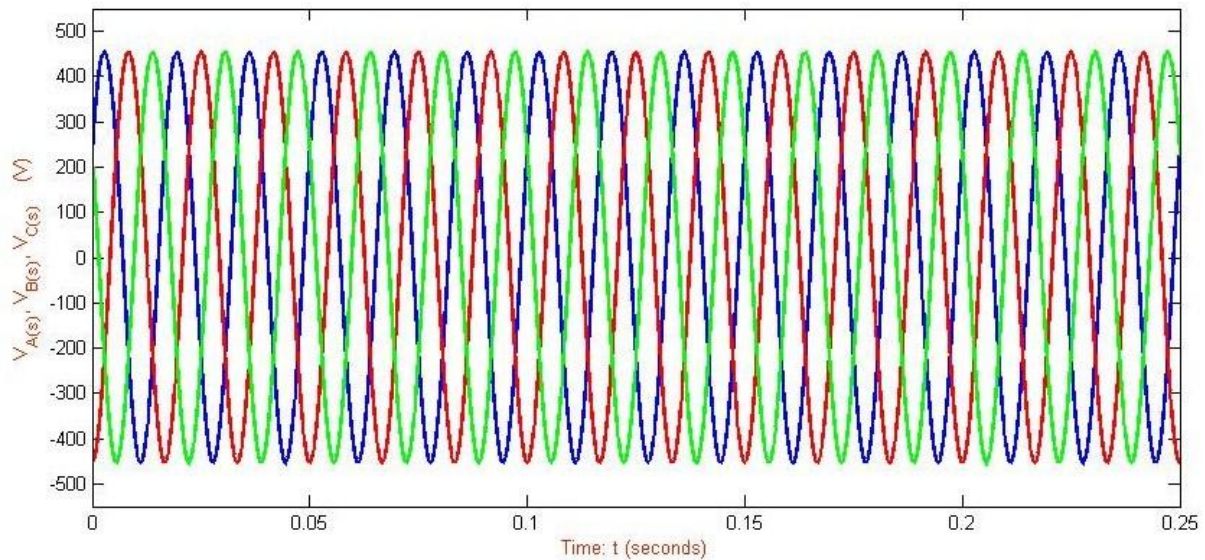


Figure 147: Three phase supply waveform phase voltages, $V_{A(s)}$, $V_{B(s)}$, $V_{C(s)}$ (321.1 V_{RMS})

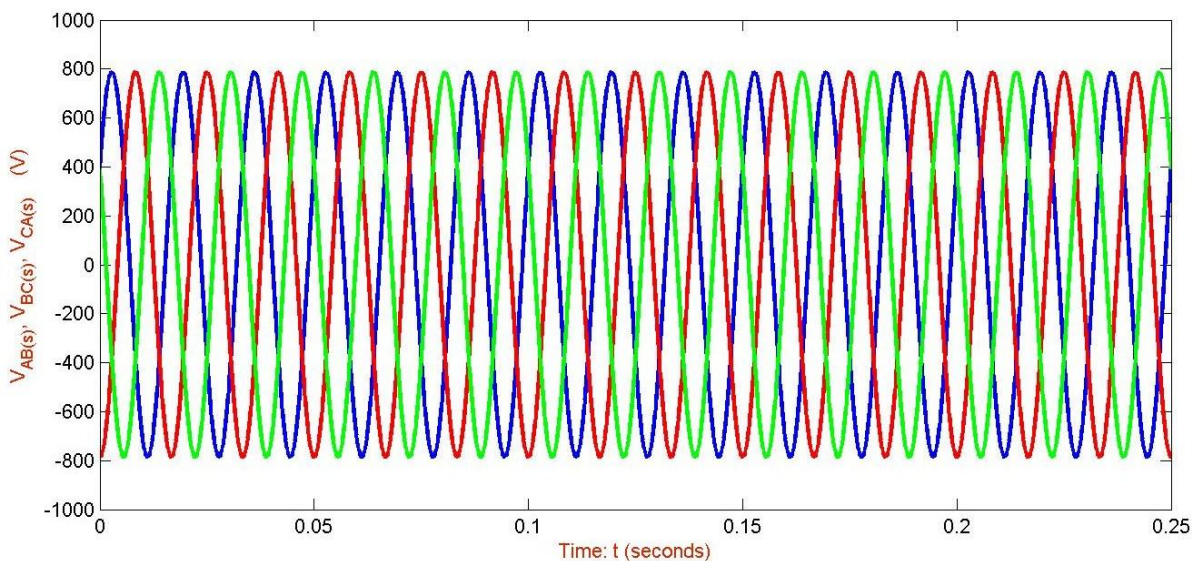


Figure 148: Three phase supply waveform line to line voltages, $V_{AB(s)}$, $V_{BC(s)}$, $V_{CA(s)}$ (556.2 V_{RMS})

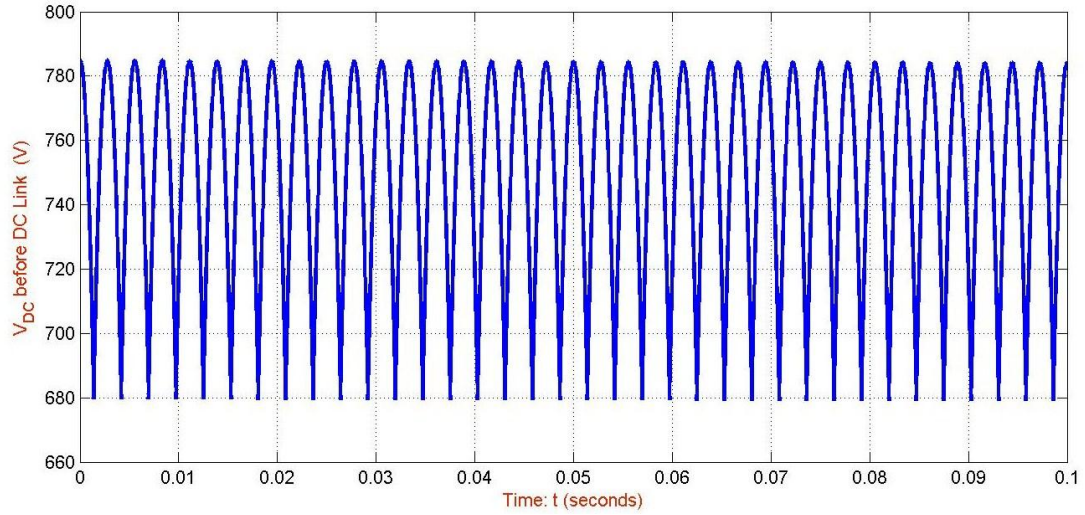


Figure 149: DC voltage with ripple

Table 11: Comparison of theory and simulation results in rectifier section

	Theory	Simulation
$V_{ph(s)\text{-RMS}}$	321.1 V	321.1 V
$V_{LL(s)\text{-RMS}}$	556.2 V	556.2 V
V_{DC}	751.2 V	745 V
V_{ripple}	30 V	35 V
VRF	0.03993	0.04697

The voltage after the DC link which is a DC voltage with an insignificant AC ripple is shown in Figure 150. Before the DC link the AC ripple was 35 Volts when after the LC circuit the ripple reduced as low as 5 Volts as shown in Figure 150. Thus, the voltage on the DC bus becomes “approximately” 755 V_{DC} .

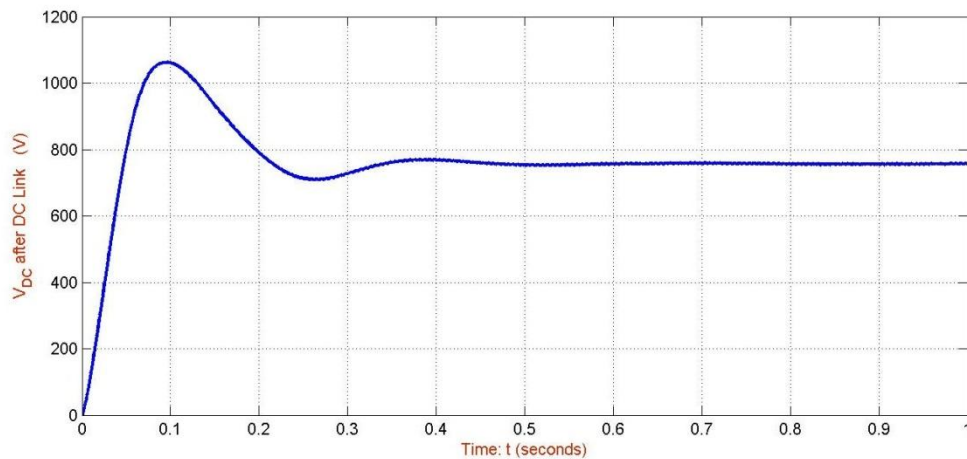


Figure 150: DC voltage after DC Link (755 V)

The sinusoidal control voltages and the triangular switching signal as well as the output voltages V_{ao} , V_{bo} and V_{co} , are shown in Figure 151. The value of modulation index, m , was chosen to be 1.0 within the linear region of the modulation technique. The load of the VSI is the induction motor/generator with a rated frequency 60Hz. So, the fundamental frequency, f_i , should be the same

as the rated frequency of the motor. For this reason, the frequency of the control voltages was selected to be 60 Hz . The outcome of the SPWM technique are the firing pulses or output voltages where they are fluctuate between $+m \cdot V_{DC}/2$ and $-m \cdot V_{DC}/2$ ($\pm 377.5\text{ Volts}$).

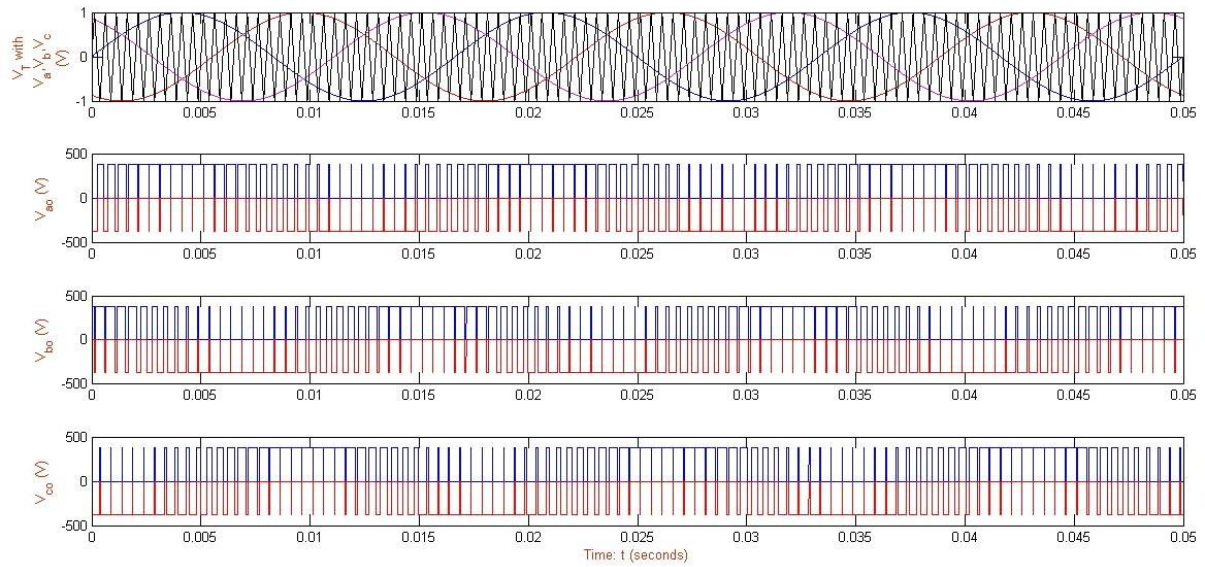


Figure 151: Triangular-Control signals (for $m=1.0$) and output pole voltages ($\pm m \cdot V_{DC}/2$) of SPWM circuit

The voltages after the inverter section are shown in Figures 152 and 153. The waveforms of line-to-line inverter voltages are fluctuate between $+m \cdot V_{DC}$ and $-m \cdot V_{DC}$ ($\pm 750\text{ Volts}$) in a rectangular scheme while the waveforms of the phase inverter voltages are fluctuate in a rectangular step scheme between $\pm m \cdot V_{DC}/3$ and $\pm m \cdot 2V_{DC}/3$.

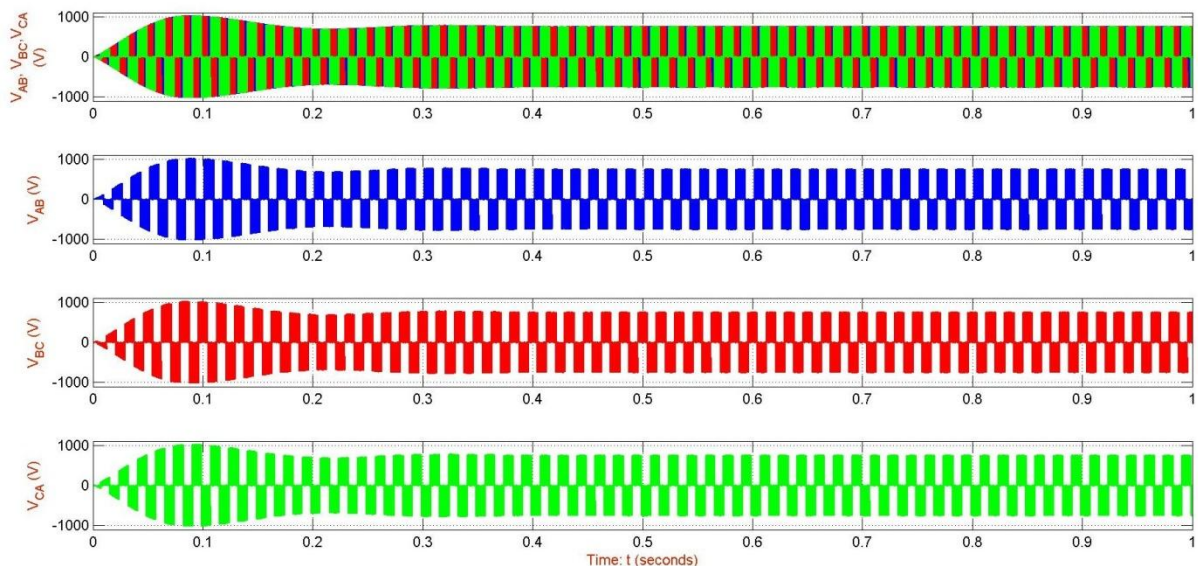


Figure 152: Three-phase line-to-line voltages ($\pm 755\text{ V}$) of the inverter before the harmonic filter

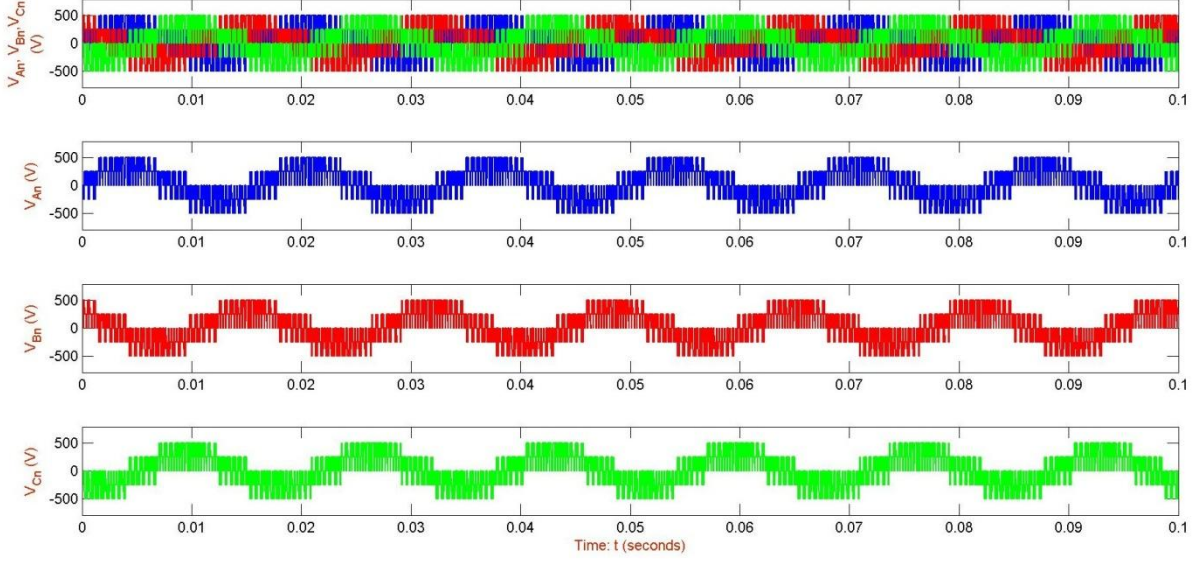


Figure 153: Three-phase phase voltages (± 503.3 V) of the inverter before the harmonic filter

Using the 2nd order passive LC filter after the inverter section, the rectangular waveform of line-to-line inverter voltages is converted to a sinusoidal waveform with same frequency as the control voltages signals, **60 Hz**, and amplitude **650 V** (459.6 V RMS), as shown in Figures 154 and 155, which means that the rms value of line-to-line voltages after the harmonic filter is **460 V**. According to Equation 3.61, the theoretical RMS value of the line-to-line inverter voltages at the fundamental frequency is **462.5 V RMS** (≈ 654 V). The difference between theory and simulation is at the level of **3 Volts** which is equal of **0.6%** and it is acceptable. Finally, the inverter phase voltages after the harmonic filter, V_{an} , V_{bn} , V_{cn} are shown in Figure 156 and they are referred to the stator phase voltages V_a , V_b and V_c according to Appendix C.

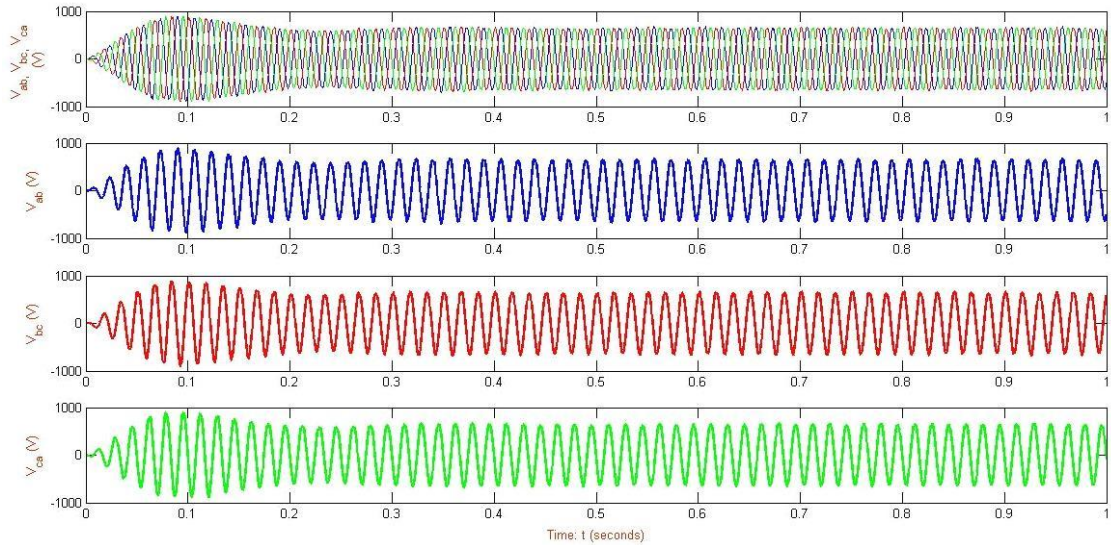


Figure 154: Three-phase line-to-line voltage (± 640 V) of the inverter after the harmonic filter

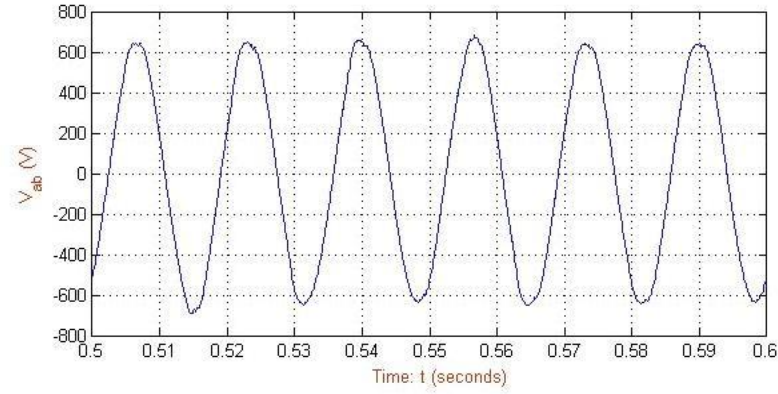


Figure 155: V_{ab} line-to-line voltage (± 640 V) of the inverter after the harmonic filter

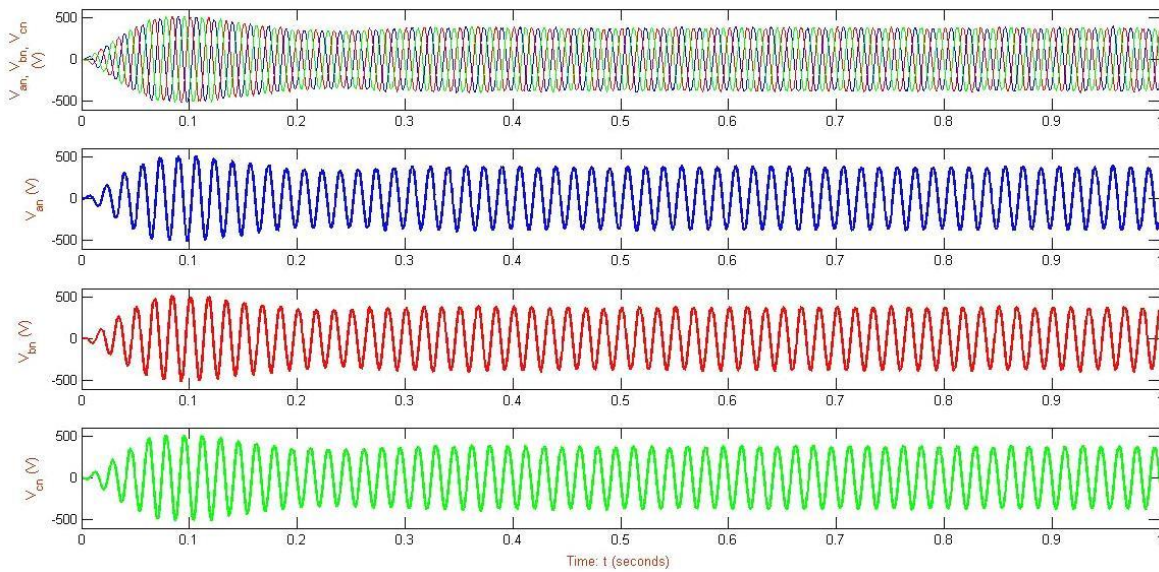


Figure 156: Three-phase phase voltages (± 369.5 V) of the inverter after the harmonic filter

3.5 Simplified Version of VSI in MATLAB/Simulink®

The scalar control method of constant V/f ratio can be implemented with the three-phase SPWM VSI presented in previous section. *The three-phase VSI of Section 3.4 consists of an uncontrollable rectifier which means that the control of voltage and frequency is held through the adjustment of amplitude modulation ratio m and the frequency (fundamental component) of the sinusoidal control signals in PWM scheme respectively.*

A simplified not realistic version of three-phase VSI as presented in Section 3.4 and the comparison among them is shown below. *The reason is the diminution of computer power needed for the simulation of the entire plant model as it will be discussed in Chapter 4.* The main and only assumption that should be done so that the comparison has a meaning is that if the stator phase voltages (or line-to-line) through the realistic VSI (inverter phase voltages after the harmonic filter), V_{an} , V_{bn} , V_{cn} (or V_{ab} , V_{bc} , V_{ca}), is the same, in frequency and amplitude, with the phase voltages from the simplified model, then the response of the induction machine will be equal in any case as the stator phase voltages are the necessary inputs for the induction motor/generator model presented in Section 2.3.

The simplified model is shown in Appendix D for constant voltage and frequency using the *Control Voltage Source (CVS)* block. An example of different frequencies and constant voltage (green color blocks) is shown in Figure 157. The same could be applied for the control of the voltage with constant or control frequency.

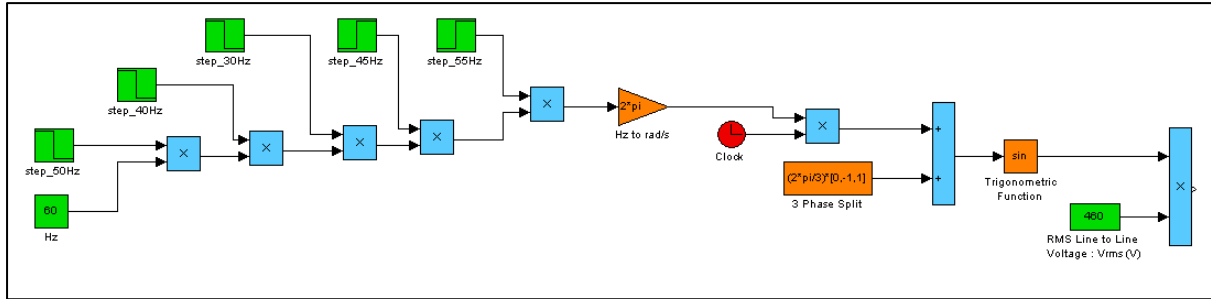


Figure 157: Simplified version of three-phase VSI with different fundamental frequencies and constant voltage in MATLAB/Simulink® environment

The line-to-line stator three-phase voltages comparison between the realistic three-phase VSI and the simplified one with constant voltage but different frequencies, as shown in Figure 158, from the rated frequency 60 Hz up to 30 Hz, which is a 50% decrease of the rated frequency, is shown in Figures 159÷161.

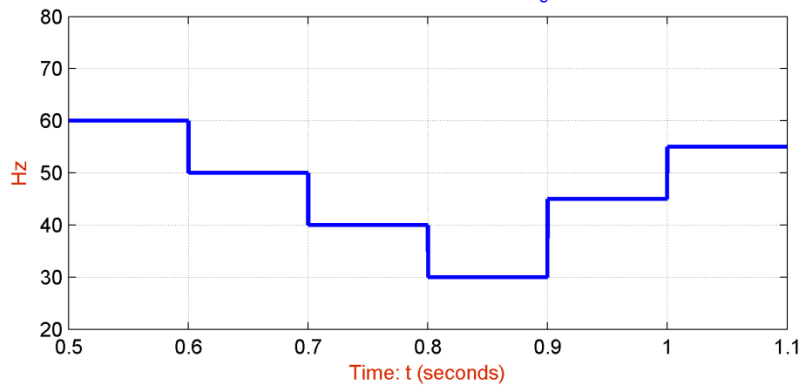


Figure 158: Stator three-phase voltage frequency (fundamental component in case of realistic VSI) versus time. Range from 100% rated frequency (60Hz) up to 50% rated frequency (30 Hz)

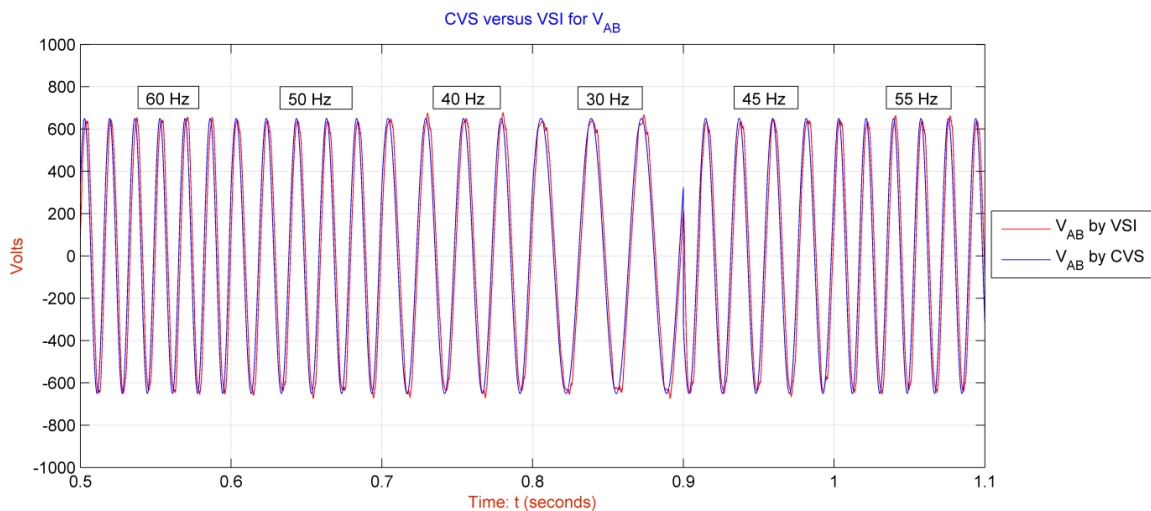


Figure 159: The line-to-line stator three-phase voltage, V_{ab} , comparison between the realistic VSI and the simplified version with CVS for different frequencies and constant voltage

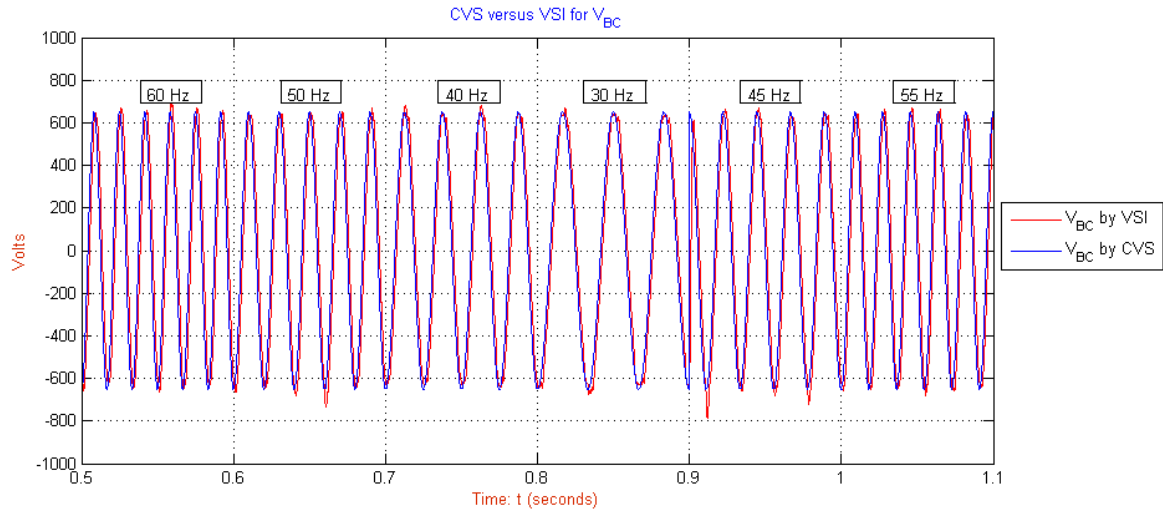


Figure 160: The line-to-line stator three-phase voltage, V_{bc} , comparison between the realistic VSI and the simplified version with CVS for different frequencies and constant voltage

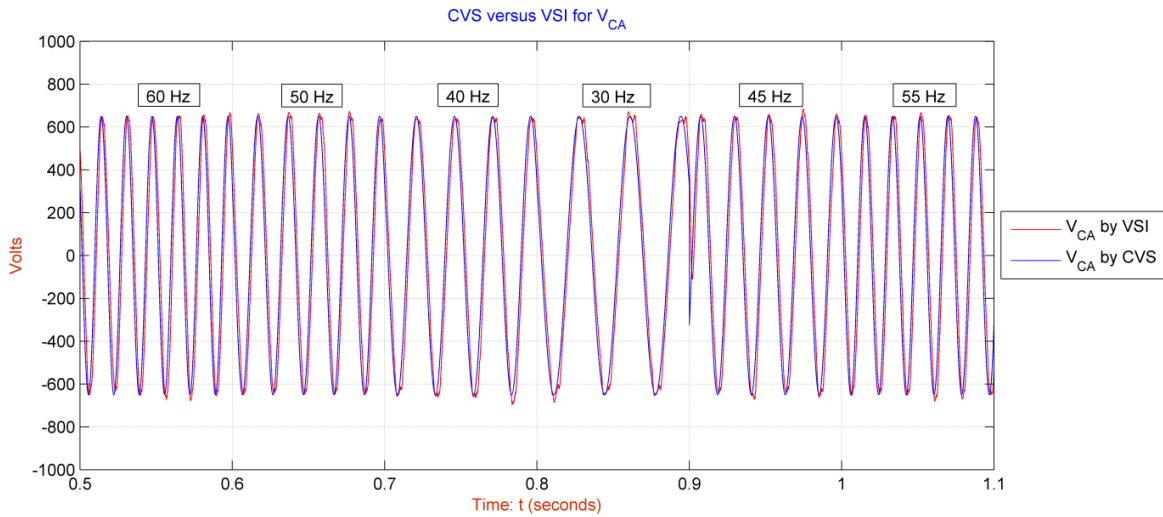


Figure 161: The line-to-line stator three-phase voltage, V_{ca} , comparison between the realistic VSI and the simplified version with CVS for different frequencies and constant voltage

CHAPTER 4

MODELING, CONTROL AND SIMULATION OF AN OVERALL OCEAN CURRENT ENERGY CONVERSION SYSTEM

4.1 The Ocean Current Energy Conversion System (OCECS)

The *major components* of an *Ocean Current Energy Conversion System* (OCECS) are as follow: ocean current turbine (OCT), gear box, shafting system, generator, power converters, transformer and the grid as shown in Figure 162 [154 and Author].

Based on the existing designs and prototypes around the world, as presented in Chapter 1, a small power capacity OCT which can operate standalone to supply power to houses, villages, farms, and islands is *costly and not feasible*. All of the OCT projects are designed to be *grid connected*, and the power will be generated is fed directly to the grid. Most generators operate at a few hundred volts, such as 460 V or 690 V. Transformers are used to increase the generator voltage to tens of kilovolts, such as 35 kV for every single OCT in case of a farm, where the voltage is further stepped up by transformers to connect to the grid, which can be at hundreds of kV, such as 230 kV [154]. A schematic diagram of the grid-connected ocean current farm is shown in Figure 163 (Author and [154]).

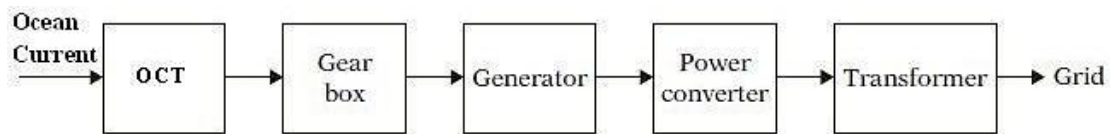


Figure 162: Major components of an OCECS (Source: Author and [154])

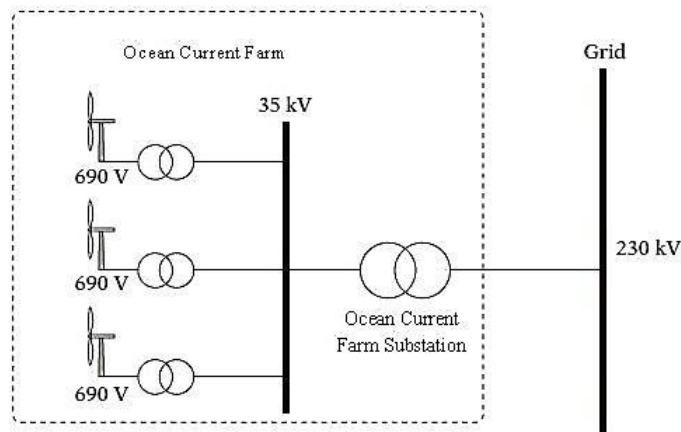


Figure 163: Grid-connected ocean current farm (Source: Author and [154])

The two (2) *main electrical components* in OCECS are the *generators* and *power converters*. Both induction generators, such as *squirrel-cage induction generators* (SCIG) or *wound rotor induction generators* (WRIG), and synchronous generators, such as *permanent magnet synchronous generators* (PMSG), have been used in the design stage or in prototypes for ocean current energy conversion systems (see Chapter 1).

The basic operation of induction generators (IG) has been discussed in Chapter 2, primarily their applications as motors. These machines are used in ocean current energy systems in their *generating mode*. The operation and control strategies of induction generator systems and power converters have been discussed in Chapter 3. Based on the existing designs around the world and the nature of the ocean currents, all the OCECS will be *variable speed systems with full capacity converters in contrast with wind turbines where fixed speed or variable speed can be found with full or reduced capacity converters* [154, 155].

An OCECS with full capacity power converters is shown in Figure 164 (Author and [154]). In this system *the generator is connected directly to the grid via a full capacity power converter*. Because of the converters, ***the generator is fully decoupled from the grid and can operate in full speed range***, and performance is greatly enhanced. Squirrel-cage induction generators (SCIG) and permanent magnet synchronous generators (PMSG) are all can be used in this configuration for high-power (several kW) ocean current generator systems. *Because of ocean current wide speed variation and in different depths and directions, the system can be operated with variable pitch blades to extract maximum ocean current energy at different current direction and depths (the variable pitch will help the OCT to change position in the space).*

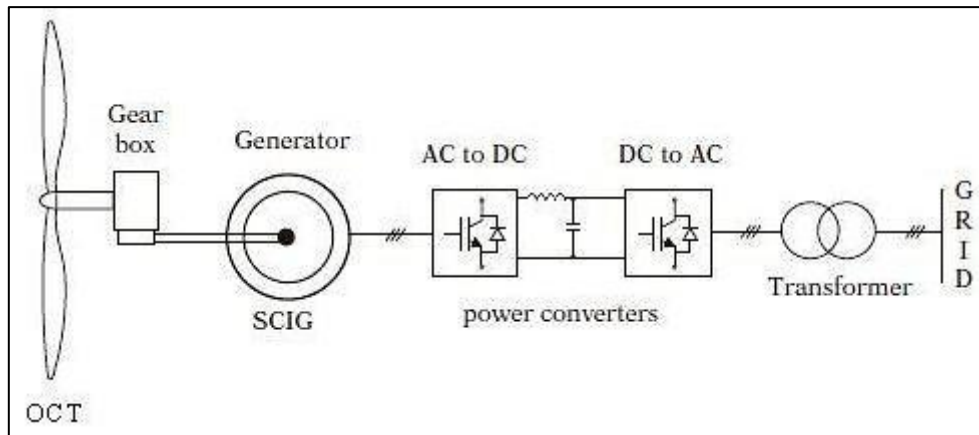


Figure 164: Block diagram of a variable speed OCECS with full capacity power converters
(Source: Author and [154])

A more realistic schematic diagram of a SCIG-based generation OCECS with full capacity power converters is shown in Figure 165 (Author and [70]). A *mechanical brake is normally placed on the high-speed shaft between the gearbox and the generator*, as shown in Figure 165. The main advantage of placing the brake on the high-speed shaft is that it ***handles much lower braking torque***. Hydraulic and electromechanical disc brakes can be used but always in a sealed environment for the protection from the water [155]. ***The mechanical brake should be normally able to bring the OCT to a complete stop under any current velocity***. Moreover, the main circuit breakers, the transformer and the medium voltage switchgear complete the auxiliary electrical equipment for the total decoupling between generator and the grid and for the correct and safe connection of the OCECS to the grid respectively. On the other hand, the control of the SCIG and the network-side power is held by PWM VSIs. The generator side PWM VSI (or a diode-based rectifier) used to control the operation of the generator (see Chapter 3.3) while the network-side PWM VSI is used to control the power flows to the network [156]. *The strategy to control the operation of the generator and power flows to the network depends very much on the type of power converter arrangement employed* [156]. Finally, the pitching mechanism (pitch drive) is attached to the low-speed shaft so that varies the blade pitch angles.

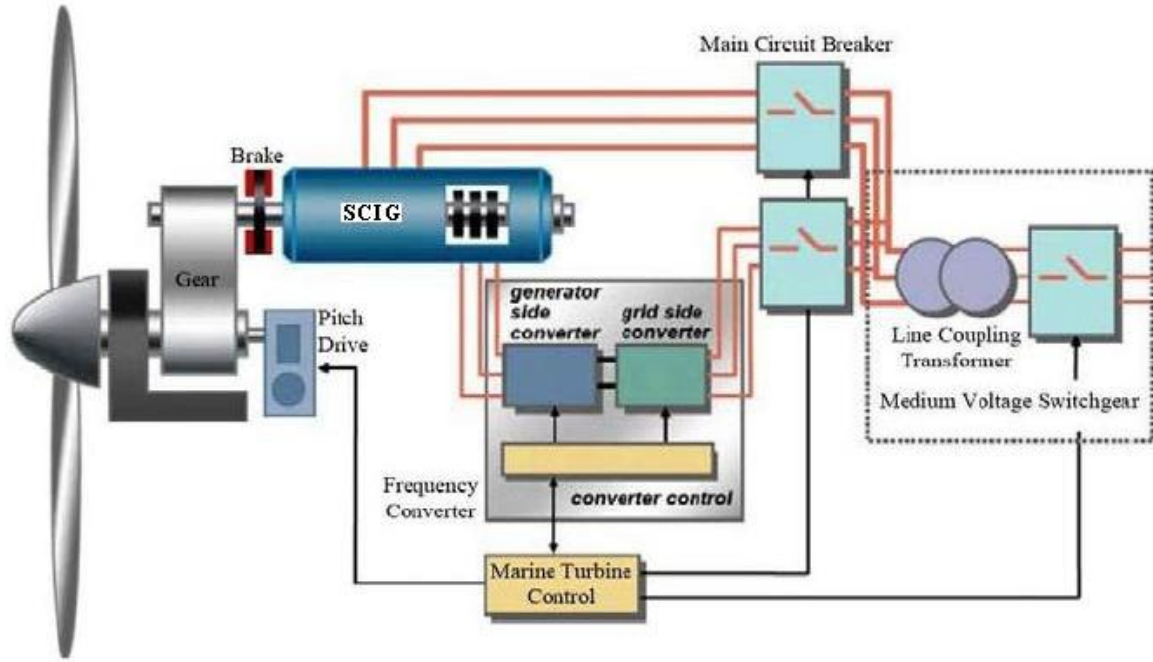


Figure 165: A realistic schematic diagram of a SCIG-based generation OCECS with full capacity power converters (Source: Author and [70])

4.2 Modelling of OCECS in MATLAB/Simulink®

In this section, the MATLAB/Simulink® overall model for the OCECS is presented based on the 720 kW IG for the 20 meters diameter variable pitch OCT. The assumptions are used for the modeling and simulation of the overall system is shown below:

- The current velocity is **constant** and **independent of time** ($V_c = \text{constant}$).
- **No losses** on the gearbox and the shafting system ($\eta_{\text{gearbox}} = \eta_{\text{shaft}} = 1$).
- The high-speed and the lower-speed part of the shaft have the **same diameter**.
- For the shaft vibrational model, we assume that the gearbox does not exist.
- For the **same current velocity**, the different RPM of the OCT based on the **control of pitch blade**.
- The control of pitch blade as well as the grid side power converter with the transformer are not examined or incorporated into the overall model.
- For the scalar control of the SCIG (constant V/Hz ratio), the simplified PWM VSI is used as presented in Section 3.5.

The model description and the numerical models are presented below.

4.2.1 Numerical Models and Description

The below sub-sections provide the numerical approach used to model each part of the OCECS. These numerical models were developed in MATLAB/Simulink® environment as already mentioned. The OCECS consists of *four (4) main modules*: the OCT hydrodynamic model, the shafting system, the SCIG model and the PID controller as shown in Figure 166. *The steady state analysis and performance of the system, including the ability of the developed controller to achieve specified rotational velocity set-points*, is examined using the model which is presented in Figure 166.

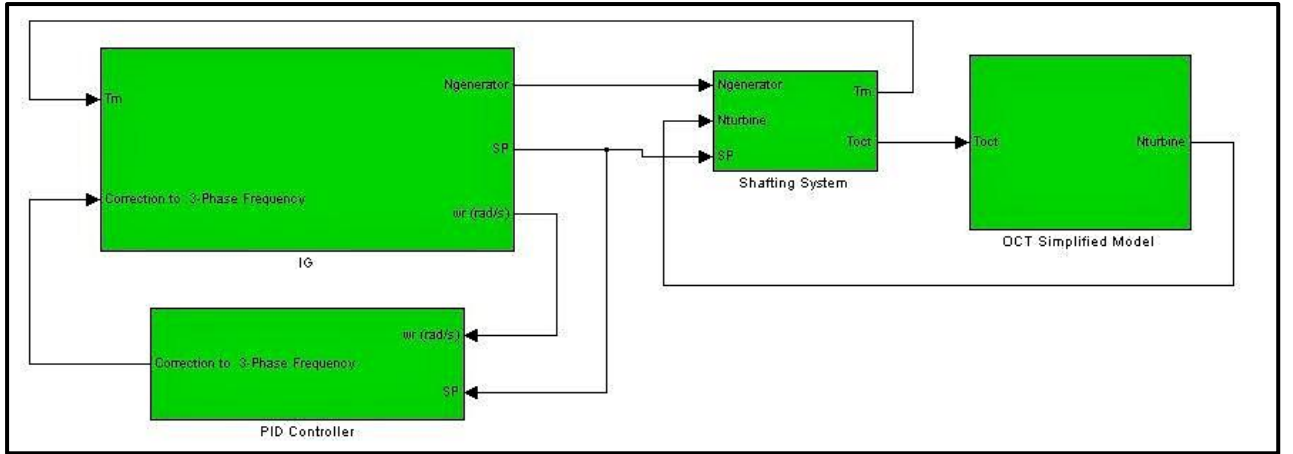


Figure 166: Steady-state OCECS model implementation in MATLAB/Simulink® environment

4.2.1.1 The OCT Model (Rigidly Mounted)

The OCT simplified model provided by *Florida Atlantic University* (FAU) and especially the *Southeast National Marine Renewable Energy Center* (SNMREC). The simplified numerical model refers to a **rigidly mounted OCT** in the seabed and it results from a detailed model which based on the *Boundary Element Momentum* approach [60, 63]. The *depth of the OCT hub is 25 meters*.

Furthermore, the OCT sub-block demands as an input the current velocity, V_C , in m/s and the rotational speed of the OCT in RPM, $N_{turbine}$, while the output is the OCT generated torque, $T_{turbine}$, in N.m. The rotational state of the OCT is calculated as shown below [156]:

$$\dot{N}_{turbine} \left(\frac{rpm}{s} \right) = \frac{60}{2\pi} \cdot \frac{(T_{turbine} - T_{shaft(low-speed)})}{J_{turbine}} \quad (4.1.1)$$

$$N_{turbine}(rpm) = \frac{d\theta}{dt} = \int_0^t \dot{N}_m dt \quad (4.1.2)$$

where the $J_{turbine}$ is the OCT moment of inertia with a value of $4.7365 \cdot 10^5 \text{ kg m}^2$ and $T_{shaft(low-speed)}$ is the torque load provided by the *low-speed* part of the axis (T_{oct} according to Figures 166 and 167).

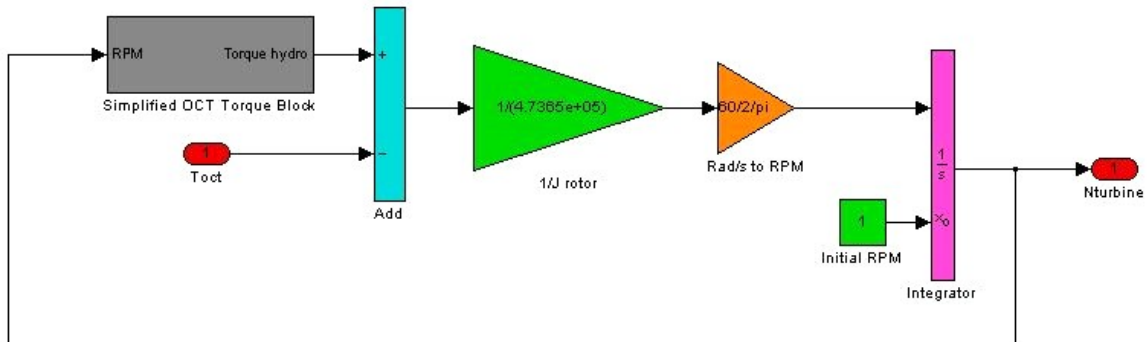


Figure 167: The OCT simplified model implemented in MATLAB/Simulink® environment

4.2.1.2 The SCIG Model and the Gearbox

The SCIG numerical model with the simplified VSI has been detailed presented in Sections 2.3, 2.4.2, 3.3, 3.4 and 3.5. The SCIG is connected with a reduction gear that has an overall efficiency of $\eta_{gear} = 100\%$ (for calculation simplicity) and gear ratio which is given from the following equation:

$$i_{gear} = \frac{N_{turbine} (rpm)}{\omega_m (rpm)} \quad (4.2)$$

Because of the gear ratio, the *high speed part* of the shafting system (generator side) has *high rotational velocity* and *lower torque* while the *slow speed part* (OCT side) has *low rotational velocity* and *high torque* so that the law of conservation of energy to be respected.

4.2.1.3 The Shafting System Vibrational Model

The shaft is modeled a series of inertias (masses) and springs with frictional losses on the mass elements. The forcing function for the system is based upon a time-dependent torque load on the SCIG end and a time-dependent driving torque from the OCT (low speed part of the shaft). The mechanical model can be represented by the one-dimensional system of masses and springs rotating on bearing surfaces [156, 157].

The last shafting element takes as an input the speed from the OCT. It shall transmit the speed to the following elements considering friction due to bearings, vibration and twist. Therefore, all characteristics of the shaft need to be modeled including the material properties, an approximation of the frictional losses and the geometry of the shaft. The model has been represented in three dimensions using Rhinoceros 3D CAD software as seen in Figure 168 [157].

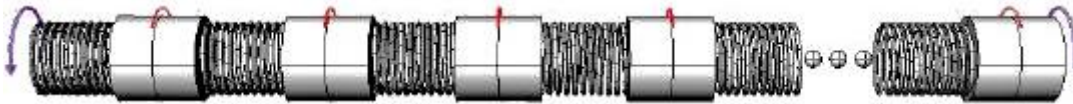


Figure 168: Representation of the OCECS shaft as a sum of masses and springs. Side view of the discretized shaft model (Source: [157])

FAU and SNMREC performing analysis of the OCT so that the diameter of the shaft and the material was selected placing the natural frequency of both OCT and shaft in an acceptable range of about twice the resonant frequency. The shaft is **4m long** and **hollow type** with one (1) bearing located between the IG (in reality the gearbox) and the OCT. The shaft is modeled as a *2 element component connected with a spring*. The OCECS shaft characteristics are shown in Table 12.

Table 12: OCECS shaft characteristics

Shaft Length	L_{shaft} : 4 m
Number of Elements	2 (-) (OCT + IG)
Number of Springs	1 (-)
Shaft Diameter (<i>Hollow Type</i>)	D_{out} : 25 cm (<i>outer</i>) , D_{in} : 20 cm (<i>inner</i>)
Shaft-OCT Flange	D_f : 60 cm , l_f : 10 cm
Number of Bearings	1 (-)
Shaft Material	Stainless Steel

Except for the above geometric characteristics and material of the shaft, the vibrational model block needs also the *density* and *shear modulus* of shaft material (77.2 GN/m^2 for stainless steel [158]), the inertia of the shaft elements (j_i) including the IG and the OCT, the frictional losses on bearings (b_i) and the torsional spring constants (k_{ti}). A representation of the shaft vibration model mechanical system for 6 elements with 5 springs and 3 bearings is shown in Figure 169 (Author).

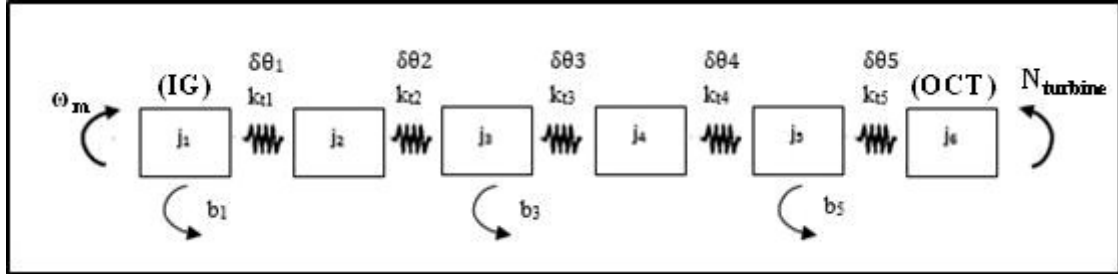


Figure 169: Representation of shafting vibrational model mechanical system for 6 elements, 5 springs and 3 bearings (Source: Author)

The governing system of differential equations that describe the vibrational model are shown below [157, 159, 160]:

$$\frac{d\vec{\omega}}{dt} = \vec{J} \cdot \vec{T} + \vec{K}_t \cdot \vec{\delta\theta} - \vec{B} \cdot \vec{\omega} \quad (4.3)$$

where \vec{K}_t is the *shaft stiffness matrix* [$n \times n-1$], \vec{J} is the *moment of inertia matrix* [$n \times 2$], \vec{B} is the *viscous frictional loss matrix* [$n \times n$], $\vec{\delta\theta}$ is the *shaft deformation vector* [$n-1 \times 1$], $\vec{\omega}$ is the *shaft rotational velocity vector* [$n \times 1$], \vec{T} is the *torque vector* [2×1] and n is the *number of elements*. The above matrices and vectors are given by the following equations [157]:

$$K_t = \begin{bmatrix} k_{t1}/j_1 & 0 & 0 & 0 & 0 \\ -k_{t1}/j_2 & k_{t2}/j_2 & 0 & 0 & 0 \\ 0 & -k_{t2}/j_3 & k_{t3}/j_3 & 0 & 0 \\ 0 & 0 & -k_{t3}/j_4 & k_{t4}/j_4 & \vdots \\ 0 & 0 & 0 & -k_{t4}/j_5 & k_{t(n-1)}/j_{n-1} \\ 0 & 0 & 0 & \dots & -k_{t(n-1)}/j_n \end{bmatrix}, \quad \delta\theta = \begin{bmatrix} \delta\theta_1 \\ \delta\theta_2 \\ \delta\theta_3 \\ \vdots \\ \delta\theta_{(n-1)} \end{bmatrix} \quad (4.4.1)$$

$$B = \begin{bmatrix} b_1/j_1 & 0 & 0 & 0 & 0 & 0 \\ 0 & 0 & 0 & 0 & 0 & 0 \\ 0 & 0 & b_3/j_3 & 0 & 0 & 0 \\ 0 & 0 & 0 & 0 & 0 & 0 \\ 0 & 0 & 0 & 0 & b_5/j_5 & \vdots \\ 0 & 0 & 0 & 0 & \dots & b_n/j_n \end{bmatrix}, \quad \omega = \begin{bmatrix} \omega_1 \\ \omega_2 \\ \omega_3 \\ \omega_4 \\ \vdots \\ \omega_n \end{bmatrix} \quad (4.4.2)$$

$$J = \begin{bmatrix} 1/j_1 & 0 \\ 0 & 0 \\ 0 & 0 \\ 0 & 0 \\ 0 & \vdots \\ \dots & -1/j_n \end{bmatrix}, \quad T = \begin{bmatrix} T_m \\ T_{oct} \end{bmatrix} \quad (4.4.3)$$

where b_n is the viscous friction coefficients of shaft n^{th} element bearing, j_n is the moments of inertia of shaft n^{th} element (where always j_1 and j_n are the IG and the OCT element respectively), $k_{t(n-1)}$ is the torsional spring constant of $(n-1)^{th}$ spring, $\delta\theta_{(n-1)}$ is the deformation angles of shaft

torsional $(n-1)^{th}$ spring, ω_n is the rotational velocity of shaft n^{th} element (where always ω_l and ω_n are the ω_m and $N_{turbine}$ respectively).

The **load torque which OCT faces** is given by the following equation [156]:

$$T_{oct} = k_{t(n-1)} \cdot \delta\theta_{n-1} = k_{t(n-1)} \cdot (\theta_n - \theta_{(n-1)}) = k_{t(n-1)} \cdot \int (\omega_n - \omega_{n-1}) dt = k_{t(n-1)} \cdot \int (N_{turbine} - \omega_{n-1}) dt \quad (4.5)$$

and in case of two elements ($n=2$):

$$T_{oct} = k_{t1} \cdot \delta\theta_1 = k_{t1} \cdot (\theta_2 - \theta_1) = k_{t1} \cdot \int (\omega_2 - \omega_1) dt = k_{t1} \cdot \int (N_{turbine} - \omega_m \cdot i_{gear}) dt \quad (4.6)$$

Thus, the *IG load torque* is derived from the following equation using the reduction gear ratio:

$$T_m = T_{oct} \cdot i_{gear} \quad (4.7)$$

The value of *torsional spring constant*, $k_{t(n-1)}$, which refers to the last spring of the system that connect to the OCT flange (OCT element – last element) depends on the geometric characteristics of flange as shown below (in case of $n=2$ then k_{t1}) [156, 161, 162]:

$$k_{t(n-1)} = \frac{G \cdot j_f}{l_f} \quad (4.8)$$

$$j_f = \frac{1}{32} \cdot \pi \cdot (D_f^4) \quad (4.9)$$

where l_f , D_f are the length and the diameter of OCT flange respectively and j_f is the polar moment of inertia of the flange. For a shafting system with uniform circular cross section, the moments of inertia and the spring constants can be estimated by the following relationships for hollow shaft type [162]:

$$k_{tk} = \frac{G \cdot j_{polar,i}}{l_i} \quad (4.10)$$

$$j_{polar,i} = \frac{1}{32} \cdot \pi \cdot (D_{out}^4 - D_{in}^4) \quad (4.11)$$

$$j_i = \frac{1}{8} \cdot m_i \cdot (D_{out}^2 + D_{in}^2) \quad (4.12)$$

$$m_i = \rho \cdot l_i \cdot \pi \cdot \left(\left(\frac{D_{out}}{2} \right)^2 - \left(\frac{D_{in}}{2} \right)^2 \right) \quad (4.13)$$

where $i=2 \div (n-1)$, $k=1 \div (n-2)$ and $j_{polar,i}$ is the polar moment of inertia of i^{th} element, m is the mass, ρ is the density of the material, G is the shear modulus or modulus of rigidity of the material and l is the length of the shaft elements which is equal of *the total length of the shaft divided by the number of elements* ($= L_{shaft}/n$). Furthermore, j_l is the IG moment of inertia and is given from the manufacturer.

As far as the frictional losses, the theory involved in computing bearing viscous friction by advanced fluid dynamic techniques is outside the scope of this research effort. For practical purposes in the marine engineering, *selecting an empirical viscous frictional loss value, as was done, is typical and reasonable*. The value of all bearings viscous friction coefficient (b_1 , b_2 and b_3) is $0,5 \text{ N}\cdot\text{m}\cdot\text{s}/\text{rad}$.

Finally, the shafting vibrational model accepts a rotational velocity from the OCT which is the OCT rotational velocity during its operation ($N_{turbine}$). The other input to the shafting vibrational model is the IG rotor mechanical angular velocity (ω_m). The shafting module outputs are the necessary torque load to the induction motor (T_m) which is the torque at the high speed side of the shaft and the load torque where OCT faces (T_{oct}) which is the torque at the low speed side of the shaft

as shown in Figure 170. The shaft vibrational model implemented in MATLAB/Simulink® environment for $n=2$ elements and one bearing is shown in Figure 171.



Figure 170: Inputs (left) and outputs (right) for the shafting vibrational model block in MATLAB/Simulink® environment

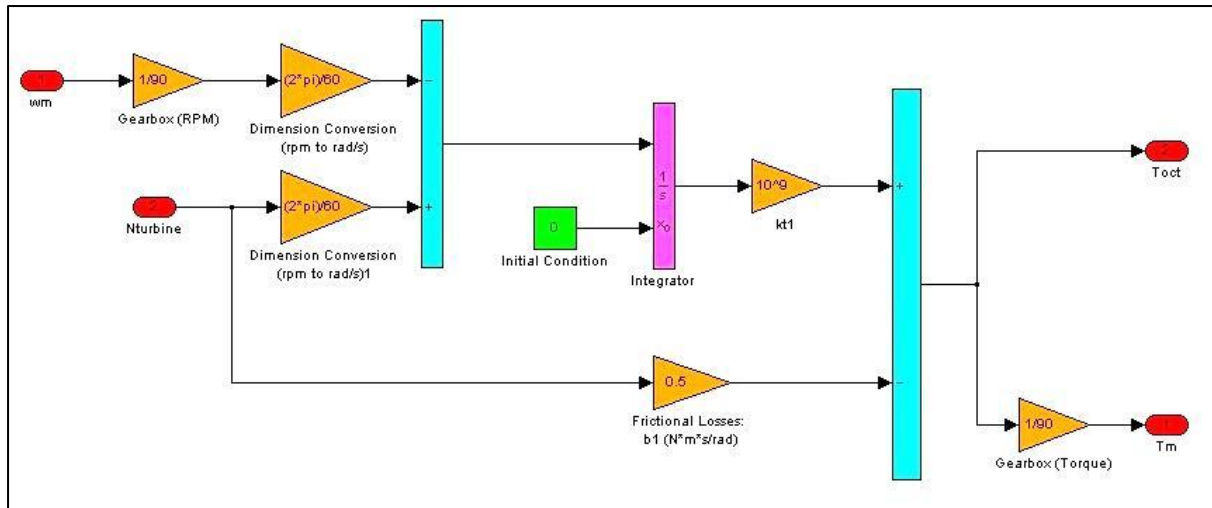


Figure 171: The shaft vibrational model implemented in MATLAB/Simulink® environment for $n=2$ elements and one bearing

4.2.1.4 The Power Controller (PID Bblock)

The *PID (Proportional-Integral-Derivative) controller*, [163], implemented for the control of the induction motor speed is designed to observe the actual angular mechanical speed of the IG via a speed sensor such as a hall effect sensor, or optical encoder, compares the value to the desired angular mechanical speed, and based on the difference between the two, generates a perturbation of the drive frequency. *This perturbation is then added to steady state (constant) rad/s set point based on the desired rpm and nominal load curve of the current turbine.*

More specifically, the scalar input signal to the feedback controller is the generator mechanical speed (rpm) error while the scalar output signal is electrical supply frequency correction (rad/s) for the SCIG in the system. The frequency correction is added to the steady state (constant) rad/s set point based on the desired rpm and nominal load curve of the current turbine.

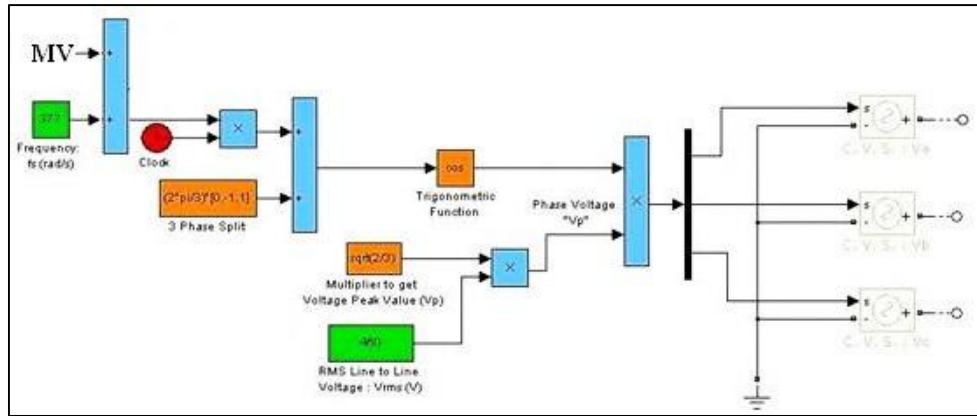


Figure 172: Model in MATLAB/Simulink® referred to the implementation of induction generator simplified scalar control (green blocks – supply frequency and voltage) with the closed loop feedback from PI controller (MV)

The PID controller is adjusted to **reduce noise** of the OCT torque and RPM. *Zielger-Nichols tuning method* is used to determine the gain parameters: K_I , K_P and K_D [164]. The integral and the derivative gain are *first set to zero* and the proportional gain is *slowly increased* until an oscillation of the control variable (RPM) can be observed. Once determined, the proportional gain is saved as the ultimate value K_u and the period of oscillation, T_u , is measured. Finally K_P and K_I are calculated based on the following equations [164]:

$$K_p = 0,6 \cdot K_u \quad (4.14)$$

$$K_I = (1,2 \cdot K_u) / T_u \quad (4.15)$$

$$K_D = 0,075 \cdot K_u \cdot T_u \quad (4.16)$$

In our case the *set point* is the *desired mechanical rotational speed of the generator*, ω_m^d , the *process value* is the *actual mechanical rotational speed*, ω_m , the process block is the SCIG block and the *manipulated variable (MV)* is the *electrical supply frequency correction signal* which is superimposed to the steady state (constant) rad/s set point as shown in Figure 172. All the above is shown in Figure 173 (Author).

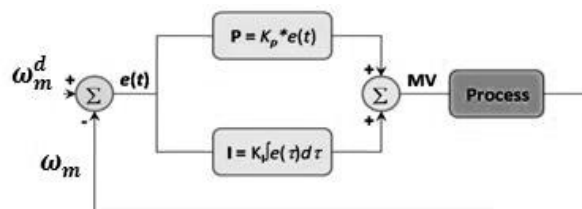


Figure 173: General form of the PI Controller (Source: Author)

The values for the gain parameters are shown in Table 13. Following establishing industrial practice, the D term of PID control is zero deliberately *due to the amplification of noise of the OCT's torque*. ***The inertia of the generator already damps the OCT so there is no need of additional term that complicates the tuning***. Another reason is that a PID controller is used rarely in industrial applications (controlling processes) and especially for the control of rotational speed of an electric motor/generator where a PI has predominated [163].

Table 13: Controller gains

K_P	0.001
K_I	0.015
K_D	0.000

4.3 OCECS Simulation Results

In this section, steady state numerical results of the Ocean Current Energy Conversion System (OCECS), which implemented in MATLAB/Simulink®, are presented. The system, as presented in Figure 166, is intended for the 720 kW SCIG which is connected with the 20 meter rotor diameter SNMREC's 720 kW variable pitch ocean current turbine (OCT).

Two different cases are examined based on different ocean current velocity (V_c). **The first case is for $V_c = 1$ m/s which consider the pessimistic scenario and the second case is for $V_c = 2$ m/s which is the optimistic scenario.** For each one of the cases, numerical simulations were conducted for different steady state operation points. The above mentioned cases are also shown here so that demonstrate the ability of the developed controller to achieve specified rotational velocity set-points, through a correction to the steady state value, when the system is operating in any operational point.

The solver parameters were used, for the simulation of the OCECS, are given in Table 14.

Table 14: Solver parameters for OCECS

Type	Variable-Step
Solver	ode23tb
Relative Tolerance	0.0001
Max Step Size	0.002
Min Step Size	0.00000000001
Solver Reset Method	Fast

Steady state analysis of the OCECS for two different current velocities and the response of the system to the PID corrections are presented in the below sections.

4.3.1 Scenario I ($V_c = 1$ m/s)

This numerical simulation run was conducted to evaluate the steady state behavior of the 720 kW OCECS which consist of the 720 kW SCIG (Section 2.4.2) with the simplified version of VSI (Section 3.5), a shaft line of 2 components ($n=2$) and length of 4 meters (Section 4.2.1.3), a PID Controller applied at $t = 2$ seconds (Section 4.2.1.4) and the 720 kW rigidly mounted OCT model (Section 4.2.1.1). The initial conditions, at $t=0$ second, are all set to zero except for the initial slip ratio of the SCIG which set to start from 100%. The reduction gear ratio, i_{gear} , was chosen **1/90** and the ocean current velocity, V_c , is **1 m/s**.

The steady state behavior of the OCECS was evaluated for three different operation points which are shown below:

- $N_{turbine} = 10$ RPM (so $\omega_m \approx 900$ RPM) and $V/Hz = \text{constant}$ (60 Hz, 460 V_{rms})
- $N_{turbine} = 7$ RPM (so $\omega_m \approx 630$ RPM) and $V/Hz = \text{constant}$ (42 Hz, 322 V_{rms})
- $N_{turbine} = 4$ RPM (so $\omega_m \approx 360$ RPM) and $V/Hz = \text{constant}$ (24 Hz, 184 V_{rms})

The above mentioned different values of $N_{turbine}$ for the same ocean current velocity V_c , based on the different pitch angle of the OCT blades (see assumptions). Simulation in steady state conditions of the 720 kW OCECS with above set parameters and the closed loop response in PID corrections are shown in Figures 174÷191.

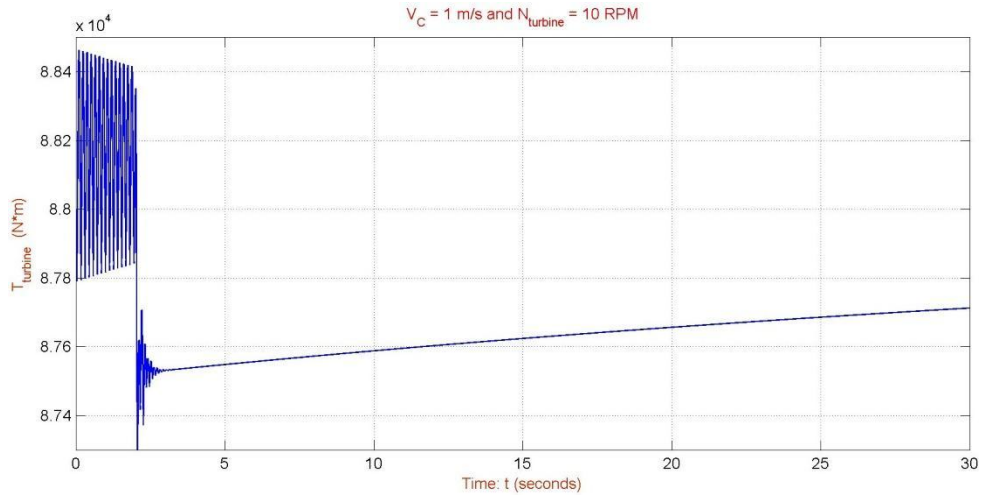


Figure 174: T_{turbine} versus time for 720 kW OCECS and steady state conditions $V_c = 1 \text{ m/s}$ and $N_{\text{turbine}} = 10 \text{ RPM}$

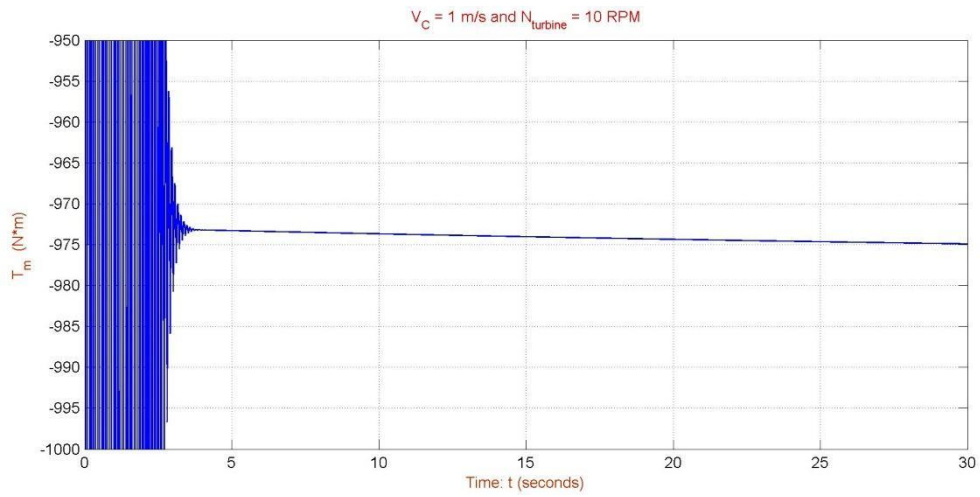


Figure 175: T_m versus time for 720 kW OCECS and steady state conditions $V_c = 1 \text{ m/s}$ and $N_{\text{turbine}} = 10 \text{ RPM}$

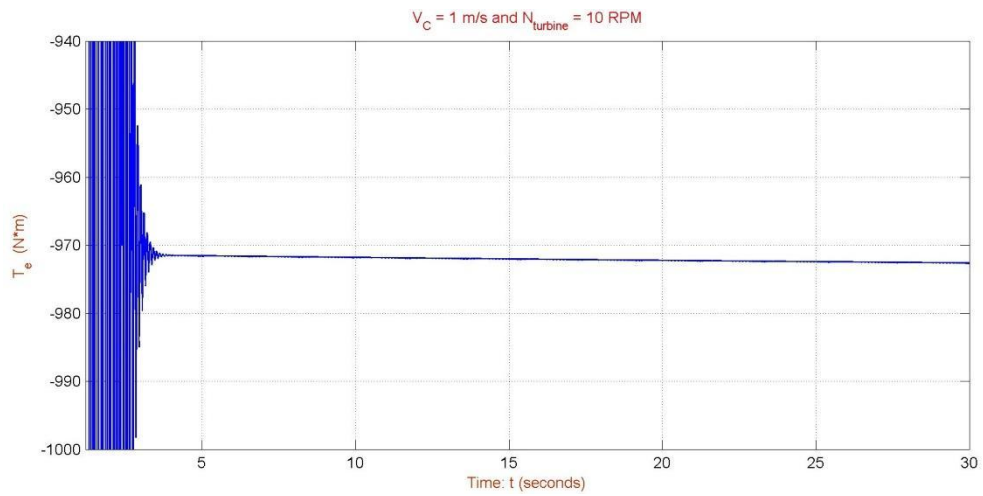


Figure 176: T_e versus time for 720 kW OCECS and steady state conditions $V_c = 1 \text{ m/s}$ and $N_{\text{turbine}} = 10 \text{ RPM}$

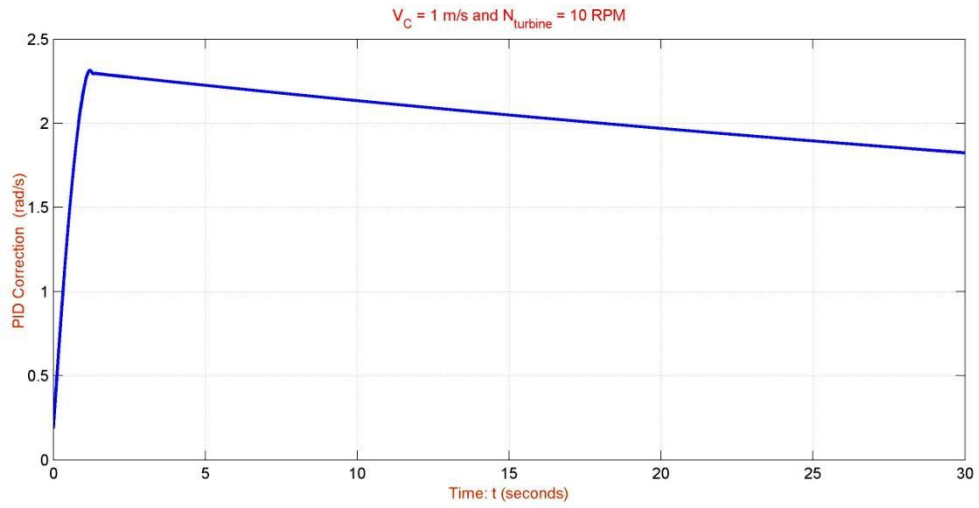


Figure 177: PID Correction versus time for 720 kW OCECS and steady state conditions $V_c = 1$ m/s and $N_{\text{turbine}} = 10$ RPM

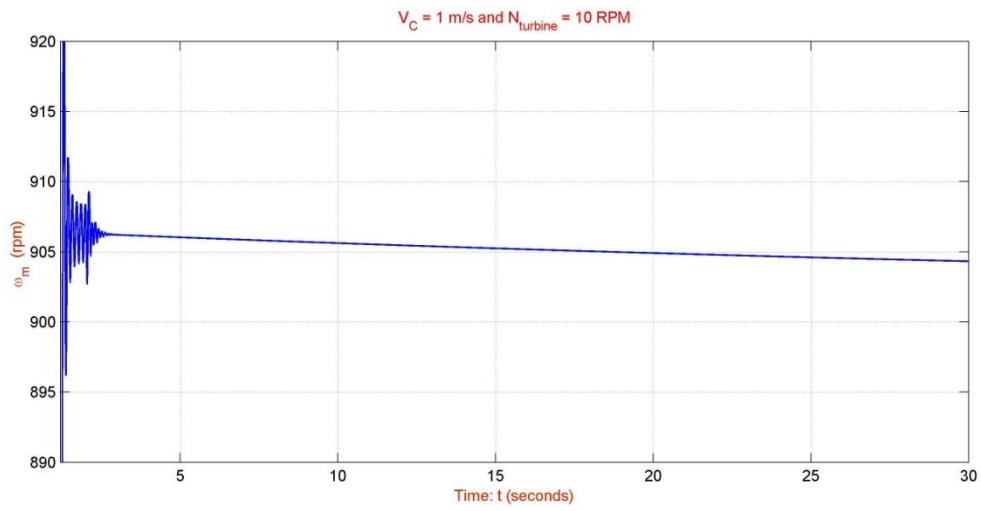


Figure 178: ω_m versus time for 720 kW OCECS and steady state conditions $V_c = 1$ m/s and $N_{\text{turbine}} = 10$ RPM

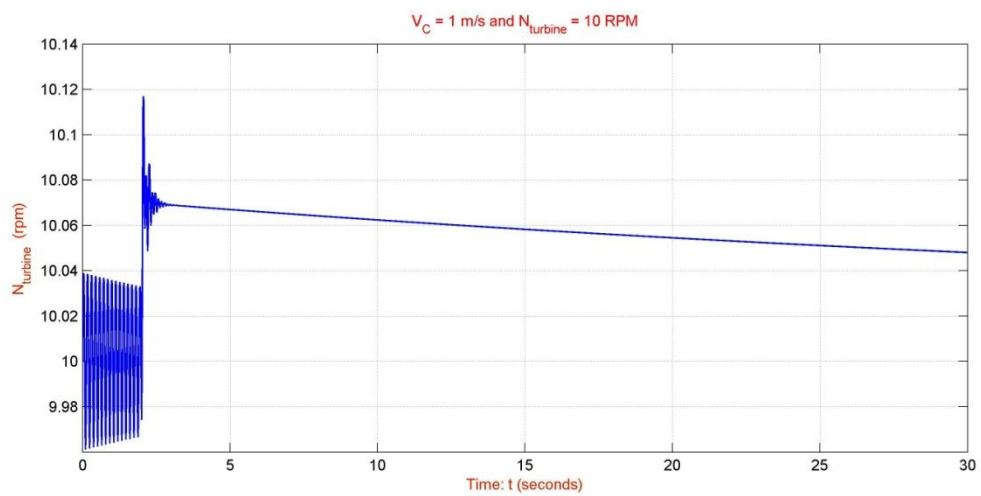


Figure 179: N_{turbine} versus time for 720 kW OCECS and steady state conditions $V_c = 1$ m/s and $N_{\text{turbine}} = 10$ RPM

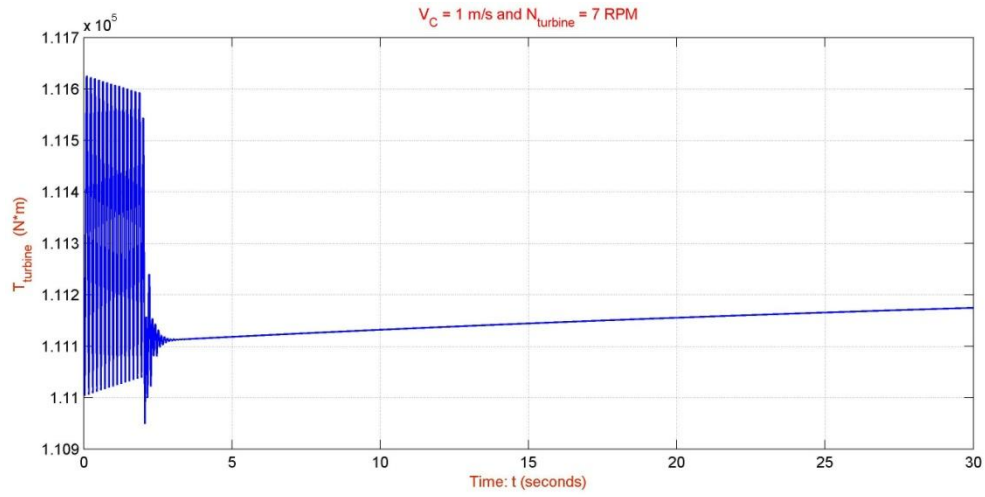


Figure 180: T_{turbine} versus time for 720 kW OCECS and steady state conditions $V_c = 1 \text{ m/s}$ and $N_{\text{turbine}} = 7 \text{ RPM}$

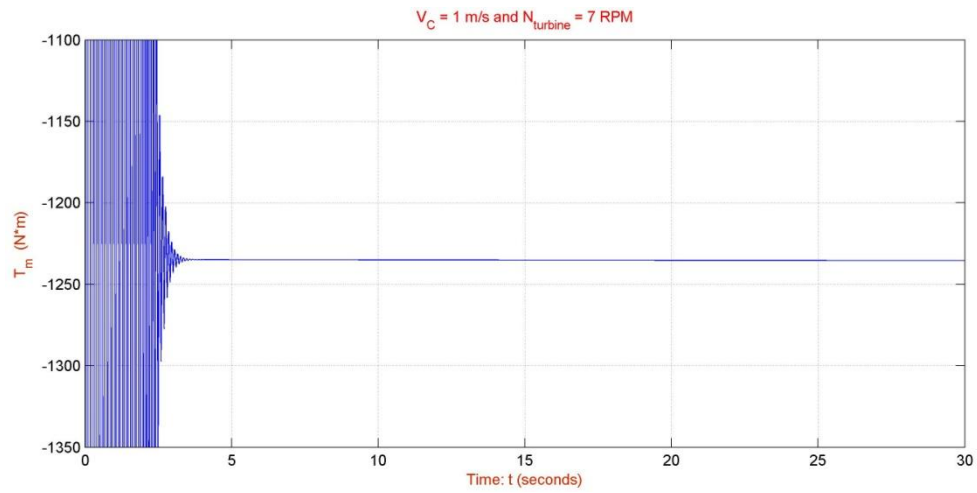


Figure 181: T_m versus time for 720 kW OCECS and steady state conditions $V_c = 1 \text{ m/s}$ and $N_{\text{turbine}} = 7 \text{ RPM}$

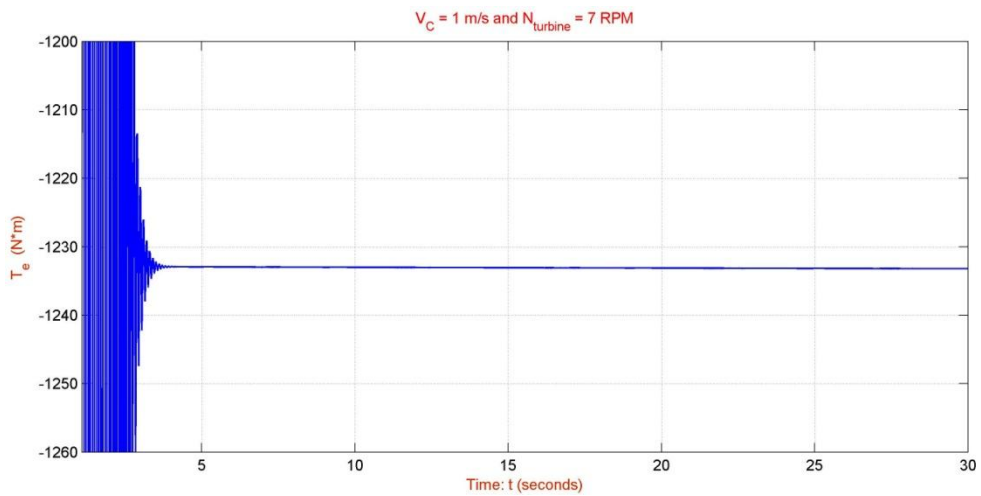


Figure 182: T_e versus time for 720 kW OCECS and steady state conditions $V_c = 1 \text{ m/s}$ and $N_{\text{turbine}} = 7 \text{ RPM}$

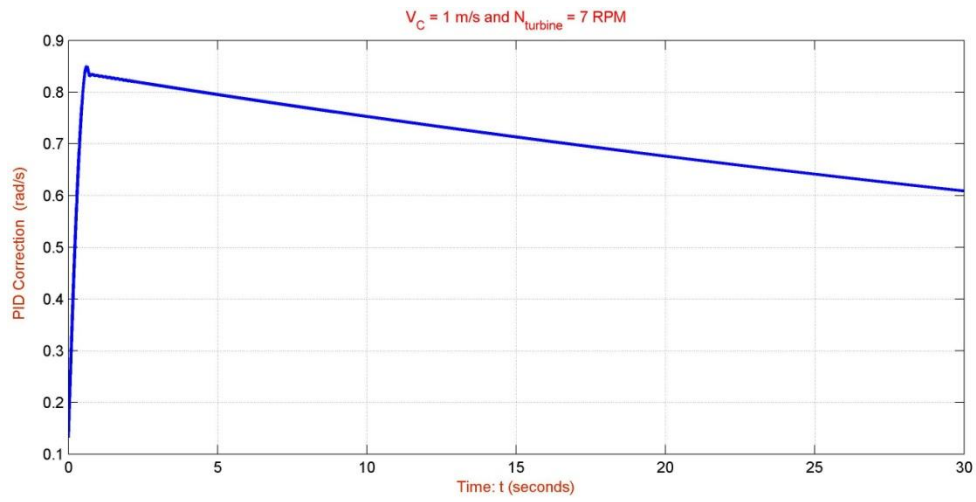


Figure **183**: PID Correction versus time for 720 kW OCECS and steady state conditions $V_c = 1 \text{ m/s}$ and $N_{\text{turbine}} = 7 \text{ RPM}$

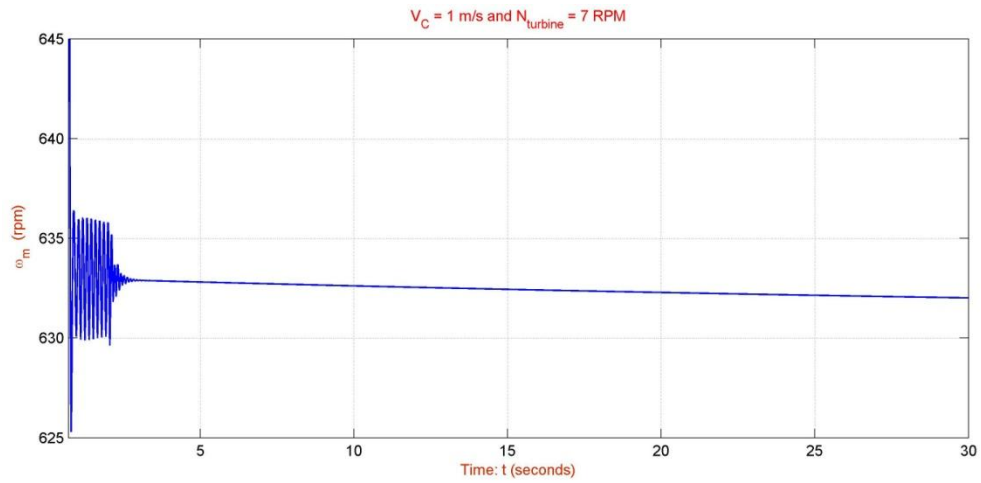


Figure **184**: ω_m versus time for 720 kW OCECS and steady state conditions $V_c = 1 \text{ m/s}$ and $N_{\text{turbine}} = 7 \text{ RPM}$

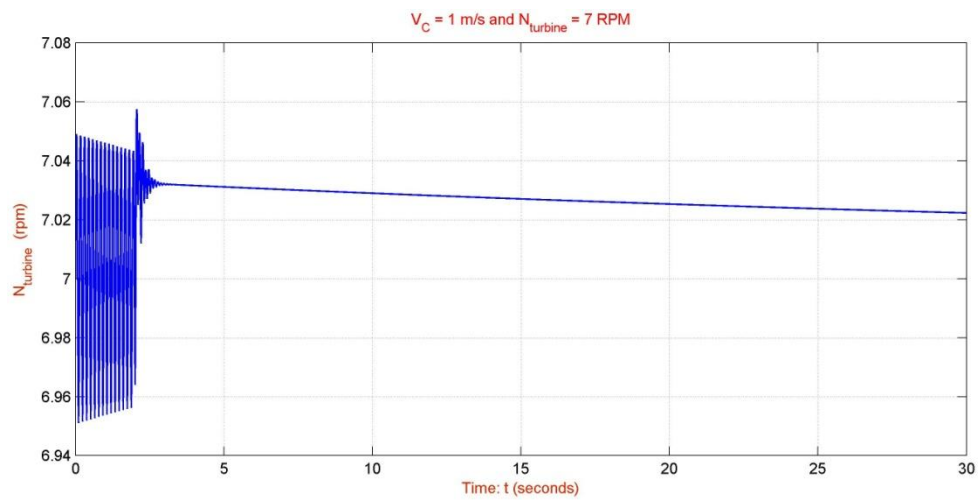


Figure **185**: N_{turbine} versus time for 720 kW OCECS and steady state conditions $V_c = 1 \text{ m/s}$ and $N_{\text{turbine}} = 7 \text{ RPM}$

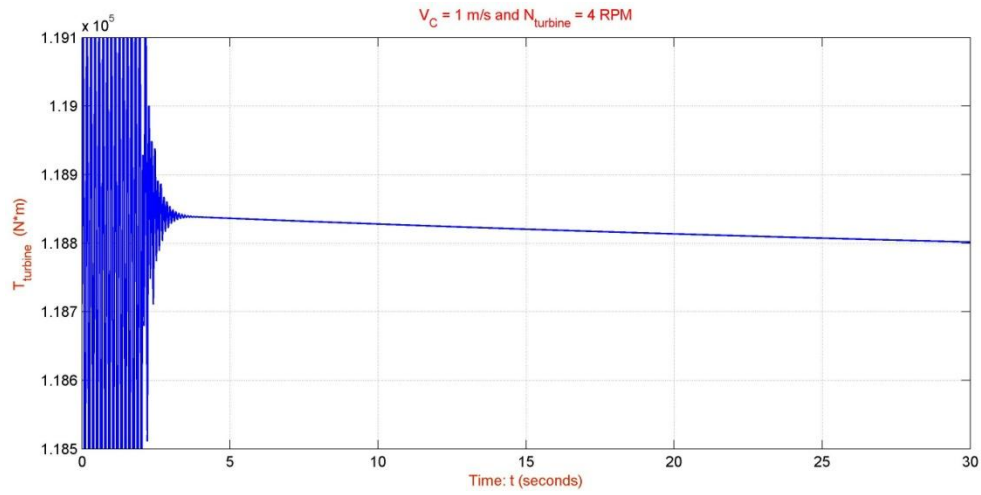


Figure 186: T_{turbine} versus time for 720 kW OCECS and steady state conditions $V_c = 1 \text{ m/s}$ and $N_{\text{turbine}} = 4 \text{ RPM}$

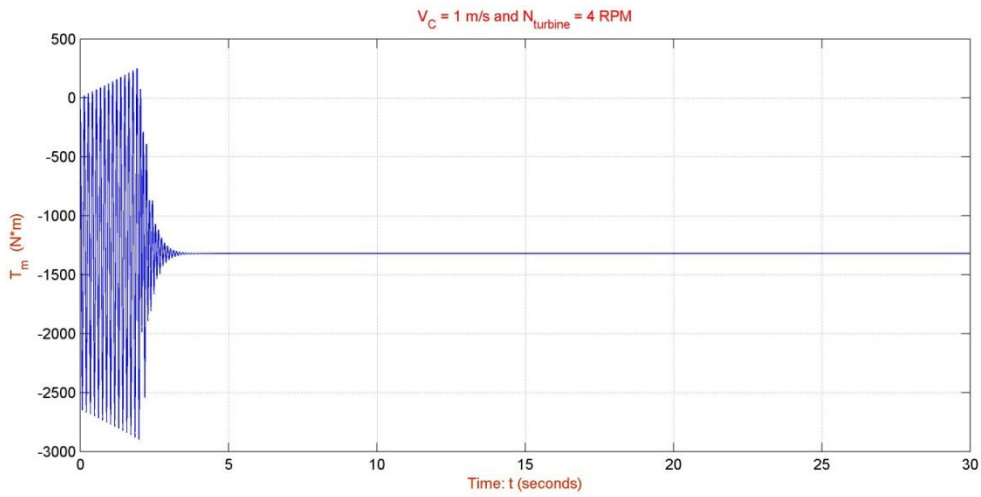


Figure 187: T_m versus time for 720 kW OCECS and steady state conditions $V_c = 1 \text{ m/s}$ and $N_{\text{turbine}} = 4 \text{ RPM}$

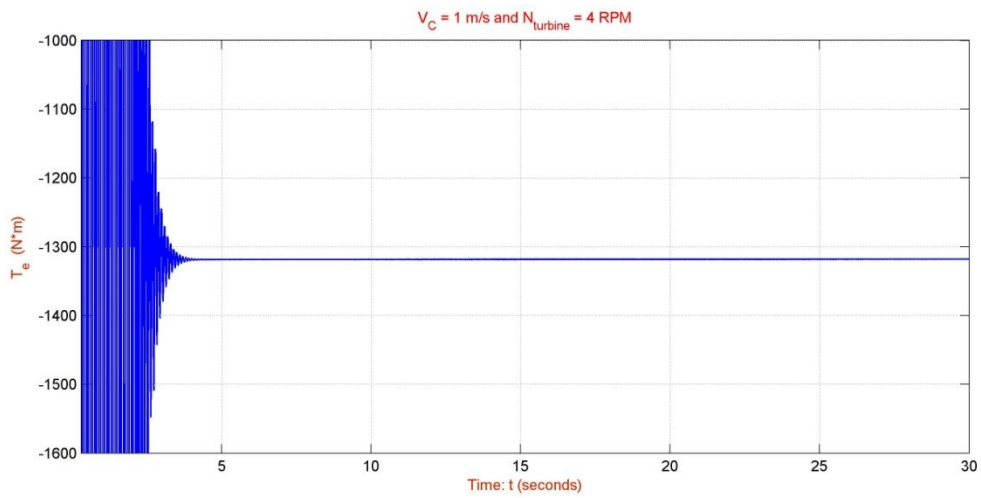


Figure 188: T_e versus time for 720 kW OCECS and steady state conditions $V_c = 1 \text{ m/s}$ and $N_{\text{turbine}} = 4 \text{ RPM}$

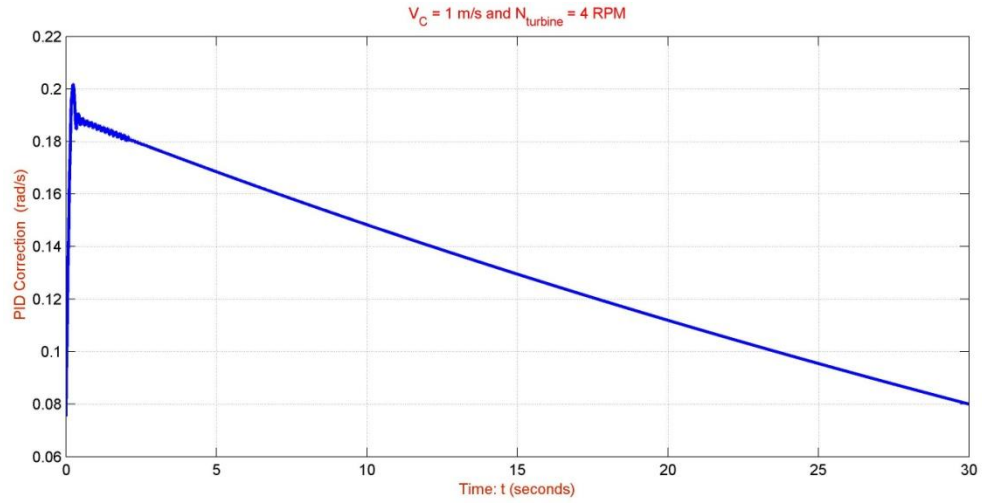


Figure 189: PID Correction versus time for 720 kW OCECS and steady state conditions $V_c = 1$ m/s and $N_{\text{turbine}} = 4$ RPM

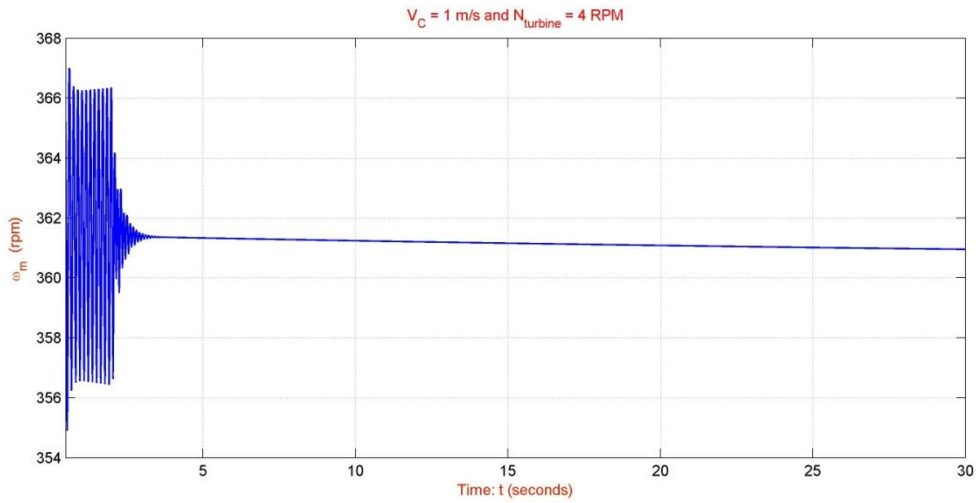


Figure 190: ω_m versus time for 720 kW OCECS and steady state conditions $V_c = 1$ m/s and $N_{\text{turbine}} = 4$ RPM

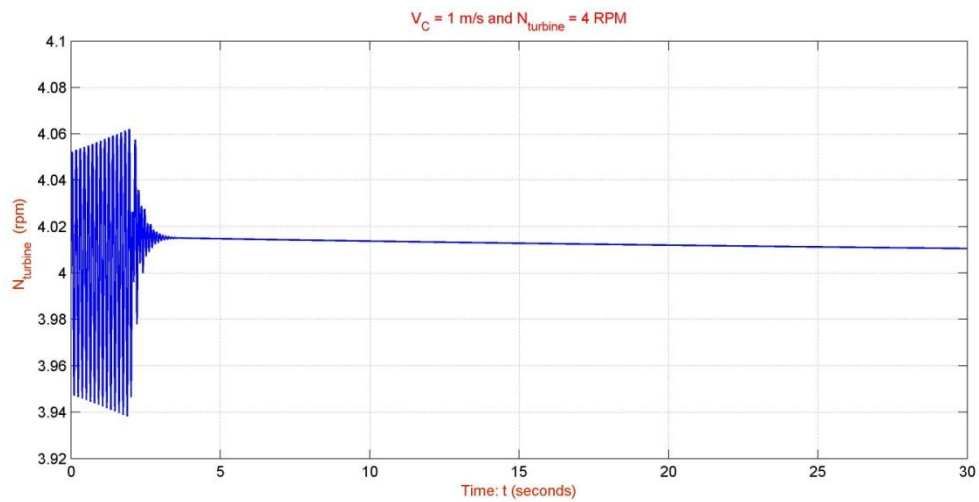


Figure 191: N_{turbine} versus time for 720 kW OCECS and steady state conditions $V_c = 1$ m/s and $N_{\text{turbine}} = 4$ RPM

The OCT generated torque, $T_{turbine}$, is shown in Figures 174, 180 and 186 for OCT angular velocity of 10, 7 and 4 RPM respectively. The mechanical load of the SCIG, T_m , is presented in Figures 175, 181 and 187 for OCT angular velocity of 10, 7 and 4 RPM respectively when the SCIG electromagnetic torque, T_e , is shown in Figures 176, 182 and 188. Moreover, the PID correction for the three different operation points of the OCECS is presented in Figures 177, 183 and 189 while the angular velocity of the SCIG, ω_m , and the OCT, $N_{turbine}$, is shown in Figures 178, 184, 190 and 179, 185, 191 respectively.

The RPM of the OCECS when the controller is applied (at $t=2$ seconds) has a very short oscillatory response, followed by a relatively slow convergence towards the RPM set point (three different operation points – 10 or 7 or 4 RPM) with approximately 50% of the initial RPM error eliminated in the first 25 seconds (Figures 178, 179, 184, 185, 190 and 191). The torques of the OCECS, $T_{turbine}$, T_m and T_e , depends directly ($T_{turbine}$) or indirectly (T_e and T_m) from the current flow speed (V_c), the RPM of the system and previous torque values and therefore since V_c is constant and the RPM are approximately constant, all the torques converges towards constant values.

For any operation point, the controller is shown to converge the mean system RPM towards the RPM-set point for the OCECS system (10, 7 and 4 RPM) as well as the SCIG and OCT torque. The only difference is the initial RPM error of the set point where as the operation point getting lower the error diminished and the convergence to the RPM set point is faster.

4.3.2 Scenario II ($V_c = 2$ m/s)

This numerical simulation run was conducted to evaluate the steady state behavior of the 720 kW OCECS which consist of the 720 kW SCIG (Section 2.4.2) with the simplified version of VSI (Section 3.5), a shaft line of 2 components ($n=2$) and length of 4 meters (Section 4.2.1.3), a PID Controller (Section 4.2.1.4) and the 720 kW rigidly mounted OCT model (Section 4.2.1.1). The initial conditions, at $t=0$ second, are all set to zero except for the initial slip ratio of the SCIG which set to start from 100%. The reduction gear ratio, i_{gear} , was chosen $1/90$ and the ocean current velocity, V_c , is 2 m/s.

The steady state behavior of the OCECS was evaluated for three different operation points which are shown below:

- $N_{turbine} = 10$ RPM (so $\omega_m \approx 900$ RPM) and $V/Hz = \text{constant}$ (60 Hz, 460 V_{rms})
- $N_{turbine} = 7$ RPM (so $\omega_m \approx 630$ RPM) and $V/Hz = \text{constant}$ (42 Hz, 322 V_{rms})
- $N_{turbine} = 4$ RPM (so $\omega_m \approx 360$ RPM) and $V/Hz = \text{constant}$ (24 Hz, 184 V_{rms})

The above mentioned different values of $N_{turbine}$ for the same ocean current velocity V_c , based on the different pitch angle of the OCT blades (see assumptions). Simulation in steady state conditions of the 720 kW OCECS with above set parameters and the response in PID corrections are shown in Figures 192÷209.

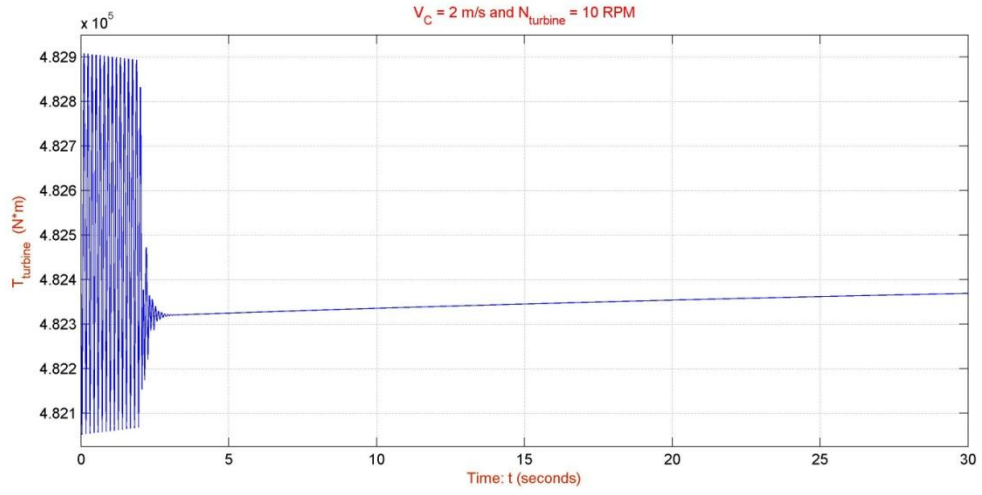


Figure 192: T_{turbine} versus time for 720 kW OCECS and steady state conditions $V_c = 2$ m/s and $N_{\text{turbine}} = 10$ RPM

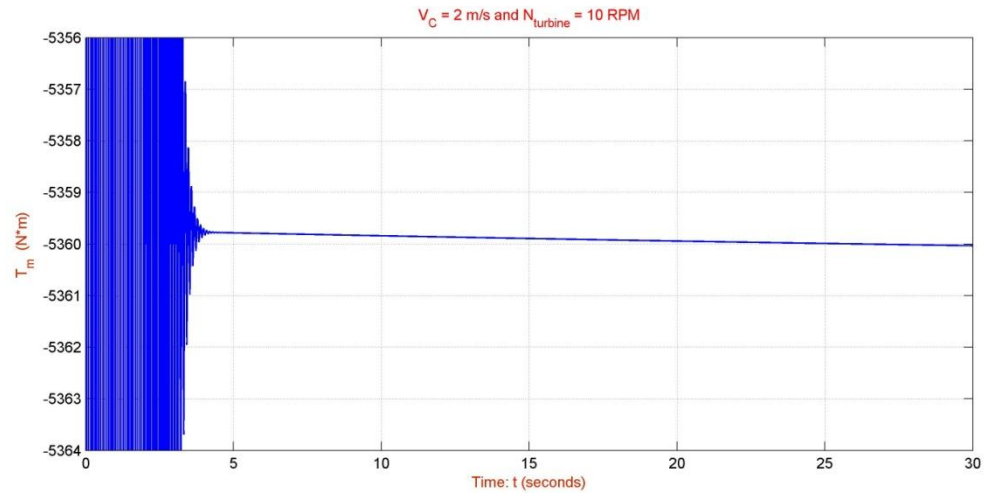


Figure 193: T_m versus time for 720 kW OCECS and steady state conditions $V_c = 2$ m/s and $N_{\text{turbine}} = 10$ RPM

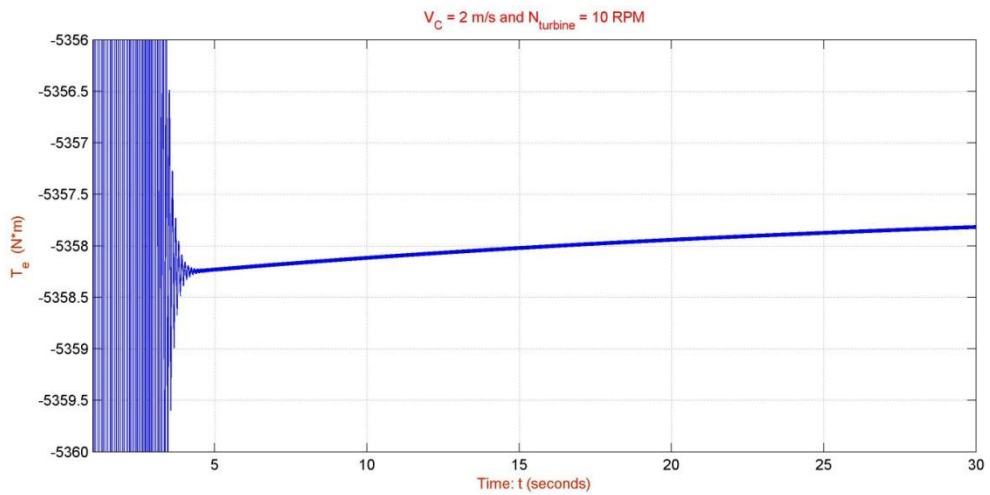


Figure 194: T_e versus time for 720 kW OCECS and steady state conditions $V_c = 2$ m/s and $N_{\text{turbine}} = 10$ RPM

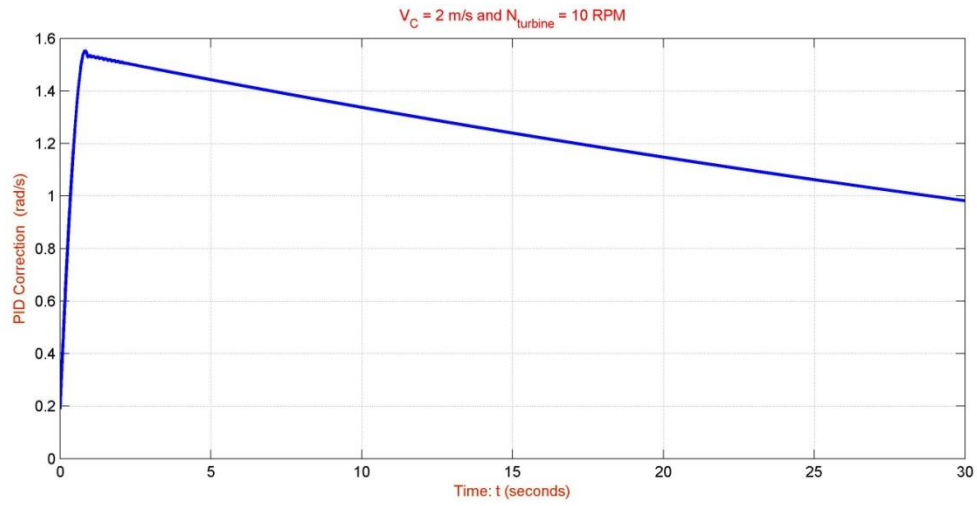


Figure 195: PID Correction versus time for 720 kW OCECS and steady state conditions $V_c = 2$ m/s and $N_{\text{turbine}} = 10$ RPM

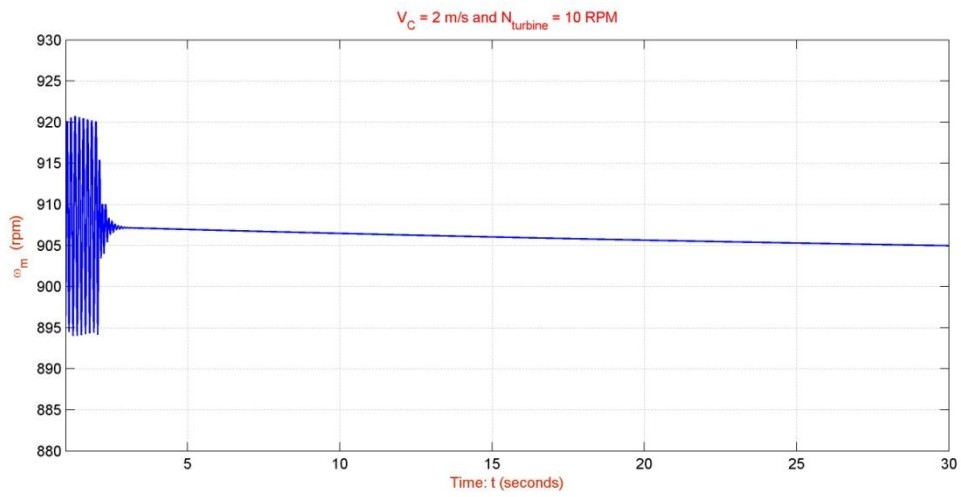


Figure 196: ω_m versus time for 720 kW OCECS and steady state conditions $V_c = 2$ m/s and $N_{\text{turbine}} = 10$ RPM

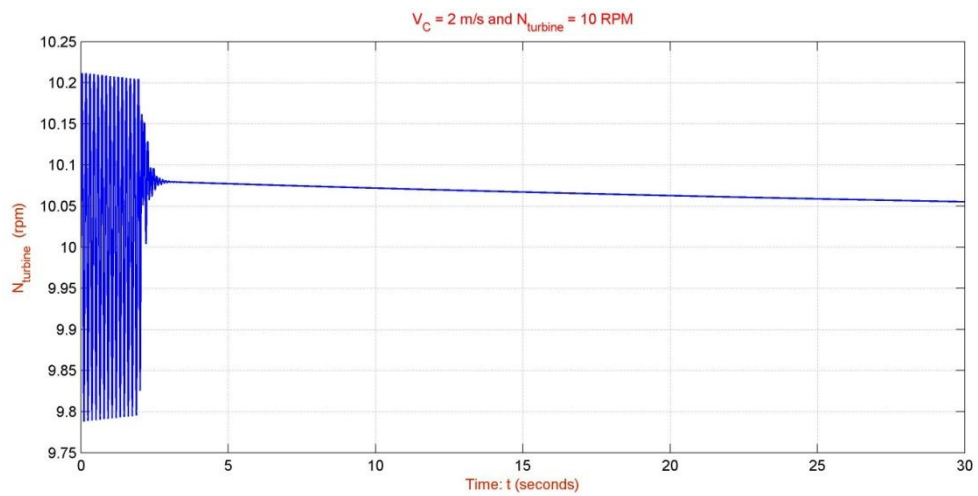


Figure 197: N_{turbine} versus time for 720 kW OCECS and steady state conditions $V_c = 1$ m/s and $N_{\text{turbine}} = 10$ RPM

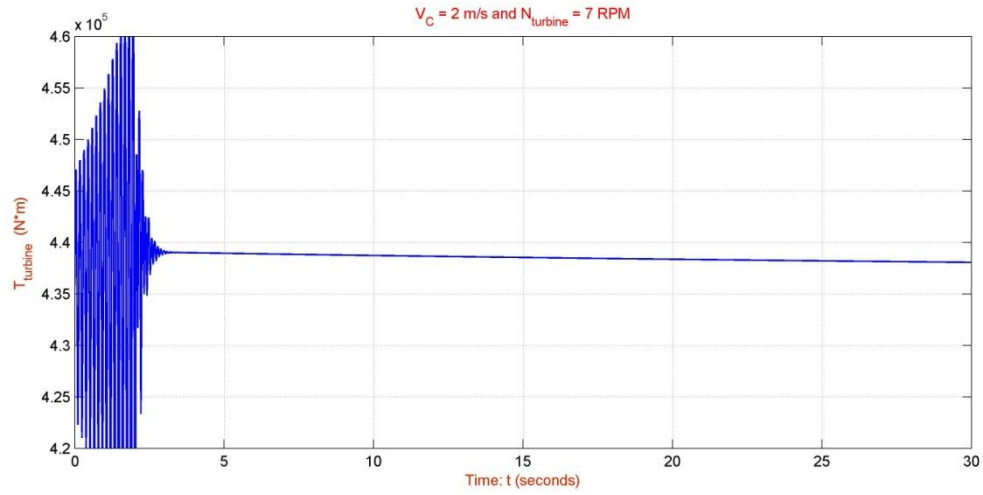


Figure 198: T_{turbine} versus time for 720 kW OCECS and steady state conditions $V_c = 2 \text{ m/s}$ and $N_{\text{turbine}} = 7 \text{ RPM}$

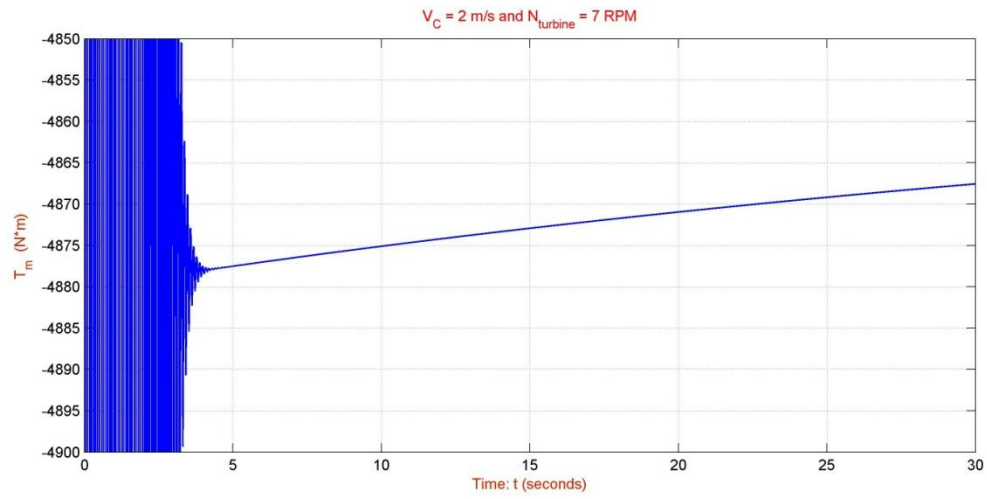


Figure 199: T_m versus time for 720 kW OCECS and steady state conditions $V_c = 2 \text{ m/s}$ and $N_{\text{turbine}} = 7 \text{ RPM}$

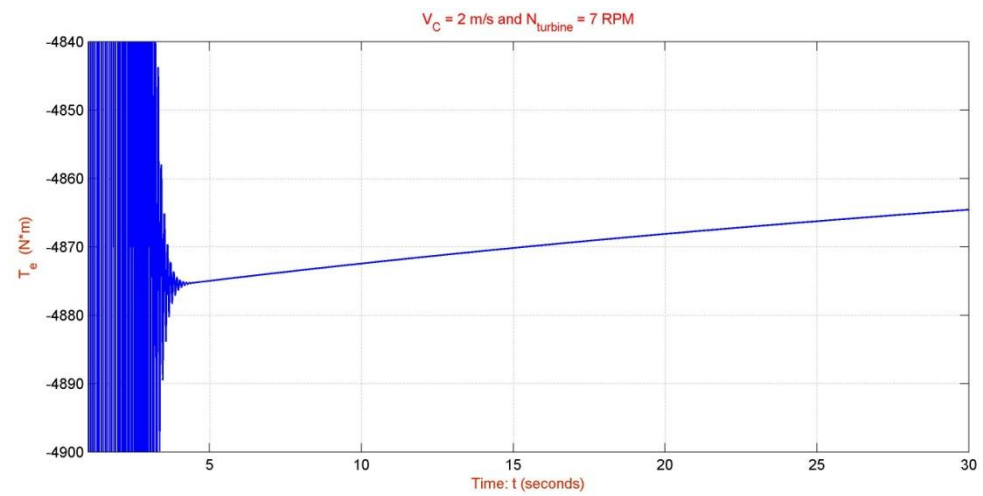


Figure 200: T_e versus time for 720 kW OCECS and steady state conditions $V_c = 2 \text{ m/s}$ and $N_{\text{turbine}} = 7 \text{ RPM}$

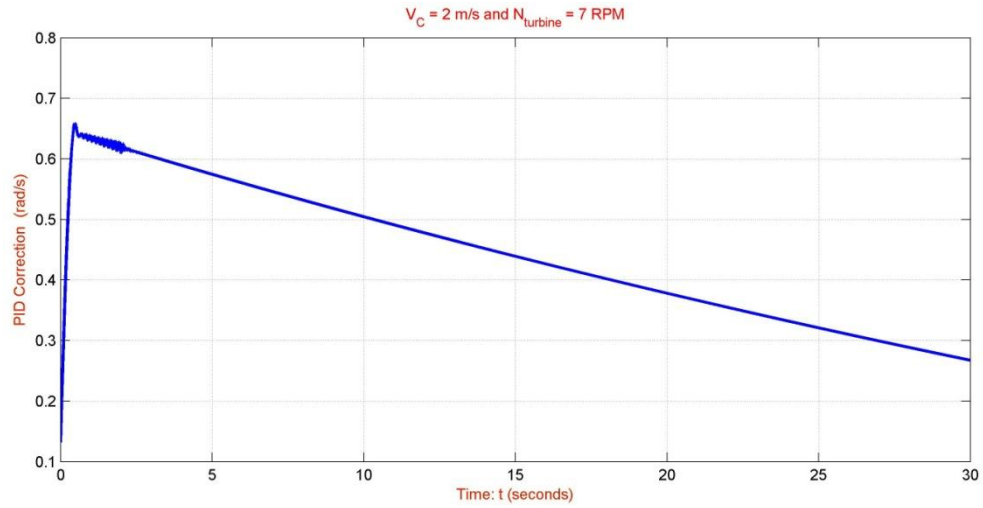


Figure 201: PID Correction versus time for 720 kW OCECS and steady state conditions $V_c = 2$ m/s and $N_{\text{turbine}} = 7$ RPM

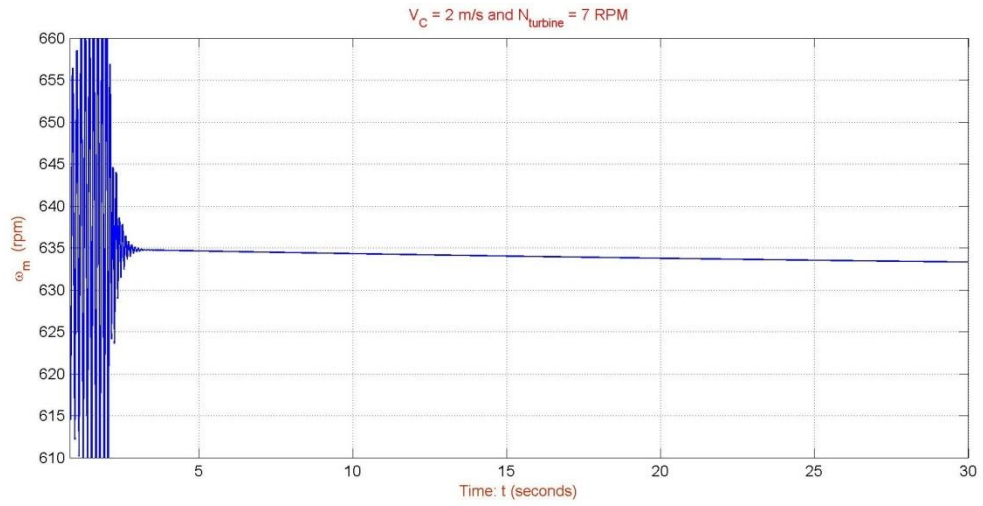


Figure 202: ω_m versus time for 720 kW OCECS and steady state conditions $V_c = 2$ m/s and $N_{\text{turbine}} = 7$ RPM

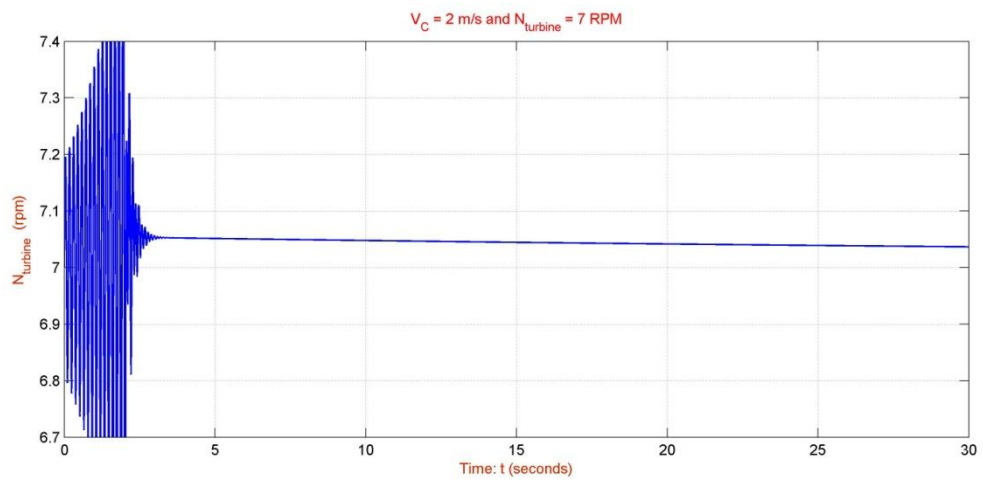


Figure 203: N_{turbine} versus time for 720 kW OCECS and steady state conditions $V_c = 2$ m/s and $N_{\text{turbine}} = 7$ RPM

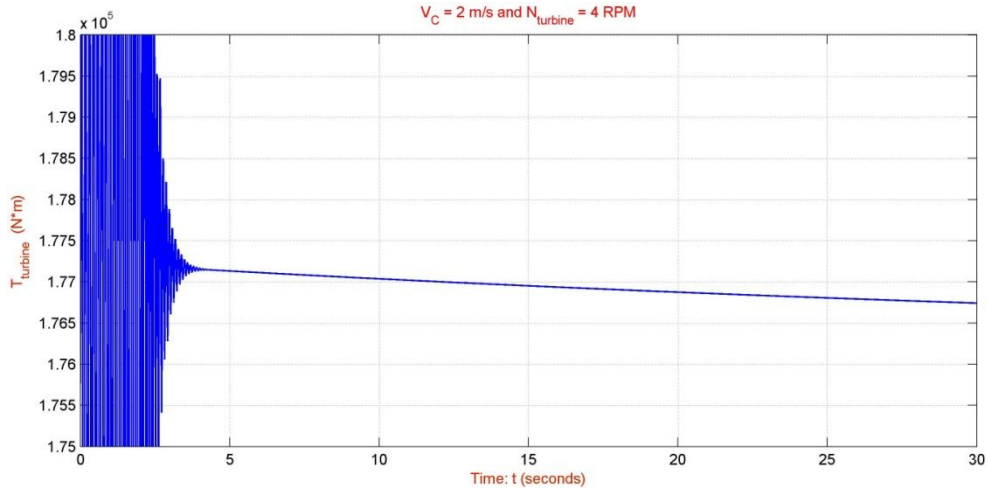


Figure 204: T_{turbine} versus time for 720 kW OCECS and steady state conditions $V_c = 2$ m/s and $N_{\text{turbine}} = 4$ RPM

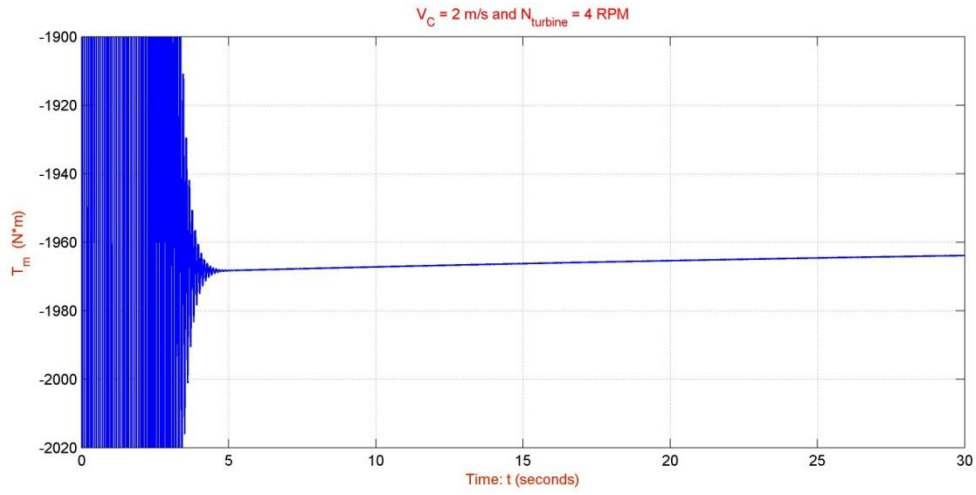


Figure 205: T_m versus time for 720 kW OCECS and steady state conditions $V_c = 2$ m/s and $N_{\text{turbine}} = 4$ RPM

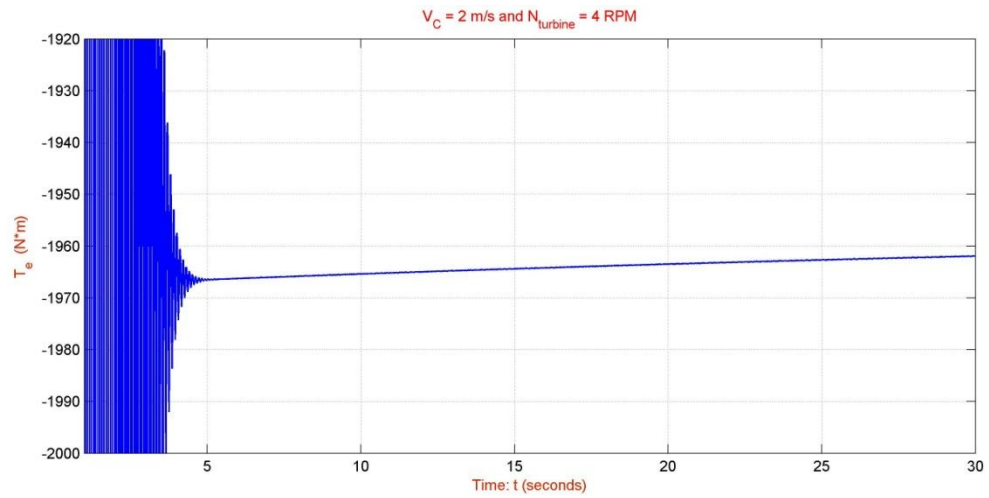


Figure 206: T_e versus time for 720 kW OCECS and steady state conditions $V_c = 2$ m/s and $N_{\text{turbine}} = 4$ RPM

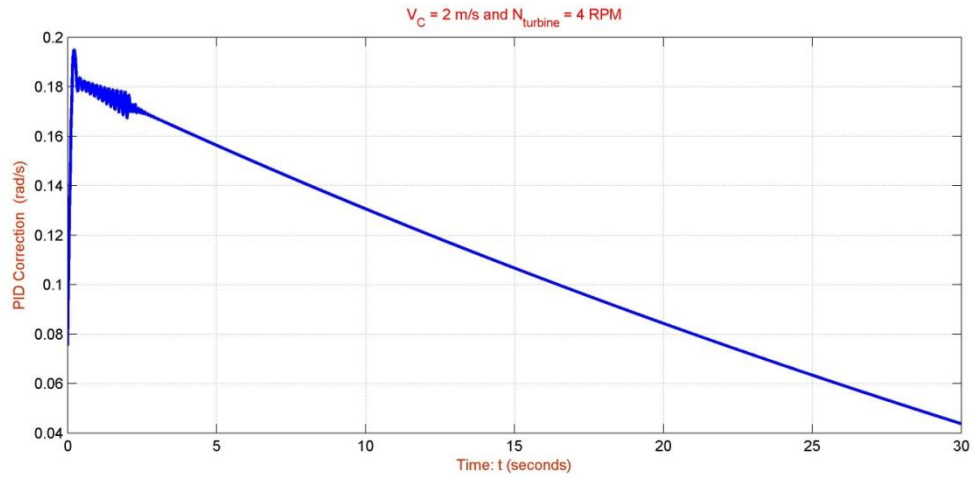


Figure 207: PID Correction versus time for 720 kW OCECS and steady state conditions $V_c = 2$ m/s and $N_{\text{turbine}} = 4$ RPM

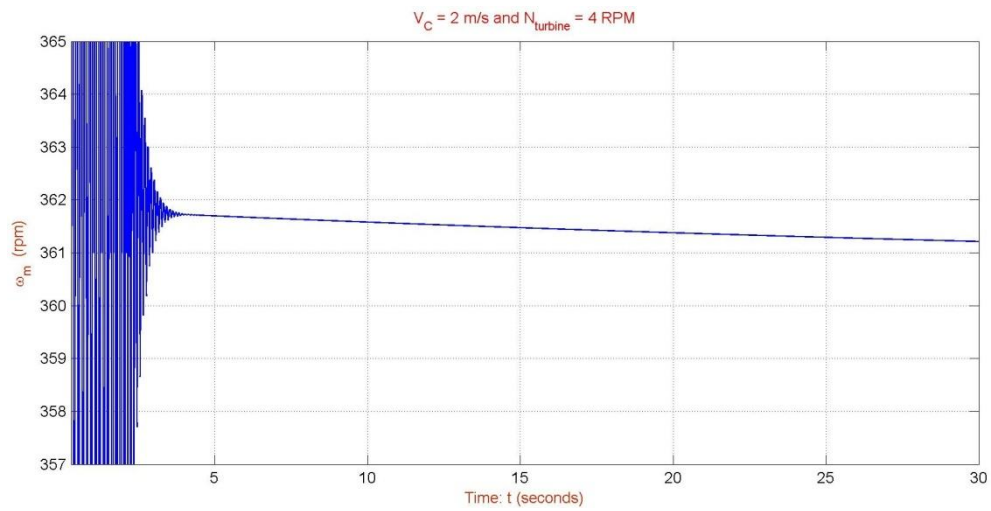


Figure 208: ω_m versus time for 720 kW OCECS and steady state conditions $V_c = 2$ m/s and $N_{\text{turbine}} = 4$ RPM

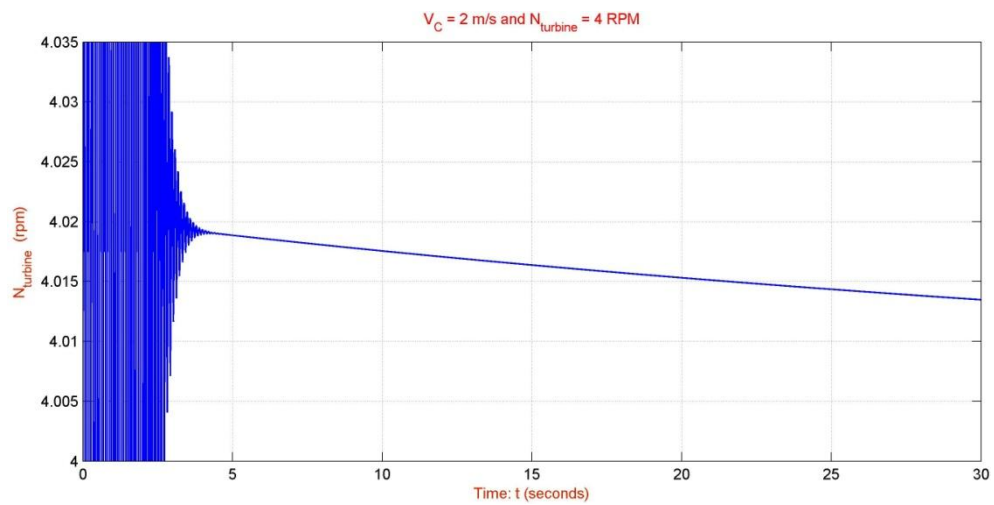


Figure 209: N_{turbine} versus time for 720 kW OCECS and steady state conditions $V_c = 2$ m/s and $N_{\text{turbine}} = 4$ RPM

The OCT generated torque, $T_{turbine}$, is shown in Figures 192, 198 and 204 for OCT angular velocity of 10, 7 and 4 RPM respectively. The mechanical load of the SCIG, T_m , is presented in Figures 193, 199 and 205 for OCT angular velocity of 10, 7 and 4 RPM respectively when the SCIG electromagnetic torque, T_e , is shown in Figures 194, 200 and 206. Moreover, the PID correction for the three different operation points of the OCECS is presented in Figures 195, 201 and 207 while the angular velocity of the SCIG, ω_m , and the OCT, $N_{turbine}$, is shown in Figures 196, 202, 208 and 197, 203, 209 respectively.

The RPM of the OCECS when the controller is applied (at $t=2$ seconds) has a very short oscillatory response, followed by a relatively slow convergence towards the RPM set point (three different operation points – 10 or 7 or 4 RPM) with approximately 25% of the initial RPM error eliminated in the first 25 seconds (Figures 196, 197, 202, 203, 208 and 209). The torques of the OCECS, $T_{turbine}$, T_m and T_e , depends directly ($T_{turbine}$) or indirectly (T_e and T_m) from the current flow speed (V_c), the RPM of the system and previous torque values and therefore since V_c is constant and the RPM are approximately constant, all the torques converges towards constant values.

For any operation point, the controller is shown to converge the mean system RPM towards the RPM-set point for the OCECS system (10, 7 and 4 RPM) as well as the SCIG and OCT torque. The only difference is the initial RPM error of the set point where as the operation point getting lower the error diminished and the convergence to the RPM set point is faster.

4.3.3 Estimation of Average Electric Power Generation

In this section, an *estimation of the average electric power generation* is presented for the 720 kW OCECS. Numerical simulation were conducted in MATLAB/Simulink®, in the same way as in Sections 4.2.3.1 and 4.2.3.2, for all the theoretical operation points (operation envelope) in each of the two different flow speeds (V_c of 1 m/s and 2 m/s) and using the MATLAB code for the calculation of the average electric power (see Appendix H), an estimation of the $kWh/year$ is given through Tables 14÷17. The assumptions have been made are shown below (see also Section 4.2):

- The *ocean current velocity is constant and independent of time* ($V_c = \text{constant}$).
- There are *no power losses after the generator* (from SCIG up to the land grid).
- *Different operation points based on different pitch angle* of the OCT blades.

The average electric power in kW, for all the operation points ($N_{turbine} = 1\div 10 \text{ RPM}$), and for two different flow speeds is presented as shown in Tables 15 and 16.

Table 15: Average electric power of OCECS for flow speed 1m/s and for different operation points

$V_c = 1\text{m/s}$	
$N_{turbine} \text{ (RPM)}$	Average Electric Power by SCIG (kW)
10	180.5
9	178
8	171
7	159.5
6	143
5	122.5
4	96
3	52.5
2	15
1	7

Table 16: Average electric power of OCECS for flow speed 2m/s and for different operation points

$V_c = 2 \text{ m/s}$	
N_{turbine} (RPM)	Average Electric Power by SCIG (kW)
10	1000
9	905
8	790
7	635
6	445
5	270
4	145
3	70
2	29.5
1	8

An energy estimation production in terms of kW·h/day and kW·h/year is given in Tables 17 and 18 for current flow speed 1 m/s and 2 m/s respectively.

Table 17: Energy production of OCECS for flow speed 1 m/s and for different operation points

$V_c = 1 \text{ m/s}$			
N_{turbine} (RPM)	Electric Energy Converted by SCIG (kW·h)	(kW·h / day)	(kW·h / year)
10	180.5	4,332	1,581,180
9	178	4,272	1,559,280
8	171	4,104	1,497,960
7	159.5	3,828	1,397,220
6	143	3,432	1,252,680
5	122.5	2,940	1,073,100
4	96	2,304	840,960
3	52.5	1,260	459,900
2	15	360	131,400
1	7	168	61,320

Table 18: Energy production of OCECS for flow speed 2 m/s and for different operation points

$V_c = 2 \text{ m/s}$			
N_{turbine} (RPM)	Electric Energy Converted by SCIG (kW·h)	(kW·h / day)	(kW·h / year)
10	1000	24,000	8,760,000
9	905	21,720	7,927,800
8	790	18,960	6,920,400
7	635	15,240	5,562,600
6	445	10,680	3,898,200
5	270	6,480	2,365,200
4	145	3,480	1,270,200
3	70	1,680	61,3200
2	29.5	708	25,8420
1	8	192	70,080

Based on the above results and considering the *average energy consumption in terms of kW·h of a household in the state of Florida in USA* [165], it can be revealed ***how many houses can be covered*** by an 720 kW OCECS. More specifically, the average energy consumption of a household in Florida is shown below [165]:

$$1,081 \text{ kW}\cdot\text{h/month} \quad \text{or} \quad 12,970 \text{ kW}\cdot\text{h/year}$$

So, according to Table 17 and the value of OCECS energy production for $N_{\text{turbine}} = 10 \text{ RPM}$, it can be shown that

$$8,760,000 \text{ kW}\cdot\text{h/year} \quad / \quad 12,970 \text{ kW}\cdot\text{h/year} \quad \simeq \quad 675 \text{ houses in Florida}$$

around ***675 houses*** in the state of Florida can be covered from a ***720 kW OCECS*** when N_{turbine} is *10 RPM* and the ***current flow speed is constant at 2 m/s***.

CHAPTER 5

CONCLUSIONS AND FUTURE WORK

Primarily, this study provides a *steady state numerical model for simulating underwater ocean current power-plants*. The numerical simulations are set to mode open and axial flow ocean current turbine connected to a 720 kW induction machine, which acting as motor-generator and using a scalar control method such as constant V/f ratio via a SPWM VSI, through a gearbox. *The ocean current power plant is modeled as being placed in 25 meters depth and also rigidly attached to the sea floor while the symmetrical induction motor/generator plant is modeled using a transient non-linear approach with flux linkages as variables*. A shaft vibrational model is also presented along with a PID controller for the regulating of the induction rotor's rotational speed under steady state conditions.

Contribution of the Study

In this study, many interesting and valuable things are presented as specifically shown below (the bullets are following the flow of the thesis):

- A technology review including ocean current turbines and generator preference (Chapter 1).
- A theoretical (not including design procedures) detailed presentation about asynchronous motors (Chapter 2).
- A detailed analysis of a mathematical modeling for three (3) phase symmetrical induction motors/generators using a transient non-linear approach with flux linkages as variables (Chapter 2).
- Detailed results for two (2) different induction motors/generators in any load condition and in different steady state operation points, including the transient behavior among them, implemented in MATLAB/Simulink® environment (Chapter 2).
- A theoretical detailed presentation about control of asynchronous motors including analysis of the steady state representation of induction motors (Chapter 3).
- Modeling of a SPWM VSI with theoretical analysis of voltages including a comparison with a simplified version in MATLAB/Simulink® environment (Chapter 3).
- A theoretical presentation about Ocean Current Conversion Energy Systems - OCECS (Chapter 4).
- Modeling and analysis of a 720 kW OCECS, including results through the whole operation envelope of the system as well as an estimation of the average electrical power generation based on specific assumptions, implemented in MATLAB/Simulink® environment (Chapter 4).
- A theoretical presentation and modeling of a shaft vibrational model in MATLAB/Simulink® environment (Chapter 4).
- Demonstration of the developed PID controller to achieve specified set-points.
- Eight (8) appendices with complementary material for the above mentioned contributions.

Future Work

Since the Ocean Current Energy Conversion Systems are in preliminary design stage or in a scale prototype level and the lack of results is apparent, the study is open to expand to all directions. As main and essential future developments, the below areas are proposed:

- ✦ Further review and monitor of all the ocean current technologies and future proposed devices along with any results through tank or in situ experiments.
- ✦ Development of a steady state linear approach for the performance and analysis of asynchronous motors as well as testing and verifying the steady state model.
- ✦ Improvement of the existing SPWM VSI model (scalar control) through controlled rectifiers and especially matching of the model with the steady state linear approach for asynchronous motors in order to create different Torque-Speed curves.
- ✦ Development of a vector control method for the control of the existing transient non-linear model implemented for asynchronous motors as well as matching, testing and verifying the control approach.
- ✦ Matching of the steady state linear model with scalar control or the transient non-linear model with vector control on the OCECS and create the optimum operation envelope of the system.

Another track of future work might aim to investigate different kind of generators and comparison between them.

Reference/Bibliography

- [1] Trujillo A.P. and Thurman H.V. (2011), "Essentials Of Oceanography", 10th Edition, Prentice Hall, USA
- [2] Rahmstorf, S. (2003), "The Concept of the Thermohaline Circulation", Nature 421 (6924): 699
- [3] http://earthobservatory.nasa.gov/Features/Paleoclimatology_Evidence/paleoclimatology_evidence_2.php
- [4] Pidwirny, M. (2006), "Fundamentals of Physical Geography", 2nd Edition, PhysicalGeography.net (online)
- [5] University of Texas Libraries (2006), "Perry Casteñada Library Collection."
- [6] Perry R. and Green D.W. (2007), "Perry's Chemical Engineering Handbook", 8th Edition, McGraw Hill Education, USA
- [7] U.S. Department of the Interior (2006), "Technology White Paper on Ocean Current Energy Potential on the U.S. Outer Continental Shelf", Washington DC, Minerals Management Service – Renewable Energy & Alternate Use Program, <http://www.boem.gov/Ocean-Current-White-Paper-2006/>
- [8] US International Energy Agency (2014), "World Energy Outlook 2014", <http://www.iea.org/Textbase/npsum/WEO2014SUM.pdf>
- [9] VanZwieten J.H. et all. (2013), "Global Ocean Current Energy Assessment - An Initial Look", Proceedings of the 1st Marine Energy Technology Symposium (METS13), April 10-11, Washington D.C, USA
- [10] Georgia Tech University (2011), "Assessment of Energy Production Potential from Ocean Currents along the United States Coastline", Georgia Tech Research Corporation, Atlanta, GA, USA, http://www1.eere.energy.gov/water/pdfs/energy_production_ocean_currents_us.pdf
- [11] <http://www.ecopedia.com/energy/how-do-underwater-turbines-work/>
- [12] Florida Atlantic University (FAU), <http://www.fau.edu>
- [13] Bedard R. (2006), " Overview: EPRI Ocean Energy Program", Presented to the Duke University Global Change Center, http://oceanenergy.epri.com/attachments/ocean/briefing/Duke_Sep_14.pdf
- [14] Betz, A. and Randall D.G. (1966), "Introduction to the Theory of Flow Machines", Oxford Pergamon Press, UK
- [15] https://en.wikipedia.org/wiki/Betz%27s_law
- [16] VanZwieten J.H., Seibert M.G and Ellenrieder K.V. (2012), "Anchor Selection Study for Ocean Current Turbines", Technical Report SNMREC/TR-12-003, Florida Atlantic University, SNMREC, USA
- [17] VanZwieten J.H., Seibert M.G and Ellenrieder K.V. (2010), "Determining Anchoring Systems for Ocean Energy Harvesting Devices off the Coast of Southeast Florida", Proceedings of the MTS/IEEE Oceans'10 Conference, September 20-23, Seattle, Washington, USA
- [18] Rokke A. and Nilssen R. (2013), "Marine Current Turbines & Generator Preferences - A Technology Review", Renewable Energy and Power Quality Journal (RE&PQJ), EA4EPQ, ISSN 2172-038 X, No.11, Paper 299
- [19] Finkl C.W. and Charlier R. (2009), "Electric Power Generation From Ocean Currents In The Straight Of Florida - Some Environmental Considerations", Journal of Renewable and Sustainable Energy Reviews, Elsevier, Vol. 13, pp 2597-2604
- [20] Charlier, R.H., and J.R. Justus (1993), "Ocean Energies: Environmental, Economic and Technological Aspects of Alternative Power Sources", Elsevier Science Publishers, Amsterdam, The Netherlands
- [21] Moreno N., Sallent R., Espi A., Bao D. and Teillet Y. (2008), "Ocean's Current Energy – How to Produce Electrical Energy thanks to the Marine Currents", University of Gavle, Project in the Course of Renewable Energy, Sweden, <http://www.exergy.se/goran/hig/re/08/ocean.pdf>

- [22] U.S. Department Of Energy (2009), “Report to Congress on the Potential Environmental Effects of Marine and Hydrokinetic Energy Technologies”, Office of Energy Efficiency and Renewable Energy, Federal Energy Management Program, http://energy.gov/sites/prod/files/2013/12/f5/doe_eisa_633b.pdf
- [23] U.S. National Geospatial-Intelligence Agency, Office of Geomatics, Transaction 8305, Version 2a, Chapter 3, <http://earth-info.nga.mil/GandG/publications/tr8350.2/tr8350.2-a/Chapter%203.pdf>
- [24] <http://oceanservice.noaa.gov/facts/oceandepth.html>
- [25] British Petroleum (2014), “BP Statistical Review of World Energy 2014”, <http://large.stanford.edu/courses/2014/ph240/zarubin2/docs/bpreview.pdf>
- [26] Rahman N. et al. (2014), “Literature Review of Ocean Current Turbine”, International Journal of Scientific & Engineering Research (IJSER), Volume 5, Issue 11, November
- [27] MCT Ltd., <http://www.marineturbines.com/>
- [28] European Commission – Directorate of Research (2005), “Synopsis of the SeaFlow project presented at the European Commission”, http://ec.europa.eu/research/energy/pdf/seaflow_en.pdf
- [29] Sea Generation Ltd (subsidiary of MCT Ltd.), <http://www.seageneration.co.uk/>
- [30] SeaGen S Product Brochure:
http://www.marineturbines.com/sites/default/files/FINAL_MCT_Product_Brochure_8pp_Seagen_UPDATE_E_HIRes.pdf
- [31] ORPC, <http://www.orpc.co>
- [32] ADAG, <http://www.adag.unina.it/english/>
- [33] GEM – the “Ocean’s Kite” Product Brochure:
http://www.adag.unina.it/gem%20volantino_ENG_v3.pdf
- [34] Minesto, <http://www.minesto.com>
- [35] Deep Green Minesto’s Project Technical Data: <http://www.minesto.com/Resources/dgtechnical-data-sheet.pdf>
- [36] Blue Energy Website – History Section: http://www.blueenergy.com/technology_development_history.html
- [37] B. V. Davis, J. R. Farrell, D. H. Swan, and K. A. Jeffers (1986), “Generation of Electric Power from the Florida Current,” Proceeding of 18th Annual Offshore Technology Conference, Houston, TX, May 5–8, OTC-5120.
- [38] Florida Hydro Power and Light Company, <https://www.fpl.com>
- [39] Eaton Corporation, www.eaton.com
- [40] Triton Submarines LLC, <http://www.tritonsubs.com>
- [41] Crowd Energy, <http://www.crowdenergy.org>
- [42] IHI Engineering Review Magazine (2014), Volume 46, No. 2,
http://www.ihico.jp/var/ezwebin_site/storage/original/application/149ee9de3149aba2e1215fd5f9cd46ec.pdf
- [43] IHI Corporation, <https://www.ihico.jp>
- [44] Toshiba Corporation, <https://www.toshiba.co.jp>
- [45] NCKU – SERC, http://serc.ncku.edu.tw/ncp-taiwan/news_detail.asp?le=english&fid=18&pid=524
- [46] VanZwieten J.H. et al. (2006), “Design of A Prototype Ocean Current Turbine: Part I: Mathematical Modeling and Dynamics Simulation”, Journal of Ocean Engineering, Volume 33(11-12), pp. 1485-1521
- [47] VanZwieten J.H. et al. (2006), “Design of A Prototype Ocean Current Turbine: Part I: Flight Control System”, Journal of Ocean Engineering, Volume 33(11-12), pp. 1522-1551

- [48] Dehlsen Associates LLC, Santa Barbara, CA and U.S. Department of Energy, Washington, DC: 002648.002 (2014), "Aquantis Ocean Current Turbine Development: Innovative Power Generation Technology."
- [49] Swales H., Coakley D., Gupta S., and Way S. (2014), "Stability and Loads Validation of an Ocean Current Turbine," in Proceedings of 2nd Marine Energy Technology Symposium, April 15-18, Seattle, WA, USA
- [50] Aquantis Inc., <http://www.ecomerittech.com/aquantis.php>
- [51] Bolin W. D. (2014), "Ocean Stream Power Generation: Unlocking a Source of Vast, Continuous, Renewable Energy," in Proceedings of 2nd Marine Energy Technology Symposium, April 15-18, Seattle, WA, USA
- [52] Hunt J.T. and Rumker J. (2012), "THOR's Power Method for Hydrokinetic Devices", Technical Report of Turner Hunt Ocean Renewable, LLC submitted in U.S. Department of Energy, TRN DE-EE0003634, <http://www.osti.gov/scitech/servlets/purl/1048072>
- [53] SNMREC, <http://www.snmrec.fau.edu>.
- [54] Driscoll F.R., Skemp S.H., Alsenas G.M., Coley C.J. and Leland A. (2008), "Florida's Center for Ocean Energy Technology," Proceedings of MTS/IEEE Oceans Conference, September 15-18, Quebec City, Canada, No. OCEANS.2008.5152102
- [55] Driscoll F.R., Alsenas G.M., Beaujean P.P., Ravenna S., Raveling J.E.B. and Slezycki C., "A 20 kW Open Ocean Current Test Turbine," Proceedings of MTS/IEEE OCEANS Conference, September 15-18, Quebec City, Canada, DOI: 10.1109/OCEANS.2008.5152104
- [56] VanZwieten J.H., Laing W.E and Slezycki C.R. (2011) "Efficiency Assessment of an Experimental Ocean Current Turbine Generator" Proceedings of the IEEE Oceans Conference, September 19-22, Kona, Hawaii, No. 110422-215
- [57] VanZwieten J.H, Oster C.M and Duerr A.E.S. (2011), "Design and Analysis of A Rotor Blade Optimized for Extracting Energy from the Florida Current", Proceedings of the 30th International Conference on Ocean, Offshore, and Arctic Engineering, June 19-24, Rotterdam, The Netherlands, No. OMAE2011-49140
- [58] VanZwieten J.H., Young M.T. and Von Ellenrieder K.D. (2012) "Design and Analysis of An Ocean Current Turbine Performance Assessment System" Proceedings of the IEEE Oceans Conference, October 14-19, Hampton Roads, Virginia, No. 120530-005
- [59] Borghi M., Kolawole F., Gangadharan S., Engblom A., VanZwieten J.H., Alsenas G., Baxley W., and Ravenna S. (2012) , "Design, Fabrication & Installation Of A Hydrodynamic Rotor For A Small-Scale Experiment Ocean Current Turbine" Proceedings of the IEEE Southeast Conference, March 15-18, Orlando, Florida, No. SECon.2012.6196973
- [60] VanZwieten J.H., Vanrietvelde N. and Hacker B. (2013), "Numerical Simulation of an Experimental Ocean Current Turbine", IEEE Journal of Oceanic Engineering (JOE), Vol. 38 (1), pages 131-143
- [61] Xiros N., VanZwieten, J.H. Jr., Cornel S., and Tzelepis V. (2014), "Power Take-off Control of In-stream Hydrokinetic Turbines, Proceeding of the ASME Dynamic Systems and Control Conference (DSCC), October 22-24, San Antonio, Texas, pp. V002T32A003, No. DSCC 2014-6247
- [62] Xiros N.I., VanZwieten J.H., Sultan C. and Tzelepis V. (2015), "An Ocean Current Turbine System with An Induction Generator and Power Electronic Control", Proceedings of the MTS/IEEE Oceans'15 Conference, May 18-21, Genoa, Italy, Session GEN 3-1 Off-shore Renewables-1, No. 141219-071

- [63] Cribbs A.R. and VanZwieten J.H. (2010), “Global Numerical Analysis of a Moored Ocean Current Turbine Testing Platform”, Proceedings of the IEEE Oceans Conference, September 20-23, Seattle, Washington, No. 100528-082, DOI: 10.1109/OCEANS.2010.5664288
- [64] SNMREC (2014), “SNMREC Turbine Tow Test 1 Video”:
<http://snmrec.fau.edu/news/snmrec-turbine-tow-test-1-video-posted>
- [65] VanZwieten J.H., Pyakurel P., Sultan C., Ngo T., Xiros N.I. (2015), “An Assessment of Using Variable Blade Pitch for Ocean Current Turbine Flight Control”, Proceedings of the 3rd Marine Energy Technical Symposium, April 27-29, Washington D.C., Session Number: METS-A-T2-B
- [66] Xiros N.I., VanZwieten J.H., Sultan C. and Tzelepis V. (2015), “Modeling, System Identification and Linearization Of Underwater Turbine Power Plant Dynamics”, Proceedings of the ASME International Mechanical Engineering Congress & Exposition, November 13-19, Houston, Texas, USA, No. IMECE2015-53455
- [67] Guney M.S. and Kaygusuz K. (2010), “Hydrokinetic Energy Conversion Systems: A Technology Status Review”, Journal of Renewable and Sustainable Energy Reviews, Elsevier, Volume 14, pages 2996-3004
- [68] Pike Research LLC – Research Report (2009), “Hydrokinetic and Ocean Energy - Renewable Power Generation from Ocean Wave, Tidal Stream, River Hydrokinetic, Ocean Current and Ocean Thermal Technologies”,
<http://www.navigantresearch.com>
- [69] Leeson Electric Corporation (2012), “Understanding AC Induction, Permanent Magnet and Servo Motor Technologies: Operation, Capabilities and Caveats”, Internal Report by Jim Murphy
http://www.leeson.com/documents/PMAC_Whitepaper.pdf
- [70] Benelghali S., Benbouzid M. and Charpentier J.F. (2012), “DFIG versus PMSG for Marine Current Turbine Applications”, Revue des Energies Renouvelables, Volume 15, Number 1, pages 29-41
- [71] Microchip Technology Inc. (2003), “AC Induction Motor Fundamentals”, Data Sheet 00887A
<http://www.t-es-t.hu/download/microchip/an887a.pdf>
- [72] Young H.D. and Freedman R.A. (2012), “University Physics With Modern Physics”, 13th Edition, Pearson Education Inc., USA
- [73] WEG Corporation S.A., <http://www.weg.net.us>
- [74] <http://www.electrical-knowhow.com/2012/05/electrical-motors-basic-components.html>
- [75] Tong W. (2014), “Mechanical Design of Electric Motors”, 1st Edition, CRC Press – Taylor and Francis Group, USA
- [76] Emerson Industrial Automation - Kato Engineering Inc. (2001), “Engineering Report: Form Wound Coils, Random Wound Coils”:
http://www.emersonindustrial.com/en-en/documentcenter/electric-power-generation/KatoEngineering/Literature/FWRW_BK_PDF_0701.pdf
- [77] Virginia Tech University – Electrical Machine Design Course (E-Notes 2012), “Design of Induction Motors”:
<http://elearning.vtu.ac.in/16/ENotes/Elec Mac Des/Unit6VH.pdf>
- [78] U.S. Department Of Energy (1992), “DOE Fundamentals Handbook – Electrical Science Volume 4/4”, Office of Nuclear Safety Policy and Standards, No. DOE-HDBK-1011/4-92:
<http://energy.gov/sites/prod/files/2013/06/f2/h1011v4.pdf>
- [79] https://www.en.wikipedia.org/wiki/Induction_motor

- [80] Nailen R.L. (2005), "The Importance of Slot Combination in AC Motor Design", Electrical Apparatus Magazine, Issue: June
- [81] Pyrhonen J., Jokinen D. and Hrabovcova V. (2008), "Design of Rotating Machinery", 1st Edition, John Wiley & Sons Ltd., UK
- [82] Electrical Engineering Portal (EEP), "Construction of 3-Phase AC Induction Motors", Technical Articles Section: <http://www.electrical-engineering-portal.com/construction-of-3-phase-ac-induction-motors>
- [83] <http://www.instructables.com/community/Axial-Flux-Wind-Turbine/>
- [84] Hughes A. and Drury B. (2014), "Electric Motors and Drives - Fundamentals, Types and Applications", 4th Edition, Elsevier Ltd., UK
- [85] Electropaedia (Woodbank Communications Ltd.), "Electrical Machines-Generators": <http://www.mpoweruk.com/generators.htm>
- [86] Fitzgerald A.E, Kingsley C. and Umans S.D. (2003), "Electric Machinery", 6th Edition, McGraw-Hill Companies Inc., USA
- [87] <http://www.electricaleasy.com/2014/02/double-squirrel-cage-motor.html>
- [88] U.S. Department Of Energy (2014), "Improving Motor and Drive System Performance: A Sourcebook for Industry", Advance Manufacturing Office (AMO), http://energy.gov/sites/prod/files/2014/04/f15/amo_motors_sourcebook_web.pdf
- [89] United States Government Energy Policy Act of 1992: <http://www.ferc.gov/legal/maj-ord-reg/epa.pdf>
- [90] National Electrical Manufacturers Association – NEMA (2014), "NEMA Standards Publication MG 1 – Section II, Part 10.4", <http://www.nema.org/Standards/Pages/Motors-and-Generators.aspx>
- [91] International Electrotechnical Commission (IEC) – TC2 Rotating Machinery Program, "IEC 60034-Part 1", http://www.iec.ch/dyn/www/?p=103:23:0:::FSP_ORG_ID:FSP_LANG_ID:1221,25
- [92] <http://www.powersystemsloss.blogspot.com/2011/12/electric-motor-nameplate-specifications.html>
- [93] Xiros N.I., Zisman Z.S. and Von Ellenrieder K. D. (2012), "A Modular Dynamical Simulation Model For All Electric Ship Powertrain With Surface Piercing Propeller", 1st International MARINELIVE Conference on "All Electric Ship", June 3-5, Athens, Greece
- [94] Costa A. et al. (2012), "MATLAB Based Simulation Toolbox For The Study And Design Of Induction Motor FOC Speed Drives", Wiley Journal of Computer Applications in Engineering Education (CAEE), Volume 20, Issue 2, pages 295–312
- [95] Aktaibi A., Ghanim D. and Rahman M.A. (2011), "Dynamic Simulation of a Three-Phase Induction Motor Using Matlab Simulink", Proceeding of the IEEE 20th Annual Newfoundland Electrical and Computer Engineering Conference (NECEC), November 1st, Newfoundland and Labrador, Canada
- [96] Salahat M. et al. (2011), "Modular Approach for Investigation of the Dynamic Behavior of Three-Phase Induction Machine at Load Variation", International Journal of Engineering (ENG), Volume 3, Number 3, pages 525-531
- [97] Shah S., Rashid A. and Bhatti M.K.L. (2012), "Direct-Quadrature Modeling Of 3-Phase Induction Motor Using MatLab Simulink", IEEE Canadian Journal on Electrical and Electronics Engineering (CJECE), Volume 3, No. 5, pages 237-243

- [98] Leedy A.W. (2013), "Simulink MATLAB Dynamic Induction Motor Model For Use As A Teaching & Research Tool", International Journal of Soft Computing and Engineering (IJSCE), Volume 3, Issue 4, pages 102-107, ISSN: 2231-2307
- [99] Batool M. and Ahmad A. (2013), "Mathematical Modeling and Speed Torque Analysis of Three Phase Squirrel Cage Induction Motor Using MATLAB Simulink for Electrical Machines Laboratory", International Electrical Engineering Journal (IEEJ), Volume 4, Number 1, pages 880-889, ISSN: 2078-2365
- [100] Shi X., Li H. and Huang J. (2014), "A Practical Scheme For Induction Motor Modeling & Control", International Journal of Control and Automation (IJCA), Volume 7, Number 4, pages 113-124, ISSN: 2005-4297
- [101] Rahaman N. and Govindraju H.V. (2014), "Modeling and Simulation of a Three-Phase Electric Traction Induction Motor Using MATLAB Simulink", International Journal Of Electrical, Electronics and Computer Systems (IJECS), Volume 2, Issue 5, pages 18-25, ISSN: 2347-2820
- [102] Phukon L.J. and Baruah N. (2015), "A Generalized MATLAB Simulink Model Of A Three Phase Induction Motor", International Journal of Innovative Research in Science, Engineering and Technology (IJIRSET), Volume 4, Issue 5, pages 2926-2934, ISSN: 2319 - 8753
- [103] Ratnani P.L. and Thosar A.G. (2014), "Mathematical Modelling of a 3 Phase Induction Motor Using MATLAB/Simulink", International Journal of Modern Engineering Research (IJMER), Volume 4, Issue 6, pages 62-67, ISSN: 2249-6645
- [104] Riaz M. (2008), "Simulation of Electric Machine and Drive Systems Using MATLAB and Simulink", University of Minnesota, Department of Electrical and Computer Engineering:
<https://www.ece.umn.edu/users/riaz/macsim/info.pdf>
- [105] The Mathworks Inc., USA, Product – MATLAB: <http://www.mathworks.com/products/matlab>
- [106] The Mathworks Inc., USA, Product – Simulink: <http://www.mathworks.com/products/simulink>
- [107] The Mathworks Inc., USA, Product – SimPowerSystems: <http://www.mathworks.com/products/simpower>
- [108] The Mathworks Inc., USA (2011), "SimPowerSystems v.5 User's Guide - R2011a":
http://www.se.mathworks.com/help/releases/R2011a/pdf_doc/physmod/powersys/powersys.pdf
- [109] Krause P., Wasynczuk O., Sudhoff S. and Pekarek S. (2013), "Analysis of Electric Machinery & Drive Systems", 3rd Edition, John Wiley & Sons Inc., USA
- [110] Krishnan R. (2001), "Electric Motor Drives - Modelling, Analysis & Control", Prentice Hall Inc., USA
- [111] Simoes M.G. and Farret F.A. (2015), "Modeling and Analysis with Induction Generators", 3rd Edition, CRC Press, USA
- [112] Boldea I. and Nasar S.A. (2010), "The Induction Machined Design Handbook", 2nd Edition, CRC Press, USA
- [113] El-Hawary M.E. (2002), "Principles Of Electric Machines With Power Electronics Applications", 2nd Edition, John Wiley & Sons Inc., USA
- [114] <http://www.electricaleasy.com/2014/02/speed-control-methods-of-induction-motor.html>
- [115] Engineering.com Website, Electronic Design Section, "Changing An Induction Motors Power Supply Frequency Between 50 and 60 Hz", Article ID 8154:
<http://www.engineering.com/ElectronicsDesign/ElectronicsDesignArticles/ArticleID/8154/Changing-an-Induction-Motors-Power-Supply-Frequency-Between-50-and-60Hz.aspx>

- [116] Pharos University of Alexandria – Electrical Machine Course (E-Notes 2012), “Induction or Asynchronous Machine”:
<http://www.pua.edu.eg/PUASite/uploads/file/Engineering/Fall%202012/EE%20380/Induction%20Motors-Chapter%282%29.pdf>
- [117] Krause P.C., Wasynczuk O. and Sudhoff S. D. (2002), “Electric Machinery & Drive Systems”, John Wiley & Sons Inc., USA
- [118] Chan T.F. and Shi K. (2011), “Applied Intelligent Control Of Induction Motor Drives”, John Wiley & Sons Inc., Asia
- [119] Blaschke F. (1992), “The Principle Of Field-Orientation As Applied To The New Transvector Closed-Loop Control System For Rotating-Field Machines, Siemens Review, Vol. 34, pp. 217–220
- [120] Hasse K (1969), “About The Dynamics Of Adjustable-Speed Drives With Converter-Fed Squirrel Cage Induction Motor”, PhD Dissertation in German, Darmstadt Technische Hochschule, Darmstadt, Germany
- [121] Marino R., Tomei P. and Verrelli C.M. (2010), “Induction Motor Control Design”, Springer, UK
- [122] De Doncker R., Pulle D.W.J. and Veltman A. (2011), “Advanced Electrical Drives - Analysis, Modeling, Control”, Springer, UK
- [123] Takahashi I. and Noguchi T. (1986), "A New Quick-Response And High Efficiency Control Strategy Of An Induction Machine", IEEE Transactions on Industrial Application, Volume IA-22, Number 5, pages 820-827.
- [124] Baader U., Depenbrock M. and Gierse G. (1992), "Direct Self Control (DSC) of Inverter-Fed-Induction Machine – A Basis for Speed Control Without Speed Measurement", IEEE Transactions of Industry Applications, Volume 28, Number 3, pages 581-588
- [125] Depenbrock M. (1988), "Direct Self Control Of Inverter-Fed Induction Machines", IEEE Transactions on Power Electronics, Volume PE-3, Number 4, pages 420-429
- [126] Depenbrock M., "Direct Self Control Of The Flux And Rotary Moment Of A Rotary-Field Machine", U.S. Patent 4,678,248.
- [127] Foo G., Sayeef S. and Rahman M.F. (2008), “Sensorless Direct Torque And Flux Control Of An IPM Synchronous Motor At Low Speed And Standstill, Proceedings of IEEE 2nd International Power and Energy Conference (PECON), December, Johor Bahru, Malaysia, Volume 1-3, pages 277-282, No. 10.1109/PECON.2008.4762484,
- [128] ABB (2011), “Technical Guide No. 1: Direct Torque Control - The World’s Most Advanced AC Drive Technology”, ABB Drives Section:
https://library.e.abb.com/public/14f3a3ad8f3362bac12578a70041e728/ABB_Technical_guide_No_1_REVC.pdf
- [129] Żelechowski M. (2005), “Space Vector Modulated – Direct Torque Controlled (DTC – SVM) Inverter – Fed Induction Motor Drive”, PhD Dissertation in Poland, Warsaw University of Technology, Faculty of Electrical Engineering, Institute of Control and Industrial Electronics, Warsaw, Poland
- [130] Trzynadlowski A.M. (2001), “Control Of Induction Motors”, Academic Press, USA
- [131] Marino R. and Valigi P. (1991), "Nonlinear Control Of Induction Motors: A Simulation Study", European Control Conference, Grenoble, France, pages 1057-1062
- [132] Marino R., Peresada S. and Valigi P. (1990), "Adaptive Partial Feedback Linearization Of Induction Motors", Proceedings of the 29th IEEE Conference on Decision and Control (CDC), December 5-7, Honolulu, Hawaii, Volume 6, pages 3313-3318, DOI: 10.1109/CDC.1990.203408

- [133] Ortega R., Loria A., Nicklasson P. J. and Sira-Ramirez H. (1998), "Passivity-Based Control of Euler-Lagrange Systems", Springer, London
- [134] Astrom K.J. and Bjorn W. (1995), "Adaptive Control", Pearson PLC, USA
- [135] Amick C. and Avery P. (2010), "The ABC's (and 1-2-3's) of Variable Frequency Drives", Yaskawa America, Inc. - Drives & Motion Division, Technical Article Number: PR.MSD.02:
<https://www.yaskawa.com/pycprd/download/search/detail?n=PR.MSD.02>
- [136] Bellar M. D., Wu T.S., Tchamdjau A., Mahdavi J. and Ehsani M. (1998), "A Review of Soft-switched DC-AC Converter", IEEE Transactions On Industry Applications, Volume 43, Number: 4, pages 847-858
- [137] Rashid M. H. (2004), "Power Electronics - Circuit's Devices and Applications", 3rd Edition, Prentice Hall, USA
- [138] Colak I. and Kabalci E. (2013), "Developing A Novel Sinusoidal Pulse Width Modulation (SPWM) Technique To Eliminate Side Band Harmonics", International Journal of Electrical Power & Energy System, Elsevier, Volume 44, Issue 1, pages 861–871, DOI:10.1016/j.ijepes.2012.08.024
- [139] Raju N.I., Islam M.S., Ali T. and Karim S.A. (2013), "Study of SPWM Technique & Simulation of Designed Analog Circuit (Op-Amp) Controlled Three Phase PWM Inverter with Harmonic Reduction", Proceedings of the 2nd International Conference on Informatics, Electronics and Vision (ICIEV), May 17-18, Dhaka, Bangladesh, DOI: 10.1109/ICIEV.2013.6572580
- [140] Rajashekara K.S. and Vithayathill J. (1981), "Harmonics In The Voltage Source PWM Inverters," International Journal of Electronics, Volume 50, Issue 5, pages 325 – 337, DOI: 10.1080/00207218108901272
- [141] The Mathworks Inc., USA, Library Power Electronics, Universal Bridge:
<http://www.mathworks.com/help/physmod/sps/powersys/ref/universalbridge.html>
- [142] Bird J. (2010), "Electrical Circuit Theory and Technology", 4th Edition, Elsevier Ltd., UK and USA
- [143] Hart D.W. (2011), "Power Electronics", McGraw-Hill Companies Inc., USA
- [144] Godse A.P. and Bakshi U.A. (2009), "Electronic Devices and Circuits I", 1st Edition, Technical Publications Pune, India
- [145] Rashid M. H. (2011), "Power Electronics Handbook", 3rd Edition, Elsevier, USA
- [146] Colak I. and Kabalci E. (2013), "Developing A Novel Sinusoidal Pulse Width Modulation (SPWM) Technique To Eliminate Side Band Harmonics", International Journal Of Electrical Power And Energy Systems, Volume 44, Issue 1, pages 861-871, DOI: 10.1016/j.ijepes.2012.08.024
- [147] Luo F.L., Ye H. and Rashid M. (2005), "Digital Power Electronics And Applications", Elsevier, USA
- [148] Patel M.R. (2013), "Introduction To Electrical Power And Power Electronics", Taylor & Francis Group LLC, CRC Press, USA
- [149] Square D Bulletin No. 8803PD9402 (1994), "Power System Harmonics Causes and Effects of Variable Frequency Drives Relative to the IEEE 519-1992 Standard", Raleigh, NC, U.S.A
- [150] Bose B. K. (2002), "Modern Power Electronics And AC Drives", Prentice-Hall, USA
- [151] Holtz J. (1994), "Pulse Width Modulation For Electronic Power Conversion", Proceedings of the IEEE, Volume 82, Issue 8, pages 1194-1214, DOI: 10.1109/5.301684
- [152] Rajashekara K., Bhat A.K.S. and Bose B.K. (2000), "Power Electronics" in the "Electrical Engineering Handbook", Dorf R. (editor), CRC Press LLC., USA
- [153] Patel M.R. (2012), "Shipboard Propulsion, Power Electronics And Ocean Energy", Taylor & Francis Group LLC, CRC Press, USA

- [154] Sen P.C. (2014), “Principles Of Electric Machine And Power Electronics”, 3rd Edition, John Wiley & Sons Inc., USA
- [155] Wu B., Lang Y, Zargari N. and Kouro S. (2011), “Power Conversion And Control of Wind Energy Systems”, John Wiley & Sons Inc., USA
- [156] Anaya-Lara O., Campos-Gaona D., Moreno-Goytia E. and Adam G. (2014), “Offshore Wind Energy Generation – Control, Protection And Integration To The Electrical System”, John Wiley & Sons Inc., UK
- [157] Zisman Z.S. (2011), “On the Simulation of an All Electric Ship Powertrain Utilizing A Surface Piercing Propeller Via A Modular Main Propulsion Plant Model”, Master Thesis in USA, Virginia Tech University, Department of Aerospace and Ocean Engineering, Virginia, USA
- [158] Peckner D. and Bernstein I. M. (1977), “Handbook Of Stainless Steels”, McGraw-Hill Book Company, New York, USA
- [159] Pain H.J. (1988), “The Physics Of Vibrations and Waves”, John Wiley & Sons, UK
- [160] Palm W.J. (1983), “Modelling, Analysis And Control Of Dynamic Systems”, John Wiley & Sons Inc., USA
- [161] Xiros N. (2002), “Robust Control Of Diesel Ship Propulsion”, Advances In Industrial Control Series, Springer-Verlag, UK
- [162] Gross D., Hauger W., Schroder J., Wall W.A. and Bonet J. (2011), “Engineering Mechanics 2 – Mechanics Of Material”, Engineering Mechanics Series, Springer-Verlag, UK
- [163] Paraskevopoulos P.N., (2002), “Modern Control Engineering”, Control Engineering Series, Marcel Dekker Inc, USA
- [164] Ziegler J. G. and Nichols N.B. (1942), “Optimum Setting for Automatic Controllers”, Transactions of ASME, Volume 64, pages 759-768
- [165] U.S. Energy Information Administration – Residential Energy Consumption Survey and State Energy Data System: <http://www.eia.gov>

Reference/Bibliography - Appendix

- [A1] Ellabban O., Abu-Rub H. and Blaabjerg F. (2014), “Renewable Energy Resources: Current Status, Future Prospects And Their Enabling Technology”, Journal of Renewable and Sustainable Energy Reviews, Elsevier, Vol. 39, pp 748-764
- [A2] International Renewable Energy Agency – IRENA (2015), “Renewable Power Generation Costs In 2014”: http://www.irena.org/DocumentDownloads/Publications/IRENA_RE_Power_Costs_2014_report.pdf
- [A3] Renewable Energy Policy Network for the 21st Century (2015), “Renewables 2015 – Global Status Report”: http://www.ren21.net/wp-content/uploads/2015/07/REN12-GSR2015_Onlinebook_low1.pdf
- [B1] National Electrical Manufacturers Association – NEMA (2011), “NEMA Standards Publication MG 1”, <http://www.nema.org/Standards/Pages/Motors-and-Generators.aspx>
- [B2] University of Calgary – Electrical Machines/Induction/Design Aspects/Motor Classes (e-Notes by Dr. Andy Knight – Department of Electrical & Computer Engineering): http://www.people.ucalgary.ca/~aknigh/electrical_machines/induction/design/motor_classes.html
- [C1] Park R.H. (1929), “Two-Reaction Theory Of Synchronous Machines—Generalized Method of Analysis—Part I”, AIEE Transactions, Volume 48, pp. 716 – 727

- [F1]** Zhou K. and Wang D. (2002), “Relationship Between Space-Vector Modulation and Three-Phase Carrier-Based PWM: A Comprehensive Analysis,” IEEE Transactions on Industrial Electronics, Volume 49, Number 1, pages 186-196, DOI: 10.1109/41.982262
- [F2]** Skvarenina T.L. (2002), “The Power Electronics Handbook”, CRC Press LLC, USA
- [F3]** Indian Institute of Technology (IIT) – Department of Electrical Engineering (EE), (E-Notes – Module 5), “DC to AC Converters”
- [G1]** Howell K. B. (2001), "Principles Of Fourier analysis", Chapman & Hall - CRC, UK & USA
- [G2]** Kazmierkowski M.P., Krishnan R. and Blaabjerg F. (2002), "Control In Power Electronics Selected Problems", Academic Press, USA

Appendix A

COMPARISON WITH OTHER RENEWABLE ENERGY SOURCES AND ECONOMIC CONSIDERATION

Renewable energy sources can be available on-site, such as wind and solar energy, or produced locally, such as biomass. One disadvantage of all renewable energy system is the difficult to generate the amount of electricity that traditional fossil fuel generators produced. This may mean that we need to build more energy facilities [21].

An important limitation of all renewable technologies is the intermittent nature which involves reliability of supply, energy production depends on environmental conditions, and they don't remain constant all day. This can be unpredictable. For example, wind turbines need wind to turn the blades, they will not provide electricity when it is not windy, solar electricity can't be generated at night, solar collectors need clear skies and sunshine to collect heat and make electricity and hydro generators need rain to fill dams to supply flowing water. Renewable energy often relies on the weather for its source of power. For this reason, a battery may be required to provide backup and power storage [21].

To compare renewable energy systems is necessary to take into account both environmental and economic sense in the long term. It is important to identify the appropriate renewable energy technology in the first instance. Factors to consider can be the type of energy which is required: mainly electricity or mainly heat; and if energy demand is constant or it fluctuates. For example, some renewables energies, such as wind and photovoltaic, just produce electricity. Others, such as solar water heating, just produce heat, while biomass can provide heat and electricity. Besides, we need to consider environmental impacts and costs of production and maintenance. The current cost of renewable energy technology is also far in excess of traditional fossil fuel generation. This is because it is a new technology and has extremely large capital cost [21].

Ocean current energy has a number of advantages over other renewable as we can see in the Table A.1 [21], which present a comparison between ocean current energy technologies and others energy generation resources such as fossil and renewable. Ocean current power is a technology that can provide bulk, nonpolluting, zero-emission energy at a cost significantly less than the best fossil fuel and nuclear technology from a renewable source and with no impact on land use and habitat.

Table A.1: Ocean current advantages compared with other energy resources

	Renewable Resource	Low Capital Cost	Low Running Cost	Minimal Environmental Impact	Predictable	Minimal Visual Impact	Modular
Fossil	×	✓	×	×	✓	×	×
Nuclear	×	✓	×	×	✓	×	×
Wind	✓	×	✓	✓	×	×	✓
Solar	✓	×	✓	✓	×	×	×
Hydro	✓	✓	✓	×	✓	×	✓
Wave	✓	×	✓	✓	×	✓	✓
<i>Ocean Current</i>	✓	✓	✓	✓	✓	✓	✓

Advantages and disadvantages of every single renewable energy system along with comparison between them can be found in references [13, 20, 21, 22, 67, A1].

A detailed comparison and analysis of the costs for wind (both onshore and offshore), solar (both photovoltaics and concentrating), hydropower, biomass and geothermal is described perfectly in reference [A2].

As far as the commercial viability of ocean renewables such as offshore wind, wave, tidal and ocean current, offshore wind costs range from 3÷8 cents per kW·h compared to 2.5÷7 cents onshore [A3]. These values have been derived based on operating experiences in Europe and reflect operating experience. Costs for offshore wind increase as projects move further offshore, necessitating more costly mooring systems and larger turbines.

As for wave and tidal, they remain subject to further refinement. The World Renewable Energy Report [A3] estimates the cost of wave energy at an average of 9 cents / kW·h and tidal and ocean current an average of 8 cents / kW·h. Recent EPRI reports, [13], have found that, presently, the cost of power from ocean technologies ranges from 7 cents to 16 cents / kW·h in a low case scenario. For tidal energy, the EPRI report found that the cost is driven by the resource, a strong resource can yield power at prices as low as 6 cents / kW·h.

As there are no commercial ocean current turbines in operation currently, it is hard to evaluate the costs of energy which is created by ocean current, and its competitiveness with other energy sources. The different cost components to be included in the capital and operating expenditures estimate for ocean current energy have been identified as follows:

1. Civil and structural costs
2. Major equipment costs
3. Balance of plant costs
4. Transmission lines and installation
5. Project indirect cost
6. Development costs
7. Maintenance costs

The single largest expenditure will relate to construction of the initial infrastructure. Setting up transmission lines will be the most expensive and challenging, as underwater lines will be necessary. Moreover, until large-scale testing and development is implemented, the cost of maintaining the ocean current turbine facility remains unknown, which would be passed on to the consumers.

Appendix B

NATIONAL ELECTRICAL MANUFACTURERS ASSOCIATION (NEMA)

The National Electrical Manufacturers Association (NEMA - a United States organization) standard has specified four major design classifications of AC squirrel cage induction motors: designs A, B, C, and D [B1]. These design classifications apply particularly to the rotor design and hence affect the performance characteristics of the motors. Figure 2.8 displays a series of torque–speed curves for these design classifications with identical power rating and rotating speed [2.14]. It illustrates that the design characteristics such as starting torque, speed, and breakdown torque can be combined in different ways [75]:

- Design **A** motors are used for applications that may undergo frequent but short time overloading and thus require high breakdown torque, such as injection molding machines. This type of motor has normal starting torque (typically 150%–170% of the rated torque) and relatively high starting current.
- Design **B** motors are general-purpose motors, designed for applications that require normal starting and running torques, such as machine tools, fans, and centrifugal pumps. This type of motor usually has a comparable starting torque with Design A but offers low starting current. The locked rotor torque is good enough to start many loads encountered in the industrial applications. The slip is about 5%.
- Design **C** motors are selected for applications that require high starting torque, such as inclined conveyors and gyratory crushers.
- Design **D** motors, called high slip motors, are sometimes used to power hoists and cycling loads, such as oil well pump jacks and low-speed punch presses.

Typical torque-speed curves for classes A-D are shown in Figure B.1 [75]. Bear in mind that the curves shown in the below figure are general shapes. In real motors, each motor would have its own distinct values different from the percentages reflected in that figure.

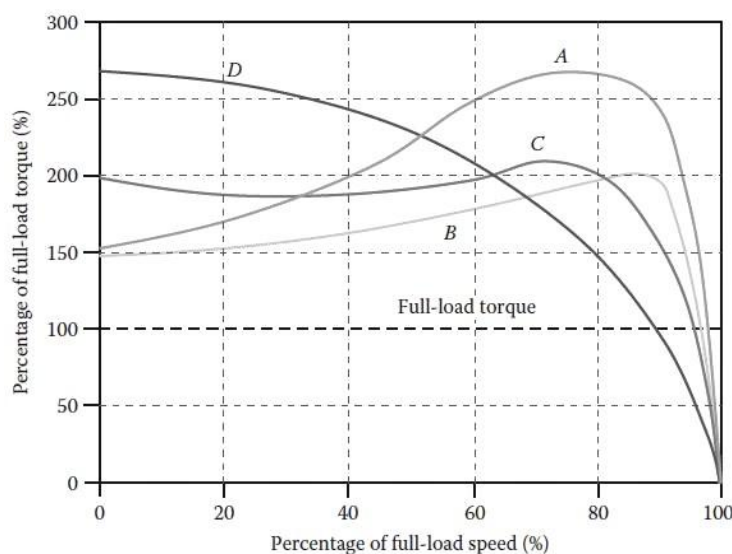


Figure **B.1**: Torque–speed characteristics for design A, B, C, and D motors defined by NEMA for constant voltage and frequency operation (Source: W. Tong [75])

Note that the starting torque ranges broadly among the design classifications, from about 150% of full-load torque for Design A motors to about 260% of rated torque for Design D motors. In addition, the speed at full-load for Design A motor is several percent less than the Design D motor.

Examples of typical rotor slots for classes A through D are shown in Figure B.2 [B2].

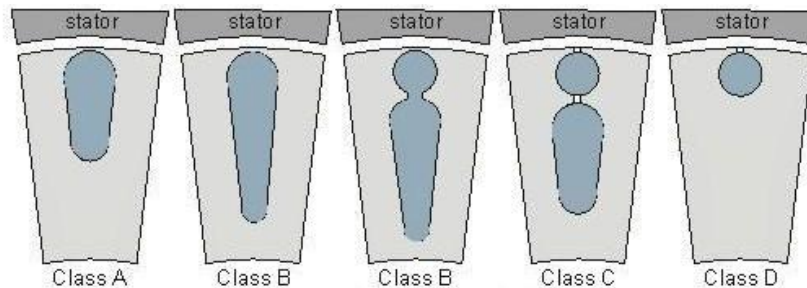


Figure B.2: Rotor typical slots from typical squirrel-cage induction motors, showing the cross section of the rotor bars; (a) NEMA design class A – large bars, near the surface; (b) NEMA design class B – large, deep rotor bars; (c) NEMA design class C – double-cage rotor design; (d) NEMA design class D – small bars near the surface (Source: University of Calgary [B2])

Motor Classes A and D are obtained by designing the rotor resistance to be either low (class A) or high (class D). Classes B and C are obtained by exploiting the effect of skin depth to obtain a variable resistance rotor circuit. Comparing classes A and B, class B has a deeper bar to exploit skin depth effects. The bar width may vary in order to enhance this effect. Class C rotors are typically fabricated with two separate cages. Only the outer cage will conduct at starting. There is air between the cages and at the top of the slot (to reduce leakage flux). Class D has a small conductor, giving a high resistance at all slips. The class D example shown above has an open slot, for a fabricated rotor design.

A summary of the performance characteristics of the NEMA classes is provided in the Table below [B1]:

Table B.1: Performance characteristics of NEMA A, B, C and D designs

	Class A	Class B	Class C	Class D
Type	General Purpose	General Purpose	High LRT	Very High LRT
LRT	70% - 275% rated	70% - 275% rated	200% - 250% rated	>275% rated
LRC	≈800% rated	500% - 700% rated	600% - 700% rated	600% - 700% rated
T_b	175%-300% rated	≥200% rated	190%-225% rated	≈275% rated
Breakdown Slip	< 2%	< 2%	-	High (as much as 1)
Rated Slip	<5% (lower than similar sized class B)	<5% (usually <3%)	<5% (higher than similar size class B)	High (typically 7% to 11%, can be up to 17%)
Applications	Fans, blowers, centrifugal pumps and compressors, motor – generator sets, etc., where starting torque requirements are relatively low	Fans, blowers, centrifugal pumps and compressors, motor – generator sets, etc., where starting torque requirements are relatively low	Conveyors, crushers, stirring machines, agitators, Reciprocating pumps and compressors, etc., where starting under load is required	High peak loads with or without fly wheels, such as punch presses, shears, elevators, extractors, winches, hoists, oil – well pumping and wire – drawing machines
Efficiency	Medium or High	Medium or High	Medium	Medium

Appendix C

AMPLITUDE-PRESERVATION-BASED PARK TRANSFORMATION

In this appendix, the direct- and quadrature-axis (dq0) theory introduced in Section 2.3 is formalized. The formal mathematical transformation from three-phase stator quantities to their direct- and quadrature-axis components is presented. These transformations are then used to express the governing equations for an induction machine in terms of the dq0 quantities so that eliminated mutual magnetic coupling between the phases and therefore makes the magnetic flux linkage of one winding independent of the current of another winding.

More specifically, the usefulness of this concept stems from the fact that although each of the stator phases sees a time-varying inductance due to the saliency of the rotor, the transformed quantities rotate with the rotor and hence see constant magnetic paths. Although not discussed here, additional saliency effects are present under transient conditions, due to the different conducting paths in the rotor, rendering the concept of this transformation all the more useful. Similarly, this transformation is useful from the point of view of analyzing the interaction of the rotor and stator flux waves and MMF waves, independent of whether or not saliency effects are present. By transforming the stator quantities into equivalent quantities which rotate in synchronism with the rotor, under steady-state conditions these interactions become those of constant MMF waves and flux waves separated by a constant θ_s . This indeed is the point of view which corresponds to that of an observer in the rotor reference frame [86].

More specifically, the amplitude preservation-based Park transform (often called dq0 transform [C1]) is a space vector transformation of three-phase time-domain signals from a stationary phase coordinate system (abc) to a rotating coordinate system (dq0) as shown in Figure 73 and is described mathematically below [C1]:

$$\begin{bmatrix} V_d \\ V_q \\ V_0 \end{bmatrix} = \frac{2}{3} \begin{bmatrix} \cos\theta_s & \cos\left(\theta_s - \frac{2\pi}{3}\right) & \cos\left(\theta_s - \frac{4\pi}{3}\right) \\ -\sin\theta_s & -\sin\left(\theta_s - \frac{2\pi}{3}\right) & -\sin\left(\theta_s - \frac{4\pi}{3}\right) \\ \frac{1}{2} & \frac{1}{2} & \frac{1}{2} \end{bmatrix} \begin{bmatrix} V_a \\ V_b \\ V_c \end{bmatrix} \quad (\text{C.1})$$

where θ_s is the stator (reference frame) angular position which describes the angle between the rotating and fixed coordinate system at each time with zero initial phase shift of the voltage.

More analytically, the above transformation is expressed:

$$V_d = \frac{2}{3} \cdot \left(V_a \cdot \cos\theta_s + V_b \cdot \cos\left(\theta_s - \frac{2\pi}{3}\right) + V_c \cdot \cos\left(\theta_s - \frac{4\pi}{3}\right) \right) \quad (\text{C.2.1})$$

$$V_q = \frac{2}{3} \cdot \left(V_a \cdot \sin\theta_s + V_b \cdot \sin\left(\theta_s - \frac{2\pi}{3}\right) + V_c \cdot \sin\left(\theta_s - \frac{4\pi}{3}\right) \right) \quad (\text{C.2.2})$$

$$V_0 = \frac{1}{3} \cdot (V_a + V_b + V_c) \quad (\text{C.2.3})$$

and it applies to all the electrical variables such as current and flux if you simply replace the symbol V with i or ϕ . Note that the dq0 transformation applies to the instantaneous values of the quantities to be transformed, not RMS values.

Appendix D

INPUTS OF INDUCTION MOTOR/GENERATOR BLOCK IN MATLAB/SIMULINK®

The inputs for the induction motor/generator block in MATLAB/Simulink® are shown in Figure D.1 and the solver parameters were used for the simulations is shown in Table D.1.

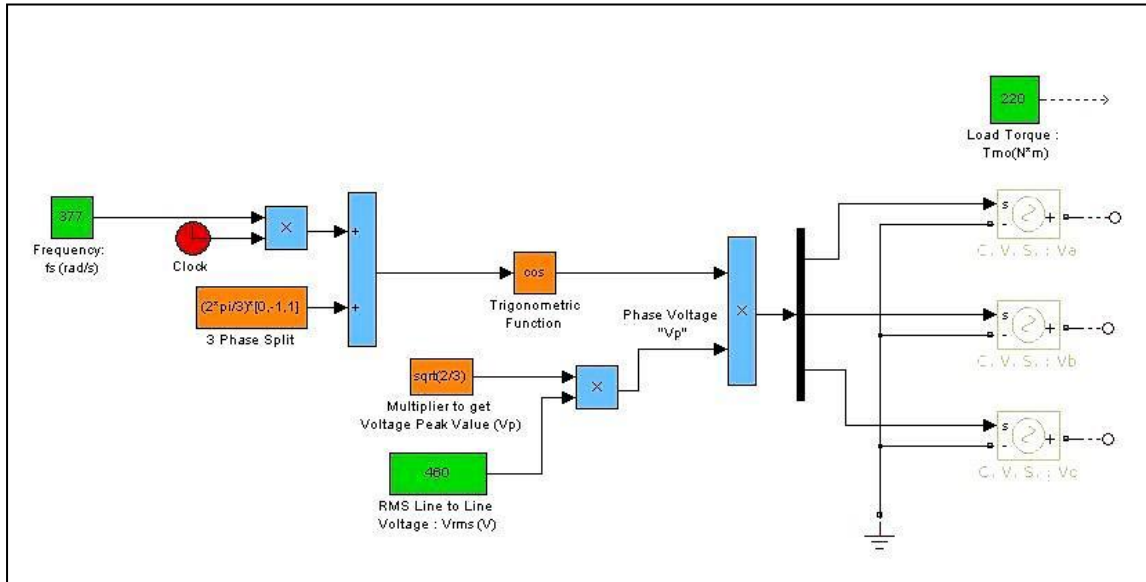


Figure D.1: Model in MATLAB/Simulink referred to inputs for the induction motor/generator block

Table D.1: Solver parameters

Type	Variable-Step
Solver	ode23tb
Relative Tolerance	0.0001
Max Step Size	15
Min Step Size	0.000000000001
Solver Reset Method	Fast

Appendix E

TESTS TO DETERMINE EQUIVALENT CIRCUIT MODEL PARAMETERS

The measurement of motor parameters is based on the equivalent circuit of the induction motor. The various tests to measure the motor parameter are shown below [110, 154]:

DC Resistance of Stator Windings

With the rotor at standstill the stator phase resistance, R_s , is measured by applying a DC voltage as well as the resulting stator current, I_s . While this procedure gives only the DC resistance at a certain temperature, the AC resistance has to be calculated by considering the wire size, stator frequency, line voltage and the operating temperature [110, 154].

No-Load Test

The no-load test on an induction machine, like the open-circuit test on a transformer, gives information about exciting current and rotational losses. The induction motor is driven at synchronous speed by another motor (preferably a DC motor). Then the stator is energized by applying rated voltage at rated frequency. The input power per phase, $P_{in/phase}$, is measured. The slip is zero so the rotor circuit is open (The rotor is kept uncoupled from any mechanical load) [110, 154].

For the present, the stator impedance can be neglected because it is small compared to the effective impedance of the magnetizing and core-loss branches. The mutual inductance, L_m , the magnetizing current, I_m , and the core-loss resistance, R_c , are calculated [110].

Locked-Rotor Test

The blocked-rotor test on an induction machine, like the short-circuit test on a transformer, gives information about leakage impedances. The rotor of the induction motor is locked to keep it at standstill and a set of low three-phase voltages is applied to circulate rated stator currents. The input power per phase, $P_{in/phase}$, is measured along with the input voltage and stator current. The slip is unity for the locked-rotor condition and hence the circuit resembles that of a secondary-short-circuited transformer. The magnetizing branch impedance is very high compared to the rotor impedance ($R_r + jX_{lr}$) and hence the approximate effective impedance is only the smaller of the two, which is the rotor impedance in this case [110, 154].

The rotor resistance, R_r , the stator inductance, L_s , and the rotor inductance, L_r , are calculated. Also, it is usual to assume that the stator leakage inductance is equal to the rotor leakage inductance [110].

Appendix F

SWITCHING CONFIGURATION OF A SPWM THREE PHASE INVERTER WITH SPACE VECTOR TECHNIQUE

The voltage source three-phase inverter is controlled by six switches, Q_1 to Q_6 , and eight inverter configurations as shown in Figure 135 and F.1 [F1] respectively. The switches are controlled in pairs (Q_1, Q_4), (Q_3, Q_6), (Q_5, Q_2) and the logic for the switch control signals is [150]:

$$\bullet \quad Q_1 \text{ is ON when } V_a > V_T, \quad Q_4 \text{ is ON when } V_a < V_T \quad (\text{F.1.1})$$

$$\bullet \quad Q_3 \text{ is ON when } V_b > V_T, \quad Q_6 \text{ is ON when } V_b < V_T \quad (\text{F.1.2})$$

$$\bullet \quad Q_5 \text{ is ON when } V_c > V_T, \quad Q_2 \text{ is ON when } V_c < V_T \quad (\text{F.1.3})$$

In each configuration, the vector identification uses a ‘0’ to represent the negative phase voltage level and a ‘1’ to represent the positive phase voltage level. In addition, the switches in one inverter branch (each leg) are in controlled in a complementary fashion (1 if the switch is on and 0 if it is off) in order to satisfy the Kirchoff's Voltage Law (KVL) constraint [F1]:

$$Q_1 + Q_4 = 1 \quad (\text{F.2.1})$$

$$Q_2 + Q_5 = 1 \quad (\text{F.2.2})$$

$$Q_3 + Q_6 = 1 \quad (\text{F.2.3})$$

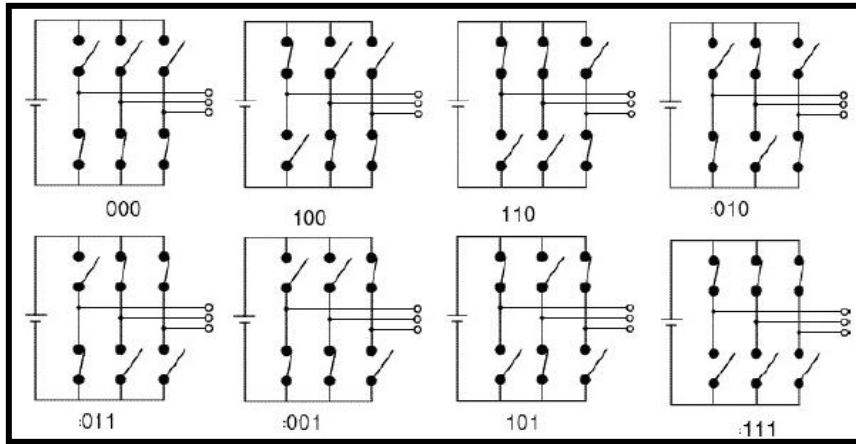


Figure F.1: Eight Switching Configuration of a Three-Phase Inverter
(Source: K. Zhou and D.Wang [F1])

The inverter output pole voltages (fundamental component) are determined as follows (*for modulation index $m=1$*) [145, 150, F1, F2]:

$$\text{if } V_a > V_T \quad \text{then } V_{ao} = 0.5 \cdot V_{DC} \quad (\text{F.3.1})$$

$$V_b > V_T \quad \text{then } V_{bo} = 0.5 \cdot V_{DC} \quad (\text{F.3.2})$$

$$V_c > V_T \quad \text{then } V_{co} = 0.5 \cdot V_{DC} \quad (\text{F.3.3})$$

$$\text{and if } V_a < V_T \quad \text{then } V_{ao} = -0.5 \cdot V_{DC} \quad (\text{F.3.4})$$

$$V_b < V_T \quad \text{then } V_{bo} = -0.5 \cdot V_{DC} \quad (\text{F.3.5})$$

$$V_c < V_T \quad \text{then } V_{co} = -0.5 \cdot V_{DC} \quad (\text{F.3.6})$$

The pole voltages are explained in Figure F.2, [F3], and they fluctuate between $V_{DC}/2$ and $-V_{DC}/2$ for $m=1$ [150, F1].

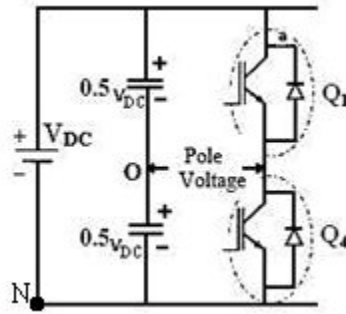


Figure F.2: Explanation of pole voltages in three-phase inverter ($m=1$) (Source: [F3])

The inverter line-to-line voltages, V_{AB} , V_{BV} and V_{CA} , are obtained from the pole voltages as [150, F2]:

$$V_{AB} = V_{ao} - V_{bo} \quad (F.4.1)$$

$$V_{BC} = V_{bo} - V_{co} \quad (F.4.2)$$

$$V_{CA} = V_{co} - V_{ao} \quad (F.4.3)$$

The relationship between the switching variable vector $[Q_1 \ Q_3 \ Q_5]$ and the line-to-line voltage vector $[V_{AB} \ V_{BC} \ V_{CA}]$ is shown in Equation F.5 [145, 150, F2].

$$\begin{bmatrix} V_{AB} \\ V_{BC} \\ V_{CA} \end{bmatrix} = V_{DC} \begin{bmatrix} 1 & -1 & 0 \\ 0 & 1 & -1 \\ -1 & 0 & 1 \end{bmatrix} \begin{bmatrix} Q_1 \\ Q_3 \\ Q_5 \end{bmatrix} \quad (F.5)$$

Choosing a neutral load point N (Figure F.2), we can obtain [150]:

$$V_{ao} = V_{An} + V_{n0} \quad (F.6.1)$$

$$V_{bo} = V_{Bn} + V_{n0} \quad (F.6.2)$$

$$V_{co} = V_{Cn} + V_{n0} \quad (F.6.3)$$

$$V_{An} + V_{Bn} + V_{Cn} = 0 \quad (F.6.4)$$

where V_{An} , V_{Bn} , V_{Cn} are the phase-to-neutral voltages of the load (before the harmonic filter) and V_{n0} is the neutral voltage or load to pole voltage, between point N and the mid-point of the DC source.

The selection of the states in order to generate the given waveform is done by the modulating technique that ensures the use of only the valid states [F1].

$$\frac{V_{DC}}{2} \cdot (Q_1 - Q_4) = V_{An} + V_{n0} \quad (F.7.1)$$

$$\frac{V_{DC}}{2} \cdot (Q_3 - Q_6) = V_{Bn} + V_{n0} \quad (F.7.2)$$

$$\frac{V_{DC}}{2} \cdot (Q_5 - Q_2) = V_{Cn} + V_{n0} \quad (F.7.3)$$

Adding the above equations together gives:

$$\frac{V_{DC}}{2} * (Q_1 + Q_3 + Q_5 - Q_2 - Q_6 - Q_4) = V_{An} + V_{Bn} + V_{Cn} + 3 \cdot V_{n0} \quad (F.8)$$

As we are dealing with balanced voltages [109]:

$$V_{An} + V_{Bn} + V_{Cn} = 0 \quad (F.9)$$

and using the conditions about the control of the switches which are described with Equations F.2.1, F.2.2 and F.2.3, the Equation F.8 yields to:

$$\frac{V_{DC}}{6} * (2 \cdot Q_1 + 2 \cdot Q_3 + 2 \cdot Q_5 - 3) = V_{n0} \quad (F.10)$$

Replacing Equation F.10 into Equations F.7, it can be obtained for the phase to neutral voltages of the load:

$$\frac{V_{DC}}{3} * (2 \cdot Q_1 - Q_3 - Q_5) = V_{An} \quad (F.11.1)$$

$$\frac{V_{DC}}{3} * (2 \cdot Q_3 - Q_1 - Q_5) = V_{Bn} \quad (F.11.2)$$

$$\frac{V_{DC}}{3} * (2 \cdot Q_5 - Q_3 - Q_1) = V_{Cn} \quad (F.11.3)$$

and in vector form

$$\begin{bmatrix} V_{An} \\ V_{Bn} \\ V_{Cn} \end{bmatrix} = \frac{V_{DC}}{3} \begin{bmatrix} 2 & -1 & -1 \\ -1 & 2 & -1 \\ -1 & -1 & 2 \end{bmatrix} \begin{bmatrix} Q_1 \\ Q_3 \\ Q_5 \end{bmatrix} \quad (F.12)$$

The phase to neutral voltages of the load can also be obtained from the line to line voltages as [145, 150]:

$$\begin{bmatrix} V_{AB} \\ V_{BC} \\ V_{CA} \end{bmatrix} = \begin{bmatrix} V_{An} - V_{Bn} \\ V_{Bn} - V_{Cn} \\ V_{Cn} - V_{An} \end{bmatrix} \quad (F.13)$$

which can be written as a function of the phase to neutral voltage vector $[V_{An} \ V_{Bn} \ V_{Cn}]^T$ as:

$$\begin{bmatrix} V_{AB} \\ V_{BC} \\ V_{CA} \end{bmatrix} = \begin{bmatrix} 1 & -1 & 0 \\ 0 & 1 & -1 \\ -1 & 0 & 1 \end{bmatrix} \begin{bmatrix} V_{An} \\ V_{Bn} \\ V_{Cn} \end{bmatrix} \quad (F.14)$$

The above equation represents a linear system where the unknown quantity is the vector $[V_{An} \ V_{Bn} \ V_{Cn}]^T$, but the matrix is singular and so the phase to neutral voltages cannot be found from matrix inversion. However since the phase to neutral voltages add to zero, they can be written as:

$$\begin{bmatrix} V_{AB} \\ V_{BC} \\ 0 \end{bmatrix} = \begin{bmatrix} 1 & -1 & 0 \\ 0 & 1 & -1 \\ 1 & 1 & 1 \end{bmatrix} \begin{bmatrix} V_{An} \\ V_{Bn} \\ V_{Cn} \end{bmatrix} \quad (F.15)$$

which implies:

$$\begin{bmatrix} V_{An} \\ V_{Bn} \\ V_{Cn} \end{bmatrix} = \begin{bmatrix} 1 & -1 & 0 \\ 0 & 1 & -1 \\ 1 & 1 & 1 \end{bmatrix}^{-1} \begin{bmatrix} V_{AB} \\ V_{BC} \\ 0 \end{bmatrix} = \frac{1}{3} \begin{bmatrix} 2 & 1 & 1 \\ -1 & 1 & 1 \\ -1 & -2 & 1 \end{bmatrix} \begin{bmatrix} V_{AB} \\ V_{BC} \\ 0 \end{bmatrix} \quad (\text{F.16})$$

which when expanded gives the phase to neutral voltages in terms of line to line voltages as shown below:

$$\frac{1}{3} * (2 * V_{AB} + V_{BC}) = V_{An} \quad (\text{F.17.1})$$

$$\frac{1}{3} * (V_{BC} - V_{AB}) = V_{Bn} \quad (\text{F.17.2})$$

$$\frac{-1}{3} * (2 * V_{BC} + V_{AB}) = V_{Cn} \quad (\text{F.17.3})$$

The Table F.1 presents the voltages of the three-phase inverter in each one of the eight different configurations.

Table F.1: Switch States and Voltages for Three-Phase SPWM inverter (for m=1)

State	Switching State/Pattern	Load Phase Voltages (Line to Neutral Load)			Line to Line Voltages			Load to Pole Voltage	Pole Voltages		
		V_{An}	V_{Bn}	V_{Cn}	V_{AB}	V_{BC}	V_{CA}	V_{no}	V_{ao}	V_{bo}	V_{co}
Q4, Q6 and Q2 are on, and Q1, Q3 and Q5 are off	[000]	0	0	0	0	0	0	$-\frac{V_{dc}}{2}$	$-\frac{V_{dc}}{2}$	$-\frac{V_{dc}}{2}$	$-\frac{V_{dc}}{2}$
Q1, Q6 and Q2 are on, and Q4, Q3 and Q5 are off	[100]	$\frac{2V_{dc}}{3}$	$-\frac{V_{dc}}{3}$	$-\frac{V_{dc}}{3}$	V_{dc}	0	$-V_{dc}$	$-\frac{V_{dc}}{6}$	$\frac{V_{dc}}{2}$	$-\frac{V_{dc}}{2}$	$-\frac{V_{dc}}{2}$
Q1, Q3 and Q2 are on, and Q4, Q6 and Q5 are off	[110]	$\frac{V_{dc}}{3}$	$\frac{V_{dc}}{3}$	$-\frac{2V_{dc}}{3}$	0	V_{dc}	$-V_{dc}$	$\frac{V_{dc}}{6}$	$\frac{V_{dc}}{2}$	$\frac{V_{dc}}{2}$	$-\frac{V_{dc}}{2}$
Q4, Q3 and Q2 are on, and Q1, Q6 and Q5 are off	[010]	$-\frac{V_{dc}}{3}$	$\frac{2V_{dc}}{3}$	$-\frac{V_{dc}}{3}$	$-V_{dc}$	V_{dc}	0	$-\frac{V_{dc}}{6}$	$-\frac{V_{dc}}{2}$	$\frac{V_{dc}}{2}$	$-\frac{V_{dc}}{2}$
Q4, Q3 and Q5 are on, and Q1, Q6 and Q2 are off	[011]	$-\frac{2V_{dc}}{3}$	$\frac{V_{dc}}{3}$	$\frac{V_{dc}}{3}$	$-V_{dc}$	0	V_{dc}	$\frac{V_{dc}}{6}$	$-\frac{V_{dc}}{2}$	$\frac{V_{dc}}{2}$	$\frac{V_{dc}}{2}$
Q4, Q6 and Q5 are on, and Q1, Q3 and Q2 are off	[001]	$-\frac{V_{dc}}{3}$	$-\frac{V_{dc}}{3}$	$\frac{2V_{dc}}{3}$	0	$-V_{dc}$	V_{dc}	$-\frac{V_{dc}}{6}$	$-\frac{V_{dc}}{2}$	$-\frac{V_{dc}}{2}$	$\frac{V_{dc}}{2}$
Q1, Q6 and Q5 are on, and Q4, Q3 and Q2 are off	[101]	$\frac{V_{dc}}{3}$	$-\frac{2V_{dc}}{3}$	$\frac{V_{dc}}{3}$	V_{dc}	$-V_{dc}$	0	$\frac{V_{dc}}{6}$	$\frac{V_{dc}}{2}$	$-\frac{V_{dc}}{2}$	$\frac{V_{dc}}{2}$
Q1, Q3 and Q5 are on, and Q4, Q6 and Q2 are off	[111]	0	0	0	0	0	0	$\frac{V_{dc}}{2}$	$\frac{V_{dc}}{2}$	$\frac{V_{dc}}{2}$	$\frac{V_{dc}}{2}$

Appendix G

Part I - Derivation of Fourier Series Formula for the Square Wave Inverter Voltages

If function f is a periodic, piecewise continuous and an odd, then its trigonometric Fourier series is given by [G1]:

$$f(\omega t) = \sum_{n=1}^{\infty} b_n \cdot \sin(n \cdot \omega t) \quad (\text{G.1.1})$$

where, for $n = 1, 2, 3, \dots$

$$b_n = \frac{2}{\pi} \int_0^{\pi} f(\omega t) \cdot \sin(n \cdot \omega t) d(\omega t) \quad (\text{G.1.2})$$

Function which describes phase voltages of square wave inverters is shown in the Figure G.1 [129].

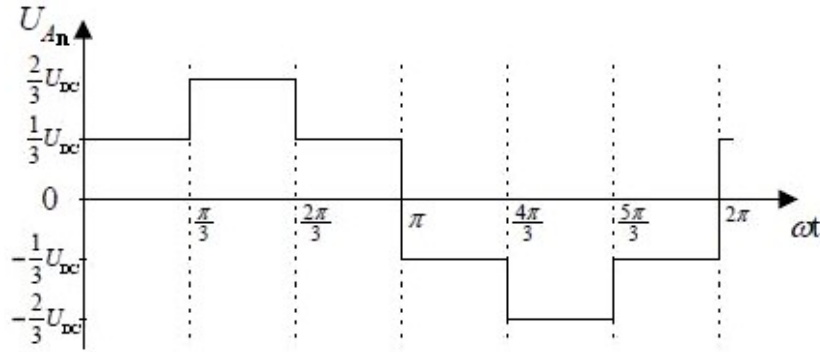


Figure G.1: A typical example of one phase voltage of the three-phase square wave inverter (Source: M. Żelechowski [129])

Taking into consideration this function coefficient b_n can be written as follows [129]:

$$\begin{aligned} b_n &= \frac{2}{\pi} \int_0^{\pi} U_{An}(t) \sin(n\omega t) d(\omega t) \\ &= \frac{2}{\pi} \left(\int_0^{\pi/3} \frac{1}{3} U_{dc} \sin(n\omega t) d(\omega t) + \int_{\pi/3}^{2\pi/3} \frac{2}{3} U_{dc} \sin(n\omega t) d(\omega t) + \int_{2\pi/3}^{\pi} \frac{1}{3} U_{dc} \sin(n\omega t) d(\omega t) \right) \\ &= \frac{2}{3\pi} \frac{1}{n} U_{dc} \left(-\cos(n\omega t) \Big|_0^{\pi/3} - 2\cos(n\omega t) \Big|_{\pi/3}^{2\pi/3} - \cos(n\omega t) \Big|_{2\pi/3}^{\pi} \right) \\ &= \frac{2}{3\pi} \frac{1}{n} U_{dc} \left(1 - \cos(n\pi) + \cos\left(n\frac{\pi}{3}\right) - \cos\left(n\frac{2}{3}\pi\right) \right) \end{aligned} \quad (\text{G.1.3})$$

for even n :

$$\begin{aligned}
& 1 - \cos(n\pi) + \cos\left(n\frac{\pi}{3}\right) - \cos\left(n\frac{2}{3}\pi\right) \\
& = 1 - 1 + \cos\left(n\frac{\pi}{3}\right) - \cos\left(n\pi - n\frac{\pi}{3}\right) = 0
\end{aligned} \tag{G.1.4}$$

and for odd n :

$$\begin{aligned}
& 1 - \cos(n\pi) + \cos\left(n\frac{\pi}{3}\right) - \cos\left(n\frac{2}{3}\pi\right) = 1 + 1 + \cos\left(n\frac{\pi}{3}\right) - \cos\left(\pi + (n-1)\pi - n\frac{\pi}{3}\right) \\
& = 2\left(1 + \cos\left(n\frac{\pi}{3}\right)\right)
\end{aligned} \tag{G.1.5}$$

From above formulas the Fourier series for U_{An} is given by:

$$\begin{aligned}
U_{An} &= \frac{4}{3\pi} U_{DC} \sum_{n=1}^{\infty} \frac{1}{n} \left(1 + \cos\left(n\frac{\pi}{3}\right)\right) \sin(n\omega t) \\
&= \frac{2}{\pi} U_{DC} \sum_{n=1}^{\infty} \frac{1}{n} \sin(n\omega t)
\end{aligned} \tag{G.1.6}$$

where:

$$n=1, 5, 7, 11, 13, \dots, \infty$$

The phase voltage of a square wave three-phase inverter can be expressed also as [F3]:

$$U_{An} = \frac{2}{n\pi} U_{DC} \sum_{n=1}^{\infty} \sin(n \cdot \omega t) \tag{G.1.7}$$

where:

$$U_{mn} = \frac{2}{n\pi} U_{DC} \tag{G.1.8}$$

is the peak value of the n^{th} harmonic. For $n=1$ is the 1st harmonic (fundamental component), for $n=5$ is the 5th harmonic etc.

Also, we can derive [F3]:

$$U_{Bn} = \frac{2}{n\pi} U_{DC} \sum_{n=1}^{\infty} \sin n \left(\omega t - \frac{2\pi}{3} \right) \tag{G.1.9}$$

$$U_{Cn} = \frac{2}{n\pi} U_{DC} \sum_{n=1}^{\infty} \sin n \left(\omega t - \frac{4\pi}{3} \right) \tag{G.1.9}$$

Furthermore, function which describes line voltages of square wave inverters is shown in the Figure G.2 [129].

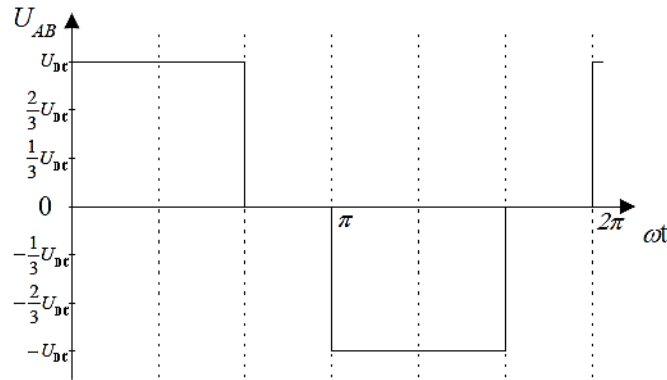


Figure G.2: A typical example of line voltage V_{AB} , of the three-phase square wave inverter (Source: M. Żelechowski [129])

In a similar way as above, can be found for the line voltages [F3]:

$$U_{AB} = \frac{2}{n\pi} U_{DC} \sum_{n=1}^{\infty} \sin(n \cdot \omega t) - \sin n(\omega t - \frac{2\pi}{3}) \quad (G. 1.10)$$

and also:

$$U_{BC} = \frac{2}{n\pi} U_{DC} \sum_{n=1}^{\infty} \sin n \left(\omega t - \frac{2\pi}{3} \right) - \sin n \left(\omega t - \frac{4\pi}{3} \right) \quad (G. 1.11)$$

$$U_{CA} = \frac{2}{n\pi} U_{DC} \sum_{n=1}^{\infty} \sin n \left(\omega t - \frac{4\pi}{3} \right) - \sin n(\omega t) \quad (G. 1.12)$$

where:

$$n=1, 3, 5, 7, 11, 13, \dots, \infty$$

The line or phase harmonic voltages of the three-phase square wave inverter are balanced (have identical magnitudes and are phase apart by 120°). It may be noted that though the line voltages have 3rd and multiples of 3rd order harmonic distortions, the phase voltages are free from these distortions [F3].

Finally, function which describes pole voltages of square wave inverters is shown in the Figure G.3 [129].

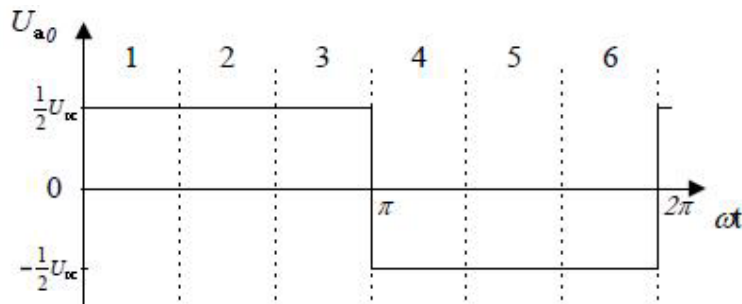


Figure G.3: A typical example of pole voltage V_{a0} , of the three-phase square wave inverter (Source: M. Żelechowski [129])

In a similar analysis with the above, can be found [F3]:

$$U_{ao} = \frac{2}{n\pi} U_{DC} \sum_{n=1}^{\infty} \sin(n \cdot \omega t) \quad (G. 1.13)$$

and:

$$U_{bo} = \frac{2}{n\pi} U_{DC} \sum_{n=1}^{\infty} \sin\left(n \cdot \omega t - \frac{2\pi}{3}\right) \quad (G. 1.14)$$

$$U_{co} = \frac{2}{n\pi} U_{DC} \sum_{n=1}^{\infty} \sin\left(n \cdot \omega t - \frac{4\pi}{3}\right) \quad (G. 1.15)$$

where:

$$n=1, 3, 5, 7, 11, 13, \dots, \infty$$

For the fundamental component (1st harmonic) of all the above voltages, the fundamental magnitude ($n=1$) is:

$$U_{ao} = U_{bo} = U_{co} = \frac{2}{\pi} U_{DC} \quad (G. 1.16)$$

$$U_{AB} = U_{BC} = U_{CA} = \frac{2 \cdot \sqrt{3}}{\pi} U_{DC} \quad (G. 1.17)$$

$$U_{An} = U_{Bn} = U_{Cn} = \frac{2}{\pi} U_{DC} \quad (G. 1.18)$$

Part II - Formula for the SPWM Inverter Voltages

In SPWM inverter the widths of the pole voltage pulses and as a result the phase and line waveforms, over the output cycle, vary in a sinusoidal manner as shown in Figure 138. The harmonic analysis of the sine-modulated pole voltage waveforms gives the below expressions [150, F3]:

$$U_{ao} = m \cdot \frac{0.5}{n} U_{DC} \sum_{n=1}^{\infty} \sin(n \cdot \omega t) + \text{High Frequency Terms} \quad (G. 1.19)$$

and

$$U_{bo} = m \cdot \frac{0.5}{n} U_{DC} \sum_{n=1}^{\infty} \sin\left(n \cdot \omega t - \frac{2\pi}{3}\right) + \text{High Frequency Terms} \quad (G. 1.20)$$

$$U_{co} = m \cdot \frac{0.5}{n} U_{DC} \sum_{n=1}^{\infty} \sin\left(n \cdot \omega t - \frac{4\pi}{3}\right) + \text{High Frequency Terms} \quad (G. 1.21)$$

For $m = 1$ the fundamental component pole voltage will have a magnitude of $0.5 \cdot V_{DC}$. This magnitude is only **78.55%** of the fundamental pole voltage magnitude output by a square wave inverter operating from the same DC link voltage (see Equation G.1.16).

The line voltage magnitude at the fundamental component it is given as follow (for $0 \leq m \leq 1$) [145, 146]:

$$V_{AB} = V_{BC} = V_{CA} = \frac{m}{2} \cdot \sqrt{3} \cdot V_{DC} \quad (\text{G.1.22})$$

and in RMS value:

$$V_{AB(rms)} = V_{BC(rms)} = V_{CA(rms)} = \frac{m}{2} \cdot \frac{\sqrt{3}}{\sqrt{2}} \cdot V_{DC} \quad (\text{G.1.22})$$

The amplitude of the fundamental component of the SPWM inverter voltage output is thus controlled by m (linearly proportional). *This is significant in the case of an unregulated DC supply voltage because the value of m can be adjusted to compensate for variations in the DC supply voltage, producing a constant-amplitude output.* Alternatively, m can be varied to change the amplitude of the inverter voltage output [143].

Moreover, to further increase the amplitude of the line voltage, the modulation ratio should be greater than 1 ($m > 1$), which leads to *over modulation*. The relationship between the amplitude of the fundamental ac component of line voltage and the DC link voltage becomes nonlinear. The whole range characteristic of the modulation methods is shown in Figure G.4 [G2].

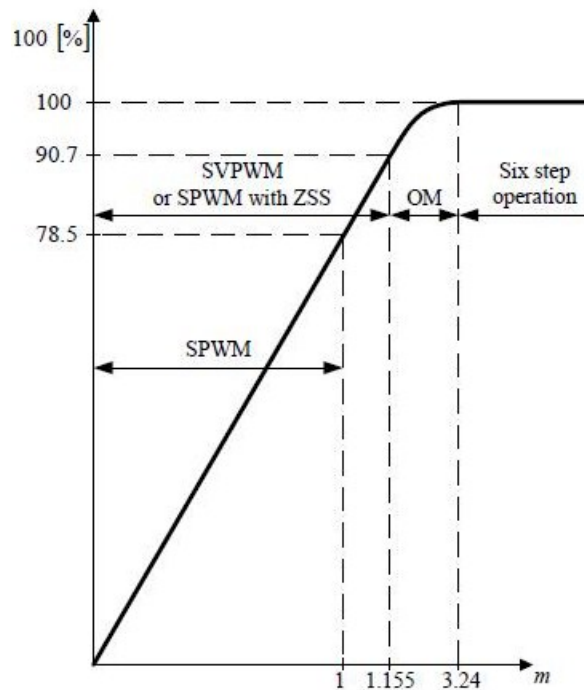


Figure G.4: Output voltage of VSI, as a percentage of square wave technique, versus modulation index for different PWM techniques. SVPWM: space vector PWM, ZSS: Zero Sequence Signal, OM: Over-modulation (Source: M.P. Kazmierkowski et al. [G2])

Appendix H

AVERAGE ELECTRIC POWER GENERATION & MATLAB CODE

The SCIG (Squirrel Cage Induction Generator) numerical model with the simplified VSI presented in Sections 2.3, 2.4.2, 3.3, 3.4 and 3.5, is also used to calculate the *electrical power delivered by the generator*. This is calculated using the *stator voltage of individual phases* V_a , V_b and V_c , and the *stator currents for individual phases* $i_{a(s)}$, $i_{b(s)}$ and $i_{c(s)}$. The *instantaneous electric power* for each of the three windings is calculated as shown below:

$$Pe_{w1} = V_a * i_{a(s)} \quad (H.1)$$

$$Pe_{w2} = V_b * i_{b(s)} \quad (H.2)$$

$$Pe_{w3} = V_c * i_{c(s)} \quad (H.3)$$

and the *total instantaneous electric power is the sum* of the three windings,

$$P_e = Pe_{w1} + Pe_{w2} + Pe_{w3} \quad (H.4)$$

From this it follows that the rate of change of electric energy, dE , can be calculated from:

$$dE = P_e * dt \quad (H.5)$$

Therefore, the average electric power of generator from t_o to t_1 will be:

$$Pe_{avg} = \frac{t_1}{t_1 - t_o} \int_{t_o}^{t_1} dE \quad (H.6)$$

The instantaneous measurement of the stator voltages and current in *stationary phases coordinate system (abc)* from the induction motor/generator block in MATLAB/Simulink® (see Figure 166 – IG Block) was held using the “Voltage Measurement” block of the SimPowerSystems toolbox as shown in Figure H.1 and the Simulink output of the “Asynchronous Machine” block which is a vector containing measurement signals, where you can *demultiplex* these signals by using the Bus Selector block provided in the Simulink library, as shown in Figures H.2 and H.3, respectively.

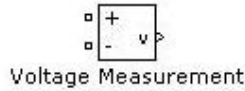


Figure **H.1**: Voltage Measurement block of the SimPowerSystems toolbox. The positive input connected with the electrical signal (V_a , V_b or V_c) and the negative with the ground.



Figure **H.2**: Bus Selector block of Simulink library. The input is the output signal of the Asynchronous Machine block and the output is the signals you choose to demultiplex as shown in Figure H.3.

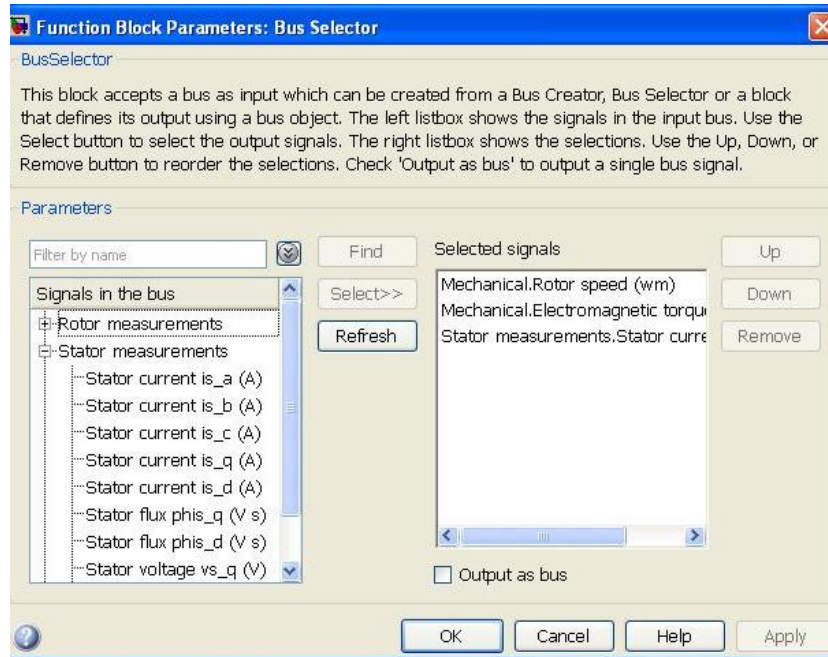


Figure H.3: Bus Selector output signals in case of Asynchronous Machine as an input. The left list box has shown the three stator currents in abc reference frame.

The MATLAB code for the calculation of average electric power is shown in Figure H.4. During each simulation run the variables V_{s_a} , V_{s_b} , V_{s_c} and I_{s_a} , I_{s_b} , I_{s_c} , which are referred to stator voltage and stator currents respectively, were saved in MATLAB Workspace as “Structure with Time” so that be able to be used by the below code.

```

1  *** Calculation of Average Electric Power for a 3-Phase AC Electric ***
2  *** Motor/Generator ***
3
4  P_electric_average = zeros(1, 1); % Zero matrix %
5  time = V_s_a.time; % Time vector (time values where the voltage and current was calculated) %
6
7  for j = 1:1
8
9      E = 0; % Initial value of Electric Energy %
10
11     for i = 10000:(length(time)-1) % Range of values from Time Vector (excluding the first 10000 seconds of simulation... %
12         % ... (10 seconds is reality) because of transient purposes) %
13
14         P_electric_instantaneous_winding_1 = V_s_a.signals.values(i,j)*I_s_a.signals.values(i,j); % Instantaneous Electric Power from first winding %
15         P_electric_instantaneous_winding_2 = V_s_b.signals.values(i,j)*I_s_b.signals.values(i,j); % Instantaneous Electric Power from second winding %
16         P_electric_instantaneous_winding_3 = V_s_c.signals.values(i,j)*I_s_c.signals.values(i,j); % Instantaneous Electric Power from third winding %
17
18         P_electric_instantaneous_total = P_electric_instantaneous_winding_1 ...
19         + P_electric_instantaneous_winding_2 + P_electric_instantaneous_winding_3; % Total Instantaneous Electric Power from all windings %
20
21         Dt = time(i+1,j) - time(i,j); % Change of time %
22
23         DE = (P_electric_instantaneous_total)*Dt; % Change of Electric Energy %
24         E = DE + E; % Total Electric Energy %
25     end
26
27     P_electric_average_j = E / (time(length(time),j) - time(10000,j)); % Average Electric Power %
28     P_electric_average(j) = P_electric_average_j; % Replace zeros at zero matrix with the values of Average Electric Power %
29 end
30
31 P_electric_average % Average Electric Power value %
32

```

Figure H.4: MATLAB code for the calculation of average electric power

VITA

The author, **Vasileios Tzelepis**, was born in *Athens, Greece* in 1989. After completing his schoolwork at 6th *High School of Piraeus* (2007), in Greece, he entered 1st at the *Technological Educational Institute of Athens* and he obtained his four (4) years *Bachelor of Science (BSc)* degree in *Naval Architecture and Marine Engineering* with honors in 2012 while his Bachelor Thesis was awarded as the “*Best Diploma Thesis*”. After his graduation, he worked for two (2) years in shipping industry for ship companies, marine consulting companies and research projects as a naval architect, cadet engineer, marine engineer consultant and research engineer. He joined the *University of New Orleans* in Louisiana, USA, to pursue a two (2) years *Master of Science (MSc)* in *Naval Architecture and Marine Engineering* with honors in 2015 and became a member of Professor Nikolaos Xiros’ research team, working on *National State Foundation (NSF)* of USA project for two (2) years, in 2014. Furthermore, the author has received scholarships from *State Scholarship Foundation* of Greece in 2007 (“**Top Student**” prize), international society of *SNAME* in 2013 (“**The Walter M. & Doris H. MacLean Scholar**”) and *University of New Orleans* in 2014 (“**The Privateer Graduate Scholarship**”). Finally, **Vasileios Tzelepis** is the author of four (4) *journals* and three (3) *conference papers* respectively and he is a *member* of *SNAME*, *SAWE*, *RINA*, *AADE* and *HELMEPA*.